ISTITUTO NAZIONALE DI FISICA NUCLEARE

Sezione di Genova
Sezione di Milano
Laboratori Nazionali di Frascati

INFN/code-09/001
12 Novembre 2008

TECHNICAL DESIGN REPORT OF A SUPERCONDUCTING MODEL DIPOLE FOR FAIR SIS300

F.Alessandria[2], S.Angius[4], G.Bellomo[2], P.Fabbricatore[1], S.Farinon[1], U.Gambardella[3], R.Marabotto[4], R.Musenich[1], R.Repetto[4], M.Sorbi[2] and G.Volpini[2]

[1)] INFN-Sezione di Genova, Via Dodecaneso 33, 16146 Genova, Italy
[2)] INFN-Sezione di Milano, Laboratorio LASA, Via Fratelli Cervi 201, 20090 Segrate (MI), Italy
[3)] INFN-Laboratori Nazionali di Frascati Via E. Fermi 40, I-00044 Frascati, Italy
[4)] ASG-Superconductors, Corso Perrone 73R, Genova, Italy

Abstract

This report deals with the R&D activities aimed at developing the high field rapidly-cycling super-conducting dipoles needed for SIS300 synchrotron of the FAIR facility at GSI. The present lattice design includes 48 long dipoles with magnetic length 7.757 m and 12 short dipoles with magnetic length 3.879 m. The coils have two main features: they are curved (the corresponding sagitta is 112.8 mm for long dipoles), and they are fast ramped (for a superconducting magnet). Both these characteristics demand a challenging R&D, aimed at the development of the required low loss conductor, a robust design with respect to fatigue issues and a suitable winding technology. The Italian National Institute of Nuclear Physics (INFN) is performing this R&D. A project, called DISCORAP ("Dipoli SuperCOnduttori RApidamente Pulsati"), started in 2006 in accordance with a specific INFN-FAIR Memorandum of Understanding signed by both institutions in December 2006. The aim is to have a complete cold mass model of the short dipole ready in the summer of 2009. After a preliminary test of the cold mass in a vertical cryostat, it will be integrated into a horizontal cryostat for a test series at GSI.

Published by ***SIS–Pubblicazioni***
Laboratori Nazionali di Frascati

A draft report of this document was submitted to a panel of international expert, who met in Genova on November 12th and 13th 2008 in a formal review session with the authors of the document. Many advices and suggestions coming from the panel resulted into some modifications of the design. The present document includes the updated design issues.

The authors acknowledge the panel experts Luca Bottura, Shomo Caspi, Arnaud Devred, Davide Tommasini and Lucio Rossi (chair) for accepting to review the design.

Table of Contents

Index of Figures

Index of Tables

1. INTRODUCTION

In the framework of a large international collaboration it is planned to construct a new accelerator complex[1)], which will be integrated in the existing GSI facility in Darmstadt and will provide high intensity primary and secondary beams of ions and antiprotons for experiments in nuclear, atomic and plasma physics. The heart of the FAIR facility is the synchrotron SIS100 (100 T·m rigidity), which will accelerate ions and protons at a high repetition rate and send them to either the targets for Radioactive Ion Beam (RIB) or Antiproton Beam production or the SIS300 synchrotron (300 T·m rigidity), for further acceleration to higher energies (90 GeV protons). In order to reach the required high intensities, the magnets of the synchrotrons[2)] have to be rapidly pulsed at a high repetition frequency. The required dipole ramp rate is 4 T/s for the SIS100 at about 1 Hz and 1 T/s for the SIS300, with a duty cycle of 50% (Fig.1 shows an aerial pictorial view of the planned facilities). The two synchrotrons are located in the same tunnel as shown in Fig.2, one above the other.

This report deals with the R&D activities aimed at developing the high field rapidly-cycling super-conducting dipoles needed for the SIS300.[3),4),5),6),7),8)] At an early stage of the FAIR facility design, the beam rigidity of the synchrotron placed after the SIS100 was 200 T·m. This rigidity was obtained through superconducting dipoles of 2.9 m magnetic length, generating a 4 T field in 86 mm aperture. During the R&D phase, it was decided to

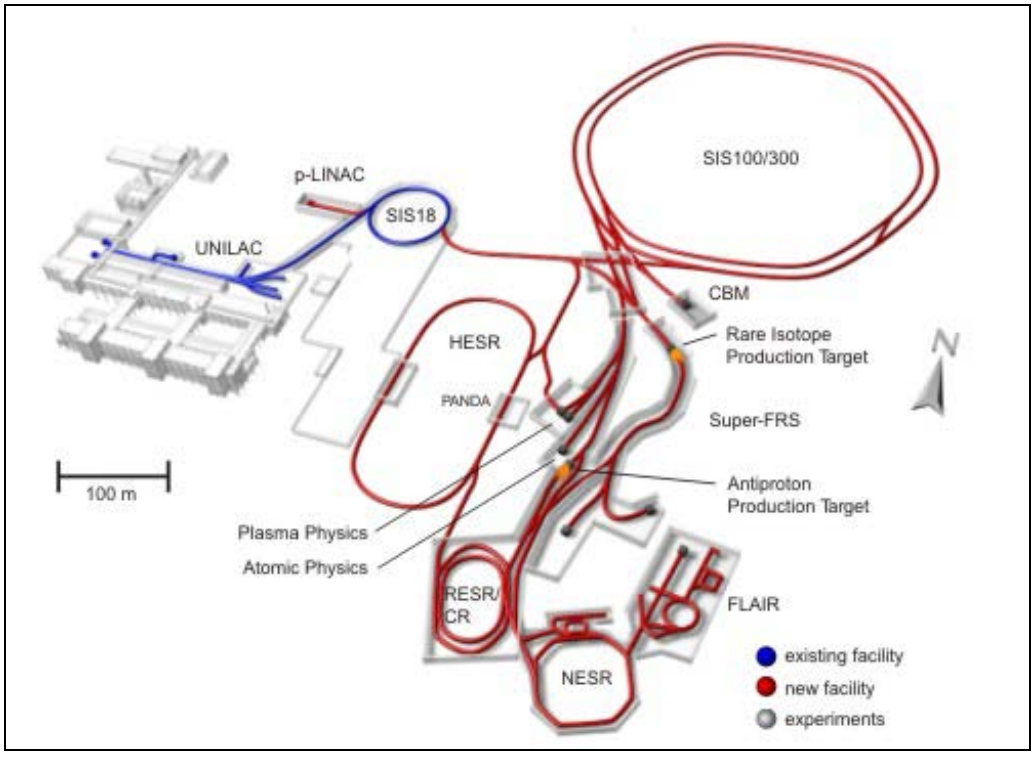

FIG.1: Actual GSI laboratories and the new facility FAIR with the two large synchrotrons. (GSI courtesy).

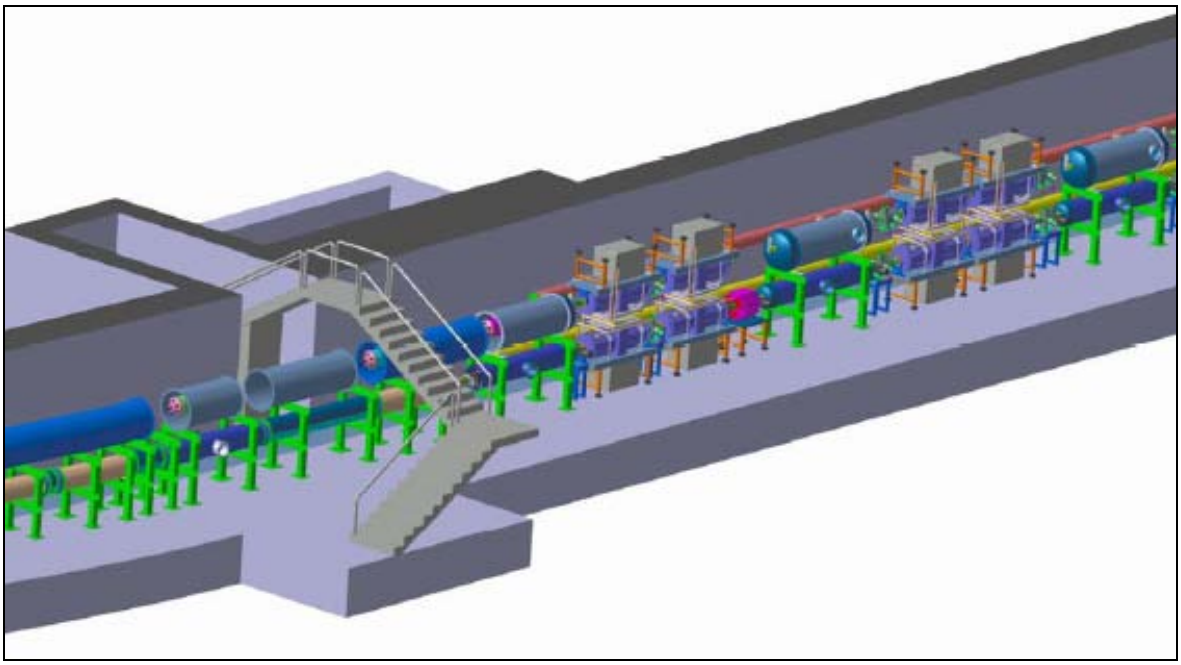

FIG.2: The squared tunnel hosting the two synchrotrons (SIS 300 is located above SIS100). (Courtesy of GSI).

increase the beam rigidity of this second synchrotron to 300 T·m, the dipole aperture field to 6 T, and in addition the inner coil diameter to 100 mm. IHEP, Protvino, prepared a Conceptual Design Report on the basis of the UNK dipole[9)]. The two-layer coil (based on LHC dipole outer layer cable with stainless steel core) was designed to be cooled with supercritical helium, re-cooled by two-phase helium within the magnet.

In a later stage of the SIS300 design, it was stressed the importance to enlarge the acceptance at a minimum field volume. A curved design for the dipoles with a curvature radius of 66.67 m was proposed. The present lattice design includes 48 long dipoles with magnetic length 7.757 m (sagitta 112.8 mm) and 12 short dipoles with magnetic length 3.94 m (sagitta 28.2 mm). Besides the curved layout, these coils have the characteristic to be fast cycled. Both these aspects demand for a challenging R&D, aimed at the development of a low loss conductor, a robust design with respect to fatigue issues and a suitable winding technology.

The Italian National Institute of Nuclear Physics (INFN) proposed to investigate the possibility to perform these R&D activities. As first step, in order to check if show-stoppers could arise at constructive level, technical feasibility studies were performed involving experienced companies. The positive answer coming from these studies together with the promising result of the cost estimates (potential cost save with respect to the 6 T straight magnet) gave the 'green light' to further design work in the framework of a project called DISCORAP (*DIpoli SuperCOnduttori RApidamente Pulsati*), according to a specific INFN-FAIR Memorandum of Understanding signed by both institutions in December 2006.

As second step some coil winding models with a curved mandrel were built to assess the constructive feasibility of the curved coil. In parallel design activities were performed.

The present Technical Design Report reflects the conclusions of these design and winding model activities.

The third step is in progress. The aim is to have a complete cold mass model of the short dipole ready by the summer of 2009. After a preliminary test of the cold mass in a vertical cryostat, it will be integrated in a horizontal cryostat for a test campaign at GSI. Once completed this R&D phase, the future activities will be devoted to the development of real prototype magnets (4 in total according to the present previsions) preliminary to a pre-series production.

This TDR is inherent in the design activities, which are discussed with many details, stressing the problematic related to the ac losses, the thermal stability, the mechanical aspects involved in a magnet to be cycled 10^7 times and the manufacturing problems to be faced.

- Section 2 includes a general description of the magnet with the relevant drawings and the genesis of the design choices.
- Section 3 reports a detailed discussion about the conductor problematic. The conductor is one of the basic aspects of the R&D activity because the main contribution to ac losses is coming from it. Hysteretic losses as well as intra and inter strand coupling losses shall be minimized, within the limit coming from the present wire technology. A special conductor has been developed for this project.
- Section 4 is dedicated to 2D and 3D magnetic analyses. Several issues are included: magnetic field distribution, geometrical harmonics, harmonics due to permanent and eddy currents, coil ends effects on field quality.
- Section 0 includes another relevant aspect for this magnet, i.e. the evaluation of heat dissipations in ac conditions. Several loss mechanisms are studied: ac losses in the conductor, hysteretic and dynamic losses in iron lamination, losses in collars and other metallic structures due to the eddy current, loss in coil ends.
- Section 6 deals with the mechanical aspects. Both 2D and 3D finite element analyses have been performed to evaluate stresses and deformations coming out during assembly, cool-down and energization. Particular emphasis is given to the possible fatigue problems ensuing from the large operating field rate over a large lifetime cycle number. The effect of the mechanical deformations on the field quality is also discussed in this section.
- Section 7 reports studies and computation related to the conductor and winding stability and to the heat transfer problematic.
- Section 8 deals with quench and protection issues.
- In Section 9 the cryostat design aspects are briefly summarized. In fact the cryostat main role is to allow a test of the cold mass in field, temperature and heat exchange conditions as real as possible for assessing the design choices. Under this view the horizontal cryostat is strictly functional to this scope, and marginal with respect the scopes of the R&D.
- Section 10 shows the results of the industrial R&D aimed at developing the constructive methods of a curved magnet.

- In Section 11 more detailed information regarding the magnet structure is given with drawings and pictures.
- Finally in Section 12 a detailed report regarding the constructive plan and future developments is given.

Appendixes report detailed studies and computations.

2. MAGNET LAYOUT

Since the beginning of the R&D activities, preliminary to the engineering design, it was clear that one of the main problems to be solved was the technical feasibility of a cos-theta curved magnet. In this frame two interconnected aspects were relevant:

a) the development of a reliable manufacturing method for a curved magnet;
b) the development of a magnet design, which minimized the difficulties of the manufacture.

These two aspects were investigated in parallel following a complex process with many feedbacks between design activities (done by INFN) and feasibility analyses (done in the industries). Here we summarize the main results in terms of coil layout and developed manufacturing method. The design activities had to face two other very important aspects. The first one is of mechanical nature, since the magnet has to support 10^7 magnetic cycles. The second one is related to the need of limiting the coil heating and removing efficiently the heat dissipation.

2.1 Main design principles

Table 1 shows the main characteristics of the model coil, corresponding to the FAIR requirements for the short dipoles of SIS300.

The starting assumption for the design was that the coil should be wound curved, because: 1) this solutions allows defining a curved geometry of the coil with no residual stresses; 2) once cured, the coil can be handled in a simple and safe way for the following manufacturing operations (collaring, insertion in the iron yoke, …).

A different solution (involving the bending of a straight coil) had to face the problem of the spring back effect during all manufacturing stages and coil operation. The unpredictability of a mechanically loaded curved coil led us to reject this option. In fact, considering a coil outer radius around 65.4 mm (50 mm inner radius + 15.4 mm of conductor radial thickness and insulation), the bending strain for obtaining a curvature of 66.67 m is about 10^{-3}. This value is too high when considering both the control of the coil geometry during the collaring and the possible shear failures of cable-to-cable insulation.

The choice of a curved winding naturally orients the design to a single layer coil mechanically supported only by the collars. These important choices are based on the reason

TAB.1: Characteristics of the model coil.

Nominal field (T) :	4.5
Ramp rate (T/s)	1
Radius of magnet geometrical curvature (m)	66 2/3
Magnetic length (m)	3.879
Bending angle (deg)	3 1/3
Coil aperture (mm)	100
Max temperature of supercritical He (K)	4.7

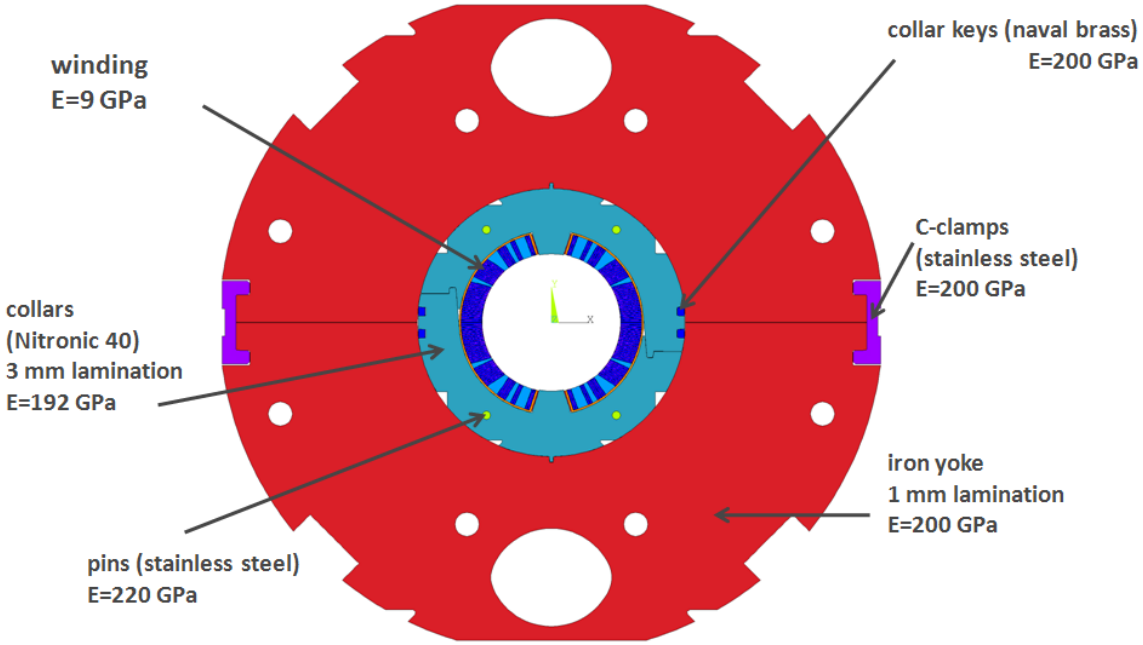

FIG.3: Cross section of the cold mass. The 5 blocks winding is in blue, the collars are in green and the iron yoke lamination in red. The two halves of the iron are clamped together using Al alloy clamps.

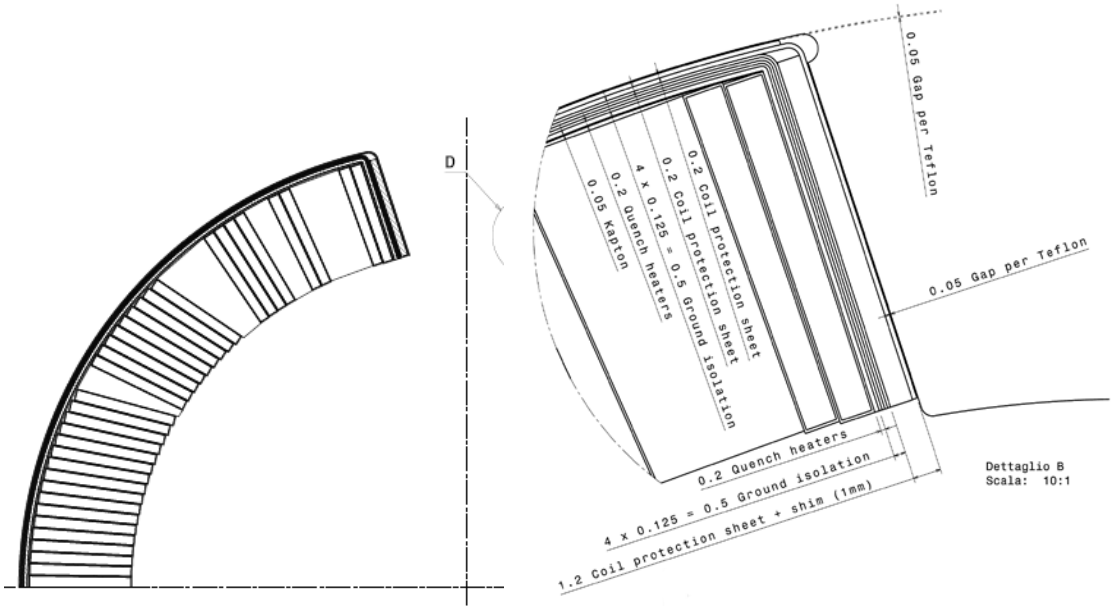

FIG.4: Details of the winding structure with the 5 blocks, the edge spacers and the ground insulation. The coil is also protected by two 0.2 mm thick stainless steel sheaths, which shall prevent the collars to damage the ground insulation.

that the mechanical coupling between two curved layers or between a curved collared coil and a curved yoke appear to be critical operations, which could be afforded only once the simplest curved layout (single collared layer) had been deeply investigated. We were helped in moving to this direction by the relatively low value of the field (4.5 T), obtainable involving one layer only. Furthermore, the magnetic forces are not significantly large to require a mechanical role

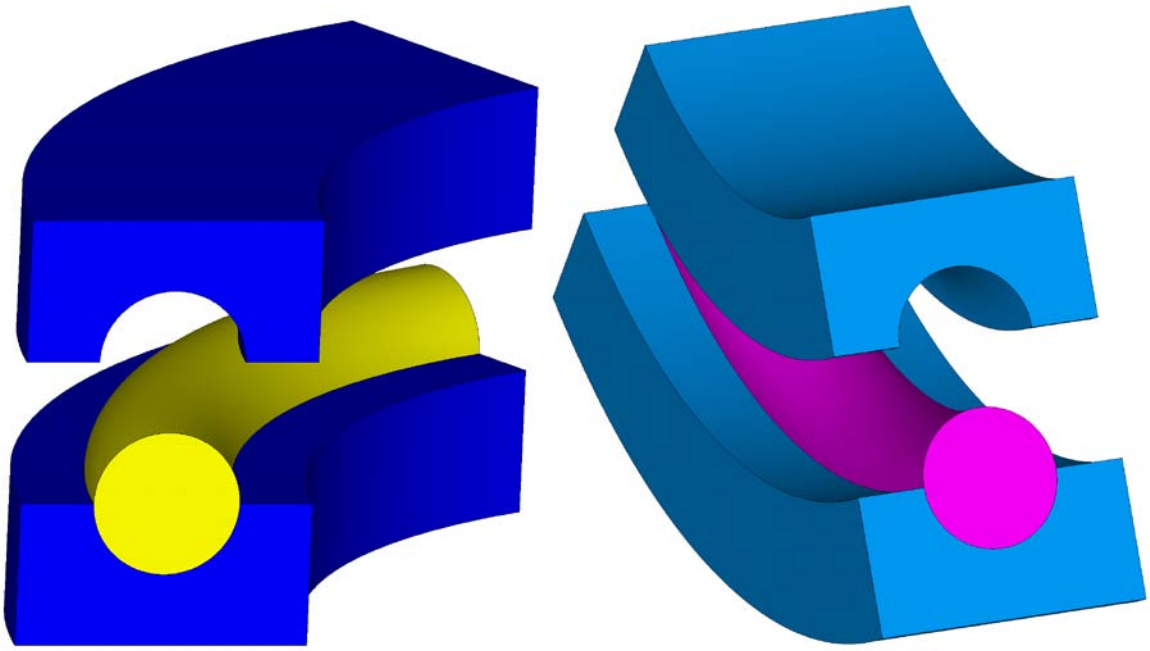

FIG.5: Sketch of the iron yoke assembly options: horizontal split (on the left) and vertical split (on the right).

of the yoke. The field had been a little higher (5 T), this path along design choices would have become impossible to be gone through.

Nevertheless, the iron yoke must have a role in limiting the mechanical deformations of the collared coil. If not, we could have fatigue failures in some locations. This point shows the difference between a small and a large number of magnetic cycles. In our case the magnet shall be cycled 10 million times. Such cycling will depress the mechanical strength of the materials. This should be taken into account both in the design (minimizing the stress variation during cycle) and in the material choice, by selecting fatigue resistant materials.

On these bases a 5 block layout was chosen. The winding is mechanically supported by 30 mm wide collars of high strength austenitic steel and is pre-stressed at 70 MPa at room temperature. The iron lamination is mechanically coupled to the collared coil in a way to give no further coil pre-stress but to limit the collar deformation during magnetic energization. Fig.3 shows the cross section of the cold mass. More details of the winding region are shown in Fig.4.

As it can be seen in Fig.3, the basic design choice was to have a horizontal iron splitting. The reason for this choice is ascribed to the geometrical curvature of the magnet in the horizontal plane. The horizontal splitting allows performing the collared coil integration into the yoke in vertical. On the contrary a vertical splitting requires the development of a difficult mounting operation in horizontal involving a tool moving with high precision the 2.5 t half yokes one against the other with the coil in the middle. In principle this latter problem could be avoided if the collared coil is rotated by 90°. This option was analyzed from the manufacture point of view and considered risky and expensive; moreover the collared-coil

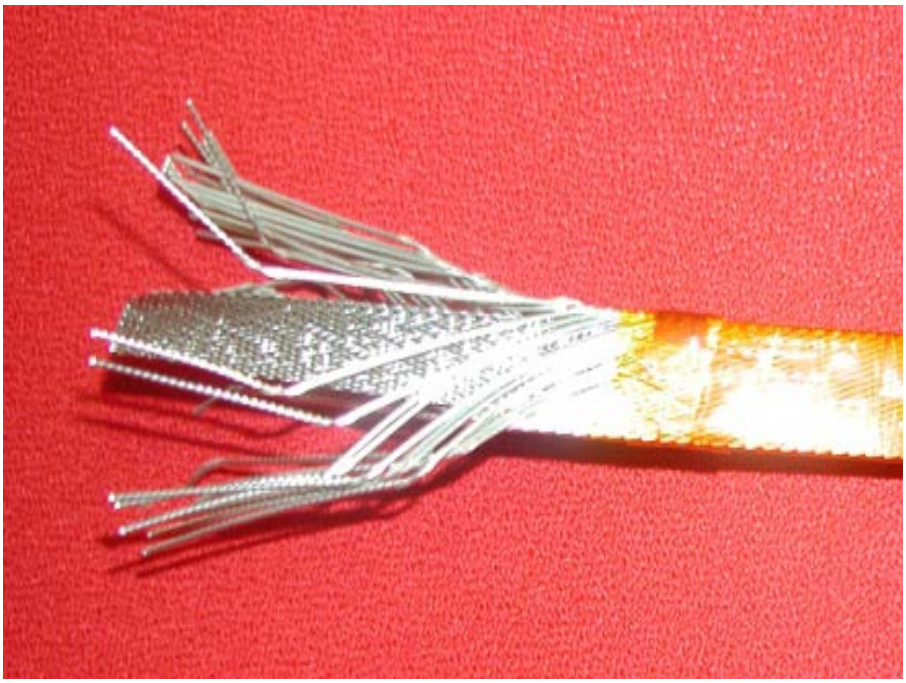

FIG.6: The 36 strand Rutherford cable. In between the strands one can see the thin stainless steel core used for depressing the inter-strand coupling currents.

to iron contact surfaces are different for lower and upper side as shown in Fig.5. The main drawback of a horizontal split is the presence of a gap between the iron poles affecting the field quality. In performing the mechanical design we analyzed in deep this point, concluding that the two poles shall be put in contact during the integration of the collared coil into the iron yoke. A small gap (~30 μm) remains open during operation with no effects on field harmonics.

The conductor chosen for this magnet (Fig.6) is based on a cored Rutherford cable with 36 strands (similar to the LHC dipole outer layer), whose main characteristics are shown in Table 2. This conductor is characterized by several features, chosen to provide low ac losses: 1) the filaments are small (down to 2.5 μm) to minimize the hysteretic losses; 2) the part of the matrix surrounding the filaments is made of CuMn, for the electromagnetic decoupling of the filaments and for increasing the transverse resistivity and, consequently, decreasing the coupling losses; 3) the cable is cored using a thin stainless steel foil (25 μm) for cutting down the inter-strand coupling currents (Section 3 discusses with many details the conductor features). This last characteristic makes the conductor stiffer than a standard Rutherford cable, causing more difficult winding operations. For this reason we considered the performance of industrial R&D, aimed at developing the winding techniques of a cored cable for a curved coil, crucial.

TAB.2: Characteristics of the conductor.

Strand characteristics :	
Filament diameter (μm)	2.5 to 3.5
Strand Diameter (mm)	0.825
Twist Pitch (mm)	5-7
Cable characteristics :	
Number of strands	36
Width (mm)	15.1
Thickness: thin/thick edges (mm)	1.362/ 1.598
Core material/thickness (μm)	AISI 304/ 25
Critical Current @5T , 4.22K	>18540 A

TAB.3: Characteristics of the winding.

Block number	5
Turn number/quadrant	34 (17+9+4+2+2)
Operating current (A)	8926
Yoke inner radius (mm)	96.85
Yoke outer radius (mm)	240.00
Peak field on conductor (with self field) (T)	4.901
B_{peak} / B_0	1.09
Working point on load line	79.8%
Current sharing temperature (K)	5.69

Table 3 shows the main characteristics of the winding.

2.2 Main materials and components

An important aspect is related to the choice of the materials: it was done aiming at limiting the ac losses and to optimizing the field quality. Here we summarized the reasons leading the material selection done at the early stage of the design and, later, confirmed by the quantitative mechanical and thermal analyses.

The coil wedges and the end spacers are in G11, in order to cut down the eddy currents during the ramps. Ceramic materials were also considered as a potential interesting solution, but the worry for possible conductor damages (ceramic materials are generally hard and brittle) led to leave aside this option, to be considered in future developments. Some reservations are related to the radiation hardness. At present the available information about the radiation load in the dipole volume has confirmed that G11 is acceptable from this point of view. In principle stainless steel could be used as well because the relatively high electrical resistivity limits the eddy currents. Nevertheless the elastic modulus of the stainless steel (200 GPa) is much higher than the modulus of the winding (11 MPa). This difference would cause the winding to be an inhomogeneous mechanical component and make easy the generation of concentrated stress in the conductors.

The collar material was chosen on the basis of the required mechanical and magnetic properties. The preliminary mechanical analysis showed that during the field ramp the peak Von Mises stress in the collar could be as high as 600 MPa (in some locations as discussed in Section 6). This stress level demands for a high strength material, also in view of the fatigue load. At the same time the relative magnetic permeability is required to be less than 1.003 to keep the field quality perturbation at the level of 0.1 units in the field region from 0.5 T (stretcher mode) to 4.5 T. Several austenitic steels with a significant Mn content were investigated in the past by laboratories developing accelerator dipole magnets.[10] We selected the Nitronic 40,[11] which has a yield stress R0.2 ranging from 700 MPa at room temperature up to 1400 MPa at 4.2 K. The thermal contraction of this alloy is 2.3‰, which, though far from the winding contraction in the azimuthal direction (around 6 ‰), is still compatible with an acceptable level of the required pre-stress during collaring (70 MPa), for having a coil with a residual pre-stress of 50 MPa in operating conditions. The collars are axially laminated to a thickness of 3 mm. In fact the ac losses due to the eddy currents would allow a larger thickness, but the envisaged construction methods (punching of thin sheaths) put a limit to the allowed thickness.

The cable insulation is made of three polyimide layers forming a total half-thickness, after curing and under 50 MPa stress, of 125 μm. Since the cooling of the coil is done through supercritical helium in contact with the coil inner wall, the temperature of the cable is greatly determined by the balance between the heat dissipation and the heat removal through this thin insulation layer.

A thermal analysis in steady state conditions demonstrated that the temperature in the winding can increase up to 0.3 K with respect to the coolant temperature (see Section 7). Computations under more realistic assumptions (transient phenomenology) have shown that the temperature increase could be lower (0.2 K).

The ground insulation has been sized following LHC main dipole design. It includes channels for supercritical He, providing an additional cooling (other than the one through the inner surface) and quench heaters.

We remind here that the excellent results obtained on the first and unique prototype of SIS300[12] (the GSI001, which was rather a model coil for ac studies operated up to 4 T/s), might be due to the holes in the insulation ensuring an optimum cooling. We do not intend to make holes in the insulation for the risks connected to sparks during quenches.

Possible materials for yoke lamination were investigated with the main aim to have low ac losses (see Appendix A) here coming from three contributions: hysteretic, eddy currents and anomalous losses. At the same time, a commercially available product was searched. In this framework only electrical steel with silicon can be considered. It can be easily verified that at the used ramp rates the main contribution to the losses is coming from the magnetic hysteresis, so we looked for silicon steel having a coercitive field as low as possible. Since the coercitive field is a decreasing function of the Si content, one would use a high Si alloy. Unfortunately also the brittleness is increasing with the Si content. A good compromise was found for a Si content of ~3% giving a coercitive field of 35 A/m. We identified the

commercial lamination M600-100A, according the EN 10106 code (1995).

2.3 3D layout

Fig.7 shows how the end coil should appear. It can be noticed that the collars under design are very similar to the ones involved in SSC main dipoles.[13)] Though many details are not visible, they are parallel packed in groups of 10 (for a total axial thickness of 30 mm), placed in a way to follow the coil curvature through the introduction of thin spacers (0.01 mm) placed only in one side of the midplane (the one corresponding to the convex part). The large block (the one with 17 conductors) is split into two for making easier the coil end construction.

Fig.8 shows the complete cold mass, with the external stainless steel shell, having mainly a cryogenic role and a limited mechanical function. In fact it only gives an axial rigidity as explained in Section 6. More 3D pictures and drawings are shown in Section 11.

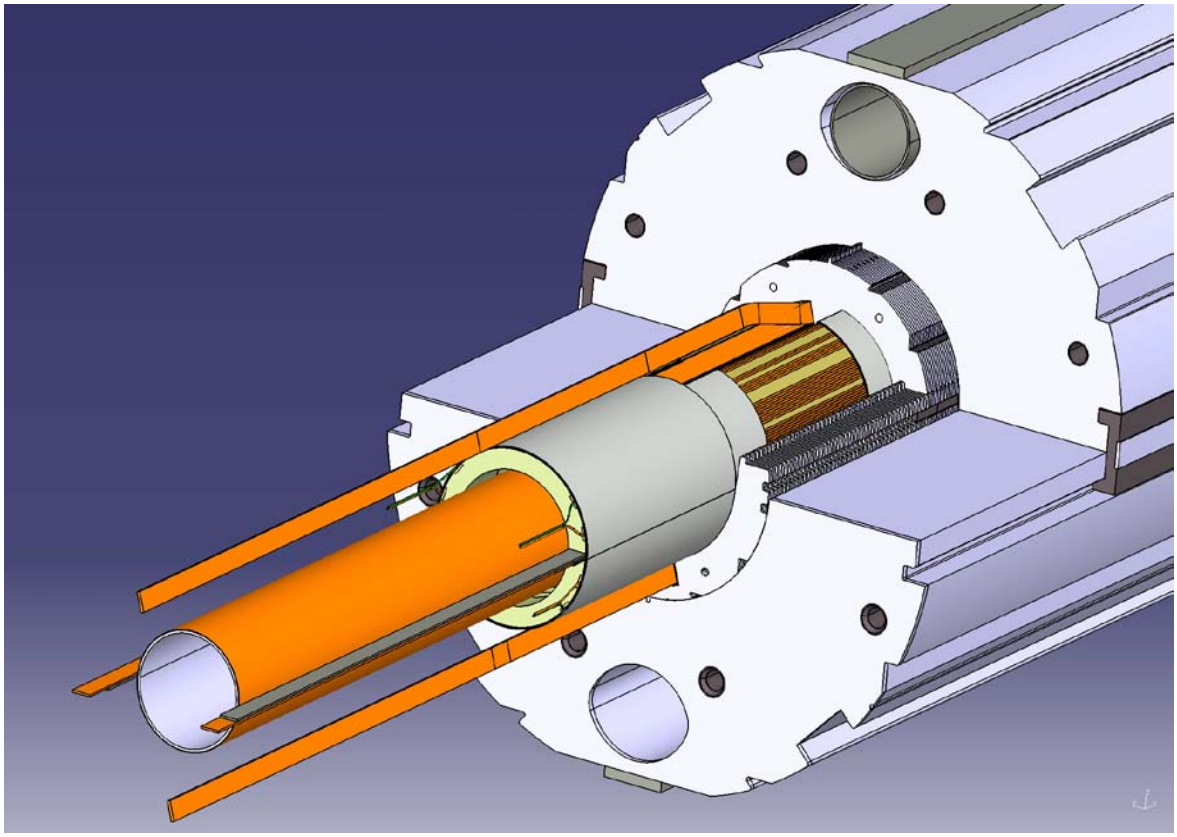

FIG.7: Detail of the coil end design. Coil ground insulation and collar structure are also shown.

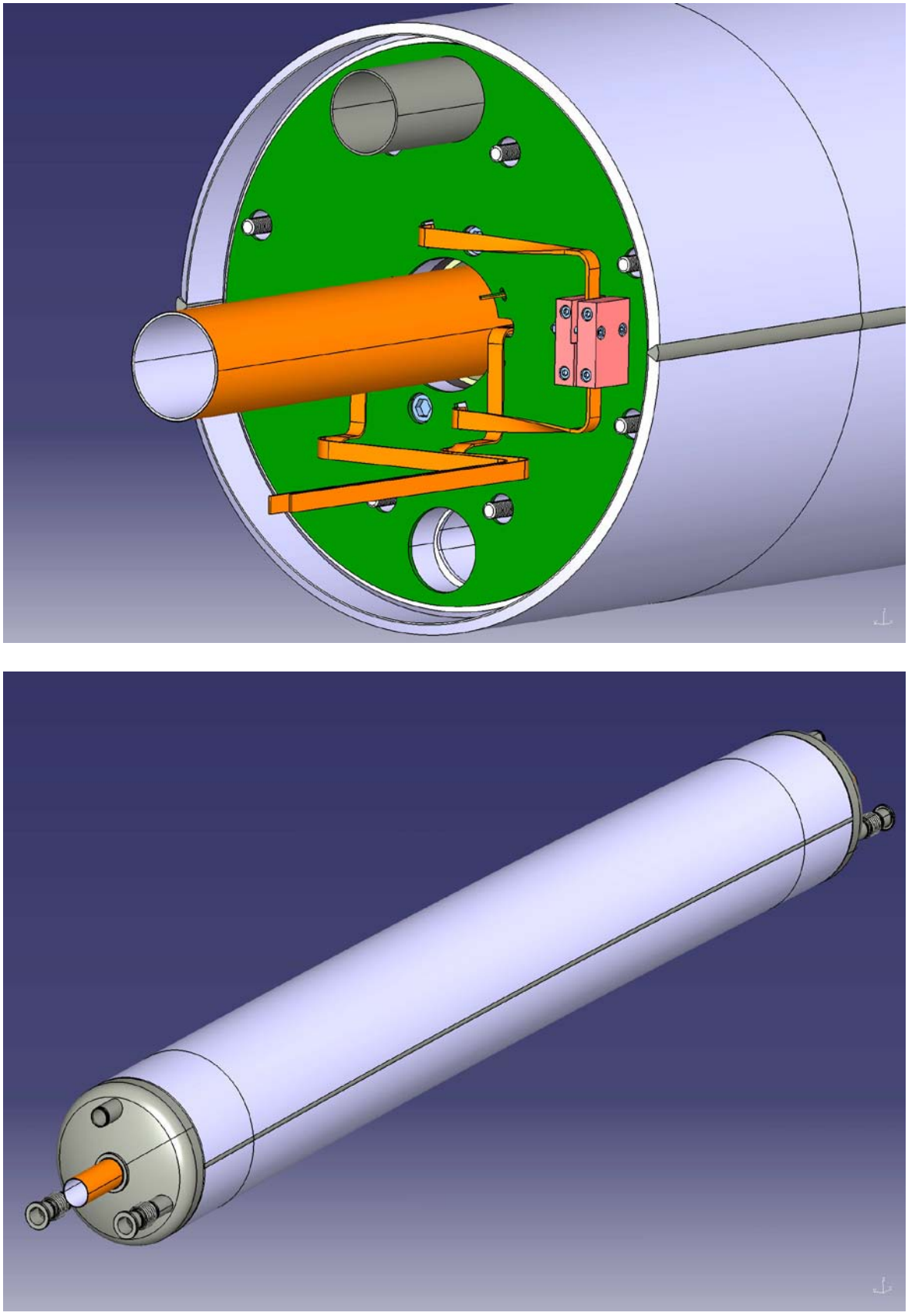

FIG.8: The cold mass.

3. CONDUCTOR

3.1 Introduction

The construction of fast pulsed superconducting magnet requires a significant upgrade of the technology of superconducting Rutherford cables, in order to reduce power dissipation in the pulsed regime, which otherwise would be so large that the cryogenic heat load in the cable would be unacceptable.

Here we present the motivations of the specifications of the Rutherford cable and the R&D activities performed for its development.

The loss reduction will be achieved by means of the following technical solutions: i) smaller filament diameter (down to 2-3 μm), ii) shorter twist pitch, iii) higher resistivity interfilament matrix, iv) higher contact resistance between the adjacent wires of the Rutherford cable and v) a high resistance metallic core.

In the past, a similar wire was developed within the R&D efforts for the SSC accelerator construction.[14)] Despite some good results, the process then developed does not appear easily reproducible, and industrial scale production cannot be guaranteed.

In order to achieve the demanding requirements of DISCORAP, we consider a two generation development, where the first generation will produce a wire with a filament diameter of 3.5 μm, in order to pave the way for the production of a second generation, 2.5 μm filament diameter wire, which would fully satisfy the SIS-300 goals.

Section 3.2 will summarize the loss sources and the formulae used in the computations, Section 3.3 will discuss the R&D activities and the technical assessments that led to the definition of the Rutherford Cable Specifications, described in Section 3.4. Section 3.5 will present the insulation scheme.

3.2 Loss sources

Here, we review the different sources of loss, along with the technical solutions adopted to minimize them.[6)]

3.2.1 Hysteretic losses

The main contribution comes from the hysteretic losses within superconducting filaments which, for the case of one round filament of diameter d_f and critical current J_c, exposed to a variable magnetic field with amplitude B_m, perpendicular to its axis, are given by:

$$Q_{hys} = \frac{4}{3\pi} J_c d_f B_m \quad [\mathrm{J/m^3/cycle}] \tag{1}$$

A reduction of Q_{hys} by reducing d_f in a wire with a high purity Cu interfilament matrix is effective only down to a filament size of about 3.5 μm due to the onset of the proximity effect. Since, even with this d_f value, the contribution of hysteresis loss to the total loss within the cable is about 60%, a smaller filament diameter, like 2.5 μm, would represent a significant improvement. Cu0.5wt%Mn is an effective suppressor of the proximity effect, due to the

paramagnetic effect of Mn, which opposes the creation of Cooper pairs, while still maintaining an acceptable thermal conductivity and workability, compared e.g. to CuNi alloys.

3.2.2 Inter-filament coupling losses & eddy current losses

A second contribution is given by the losses generated by Joule dissipation in the resistive matrix due to the currents induced by a changing external magnetic field, normal to the wire axis. These currents flow:

i) in loops composed by different superconducting filaments and closed through the matrix, in a plane normal to the wire axis. These are the interfilamentary currents;

ii) in circuits laying in planes parallel to the wire axis, entirely in the resistive matrix. These are the eddy currents.

The power per unit volume due to the interfilamentary currents is given by:

$$P_{if} = \frac{\dot{B}^2}{\rho_t}\left(\frac{L_p}{2\pi}\right)^2 \quad [\mathrm{W/m^3}] \tag{2}$$

P_{if} can be minimized by a suitable choice of the filament transposition pitch L_p and of the transverse resistance ρ_t, which depends on the cross-section geometry, on the bulk resistivity of the matrix materials, and possibly on the contact resistance between the superconducting filaments and the matrix itself. The interfilamentary CuMn also plays an important role here through its rather high resistivity at 4 K ($2.5\cdot10^{-8}$ Ω·m), which increases ρ_t.

The contribution from the eddy currents, P_{ec}, is given by $P_{ec} = j^2/\sigma = \sigma \dot{B}^2 x^2$ [W/m^3]. These losses take place essentially in the low-resistance, Cu part of the matrix, and they do not depend on the wire transposition pitch. From an empirical point of view, their contribution to the wire losses cannot be disentangled from the one of the interfilamentary currents, since they both depend on $\dot{B}^2$. The contribution from eddy-currents to the total losses for dB/dt=1 T/s, ranges from 10% to 15%, depending on the hypotheses.

We therefore consider the two contributions together and we make explicit the dependence on L_p:

$$P_{tot}(L_p) = P_{if} + P_{ec} = \Pi_{if} L_p^2 + P_{ec} \tag{3}$$

and we introduce an effective transverse resistance, defined as

$$\rho_t^{eff}(L_p) = \frac{\dot{B}^2}{\Pi_{if} L_p^2 + P_{ec}}\left(\frac{L_p}{2\pi}\right)^2 \tag{4}$$

With this definition, ρ_t^{eff} is a function of L_p; this approach has the advantage that it gives directly the $\dot{B}$ -dependant component of the losses, which is the only quantity directly measurable. From now on the term “transverse resistivity” will be used only in the above explained meaning, and therefore we drop the superscript “eff” from ρ_t^{eff}. The computation of the transverse resistivity are described in the next section, while the experimental results on the minimum permissible transposition pitch are reported in Section 3.3.2.

3.2.3 Transverse resistivity computations

We have computed the transverse resistivity[15)] starting from a preliminary analysis of M.N. Wilson.[16)] The interfilament coupling plus the eddy current power loss per unit volume can be expressed as:

$$P_{tot} = j^2/\sigma = \sigma\,[\dot{B}^2 x^2 + (\partial_x\varphi)^2 + (\partial_y\varphi)^2] \quad [\mathrm{W/m^3}] \tag{5}$$

(j is the modulus of the total current flowing in the resistive matrix, dB/dt is the external magnetic field ramp rate, σ is the resistive matrix conductivity and x the direction normal to the magnetic field and to the wire axis), where the first term between square parentheses accounts for the eddy currents, and the gradient terms describe the interfilamentary currents.

The potential may be computed from the Laplace's equation,

$$\nabla^2\varphi(x,y) = 0 \tag{6}$$

with proper boundary conditions:

$$\partial_n\varphi(R_0,\vartheta) = 0 \tag{7}$$

which describe the confinement of the currents inside the wire (R_0 is its radius), and

$$\varphi_{BC}(R,\vartheta) = \frac{\dot{B}\,L_p\,R}{2\pi}\cos(\vartheta) \tag{8}$$

valid on the filamentary zone boundaries, which takes into account the current entering/exiting into/from the filaments.

Once the potential φ has been determined, we find the total power dissipation P_{tot} by averaging Eq. (5) over the wire cross section, and eventually we compute the transverse resistivity by means of Eq. (4).

Eq. (5) and (6) were solved both analytically, assuming a simplified geometry based on concentric shells, and also through a FEM simulation. Considering the geometry presented in Section 3.3.1 and shown in Fig.9, we found from FEM simulations transverse resistivity values between 0.42 nΩ·m and 0.71 nΩ·m @ 0 T and field ratio around 0.1 nΩ·m/T depending on the presence of further CuMn barriers between the filamentary zone, and on the nature of the electrical contact between the NbTi filaments and the contiguous matrix. These results were confirmed by the analytical models which agreed to within 15% or better. We have therefore set a minimum specification value of the transverse resistivity of 0.4 + 0.09 B [T] nΩ·m. An example of the coupling current pattern is shown in Fig.10.

3.2.4 Inter-strand coupling losses

These losses are similar in nature to the inter-filament coupling losses, involving loops that embrace different strands within the same Rutherford Cable.

In this case, the dissipation takes place through the contact resistances between adjacent strands (R_a) and between the strands on the opposite sides of the Rutherford cable (R_c), which can be controlled through use of, respectively: a high resistance metallic core within the Rutherford cable (for R_c), and the choice of a proper thickness for the SnAg wire coating, followed by air oxidation (for R_a).

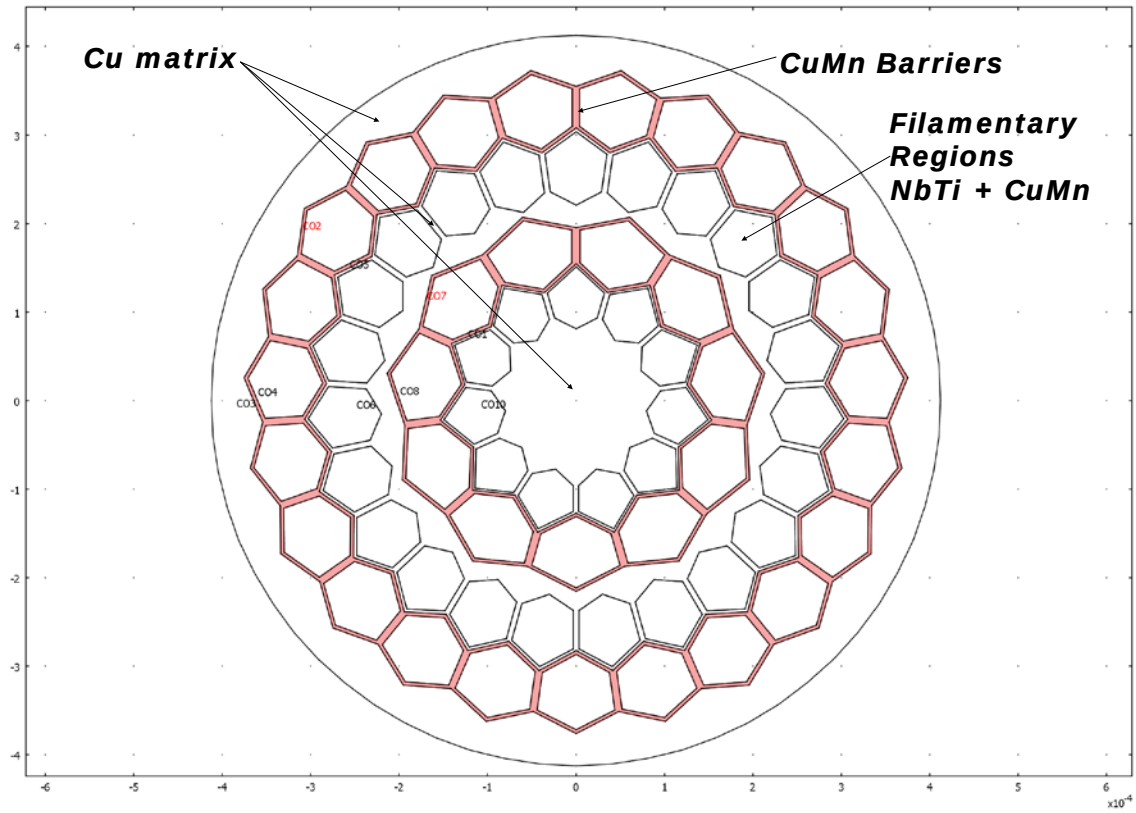

FIG.9: An example of wire cross section design.

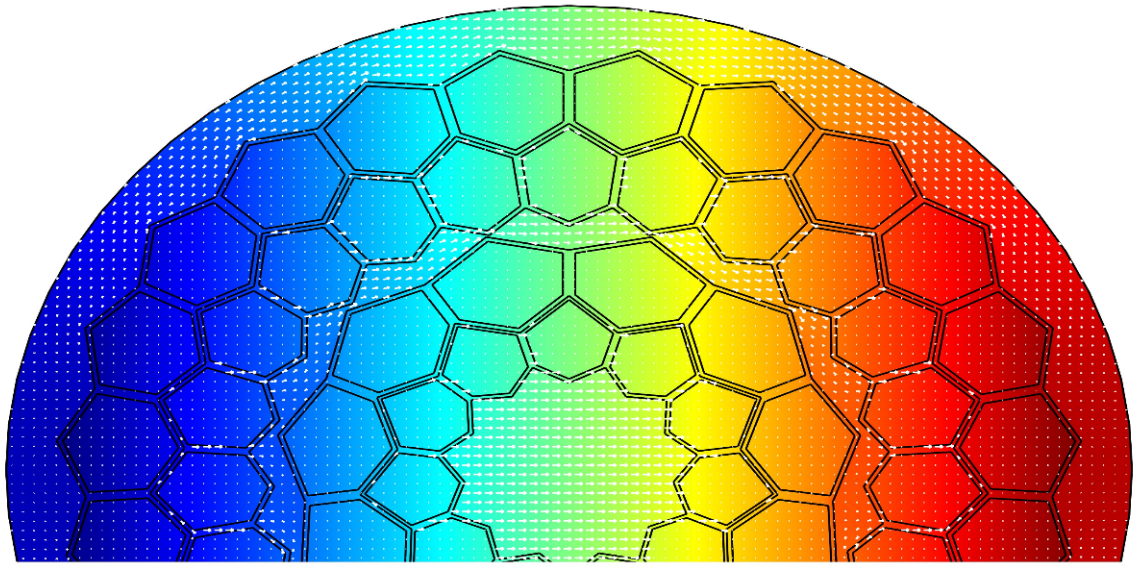

FIG.10: The coupling currents flowing in the matrix, of the wire shown in Fig. 9. The wire is subjected to an external changing field, directed in the figure's plan, along the horizontal direction. The current loops are closed through the filaments. White arrows show the current magnitude and direction, and the color gives the potential φ.

3.3 R&D activities and the technical assessments

The first developments of a superconducting Rutherford Cable suitable for the construction of the SIS-300 dipoles were performed in 2002-2004 by GSI. Our work on the Rutherford Cable started from those results.[17),19),20),21)]

3.3.1 Rutherford cable layout

The Rutherford cable layout, its dimensions and the number of strands, was taken from the LHC dipole outer cable, with the insertion of a stainless steel core to increase R_c. These numbers were chosen immediately after the change from the SIS 200 to SIS 300 synchrotron design.[17)] Given the successful performance of the SIS 200 model magnet GSI 001, a cored Rutherford cable was chosen also as the conductor for the SIS 300 double-layer, 6 T, dipole. GSI 001 Rutherford design was based on RHIC dipole, with thirty 0.648 mm strands. In order to reach a 1 K temperature margin (like other large projects, such as HERA, RHIC and LHC) it would have been necessary to have more than forty eight 0.648 mm strands, which is impractical for cabling. Therefore, a larger diameter strand with the dimensions of the existing LHC dipole outer layer conductor was chosen.

The preliminary magnetic analyses of the 4.5 T, single layer, INFN design have shown that an analogous margin could be achieved with designs based on the same Rutherford design, which was therefore adopted.

3.3.2 Wire characteristics

The small filament diameter, between 2.5 μm and 3.5 μm, requires a number of filaments in the range 30.000 to 70.000. Such a large number can be practically achieved only by means of a two stage re-stacking process.

A possible layout is shown in Fig.9: this is only an example since the specifications do not indicate the details of the cross-section, leaving to the manufacturer the possibility to propose their own geometry. The coloured zones represent the inter-bundle barriers, the hexagons represent the filamentary zones, with NbTi filaments embedded in a CuMn matrix both in the 1st and in the 2nd generation. The rest of the wire is in high-purity copper.

Critical current density J_c in excess of 3000 A/mm² @ 4.2 K, 5 T can be achieved on commercially available NbTi wire with large filament diameters, and values as large as 2650 A/mm² @ 4.2 K, 5 T were obtained on LHC dipole outer layer cable, with a filament diameter of 6 μm.

In general we should expect lower J_c values as long as we go for smaller filaments diameter. We have defined the specifications assuming a 2700 A/mm^2; this value was reached on R&D wire, with a 0.648 mm diameter, 2.5 μm geometrical filament diameter and CuMn interfilament matrix.[18)] More recently, INFN has performed a R&D activity with Luvata Fornaci di Barga: a “prototype wire”, based on materials already in stock at Luvata has been designed, built, and tested. This wire, although significantly different from the final wire, has allowed to assess which J_c and twist pitch can be realistically achieved on wires with NbTi

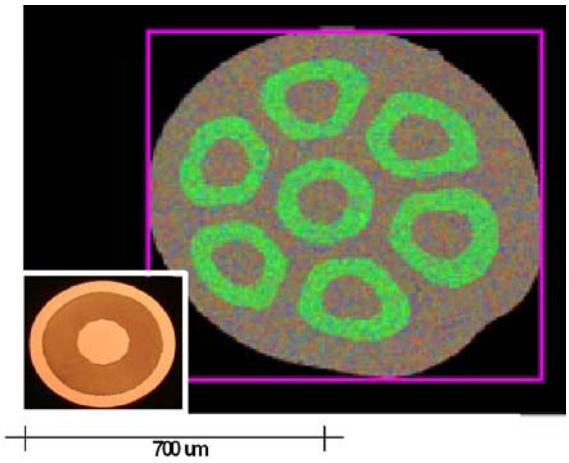

FIG.11: A SEM image of the cross section of the prototype wire, composed of seven elements of the Luvata OK3900 wire, shown in the inset. Scale refers to the main figure, not to the inset.

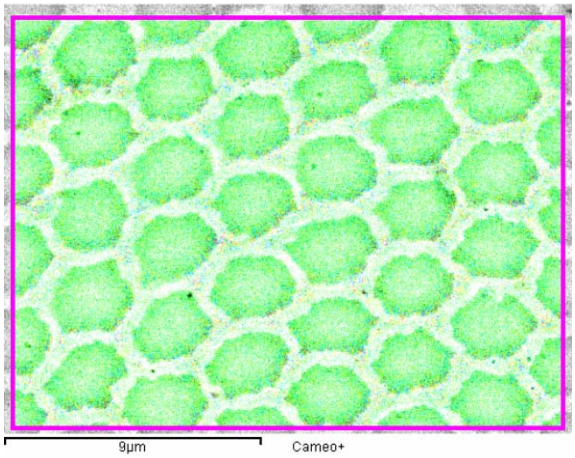

FIG.12: Detail of the filament array pattern. The scale length on the lower left corner is 9 µm wide.

fine filaments embedded in a CuMn matrix, with a diameter around 2-3 µm. It is based on cold drawing of seven elements of Luvata OK3900 wire (each with about 3900 NbTi filaments), restacked within a pure Cu tube at an early stage of their manufacture process (Fig.12). Its diameter is 0.82 mm and the geometrical filament diameter is 2.52 µm.

The critical current density at 4.22 K, measured by a transport method, as a function of the twist pitch, is shown in Fig.13. As it can be seen, J_c as large as 2500 A/mm^2 can be reached for a twist pitch of 5 mm, while strong degradation can be observed at 3 mm. The same behavior can be seen in the n transition index as a function of the twist pitch, shown in Fig.14. These results confirm the common wisdom that twist pitch should be at least 6-7 times the wire diameter.

The filament array pattern (Fig.12) does not show excessive geometrical deformation, thus indicating that a two stage manufacture process should not pose any significant concern in this respect.

A further improvement of J_c could be possible, considering that the OK3900 wire Nb filament barrier was not optimized for these values of the filament diameter.

An important issue of a wire with interfilament matrix in CuMn is its dynamic stability. The thermal conductivity of the CuMn is rather poor, about 4 W·m^{-1}·K^{-1} wrt 0.1 W W·m^{-1}·K^{-1} for NbTi and ~600 W·m^{-1}·K^{-1} for a RRR=100 copper (all values at 4.2 K, 0 T). As a consequence, the appropriate scale length for the dynamic stability is determined not by the single filament, but rather by the filamentary area, whose width must satisfy:

$$D_{bundle} < D_{\max} = 4\sqrt{2}\sqrt{\frac{k_{th}\Delta\theta\,(1-\lambda)}{\lambda\, J_c^2 \rho_{el}}} \qquad (9)$$

where: k_{th} is the filamentary bundle thermal conductivity, estimated assuming a weighted average between NbTi and CuMn yielding 1.9 W/mK; $\Delta\theta$ is the temperature margin; λ is the

NbTi fill factor in the filamentary bundle, 0.588; J_c is the critical current @ 4.2 K, 5 T, 2,700 A/mm²; ρ_{el} is the matrix copper resistivity @ 4.2 K, 5 T, 0.35 nΩ·m.

With these numbers D_{max}=137 μm; for the geometry shown in Fig.9 the bundle area width is 60−70 μm, which is reasonably smaller than D_{max}.

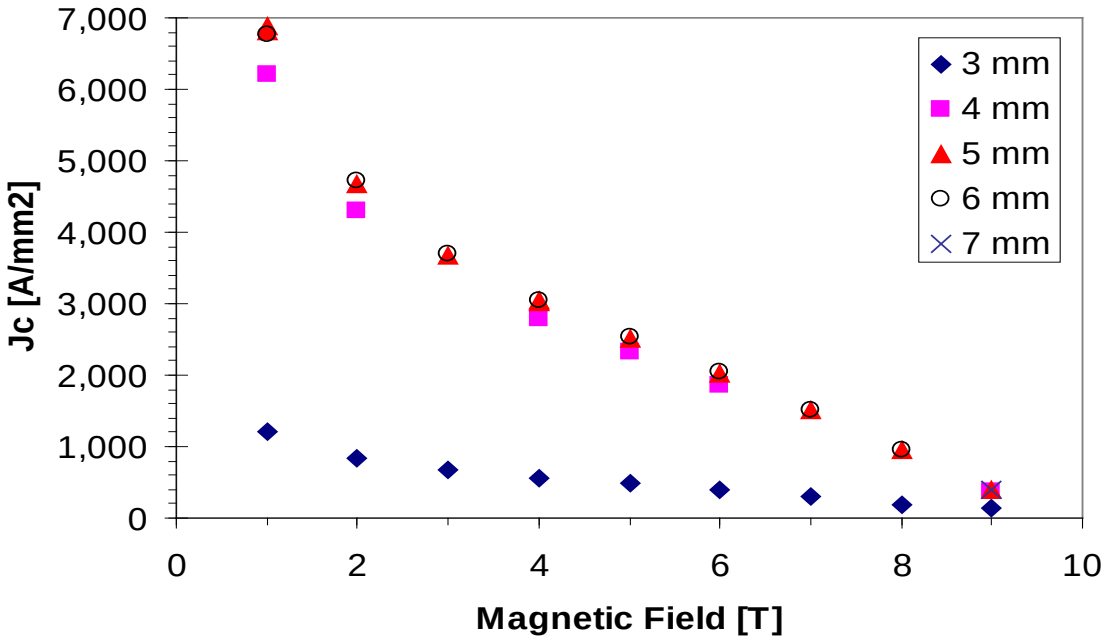

FIG.13: Critical current density J_c as a function of B, at 4.22 K for different twist pitch lengths, shown in the caption.

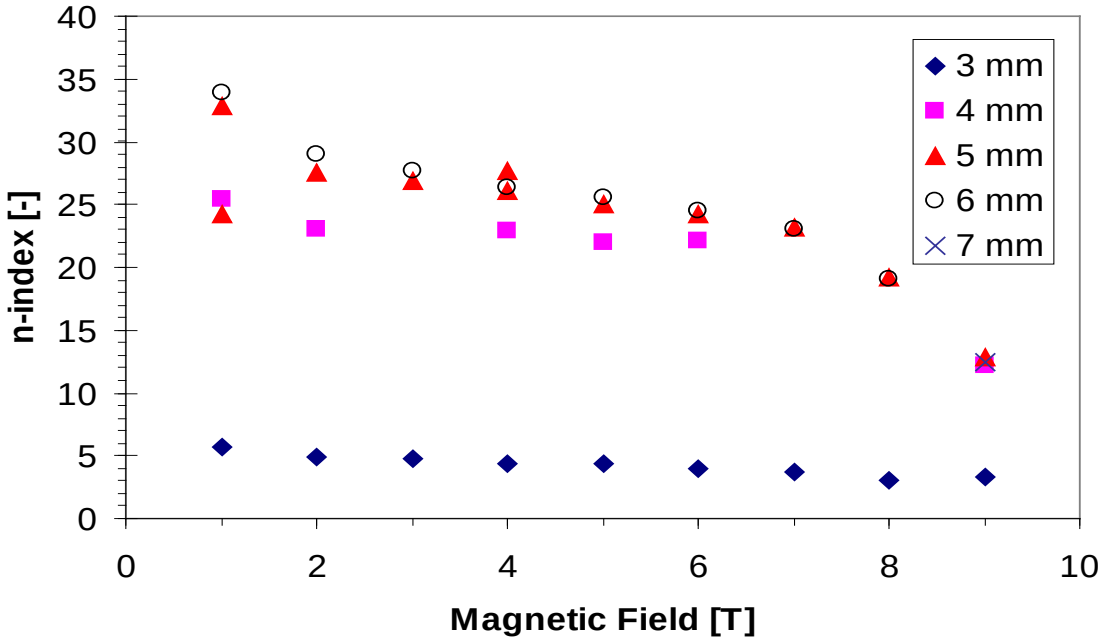

FIG.14: Transition n-index as a function of B for different twist pitch lengths, shown in the caption.

3.3.3 Rutherford transverse and adjacent resistance

Interstrand coupling losses depend on the inverse of the adjacent and transverse resistance, (R_a and R_c), the latter giving the higher contribution, for comparable R_a and R_c. These two values can be controlled independently, by means of a high-resistance metallic core (R_c) and proper oxidation of the wire surface (R_a). The specification values for R_a and R_c, 200 μΩ and 20 mΩ, respectively, were based on the values selected by GSI between 2004[19] and 2005;[20] the rationale for this choice is explained below.

Following Reference 21) we adopted a 316L stainless steel, 25 μm thick, annealed core. With such a core R_c values larger than 64 mΩ[21] and between 12.5 and 14 mΩ[22] were obtained. With the nominal value of R_c (20 mΩ) the interstrand losses via R_c account for less than 5% of the total cable losses. In principle any larger value would be acceptable, and also a value twice as lower would have only a minor impact on the total losses.

Some uncertainty is still present in the literature about the effect of the punch-trough, which unavoidably arises during cabling, and of the impact of the Rutherford cable bending in the magnet end, on core integrity. The winding tests now in progress at ASG should help to clarify this issue.

R_a value is more critical. We have adopted a nominal value of 200 μΩ; with such a value the interstrand losses via R_a account for about 25% of the total cable losses.

R_a value is driven by the wire surface oxidation, which can be controlled changing the duration of the air oxidation at 200 °C. Values in the range of mΩ's can be obtained extending suitably the oxidation period. A too large value of R_a[23] could lead to an instability against thermal disturbance of the Rutherford cable, whose MQE would essentially be equivalent to the MQE of the single strand; this behavior is called *regime II*, as opposed to the *regime I*, where the whole Rutherford contributes to the stability. The transition from regime I to regime II is governed by the ratio I/I_c, where I is the current flowing in the Rutherford and I_c its critical current at the same magnetic field. It has also been shown that for R_a values between 40 μΩ and 700 μΩ the transition between the two regimes takes place for I/I_c between 0.8 and 0.9, while our magnet is designed to work at 0.57 (Section 3.6).

3.4 Rutherford specifications

3.4.1 General strategy of Rutherford cable development

The contract for the manufacture of superconducting Rutherford cable for the DISCORAP dipole model magnet foresees the delivery of five unit lenghts;[24] two units will have a larger filament diameter, and three a smaller one; these will referred to as 1st and 2nd generation, respectively. Only two units are strictly required for the magnet manufacture and this redundancy should allow the comparison of different wire design solutions and to face manufacture problems.

The specified characteristics of the superconducting wire are described in Table 5.

A possible cross section of the wire is shown in Fig.9; we are presently finalizing the

wire layout geometry, based on a two-stage re-stacking. The target value for α is now 1.56, and the volume fractions of the different components are given in Table I.

3.4.2 Wire main characteristics

The characteristics of the superconducting wire are described in Table 5.

3.4.3 Rutherford cable main characteristics

The characteristics of the cable are described in Table 6.

TAB.4: Wire component volume fractions.

	Generation I	Generation II
(Cu+CuMn)/NbTi	1.56	
NbTi	39.0%	39.0%
Cu	43.9%	36.3%
CuMn	17.1%	24.7%

TAB.5: Wire main characteristics.

Wire		units	notes
Diameter after surface coating	0.825 ± 0.003	mm	
Filament twist pitch	5 +0.5 -0	mm	
Effective filament diameter for 1st generation wire	3.5	μm	a)
Effective filament diameter for 2nd generation wire	2.5	μm	a)
Interfilament matrix material	Cu-0.5 wt% Mn		
Filament twist direction	right handed screw (clockwise)		
I_c @ 5 T, 4.22 K	> 541	A	b)
n-index @ 5 T, 4.22 K	> 30		
Stabilization matrix	Pure Cu		
Strand transverse resistivity at 4.22 K	0.4 + 0.09 B [T]	nΩ·m	
Cu+CuMn:NbTi ratio (α ratio)	>1.5		c)
α ratio tolerance	± 0.1		
Surface coating material	Staybrite (Sn-5 wt% Ag)		d)
Surface coating thickness d	0.5	μm	e)

Notes:

a) As measured from magnetization.

b) This is the primary value for virgin wire. It is 5% higher than the cabled values, to take into account degradation during cabling. It amounts, e.g., to 2.529 A/mm² for α=1.5 or 2.832 A/mm² for α=1.8, @ 5 T, 4.22 K.

c) The supplier may propose an alpha value, provided it is larger than 1.5. Tolerance during the production must remain between ± 0.1 from the nominal value.

d) Same coating material used for LHC dipoles.

e) This is a preliminary value, to be better defined later.

TAB.6: Cable main characteristics.

Geometrical		units	notes
Strand Number	36		a)
Width	15.10 +0 -0.020	mm	
Thickness, thin edge	1.362 ± 0.006	mm	
Thickness, thick edge	1.598 ± 0.006	mm	
Mid-thickness at 50 MPa	1.480 ± 0.006	mm	
Edge radius	≥ 0.30	mm	
Core material	AISI 316 L stainless steel, annealed		
Core width	13	mm	
Core thickness	25	μm	
Transposition pitch	100 ± 5	mm	
Cable transposition direction	left-handed screw thread		
Electrical		units	notes
Ic @ 5 T, 4.22 K	>18,540	A	b)
Stabilization matrix RRR	>70		

Notes:

a) The geometrical layout is the same as that of the LHC dipole outer cable design. Dimensions are specified at 20 °C.

b) I_c @ 5 T, 4.22 K for the extracted strand must be equal to or above 515 A.

3.5 Rutherford cable insulation

Following the experiences of SSC, RHIC and LHC we adopted an all-kapton insulation scheme. We retained the same kapton total thickness adopted for GSI-001, 125 μm, although obtained by means of only two types of tapes, instead of three (see Fig.15). We refrain from using cooling slots cut into the Kapton insulation along one edge of the cable, as it was done on the GSI-001 cable, since we fear that these windows could represent weak point for electrical discharges. The curing will be performed according the LHC scheme, the nominal dimensions of the insulated conductor, used for the electromagnetic design, are reported in Table 7. They were computed assuming the nominal dimensions of the bare cable (from Table 6), the nominal width of the Kapton on the side edges, and a reduced thickness (98 μm) of the Kapton on the wide faces of the Rutherford cable, to take into account the azimuthal compression.

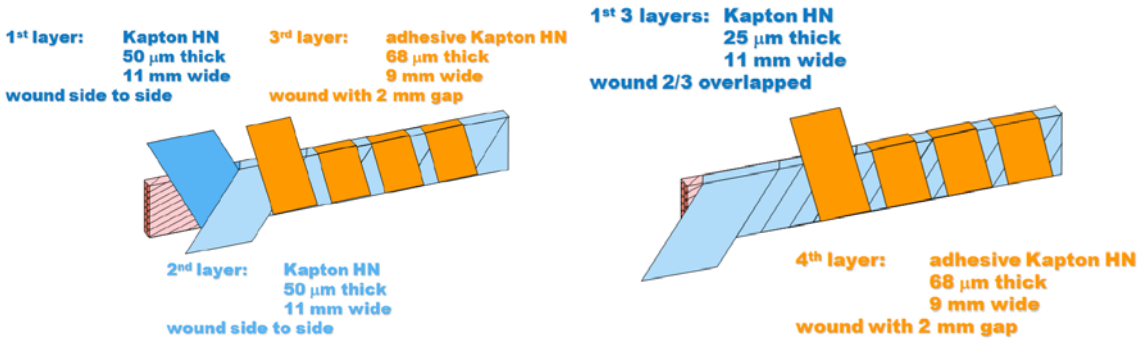

FIG.15: GSI-001 insulation scheme (left), and modified version adopted for this design (right).

TAB.7: Insulated Rutherford cable nominal dimensions at 20 °C, under an applied load of 50 MPa.

Width	15.350	mm
Thickness, thin edge	1.556	mm
Thickness, thick edge	1.796	mm

3.6 Magnet load line

We show in Fig.16 the magnet load line, vs. the Rutherford Cable critical current. The expression for the J_c dependence on magnetic field and temperature proposed by L. Bottura has been used, with the parameters set given by A. Devred for the LHC wire,[26] reported in Table 8.

$$I_c(B,T) = I_c(@5T\ \&\ 4.2K)\cdot\frac{C_{NbTi}}{B}\left[\frac{B}{B_{C2}(T)}\right]^{\alpha_{NbTi}}\cdot\left[1-\frac{B}{B_{C2}(T)}\right]^{\beta_{NbTi}}\cdot\left[1-\left(\frac{T}{T_{C0}}\right)^{1.7}\right]^{\gamma_{NbTi}} \quad (10)$$

$$B_{c2}(T) = B_{C20}\left[1-\left(\frac{T}{T_{C0}}\right)^{1.7}\right] \quad (11)$$

At an operating current of 8926 A the magnetic field in the bore center is 4.5 T and the peak field on the conductor is 4.901 T; the current sharing temperature is 5.67 K, and at a temperature of 4.7 K the magnet is at 79.8% of the critical current along the load line, or the 57.1% of the critical current at constant magnetic field (the latter quantity is relevant for the cable stability, see Section 3.3.3). The theoretical short sample limit is 11190 A.

TAB.8: Parameters used in Eq.(10).

C_{NbTi}	α_{NbTi}	β_{NbTi}	γ_{NbTi}	T_C	B_{C20}
31.4	0.63	1.0	2.3	9.2	14.5

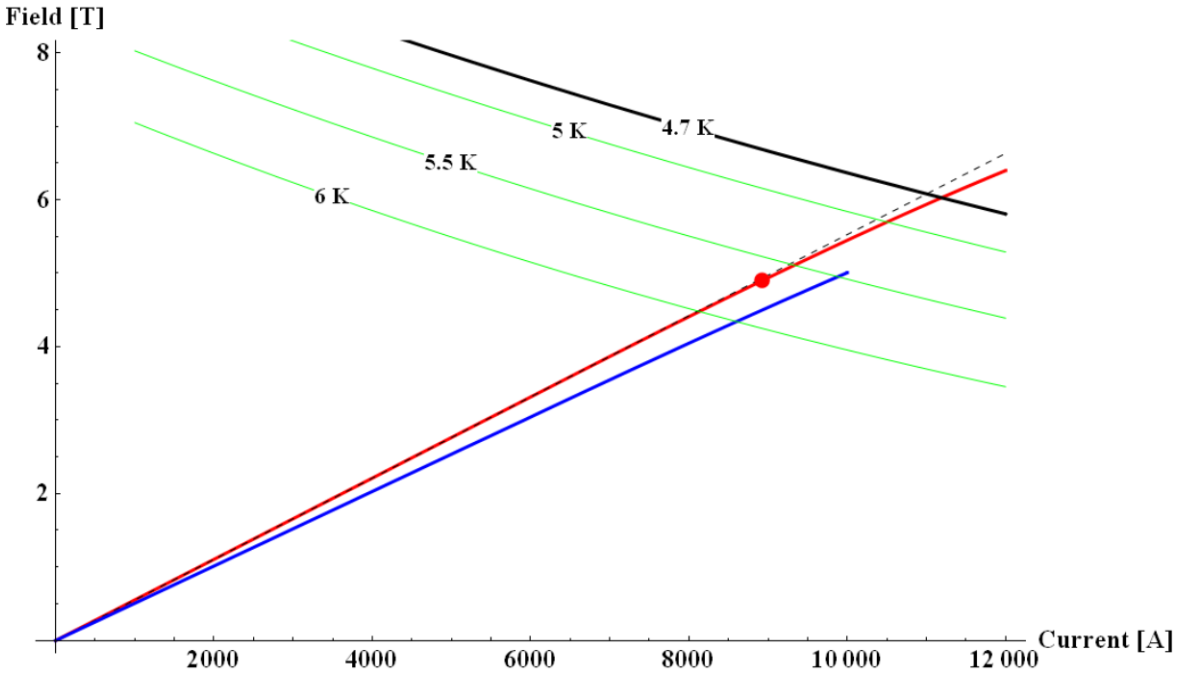

FIG.16: Magnet load line vs. Rutherford cable critical current. The red point shows the magnet operating point at 4.5 T (central field). Red: peak field on conductor. Blue: central field. Dashed: peak field on conductor w/o iron saturation. Black: Rutherford cable critical current at 4.7 K. Green: Rutherford cable critical currents, at the temperature values shown.

4. MAGNETIC DESIGN

The magnetic design and field quality analysis have been performed in various steps which are here summarized as:

1. effects of the curvature;
2. 2D design with iron at $\mu_{iron}=\infty$;
3. 2D design with finite permeability for the iron;
4. field perturbations;
5. end coil design.

In the following sections are reported the methods used and the obtained results.

4.1 Effect of the curvature

The effects of the curvature of the magnet (r=66.667 m) on the field quality has been investigated with a simplified model assuming the iron with $\mu_{iron}=\infty$. No effects have been detected on the field quality respect to the same design with a straight magnet.

Since the laminations of the iron have a constant thickness in the curved magnet there is a stacking factor *st* decreasing with the radius from *st*=1 at *r*=66.42 m to *st*=0.993 at *r*=66.92 m (yoke outer diameter assumed 250 mm). A pessimistic model has been used assuming *st*=1 on the left side of the magnet and *st*=0.993 on the right side with an abrupt transition at the pole: no variation in the field quality has been detected.

To further check the calculations a curvature radius *r*=10 m has been used; in this case there is a quadrupole component b_2=+1.5 units and a sextupole variation Δb_3=-0.3 units.

In conclusion the curvature of the magnet has no detectable effect on the field quality and the design of the magnet can be performed assuming a straight magnet, therefore simplifying the process.

4.2 2D design with $\mu_{iron}=\infty$

As a first step, a 2D configuration for the cross section of the dipole has been sought assuming an infinite permeability for the iron and in stationary condition (i.e. zero contribution

TAB.9: Main parameters of the magnet.

Nominal field	1.50 T – 4.50 T
Ramp rate	1 T/s
Flat top	10 s
Coil aperture diameter	100 mm
Magnetic length (full scale magnet)	7.757 m
Curvature radius	66.667 m
Bending angle	6 2/3 deg
Max temperature of cooling GHe	4.70 K
Yoke outer radius	< 250 mm
Reference radius for field quality	35 mm
Field quality	$2\ 10^{-4}$

due to persistent currents and to eddy currents).

Table 9 reports the required characteristics for the magnet.

The inner radius of the yoke has been set at 96.85 mm because of a collar thickness of 30 mm. Even if this value of collar thickness seems overestimated, it has been chosen considering the high stress due to the fatigue (10^7 estimated cycles for the dipole). The nominal dimensions of the bare and insulated conductor (at 300 K and at 50 MPa) are reported

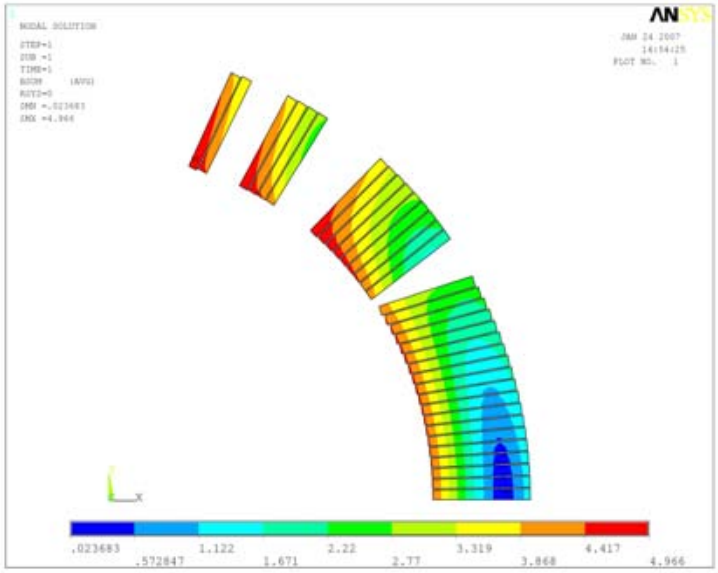

FIG.17: Cross section of the coils with 4 blocks and 34 turns (19+9+4+2) I=8890 A, B_{peak}=4.966 T (μ_r=∞).

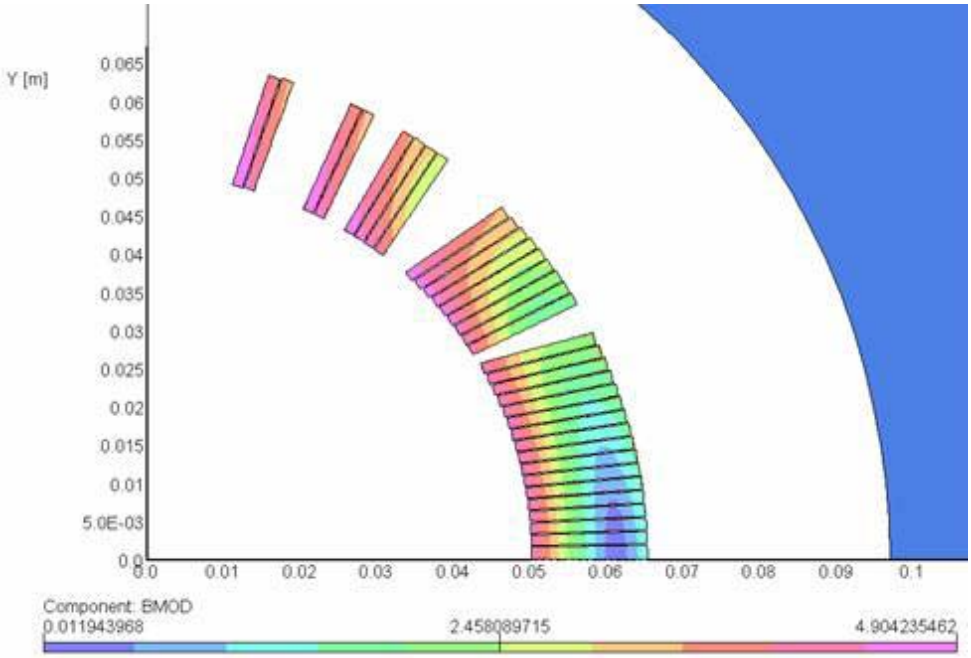

FIG.18: Cross section of a quadrant of the magnet with the field map for the selected 5 blocks 34 conductors (17+9+4+2+2) I=8870 A, B_{peak} =4.904 T (μ_r=∞).

respectively in Table 6 and 7. The magnetic design has been carried out at room temperature. The thermal and mechanical effect has been considered in Section 4.5.

The design of the coils has the following constraints:

- one single layer to reduce the complexity and the cost of the magnet,
- a cable with a number of strands and dimension of the LHC dipole outer layer to reduce the developments cost.

Within the given constraints it is imperative to maximize the number of turns per quadrant to have a reasonable temperature margin.

A deep analysis and optimization has been performed for a cos-theta magnet with 34-35 turn and 4-5 blocks per quadrant. Genetic algorithm has been employed in ROXIE and in connection with ANSYS to obtain a configuration with good field quality and maximum temperature margin.

No solution with 35 turns has been found either with 4 or 5 blocks. Solutions have been found with 34 turns with 4 or 5 blocks.

The best solutions with 4 and 5 blocks are presented respectively in Figs. 17 and 18 with the field map.

The advantage of the 5 blocks configuration (Fig.18), with only two conductors in the last two blocks, is to reduce the peak field in the conductor. Scaling laws used to fit the ratio B_{peak}/B_0 on the existing superconducting dipoles have shown that this optimized configuration has 7% less peak field than it would be expected,[27] with a clear benefit for the temperature margin. Moreover, this solution maximizes the number of conductors, and consequently reduces the operating current in the magnet. Therefore this solution has been selected; Table 10 reports the main parameters and Fig.98 describes the turn distribution with their exact angular positions.

The values of the field harmonics have been calculated with different codes: Roxie, Opera, Ansys, and 2 different codes developed at LASA. Some of these codes assume that the currents flow in infinitely thin wires located at the center of each strand of the conductor

TAB.10: Main parameters of the optimized solution ($\mu_{iron}=\infty$).

Block number	5
Turn number/quadrant	34 (17+9+4+2+2)
Operating current (at B_0=4.5 T)	8870 A
Yoke inner radius	96.85 mm
Peak field on conductor (with self field)	4.904 T
B_{peak}/B_0	1.09
Current sharing temperature	5.70 K
Inductance per unit length	2.95 mH/m

TAB.11: Field harmonics (units) at 35 mm, $\mu_{iron}=\infty$ for ideal geometry.

b_3	b_5	b_7	b_9	b_{11}	b_{13}
-0.19	0.07	0.41	0.50	0.97	-1.18

(Roxie and one analytical code); the other codes assume, instead, a current density in the conductor cross section, which is not uniform to take into account the current grading due to the key-stoning of the conductor. The agreement between the codes is excellent, and the values of the harmonics are reported in Table 11, using the standard European notation:

$$B_y + iB_x = 10^{-4} B_0 \sum_{n=1}^{\infty} (b_n + ia_n) \left(\frac{x+iy}{R_{ref}} \right)^{n-1} \qquad (12)$$

where B_0 is the central field and b_n and a_n are the normal and skew field harmonics measured in "units".

4.3 2D design with finite permeability for the iron

For the chosen iron (M600-100A) the estimated magnetization curve (pending measurements on a real sample) is shown in Fig.19 with the label LASA-GE. For comparison, other magnetization curves are reported in the same graph. The stacking factor used for the 2D analysis is 0.97.

The iron has inner/outer radii of 96.85/240 mm; the magnetic model studied is as close as possible to the mechanical model described in Section 6. It includes the cooling hole, the notch for the bus-bar and the assembly of the yoke. The yoke and collar pins and keys have been considered with a relative magnetic permeability μ_r=1.

The 2D model of Opera, with the magnetic flux lines at B_0=4.5 T is shown in Fig.20.

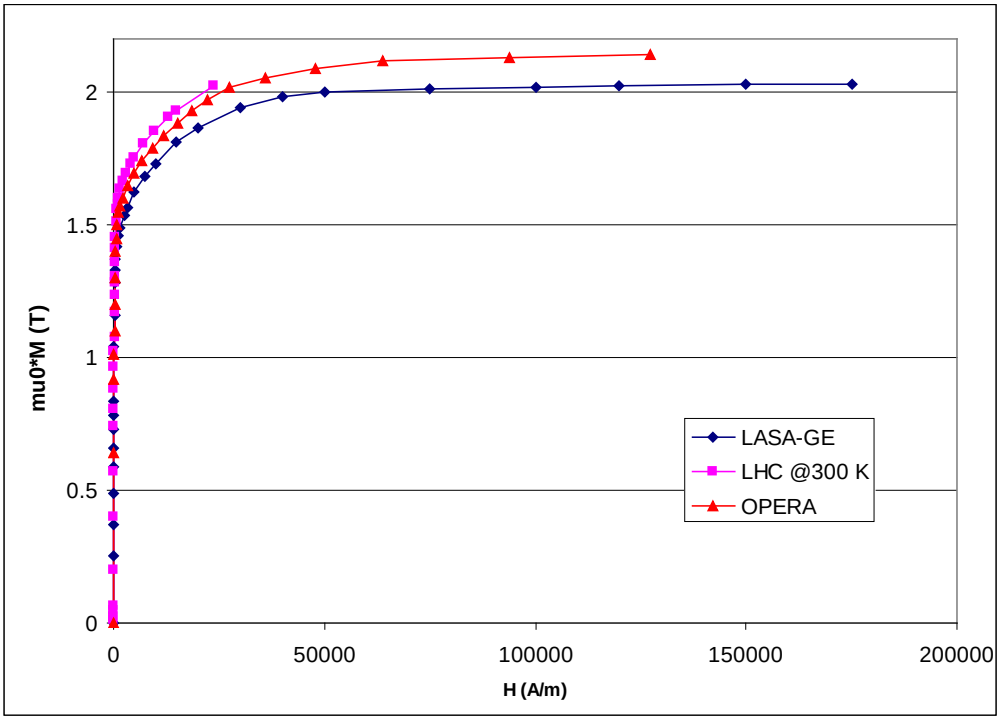

FIG.19: Magnetization curve used in the non-linear analysis (LASA-GE). Other magnetization curves are reported for comparison: the LHC iron measured at room temperature (LHC curve), and the default magnetization of Opera (OPERA curve).

Table 12 reports the operating current, peak field and current sharing temperature. Respect to the basic design with $\mu=\infty$ reported in the section 4.2, there is a small increase of the operating current of 56 A. The peak field on conductors has not been changed and the reduction of the current sharing temperature is almost negligible (0.01 K).

Fig.21 shows the behavior of b_3 and b_5 vs. the central field B_0. Respect to the analysis with $\mu=\infty$, at low field there is a shift of about +0.25 units of b_3 for the tooth 3.5 mm long in the pole region for the alignment of the yoke and collar. It can be noted that up to B_0=2.5 T the

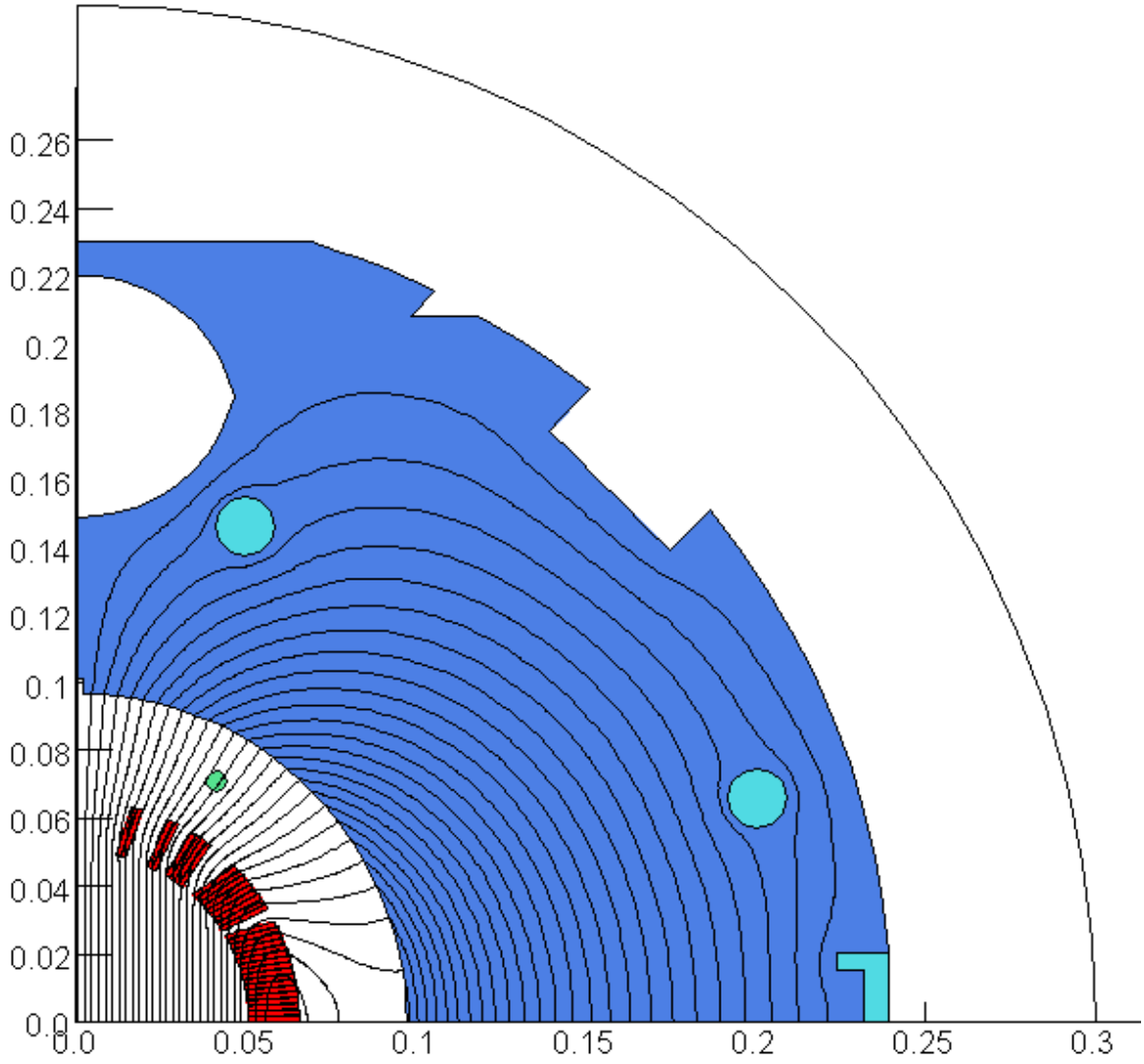

FIG.20: The 2-D model of the magnet, with the magnetic flux lines at B_0=4.5 T.

TAB.12: Main parameters of the optimized solution with finite permeability of iron.

Operating current (at B_0=4.5 T)	8926 A
Peak field on conductor (with self field)	4.901 T
B_{peak}/B_0	1.087
Current sharing temperature	5.69 K
Working point on load line	79.8%
Stored energy per unit length @ 4.5 T	116 kJ/m

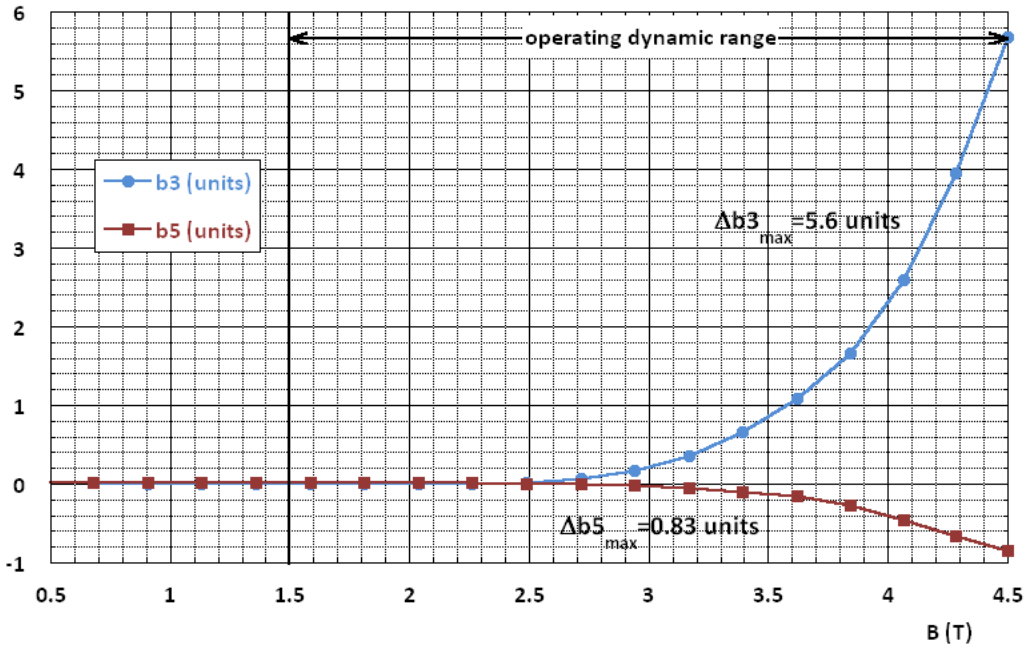

FIG.21: Sextupole and decapole component vs. central field due to the saturation of the iron yoke.

variation of b_3 and b_5 is negligible, as can be expected since the maximum field in the iron is of the order of half the central field B_0.

At the maximum central field, the sextupole component is quite large, b_3=5.5 units. In order to reduce this variation some additional holes can be drilled in the yoke lamination and optimized in position and dimension to reduce the effect of the saturation of the iron.

4.4 Field perturbations

The magnetic field perturbations can be classified in two main groups, whether they appear in static or in dynamic conditions.

In static conditions, the field quality is mainly affected by:

1 the magnetization of collars, shimmings, collar keys and beam tube,

2 the paramagnetism of the copper-manganese component of the conductor,

3 persistent currents in the superconducting filaments.

The field quality changes significantly, with respect to stationary condition, during the ramp of the magnet. The most affected harmonics are b_3 and in some case b_5. The main causes for this field perturbation are:

4 eddy currents inside the strand (usually called inter-filament coupling currents);

5 eddy currents between the strands of the Rutherford cable (inter-strand coupling currents);

6 eddy currents in the beam tube.

In “conventional” superconducting dipole for accelerator, usually the most relevant effects are due to persistent and inter-strand currents.[28] For a pulsed superconducting dipole all the components have to be taken into account.

In the following paragraphs we will treat these points; a brief description of the methods used to calculate these effects will be given, and the results will be compared.

4.4.1 Magnetization of collars, shimmings, collar keys and beam tube

The magnetization of the collars has not a negligible effect in harmonic perturbation. Fig.22 shows the sextupole and decapole perturbation vs. the magnetic permeability of the collar, at B_0=4.5 T. If standard stainless steel is used ($\mu_r \approx 1.02$), the perturbation is of the order of several units. In order to keep this variation of the harmonics within acceptable limits (Δb_3=-0.77 units and Δb_5=+0.39·units), a qualified stainless steel material has to be used, with a magnetic permeability μ_r of about 1.002.

Also the effect of the stainless steel shimming, 1 mm thick, located between the winding and the collar nose (see Fig.23), is not negligible. It contributes to harmonics perturbation with Δb_3=-0.39 units and Δb_5=+0.15·units. The collar keys, instead, do not perturb significantly the magnetic field.

The perturbation for the magnetization of the beam tube can be calculated analytically. The only relevant effect is the reduction of the main component of the field:

$$B_{inner} = B_0\left[1-\frac{(\mu_r-1)^2}{4\mu_r}\left(1-\frac{r_{\text{int}}^{\,2}}{r_{ext}^{\,2}}\right)\right] \qquad (13)$$

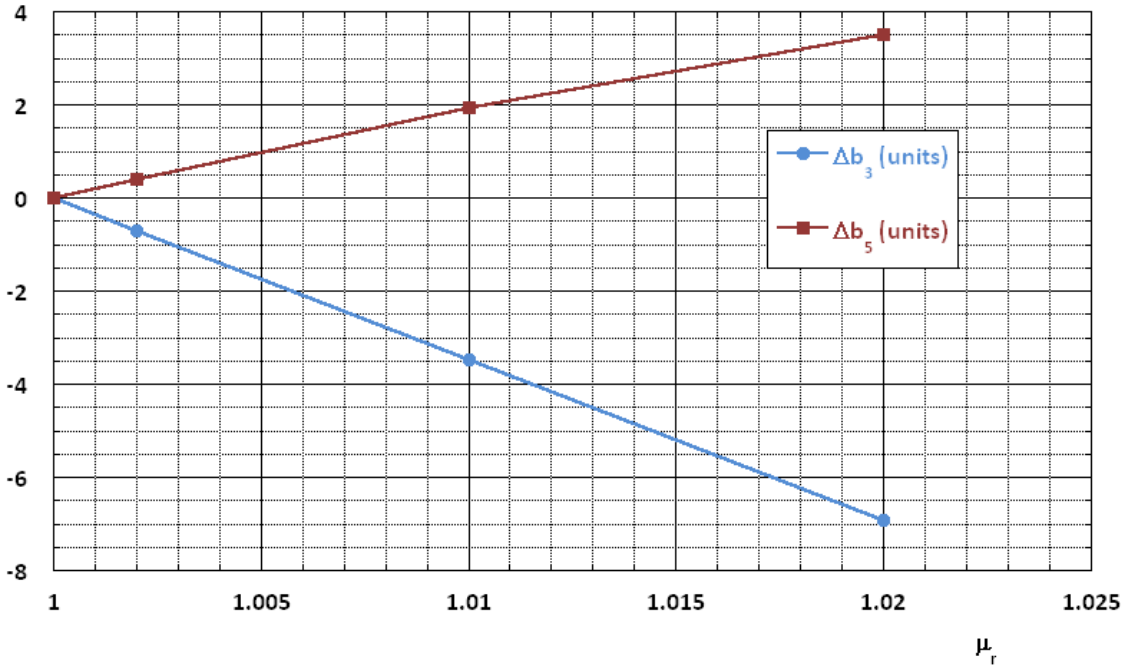

FIG.22: Effect of collar magnetization: Δb_3 and Δb_5 as function of collar relative permeability.

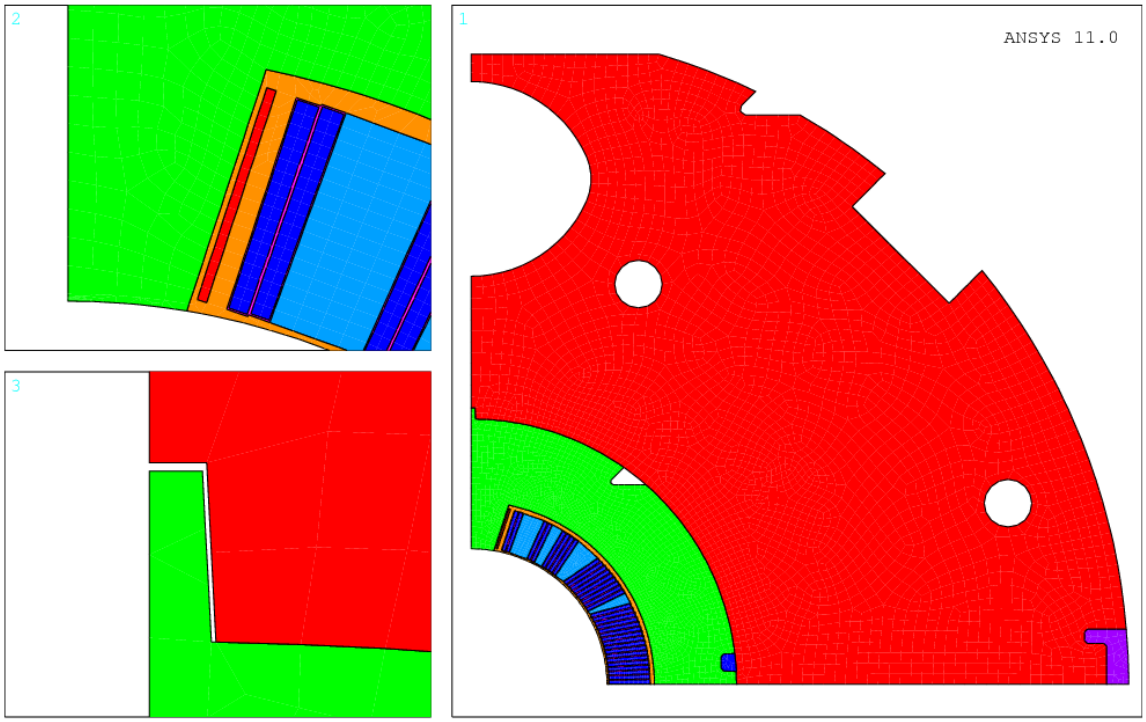

FIG.23: Ansys model for magnetic calculations; details of the shimming (top left in red) and of the joint between collar and iron yoke (bottom left) are shown.

where B_{inner} is the field inside the tube (reduced by magnetization), μ_r the magnetic permeability, r_{int} the inner radius of the beam tube and r_{ext} the outer radius.

A very small reduction of the main dipole component can be expected, less than b_1=-0.1 units. This result has been confirmed by 2D FE calculation with Opera.

4.4.2 Paramagnetism of copper-manganese matrix

Measurements of the magnetization in similar strands have shown that there is a paramagnetic component on the whole magnetization, which has been individuated in the copper-manganese part of the matrix. The bulk Cu-0.5%wt Mn alloy to be used in the strands, has been measured. The paramagnetic effect is shown in Fig.24.[29)]

The perturbation in the field harmonic has been calculated with Opera and Ansys (using a linear model for the iron); the MnCu fraction in the strand is assumed 17% (see Table 4) and a filling factor of conductor λ_c=0.861 has been considered. The sextupole variation is about 0.14 units at B_0=1.5 T, 0.11 units at B_0=3 T and 0.09 units at B_0=4.5 T, whereas the decapole variation is negligible.

4.4.3 Persistent currents in superconducting filaments

During the variation of the field in the magnet, screening currents arise in the filaments which oppose to the variation of the main field inside the filament. These screening currents generate magnetic dipoles which are localized at the centre of each filament. Therefore to each

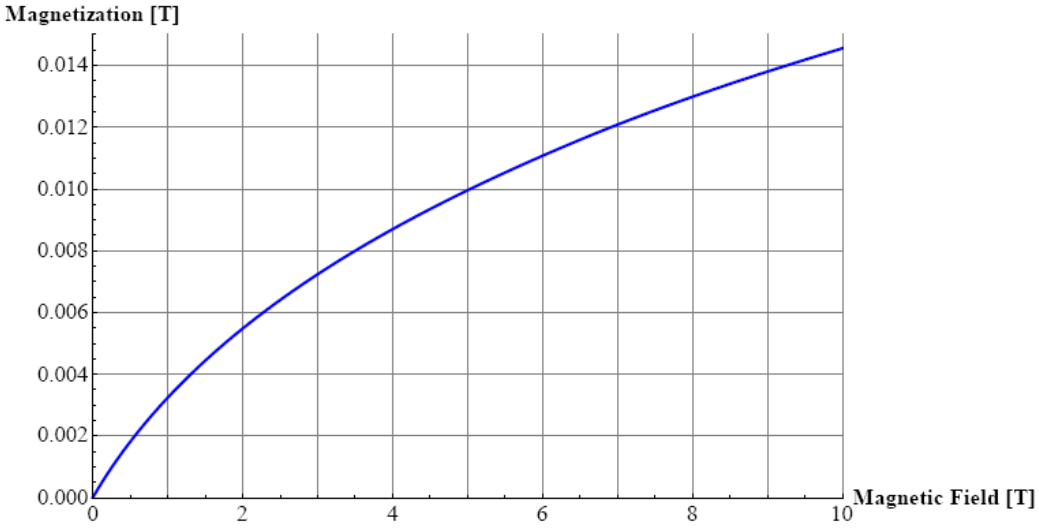

FIG.24: Magnetization of bulk Cu-0.5%wt Mn alloy.

conductor strand, an average magnetic dipole per unit length m_{pc} can be associated. For a cylindrical filament fully penetrated, the magnetic dipole can be approximated by:[30)]

$$m_{pc} = -\frac{1}{6}\lambda_f J_c(B) d_f d_s^{\,2} \qquad (14)$$

where λ_f=0.357 is the assumed filament filling factor in the strands, $J_c(B)$ is the critical current density (in the superconductor only), d_f=3.5 μm is the filament diameter and d_s=0.825 mm is the strand diameter. The negative sign indicates that m_{pc} is oriented in the opposite direction of B during the ramp-up. The critical current density $J_c(B)$ has been calculated using the LHC parameters.[26)] With an analytical code (in the following called Fortran code), the contribution to the field harmonics due to the persistent currents has been calculated, assuming a distribution of magnetic dipole per unit length given by (14). The same calculation has been executed with Ansys, describing each conductor strand by two half-ellipsis, with current density $\pm J_c(B)$, in order to give the equivalent magnetic dipole; this method has been called Ansys dipole.

In the third method, the equivalent magnetization M_{pc} of the conductor has been calculated by (14), giving:

$$M_{pc} = -\frac{2}{3\pi}\lambda_f \lambda_c J_c(B) d_f \qquad (15)$$

where λ_c=0.861 is the filling factor of conductor. As direct consequence, the conductor can be treated like a non-linear material. The complete and coupled problem of the field generated by the transport and persistent currents has then been solved using both Ansys and Opera.

Finally as fourth method, the Roxie code has been used. It calculates the contribution of the persistent currents in a similar way of the first method described above, but the magnetic dipole m_{pc} associated to each strand is evaluated with a more sophisticated routine, taking into account the field variation inside the filament due to the self-field.[31)]

TAB.13: Sextupole and decapole field harmonics (units) due to persistent currents at r=35 mm.

B_0 (T)	0.5 δb_3 / δb_5	1.5 δb_3 / δb_5	3.0 δb_3 / δb_5	4.5 δb_3 / δb_5
Fortran code	-3.65/-0.44	-0.72/-0.09	-0.25/-0.03	-0.13/-0.02
Ansys dipole	-3.41/-0.55	-0.70/-0.08	-0.24/-0.05	-0.12/-0.03
Opera	-3.67/-0.45	-0.72/-0.09	-0.25/-0.04	-0.13/-0.02
Ansys	-3.54/-0.38	-0.74/-0.09	-0.26/-0.04	-0.14/-0.02
Roxie	-3.49/-0.37	-0.72/-0.09	-0.25/-0.04	-0.13/-0.02

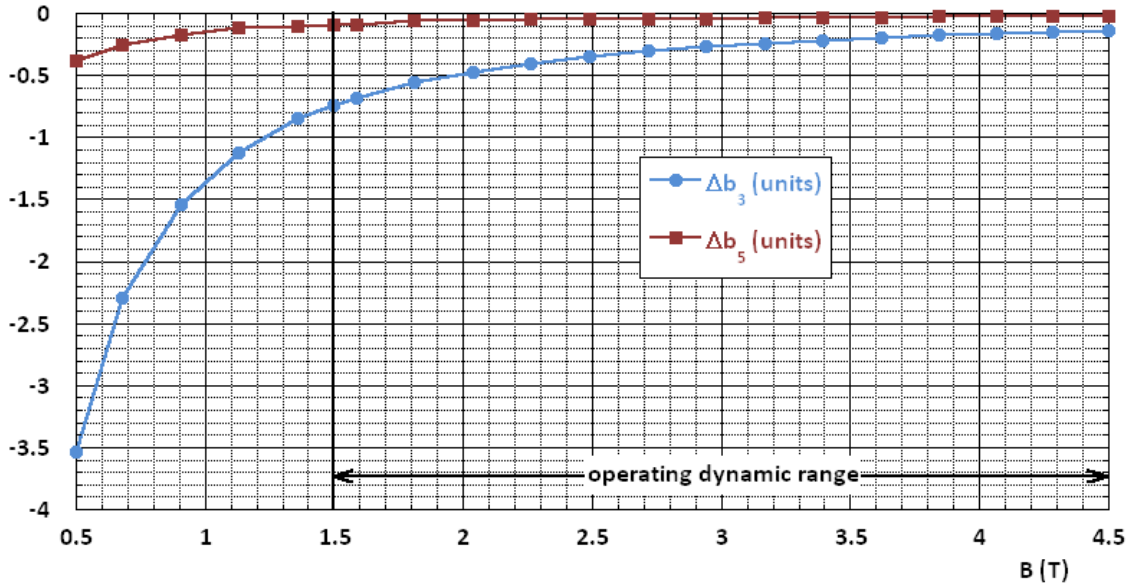

FIG.25: Variation of sextupole and decapole component vs. central field due to persistent currents.

Table 13 reports the sexstupole and decapole variation calculated with the different codes; the agreement is very good. The behavior as function of field of b_3 and b_5 is shown in Fig.25.

4.4.4 Inter-filament coupling currents

These types of induced currents are due to the coupling of the filaments in the same strand. Similarly to what has been done for the persistent currents, a magnetic dipole per unit length can be associated to each strand, given by:[32)]

$$m_{fc} = -\frac{\pi}{2\mu_0}\lambda_{fb}\dot{B}\cdot d_s{}^2\tau(B) \qquad (16)$$

and the correspondent conductor magnetization is:

TAB.14: Sextupole and decapole field harmonics (units) due to inter-filament coupling currents at r=35 mm.

B_0 (T)	0.5 δb_3 / δb_5	1.5 δb_3 / δb_5	3.0 δb_3 / δb_5	4.5 δb_3 / δb_5
Fortran code	-0.63 / 0.10	-0.16 / 0.02	-0.06 / 0.01	-0.04 / 0.00
Opera	-0.63 / 0.08	-0.17 / 0.02	-0.06 / 0.01	-0.03 / 0.00
Ansys	-0.63 / 0.10	-0.17 / 0.02	-0.06 / 0.01	-0.04 / 0.00
Roxie	-0.63 / 0.09	-0.17 / 0.02	-0.06 / 0.01	-0.03 / 0.00

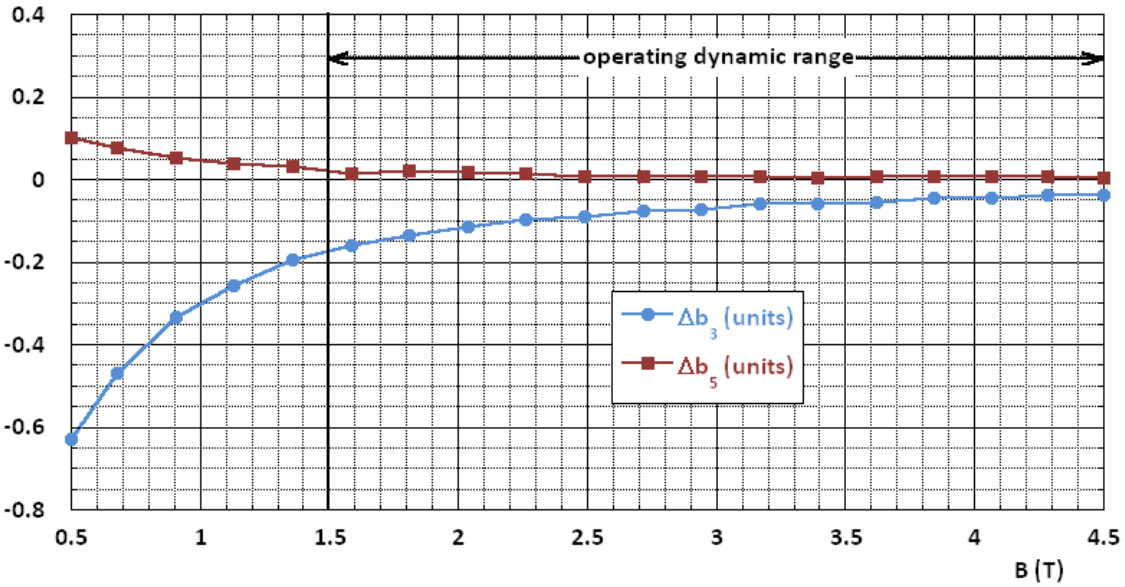

FIG.26: Variation of sextupole and decapole field harmonics (units) due to inter-filament coupling currents at r=35 mm.

$$M_{fc} = -\frac{2}{\mu_0}\lambda_{fb}\lambda_c \dot{B}\tau(B) \qquad (17)$$

where λ_{fb}=0.80 is the occupancy factor of the filaments in the strands, $\dot{B}$ is the field variation in the strand and $\tau(B)$ is a time factor dependent by the filament twist pitch and matrix resistivity (the dependence of τ on the field B is due to the copper magneto-resistivity). Consequently the harmonic contribution due to the inter-filament coupling currents has been calculated with the same methods and codes described in the previous paragraph. Also in this case the agreement is very good. Table 14 reports the results calculated with the Fortran code, Opera, Ansys and Roxie. The behavior as function of field of b_3, b_5 and b_7 is shown in Fig.26.

4.4.5 Inter-strand coupling currents

The inter-strand coupling currents are due to the coupling of the strands in the Rutherford cable. Usually the different contributions are separated in inter-strand coupling currents via crossover resistance, via adjacent resistance in parallel field and via adjacent

TAB.15: Sextupole and decapole field harmonics (units) due to inter-strands coupling currents at r=35 mm

B_0 (T)	0.5 δb_3 / δb_5	1.5 δb_3 / δb_5	3.0 δb_3 / δb_5	4.5 δb_3 / δb_5
Excel code	0.03 / -0.08	0.01 / -0.03	0.00 / -0.01	0.00 / -0.01
Roxie	0.04 / -0.15	0.01 / -0.04	0.00 / -0.02	0.00 / -0.01

resistance in transverse field.[32)] Among these three contributions, the most relevant is the last one (the cross over resistance has been greatly increased by the stainless steel core inside the cable), which can be evaluated integrating numerically the transverse field along the conductor width; this gives the following expression for the current density $J_z(x)$ on each conductor (the coordinate x is chosen parallel to the width of the considered conductor, and z is the conductor direction):

$$J_z(x) = \frac{2p_c}{R_A b \cdot c}\left(\int_0^x \dot{B}_t dx' - \frac{1}{c}\int_0^c dx' \int_0^{x'} \dot{B}_t dx''\right) \qquad (18)$$

where p_c is the cable twist pitch, b the conductor average thickness, c the conductor width, $\dot{B}_t$ the transversal component of the field variation (perpendicular to the conductor width) and R_A is the adjacent resistance. Obviously the integral of $J_z(x)$ satisfies to the condition to vanish over each conductor cross section. The expression (18) for the inter-strand currents has been used to evaluate the field harmonics variation, and the results are reported in Table 15 (Excel code).

A comparison with Roxie has been carried out, and again the agreement is good (see Table 15). It is worth noting that Roxie uses a network model for the Rutherford cable and necessarily gives an integral result, which takes into account all the different contributions of the inter-strands coupling currents; but among all, the coupling currents via adjacent resistance in transverse field prevail. These results show that the inter-strands coupling currents have a negligible effect in the field quality.

4.4.6 Eddy currents in the beam tube

The eddy currents in the beam tube can be calculated analytically by assuming a uniform magnetic field in the bore of the magnet:

$$J_{Z\,eddy}(\vartheta) = -\frac{1}{\rho_0}\,\dot{B}_0 r_{av.} \cdot \cos(\vartheta) \qquad (19)$$

where ρ is the electrical resistivity of the tube and r_{av} the average radius. Because this current density has a cos-theta distribution, it does not introduce any harmonic perturbation, except a negligible reduction of the main dipole component.

4.5 Thermal and mechanic effects

Deformation of the ideal geometry of the windings due to the collaring process, to the differential thermal contraction of the materials and to the deformations induced by the

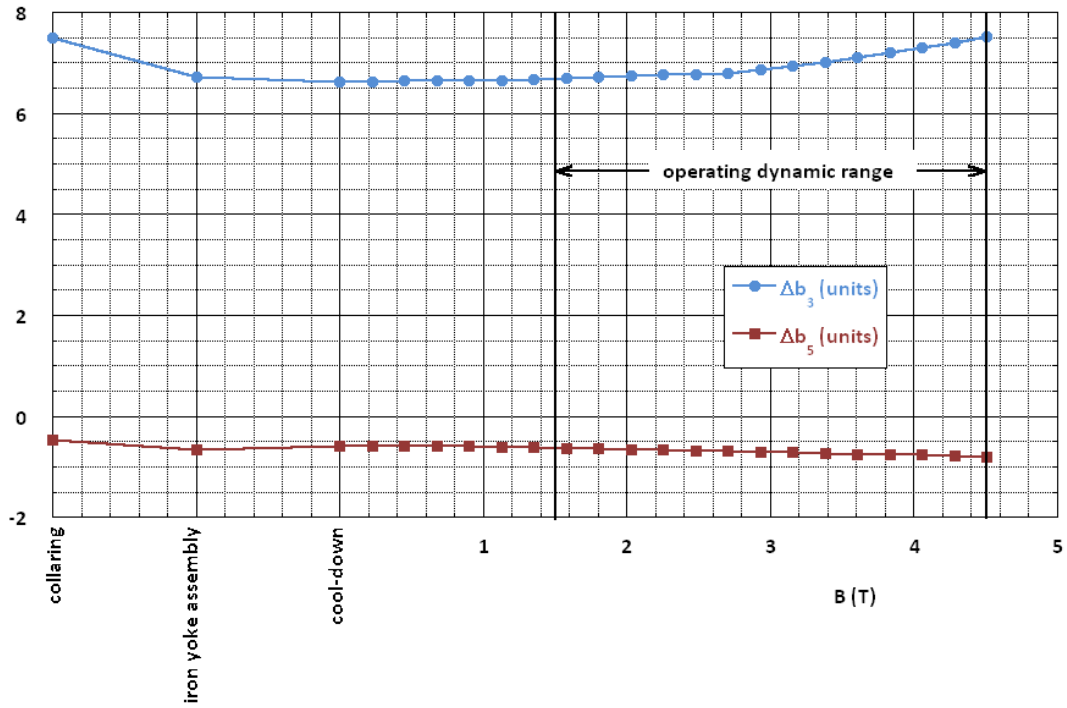

FIG.27: Variation of sextupole and decapole component vs. collaring, fitting of iron yoke, cool-down and energization operations.

Lorentz forces are described in details in Section 6. It is worth noting that the present magnetic design has not been optimized to minimize the thermal and mechanical effects on harmonics. A first estimate of the field perturbation is given in Fig.27. There is a large effect due to the assembly operation, acting as an offset on b_3 component ($\Delta b_3 \sim +7$ units and $\Delta b_5 < 1 \cdot$unit). This is mainly due to the increase of the average pre-stress in the winding from nearly 50 MPa to 70 MPa (see Section 6.1.1). The consequence is that the volume available for the winding is reduced with respect to the design, resulting in a significant effect on harmonics behavior. Fitting of collared coils into the iron yoke and cool-down have no special impact. Finally, the Lorentz forces have a not negligible effect, giving $\Delta b_3 \sim +1$ unit and $\Delta b_5 < 0.2$ units.

4.6 Coil-end design

The design of coil-ends is aimed at minimizing the integral value of sextuple and decapole in the end region of the magnet, to control the peak field in conductor and to find a geometry for the conductor as much as possible feasible during the winding.

The geometric design has been performed with Roxie,[31)] with the “constant perimeter” option. The first block of the coil (close to the median plane) has been split in two sub blocks with 9 and 8 conductors to better control the geometry and to have end blocks of manageable sizes. Fig.28 shows a view of symmetric size of the coil end, whereas Fig.29 shows a cross section of the coil end with the behavior of sextupole and decapole field components.

The integral value of sextupole and decapole, without the contribution of the iron yoke, is given by:

$$b_3^{coil-end} = \frac{1}{B_0}\frac{1}{\Delta z}\int_0^{\Delta z} \mathrm{B}_3 dz = 0.63\,\text{units} \tag{20}$$

$$b_5^{coil-end} = \frac{1}{B_0}\frac{1}{\Delta z}\int_0^{\Delta z} \mathrm{B}_5 dz = 0.04\,\text{units} \tag{21}$$

with:

$$B_0 = 4.5\,\mathrm{T}\,, \quad \Delta z = 300\,\text{mm} \tag{22}$$

In order to decrease the conductor peak field, the iron yoke in the coil-end region is substituted by stainless steel (from z=0 in Fig.28). In this way the peak field is 4.59 T, i.e. 0.37 T less respect to the configuration with “long yoke”. The peak field in the coil ends is also lower than the peak field in the 2D section of the magnet (4.90 T). The magnetic length of the symmetric coil end at B_0=4.5 T is 102 mm (z=0 is the starting plane of the coil end, as reported in Figs. 28 and 29).

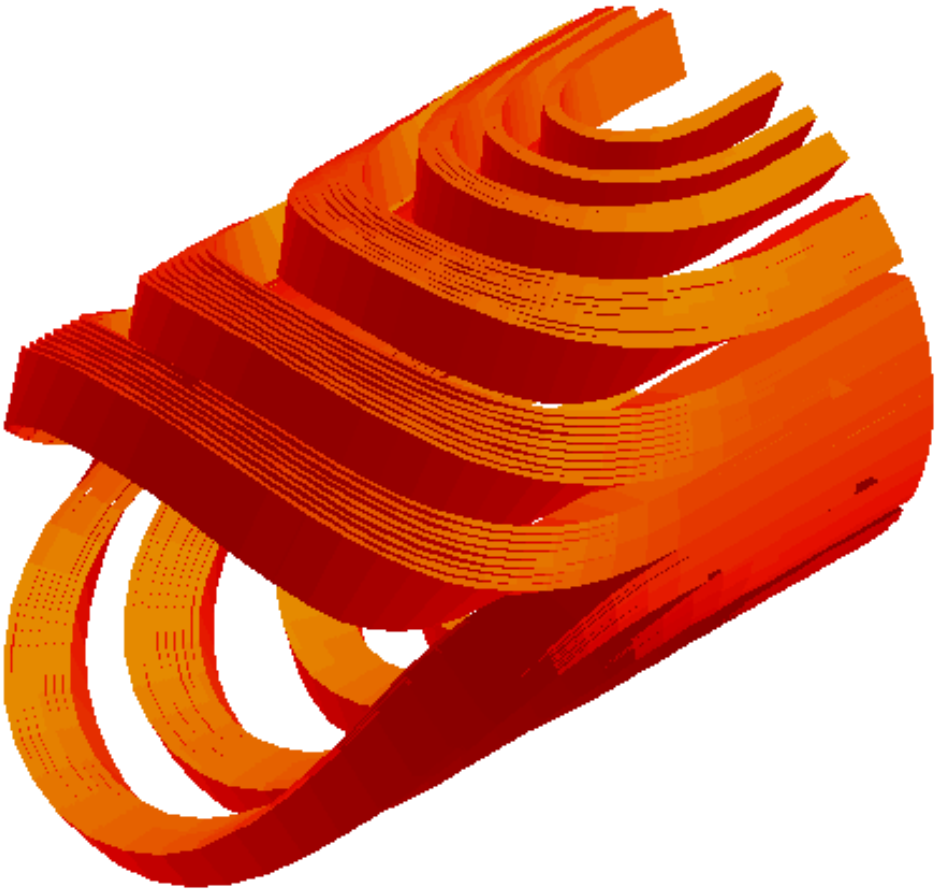

FIG.28: View of the symmetric side of the coil end.

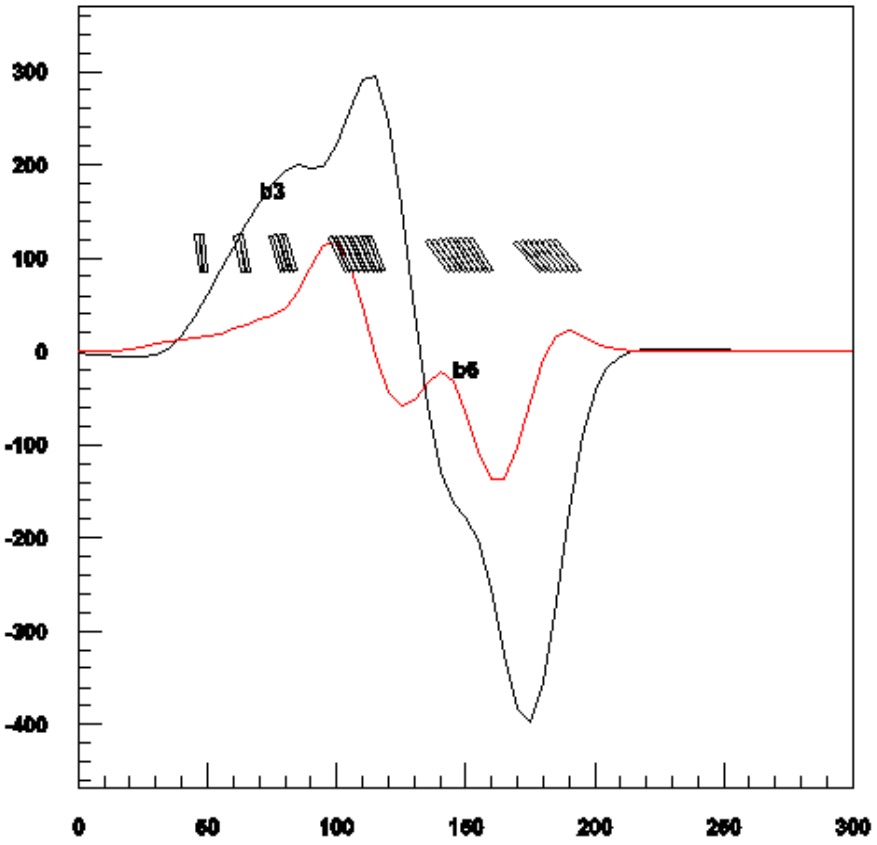

FIG.29: Cross section of coil ends, with the sextupole and decapole harmonics (units) as function of the position (mm). The iron contribution has not been taken into account.

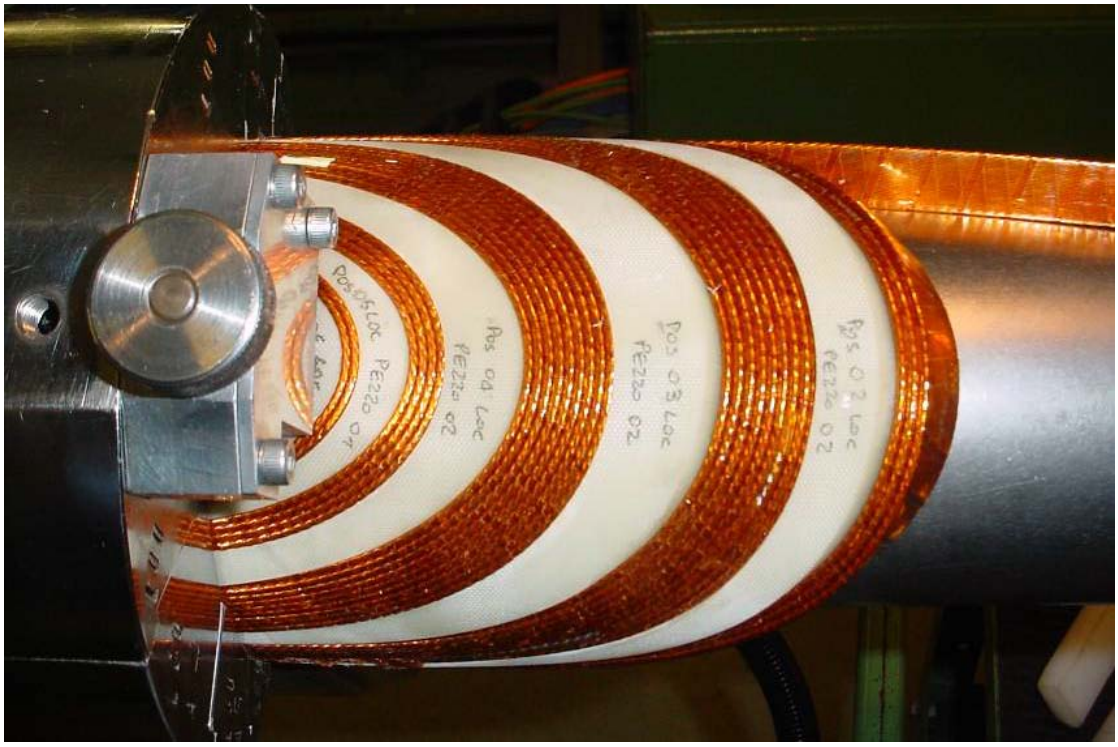

FIG.30: Photo of the coil-end during winding tests at ASG Superconductors.

Winding tests have been performed by ASG Superconductors (Genova) with a dummy cable (superconducting cable with the inner stainless steel core). The tests have shown that the designed shape is stable during the winding (see Fig.30) and does not present particular problems. Only the final “shoe”, which covers the last block, needs some refinements to completely fit the conductors. However the geometry of the “as built” coil-ends present some significant differences with respect to the “as designed”. The most remarkable variation is a shift of the blocks along the z-axis, especially for the last 3 large blocks. As consequence, the total coil-end lengths result about 12–14 mm longer than the design value. The shift of the blocks seems due to the fact that the conductors in the coil-heads are “fatter” in the narrow side. Consequently, each block in coil-ends is longer in the z-direction. From the magnetic point of view, the main inconvenient is a larger value of sextupole and decapole. The contribution of coil-end sextupole and decapole scaled to the 2-D section of the magnet (i.e. averaged on half-length of the 3.9 m long magnet) would be: $b_3 \approx +2.5$ units and $b_5 \approx +0.5$ units.

A new coil-head geometry could be recalculated with Roxie, with a conductor narrow side more “fat”. However this new geometry produces wedges more “tight” along the x-axis, due to the construction of the isoperimetric conductor blocks of Roxie. This modification has been judged pejorative by ASG, and consequently has been rejected. A compensation of sextupole and decapole component in the coil-ends has been carried out with a small inner shift of the last two coil-end blocks.

A survey of the cured coil ends is discussed in Section Industrial developments.

4.7 Conclusions

The effects on the field quality due to the main contributions, namely iron, dynamic effects in the conductor, magnetization of collars and beam tube, thermal and mechanics effects, have been investigated and properly evaluated.

The total variation of sextupole and decapole field harmonics (with respect to the static condition) vs. the central field B_0 due to the saturation of the iron and to the dynamic effect inside the conductor are shown in Fig.32. Fig.31 includes also the effects coming from the mechanical analysis.

In our opinion it is not wise to sum all these contribution and try to optimize the results since there is some uncertainness on the input data for almost all of them.

The purpose of the magnet is to show that a fast pulsed magnet can be reliably built and operated; in this respect the optimization of the field quality can be done at a later stage when the magnet has already been operated and measured and the influence of the various contributions better understood.

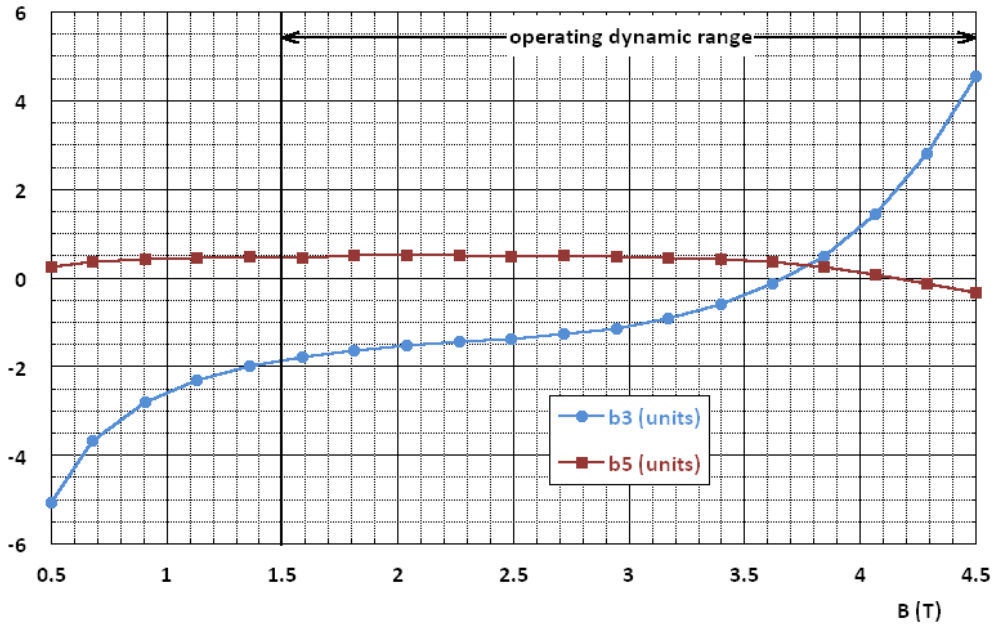

FIG.32: Sextupole and decapole component vs. central field due iron saturation, magnetization of collars and shimming, persistent currents, inter-filament coupling currents and paramagnetism of copper-manganese matrix.

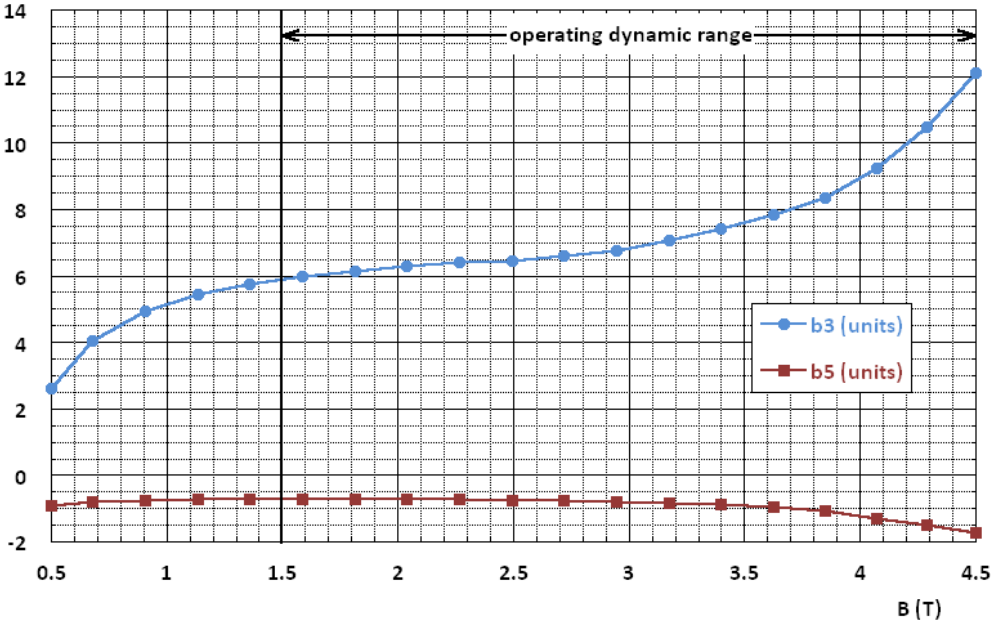

FIG.31: Sextupole and decapole component vs. central field due iron saturation, magnetization of collars and shimming, persistent currents, inter-filament coupling currents, paramagnetism of copper-manganese matrix and thermal and mechanical effects.

5. LOSSES

For fast pulsed dipoles it is particularly critical to evaluate and control the power dissipated in the cold mass during the rapid cycle of the magnet. The main dissipative sources are:

1. magnetic hysteresis in the superconductor;
2. eddy currents in the conductor (inter-filament and inter-strand coupling currents);
3. eddy currents in collar and yoke;
4. eddy currents in the beam tube;
5. magnetic hysteresis of iron yoke.

In the following sections, we describe the methods used to calculate these power sources.

5.1 Magnetic hysteresis in the superconductor

The hysteretic power per unit volume p_{pc} can be calculated by the relation:

$$p_{pc} = M_{pc} \cdot \dot{B} \tag{23}$$

where M_{pc} is the magnetization of conductor due to the persistent currents and has been defined by relation (15). Because this power density is a function of the local magnetic field on the conductor, it has been evaluated from the 2-D map of magnetic field calculated by Opera©. Moreover the results have been compared with the ones obtained with Roxie and the agreement is very good. The power in every point is not constant during the ramp because the

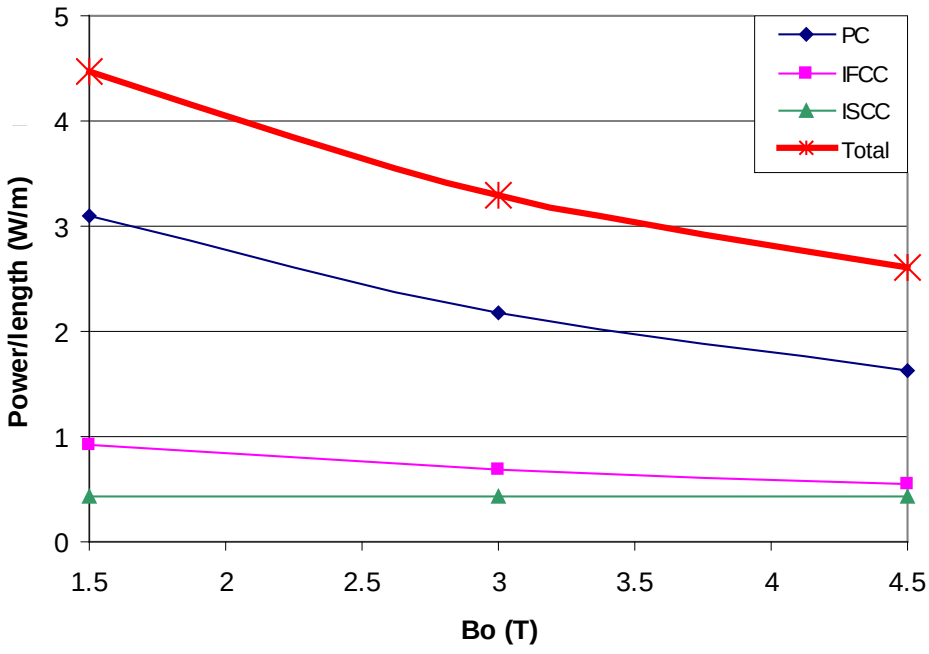

FIG.33: Power losses per unit length in conductors over coil cross section; PC=hysteresis losses, IFCC= inter-filament current losses, ISCC= inter-strand current losses.

magnetization M_{pc} decreases as the field increases. The "PC" curve in Fig.33 gives the power density, per unit length of magnet, over the coil cross section.

5.2 Losses due to eddy currents in conductor

The part of this loss due to the inter-filament coupling currents has been calculated using again relation (23), where obviously the magnetization is the one due to the inter-filament currents, calculated with (17). Hence, also for this component, the power has been calculated with Opera© from the 2-D magnetic field map, and the agreement with the Roxie results is very good. The power in each point of the magnet is not constant during the ramp up because of the copper magneto-resistivity. The "IFCC" curve in Fig.33 gives the integrated power over the dipole cross section.

The volumetric loss p_{RA} due to the inter-strand coupling currents via adjacent resistance in transverse field has been calculated with:

$$p_{R_A} = \rho_{R_A} J_z^{\,2} = R_A \frac{b \cdot c}{2 p_c} \cdot J_z^{\,2} \tag{24}$$

where ρ_{RA} represents the resistivity associated to the adjacent resistance R_A and all the other terms have been already defined in relation (18). Beside this term, the other contributions to inter-strand coupling currents have been considered (via crossover resistance and via adjacent resistance in parallel field). They have been calculated with the model given in reference 32) and by numerically integrating the magnetic field in the conductors. The "ISCC" curve of Fig.33 gives the total inter-strand loss over the magnet cross section. This loss is constant during the ramp. Again the agreement with Roxie is very good. Fig.34 shows a map of the

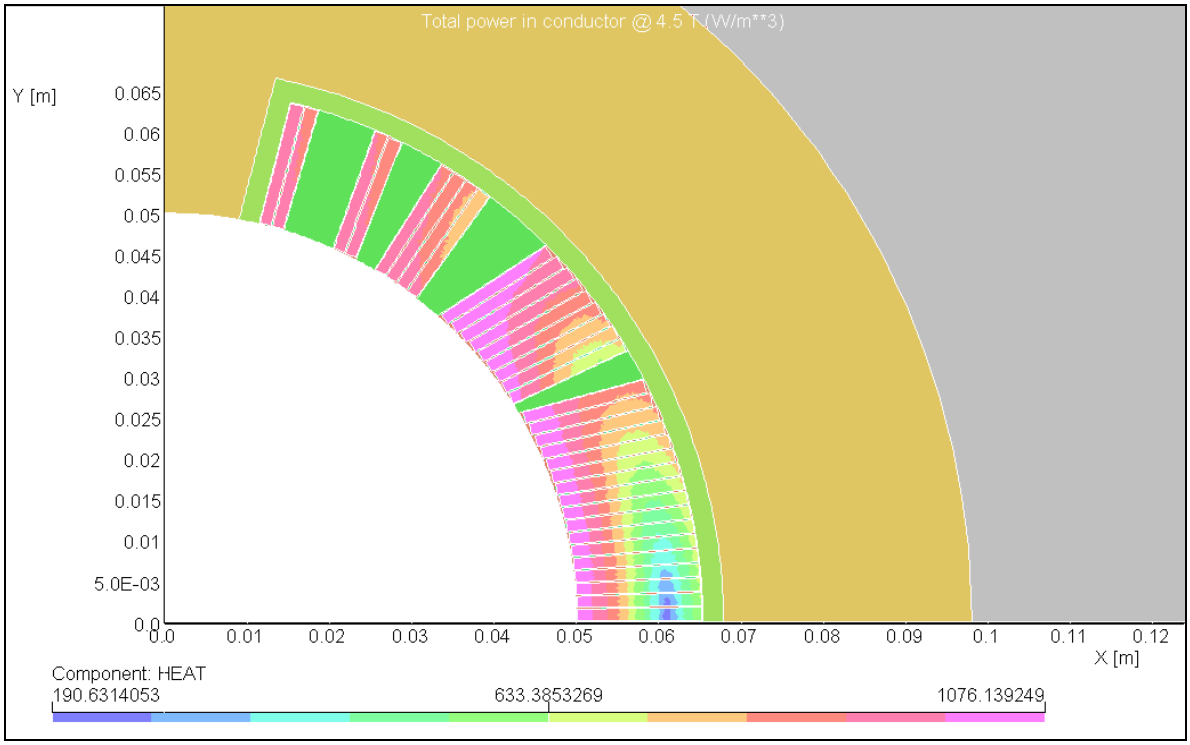

FIG.34: Total power density [W/m^3] in the conductors during the ramp at B_0=4.5 T. The peak power is 1076 W/m^3.

total power density on conductor at the maximum field ramp (B_0=4.5 T), where the temperature margin is more critical. The peak power density is 1076 W/m^3.

5.3 Eddy currents in collar and yoke

A not negligible fraction of the losses is due to the eddy currents in the laminations of the collar and of the iron yoke and in other components like pins and keys. Table 16 reports the main characteristics of the yoke and collar laminations. In order to simplify the study and the calculation of these losses, they have been divided in three types.

A. Losses due eddy currents for the parallel component of the magnetic field in laminations.

B. Losses due to eddy currents for perpendicular components of the magnetic field in laminations.

C. Losses for eddy currents in pins and keys of the collar and yoke.

5.3.1 Eddy currents for parallel field

These eddy currents are present both in the coil-end region and in the 2D section of the magnet: in fact in this last section, the 2D magnetic field B has only components parallel to the lamination. The eddy currents have components mainly parallel to the lamination and have simple symmetries along the lamination thickness (they decrease from boundary planes of the lamination and vanish in the central plane). From a simplified analytical analysis, the volumetric losses (averaged along the thickness of the lamination) can be calculated easily from the variation of the magnetic field parallel to the lamination:

$$p_{B//}(x,y) = \frac{1}{12\rho}\dot{B}_{//}(x,y)^2 \Delta s^2 \qquad (25)$$

where ρ is the electrical resistivity, Δs is the lamination thickness and *(x, y)* is the lamination plane.

The variation of the magnetic field is proportional to the magnetic field and can be evaluated from a magnetostatic analysis. The accuracy of this method and of relation (25) has been validated by a more complete analysis, where a single lamination, with its true thickness, has been represented in a FE analysis with ELEKTRA©. The agreement resulted excellent.

5.3.2 Eddy currents for perpendicular field

In the coil-end regions, beside the losses due to the parallel component of the field, there are additional losses due to the eddy currents generated by the field component

TAB.16: Main characteristics of yoke and collar laminations.

Collar lamination thickness	3 mm
Yoke lamination thickness	1 mm
Collar electrical resistivity @ 4.2 K	5.3 10^{-7} Ω·m
Yoke electrical resistivity @ 4.2 K	4.4 10^{-7} Ω·m
Yoke average packing factor	0.97

perpendicular to the lamination plane. If the perpendicular component of the magnetic field varies smoothly along the thickness Δs of the lamination, i.e.:

$$\frac{1}{B_z}\frac{\partial B_z}{\partial z}\Delta s << 1 \qquad (26)$$

the currents can be assumed constant along the thickness of each lamination.

The values of these currents have been calculated with the FE code ELEKTRA© assuming for the laminations a continuum anisotropic material, with zero electrical conductivity in the direction normal to the lamination. In the yoke lamination, the perpendicular component of the field is strongly dependent on the actual reluctivity of iron, which is reduced by the stacking factor (97%). As a consequence, the iron yoke has been considered as a magnetic non-linear material, with an anisotropic behavior both for the reluctivity and for the electrical conductivity.

It is easy to demonstrate that the total ac loss in the laminations is then given by the arithmetic sum of the losses due to the perpendicular component of the field (calculated with ELEKTRA©) and the losses due to the parallel component of the field (calculated by means of equation (25) with a magnetostatic analysis).

Fig.35 shows 1/8 of the model of ELEKTRA©, which is 1.40 m long in order to reduce the number of the mesh nodes. The colors assigned to the different components of the magnet are the following: in yellow the collar, in green the iron yoke and in violet the stainless steel which substitutes the iron yoke in coil end regions. In the model also the keys and pins which connect and keep closed the laminations, are represented.

A preliminary analysis has shown that a large fraction of the currents would flow from the lamination through the cylindrical helium vessel (not represented in Fig.35), which is an isotropic material surrounding the yoke. In fact the cylindrical helium vessel acts as a short circuit between the yoke laminations, allowing additional path for the eddy currents. Consequently, during the assembly of the magnet, a particular care has to be put to

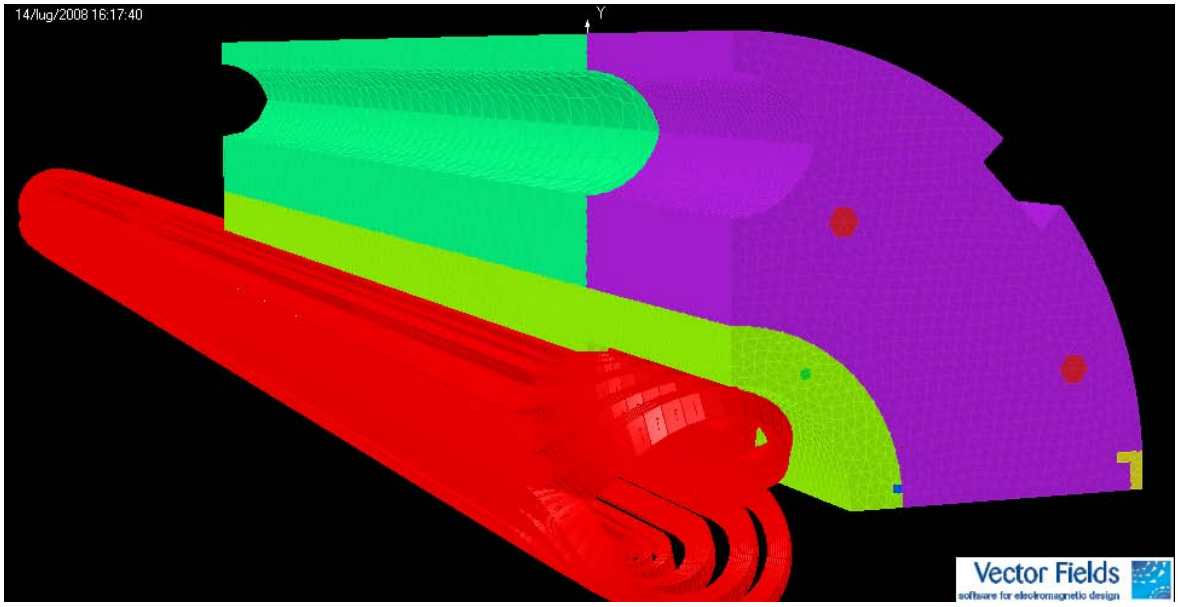

FIG.35: 1/8 of the ELEKTRA FE model.

electrically insulate the cylindrical vessel from the lamination, at least in the coil-end region, in order to avoid these types of losses.

Figs. 36 and 37 represent a view of the eddy currents (arrows) and losses (colour) in the laminations, during the ramp-up of the magnet (dB_0/dt=1 T/s), respectively at B_0=1.5 T and B_0=4.5 T. It is possible to observe that at low field currents and losses are especially concentrated at the interface between the yoke-end and the stainless steel lamination (Fig.36). At higher field, currents and losses spread much more in the yoke and collar lamination, because the iron in the yoke end region presents a much lower reluctivity and consequently B_z component of the magnetic field penetrates more deeply in the yoke (Fig.37).

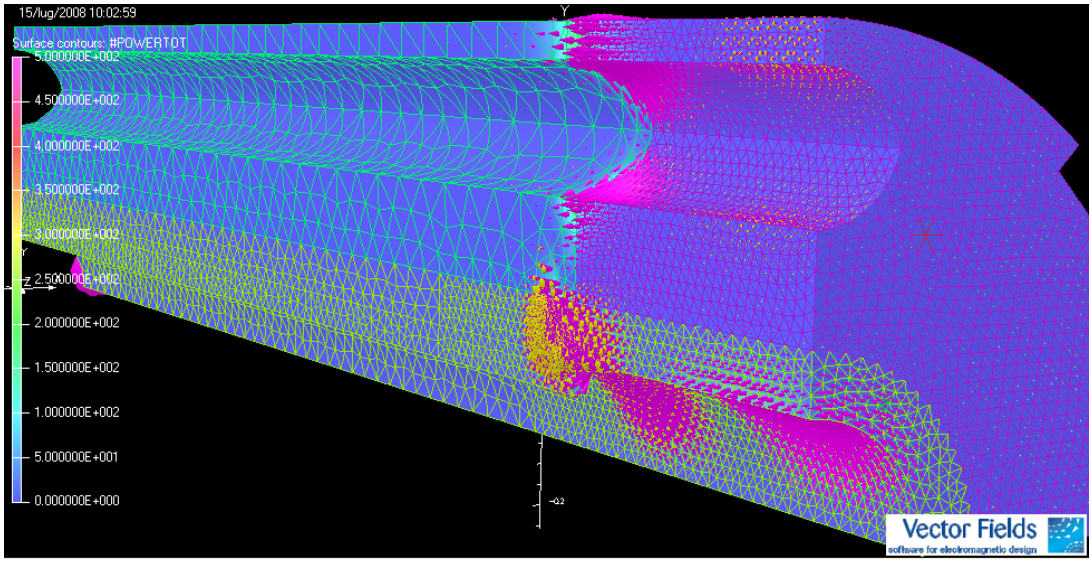

FIG.36: View of eddy currents (arrows) and losses (colors, W/m^3) during the magnet ramp-up (dB_0/dt=1 T/s), at B_0=1.5 T.

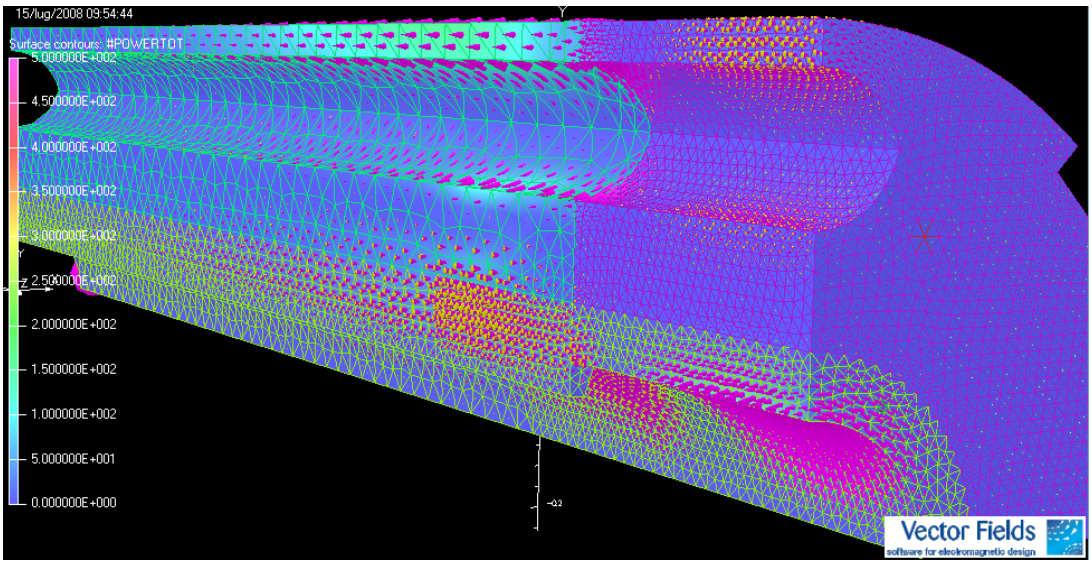

FIG.37: View of eddy currents (arrows) and losses (colors, W/m^3) during the magnet ramp-up (dB_0/dt=1 T/s), at B_0=4.5 T.

5.3.3 Eddy currents in pins and keys

A fraction of the total losses of the magnet is due to the eddy currents that flow through the pins of the yoke and collar lamination and through the keys of the collars. In fact these components present electrical conductivity also in the z direction and for this reason give additional paths for the currents. The yoke pins (represented in red in Fig.35) are 1 m long and are constituted by stainless steel tube 2 mm thick. The collar pins (in green) are 30 mm long and are stainless steel bulk. The keys of collar (in blue) and of the yoke (in yellow) are supposed continuous and are both made of stainless steel.

With analytical consideration, it is possible to demonstrate that, in the 2-D region of the magnet, the eddy currents in pins and keys are only due to the variation of magnetic flux between these components and the symmetry plane that passes through the poles: this means that it can been neglected the flux which passes between, for example, a pin and a key (or a pin and another, not symmetric, pin). For this reason, the eddy currents in the yoke key are almost zero (except in the coil end region). Based on these considerations, the positions of the yoke pins have been optimized in order to minimize the magnetic flux between them and the symmetry plane through the pole. In this way the losses associated to these components have been drastically reduced. The position of the collar pin and key is instead strictly motivated by their mechanical functions.

Fig.38 presents another view of the currents (arrows) and losses (colors) at B_0=4.5 T. The stainless steel lamination, which substitutes the yoke in the coil-end region, has been removed in order to show the current in the yoke pins and in the collar key.

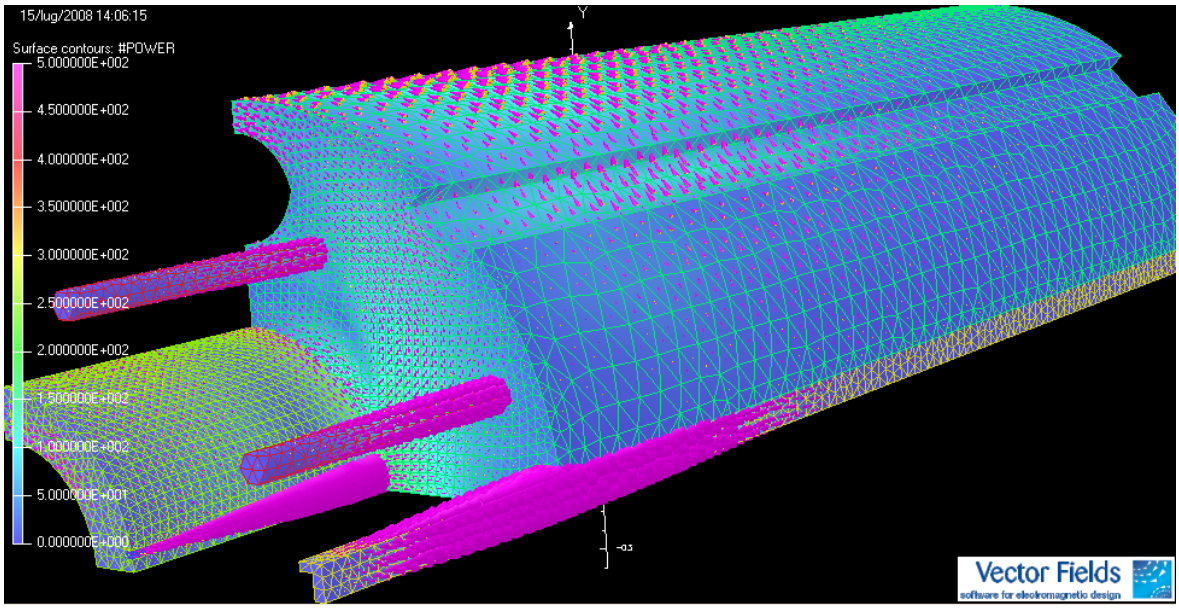

FIG.38: View of eddy currents (arrows) and losses (colors, W/m^3) during the magnet ramp-up (dB_0/dt=1 T/s), at B_0=4.5 T. The stainless steel which substitutes the yoke in the collar end has been remove to show the current in the yoke pins and collar pins.

5.4 Eddy currents in the beam tube

The variation of the magnetic field induces eddy currents also in the beam tube. If we neglect the coil end region, these currents are only z-directed. Assuming that the field is uniform in the beam tube, the power per unit length P can be evaluated analytically:

$$P = \int_{r_{inner}}^{r_{outer}} \int_{0}^{2\pi} \rho \cdot J_Z{}^2 \cdot r \cdot d\theta dr \approx \frac{\pi}{\rho_0} \dot{B}_0^2 \cdot r_{av}{}^3 \cdot \Delta r \qquad (27)$$

where r_{av}=44 mm is the average radius of the beam pipe, Δr=2 mm is the pipe thickness and ρ=5.3 10^{-7} Ωm is the electrical resistivity (stainless steel). This give a power per unit length P=1.0 W/m.

5.5 Eddy currents in the coil protection sheet

The coils need to be covered by a stainless steel protection sheet before being collared (see Fig.99). This sheet will be likely in electrical contact with the collars and will allow some eddy currents in the z-directions. Assuming a total thickness for the sheet of 0.4 mm and considering the presence of the shim 1 mm thick between the large side of the 34th conductor and the collar, the total losses per unit length can be evaluated in 0.48 W/m. Fortunately most part of this loss is localized in the low-field blocks, whereas the loss dissipated by each 1 mm thick shim (in contact with the peak-field conductor) is only about 0.005 W/m.

5.6 Hysteretic losses of iron yoke

An important source of losses is due to the hysteretic cycles of the iron. The iron lamination proposed for the construction is classified as M600-100A according to the European norm EN 10106-2007. This material is a non-oriented laminated low carbon steel with high Si content (about 3%), 1 mm thick. The relevant properties extracted from commercial suppliers and literature data[33)] are: mass density δ=7600 kg/m^3, electrical resistivity ρ=44 μΩ cm; coercitive field H_c=40 A/m and saturation magnetic field B_{sat}=2.04 T. According to the norm, M600-100A is certificated by the supplier with a maximum total losses of 6 W/kg, when subjected to a sinusoidal field with frequency ν=50 Hz and peak field B_p=1.5 T, at room temperature. From these total losses, the contribution due to ac losses can be easily calculated by means of the following expression, similar to equation (25):

$$p_{ac} = \frac{\pi^2 \cdot \nu^2}{6\rho \cdot \delta} B_p{}^2 \Delta s^2 \qquad (28)$$

In our case this term contributes to the losses with 2.8 W/kg. The remaining losses are due to magnetic hysteresis, which scales linearly with frequency ν, and to anomalous losses[34)], which scales with $\nu^{1.5}$. From measurements on similar materials carried out at IHEP[35)] one can evaluate the contribution of the magnetic hysteresis as 1.75 W/kg. The anomalous losses shall then contribute for the remaining 1.45 W/kg.

In the magnet operating conditions the field rate is very slow compared to 50 Hz cycling, causing a dramatic reduction of eddy and anomalous losses, while the hysteretic

losses can still give an important contribution. We have evaluated this contribution starting from the knowledge of hysteretic losses at 50 Hz. First we performed ac computations introducing a suitable constant phase lag between B and H, simulating in this way the magnetic hysteresis[36], but increasing artificially the electrical resistivity to very high value, in order to eliminate the eddy current contribution. A phase lag of 10° is needed for having a loss of 1.75 W/kg on our lamination at 50 Hz and B_p=1.5 T. The same phase was eventually introduced in 2D ac loss computation (using code FEMM[37]), simulating the real operative conditions. We found that the magnetic hysteresis contributes to the magnet losses with 1.8 W/m. According to reference 30) there are negligible differences between losses at room temperature and at the operating temperature of 4.2 K.

5.7 Summary of losses

The summary of all the losses in the 2D section of the magnet and in the coil-end region are reported in Table 18. These losses include all the powers dissipated in the magnet cold mass, except the thermal loads. The conductor losses in the coil-ends have been calculated both considering the power dissipated for the persistent and inter-filament currents in transverse field (analysis performed with TOSCA©), and estimating the power due to persistent currents for the parallel component of the field.[30]

It is possible to observe that almost all the loss contributions have large variations during ramp-up. In the 2D section, the largest contribution is given by the power dissipated in the conductor, but other considerable fractions are given by the iron hysteresis, eddy currents in beam tube and collar keys. In the coil-end region, the power dissipated for eddy currents in the lamination are important, especially at intermediate field (B_0=3.0 T÷3.5 T).

The total losses, integrated on the whole 3.9 m long magnet, varies between 36 W at B_0=1.5 T and 30 W at B_0=4.5 T (see Table 18). In case of a full length magnet (7.8 m long), the power would scale almost linearly, because the contribution of eddy currents in coil-ends is not so large respect to the losses in the 2D part of the magnet.

It is possible to conclude that the specific dissipation for this pulsed magnet is between 7.7 W/m and 9.2 W/m, (including the coil-end contributions). These values can be considered acceptable.

TAB.17: Summary of losses in the 2D section and coil end region of the magnet during ramp-up ($\dot{B}_0$ =1 T/s).

	In straight section (W/m)			In each coil end (W)			% in 3.9 m long magnet		
B_0	1.5 T	3.0 T	4.5 T	1.5 T	3.0 T	4.5 T	1.5 T	3.0 T	4.5 T
Conductor	4.500	3.300	2.600	0.630	0.462	0.364	51%	38%	36%
Collar eddy	0.006	0.006	0.006	0.144	0.393	0.197	1%	2%	1%
Yoke eddy	0.002	0.002	0.002	0.234	1.111	0.978	1%	6%	7%
Collar pins	0.140	0.138	0.102	0.004	0.004	0.004	1%	2%	1%
Collar keys	0.568	0.552	0.436	0.013	0.014	0.014	6%	6%	6%
Yoke pins	0.062	0.533	0.167	0.030	0.035	0.049	1%	6%	2%
Yoke keys	0.000	0.000	0.000	0.058	0.169	0.074	0%	1%	1%
Yoke hyst.	1.8	1.8	1.8	0.35	0.35	0.35	21%	21%	25%
Coil protec. sheet	0.484	0.484	0.484	0.094	0.094	0.094	6%	6%	7%
Beam tube	1.000	1.000	1.000	0.195	0.195	0.195	12%	12%	14%
TOTAL	**8.56**	**7.82**	**6.60**	**1.75**	**2.83**	**2.32**	**100%**	**100%**	**100%**

TAB.18: Total losses in the magnet during ramp-up at $\dot{B}_0$ =1 T/s, in case of the model magnet (3.9 m long) and full length magnet (7.8 m long). The thermal loads have not been considered.

B_0 (T)	In the 3.9 m long dipole (W)	In the 7.8 m long dipole (W)
1.5	36.0	68.6
3.0	35.4	65.1
4.5	29.7	54.8

6. MECHANICAL ANALYSES

The 2D cross-section of the dipole mechanical structure is shown in Fig.3. It is based on 3 mm thick laminated stainless steel collars, assembled through stainless steel keys, and 1 mm thick iron yoke laminations, assembled through large stainless steel C-shaped clamps.

The main mechanical function of collars is to give axial pre-stress to the winding. During energization up to 4.5 T, the winding experiences very large Lorentz forces, 0.68 MN/m radially, outward directed, and 0.30 MN/m axially, inward directed. The radial component of the Lorentz force is mechanically sustained by collars, the axial component has to be compensated by an adequate axial pre-stress. Its average value is determined requiring continuous contact between the winding pole and the collars even when the winding is fully energized. This corresponds to have an average pre-stress in the winding at the end of the assembly operations of about 70 MPa.

The shape of the collars (Fig.103) is very similar to what was designed for SSC.[13)] They are parallel packed in alternate position (see Fig.39) in groups of 10, for a total longitudinal thickness of 30 mm. The curvature is rendered introducing thin spacers (~0.1 mm) on one side only of the midplane, close to the outer radius. The collar width is 30 mm, leading to an inner iron yoke radius of 96.85 mm.

The iron yoke laminations are 1 mm thick and ~140 mm wide. The external radius is 240 mm, but the axial dimension has been cut down to 230 mm (see Fig.105), due to a space constraint in the press already existing at ASG-Superconductors premises. The iron yoke laminations are assembled on a curved template, which gives the right curvature radius (66.67 m). Then, the curvature is retained through the insertion of 0.05 mm thick spacers nearly each 25 laminations. The basic unit of the iron yoke assembly is 1 m long: the laminations are kept together through 4 hollow tie rods per side passing through the small holes visible in Fig.105. A proper tension applied to these tie rods will also ensure to reach

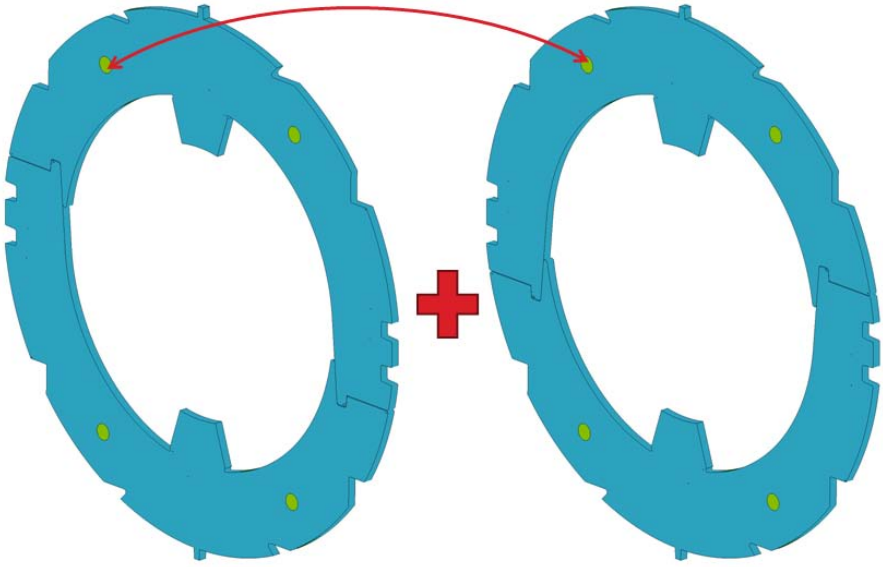

FIG.39: Collars are assembled in alternate position and kept together through stainless steel pins.

TAB.19: Material properties of the FE analysis.

Component	Material	Young Modulus (GPa)	Yield strength 300 K/4.5 K (MPa)	Thermal expansion coefficient (300 K to 4.5 K)
Insulated conductor	—	9	—	$5.63 \cdot 10^{-3}$
Collars	Nitronic40	192	683/1427	$2.4 \cdot 10^{-3}$
Collar keys	Stainless steel AISI 316LN	220	—	$3 \cdot 10^{-3}$
Collar pins				
Pole shimming				
Wedges	G11 (normal to fibers)	25.5	—	$2.47 \cdot 10^{-3}$
Iron yoke	Lamination M600-100A	200	365/705	$1.8 \cdot 10^{-3}$
Yoke C-clamps	Stainless steel AISI 316L	200	250/600	$3 \cdot 10^{-3}$
Ground insulation	Kapton	2.5	—	$9 \cdot 10^{-3}$

the design packing factor (0.97 on the internal radius). This procedure should ensure a good mechanical coupling between the curved collared coil and the curved iron yoke itself. Finally, the iron yoke has been designed to give no further pre-stress to the winding but to limit the deformations arising during the magnetic energization.

Table 19 resumes the material properties used in the finite element analysis. A description of the involved materials with some explanation is given in Section Main materials and components. In addition to that, the conductor is a composite material especially designed for the SIS300 dipole (see Section Conductor). Qualitatively, it is the same Rutherford cable as the LHC dipole outer layer but with a high resistance metallic core, 25 μm thick, in order to reduce power dissipations in the cycled regime. Mechanical properties of such a conductor cannot be found in literature but have to be measured. For this reason, we have started a measurement campaign of short straight samples, both stacked and arc piled, as shown in Figs. 120 and 123. First results, resumed in Appendix B, indicate for the conductor a Young modulus ranging between 7 and 9 GPa.

All the materials are modeled with elastic properties, except iron and stainless still in collars and C-clamps. They are modeled with a bilinear stress-strain curve depending on temperature as indicated in the Table.

6.1 2D analysis

The finite element analyses have been carried out using the commercial code ANSYS®. The adopted element is PLANE82, in plane stress configuration with thickness real constant input. The finite element mesh, containing nearly 150˙000 nodes, is shown in Fig.40. Both the back and the front collars shown in Fig.39 have been modeled, even if, for clarity, only the front collars are shown in Fig.40.

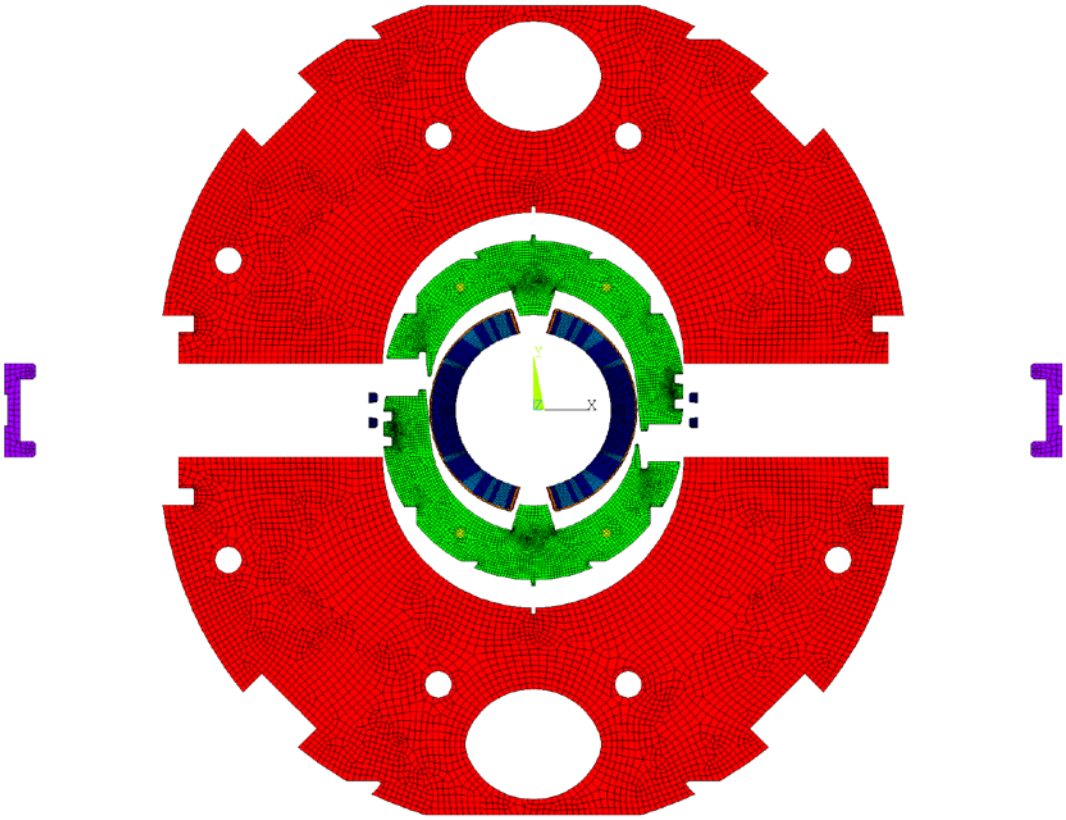

FIG.40: Mesh of the 2D mechanical finite element model.

Each collar has an equivalent thickness which is half of all the other components; they can slide without friction and are connected through stainless steel pins. Contact surfaces have been modeled between all the sliding parts using the ANSYS® flexible-to-flexible contact technology, through CONTA172 and TARGE169 elements.

The loads which are subsequently applied are:

1 Collaring

2 Fitting of the collared coils into the iron yoke

3 Cool-down

4 Energization up to 4.5 T

6.1.1 Collaring

To perform the collaring operation, we have to press the collars, acting on the flat surfaces purposely grooved with this aim, until the holes which will host the keys on front and back collars, are perfectly aligned. Once this step is completed, the keys can be easily inserted and then the force released, as sketched in Fig.41. This operation needs a total pressing force of 505 tons/m.

A special comment has to be made on the pre-stress really acting on the winding. The reference design, shown in Fig.98, has been carried out using the nominal dimensions of the conductor at 50 MPa, described in Section 3.4, Table 6. This means that in the conditions

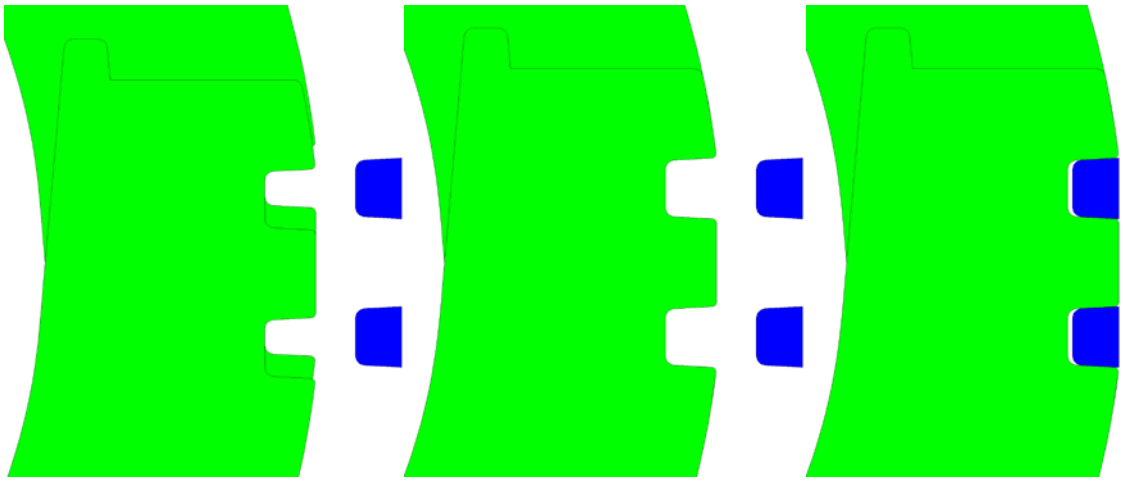

FIG.41: Collaring operation sequence.

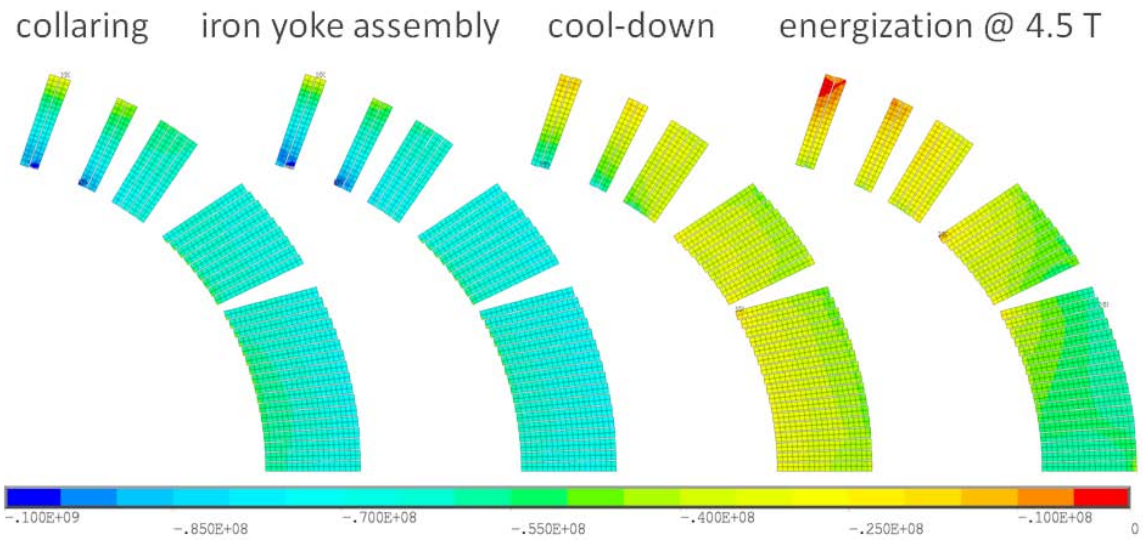

FIG.42: Azimuthal stress (Pa) in winding after collaring, iron yoke assembly, cool-down and energization @ 4.5 T.

represented in Fig.98 the winding will experience an average azimuthal pre-stress of 50 MPa. We verified that this value is not enough, as it will reduce down to 30 MPa after cool-down, leading to a partial detaching of the winding from the collars in the pole region. To have a reasonable confidence of a continuous contact between collars and winding, we need to increase the azimuthal pre-stress at warm after collaring up to nearly 70 MPa, by introducing a stainless steel shimming 0.25 mm thick between winding and pole. As shown in Fig.99, this shimming has been later on increased up to 1 mm, to enhance the flexibility of the system, but analogously reducing the pole of the same amount.

Table 20 resumes the main data concerning the average azimuthal stress in the winding and the minimum, in absolute value; azimuthal stress of the last turn, the one in contact with the collar pole. The negative sign ensures that the winding, including the last turn, is always in compression, i.e. it never comes off the collars.

TAB.20: Average and maximum azimuthal stress in the winding.

	collaring	iron yoke assembly	cool-down	energization @4.5 T
Average azimuthal stress in the winding (MPa)	-64	-68	-38	-43
Maximum azimuthal stress of last turn (MPa)	-27	-30	-16	-1

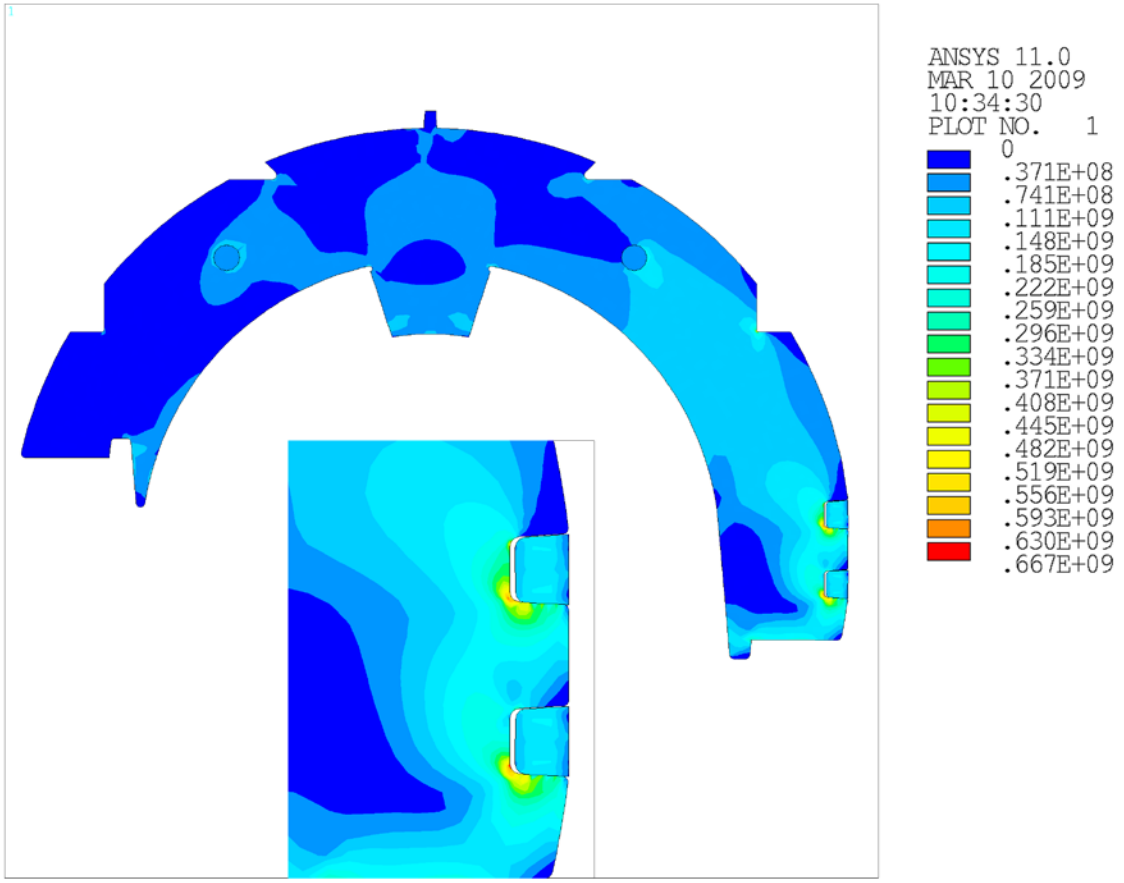

FIG.43: Von Mises stress (Pa) in collars after collaring operation.

It is worth noting that the insertion of this 0.25 mm thick shimming “breaks” the initial cross section optimization, actually reducing the real volume occupied by the winding. As it could be expected, this has a negative impact on the harmonic component of the magnetic field, which can be estimated (see Section Thermal and mechanic effects) and avoided simply designing from beginning a dipole optimized to have a pre-stress of 70 MPa at warm.

The peak stress at the end of the collaring operation, 667 MPa (see Fig.43), is located in the collars around the keys. Those regions moderately plasticize, but they will not experience any especially critical fatigue issue, as it will be described in Section Energization. A secondary peak stress of 160 MPa is located in the pole corner and is not especially critical at this stage.

6.1.2 Fitting of the collared coils into the iron yoke

The iron yoke has an important mechanical function: it has to contain the radial movement of the winding at the midplane level, which is the main responsible of the peak stresses between cool-down and energization. Schematically, the iron yoke is divided into two halves which are kept together by the stainless steel C-clamps shown in Fig.44. It is clear that this system works as long as there is a whatever small gap between them. If the two halves of the iron yoke enter into contact, the C.-clamps can apply no further compression. As a consequence, we need to cut away a gap from the iron yoke at the midplane level. In order to assess its thickness, two aspects have to be taken into account: the effect of the differential thermal contraction from room temperature to 4.5 K of iron (~$1.8 \cdot 10^{-3}$) and Nitronic40 (~$2.4 \cdot 10^{-3}$), so that collars contract more than yoke, and the fact that the inner radius of iron yoke is 40 μm larger than the outer layer of collars, to make the assembly easier. A reasonable gap is the one that keeps the two halves of the yoke at a distance which never becomes less than the manufacturing tolerance of the iron laminations, i.e. 20 μm. Table 21 and Fig. 45 resume the behavior of the distance between the two halves of the iron yoke as function of the

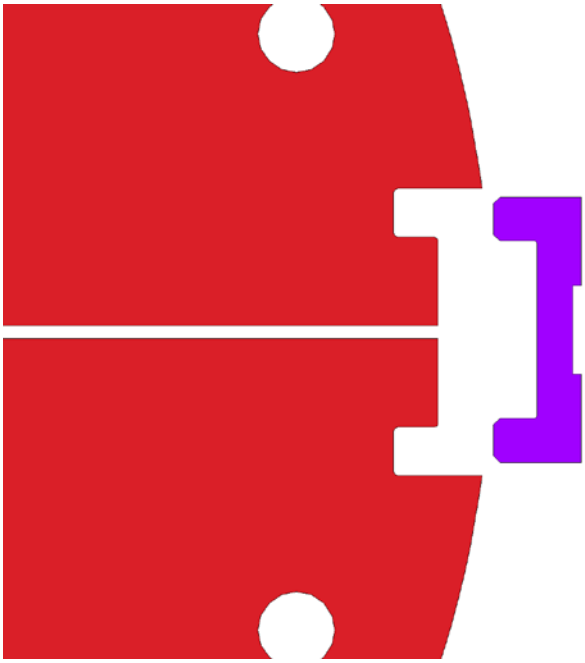

FIG.44: Insertion of C-clamps into the iron yoke.

TAB.21: Distance between the two halves of the iron yoke as function of the load.

	As designed	Iron yoke under pressure	Pressure releasing	Cool-down	Energization @4.5 T
Inner distance (μm)	160	4	236	69	36
Outer distance (μm)	160	56	152	41	39

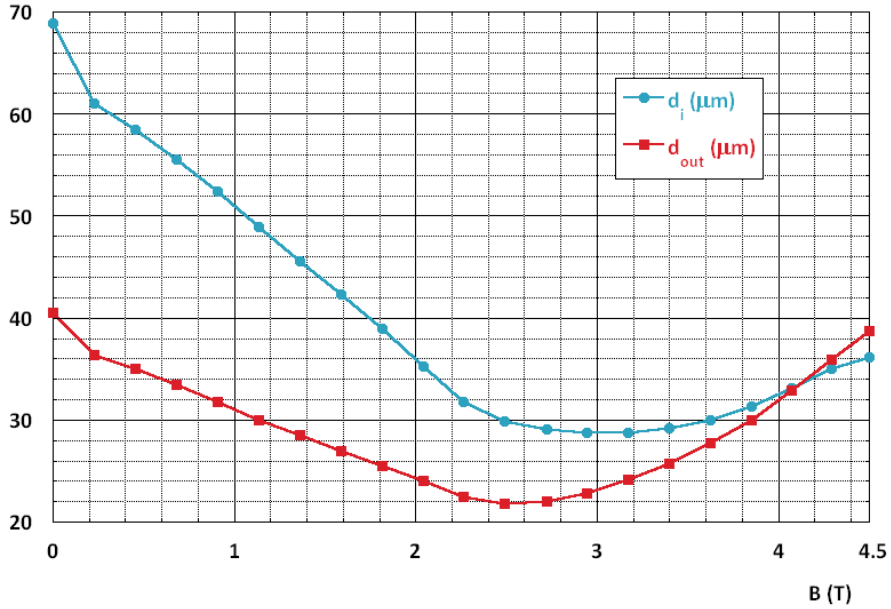

FIG.45: Distance between the two halves of the iron yoke as function of the magnetic field, from cool-down to full energization.

load with an initial geometrical gap of 160 μm, 80 μm per side. The outer distance reaches 21.8 μm at 2.5 T, which is an acceptable minimum value. With this gap, the force we need to apply to put into contact the two halves of the iron yoke is 470 tons/m. This contact happens to be at the inner radius, so that to ensure the insertion of the C-clamps with no or limited applied force, they are foreseen to be heated.

Between cool-down and energization, the yoke gap is small enough to have very small effects on the harmonics. To understand its impact, let's consider the worst possible configuration, that is a model in which one side of the iron yoke is perfectly closed while the other has a gap two times of the average distance thick, i.e. $2\cdot(d_{in}+d_{out})/2=(d_{in}+d_{out})$, as shown in Fig.46. Looking at Fig.47, in which $d_{in}+d_{out}$ as function of field is shown, we can indentify two main regions, the very low field region, in which $d_{in}+d_{out}$ is around 100 μm, and the region between 1.5 and 4.5 T, in which $d_{in}+d_{out}$ is at worst around 75 μm. The corresponding quadrupole and sextupole variation with respect to the designed geometry (no gap) are shown in Figs. 48 and 49. The worst case in the worst conditions leads to a maximum quadrupole variation around -0.3 units and a maximum sextupole variation around -0.1 units (the sign depends on the side we cut away the gap with respect to the verse of the current). These values are within acceptable limits.

As expected, once the collared coils are fitted into the iron yoke and the pressing force is discharged, there is a general release of stress in the collars, whose peak value, still in the region around the keys, decreases from 667 MPa down to 503 MPa (Fig.50). This has to correspond to a rise of the stress level in iron yoke and C-clamps, whose peak values, 193 MPa and 192 MPa, are acceptably within the yield limits of the materials.

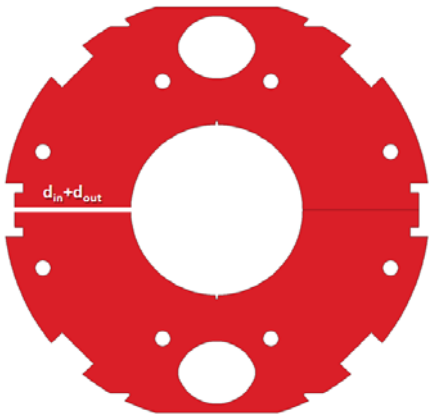

FIG.46: Special magnetic model for assessing the impact of iron yoke gap on harmonics.

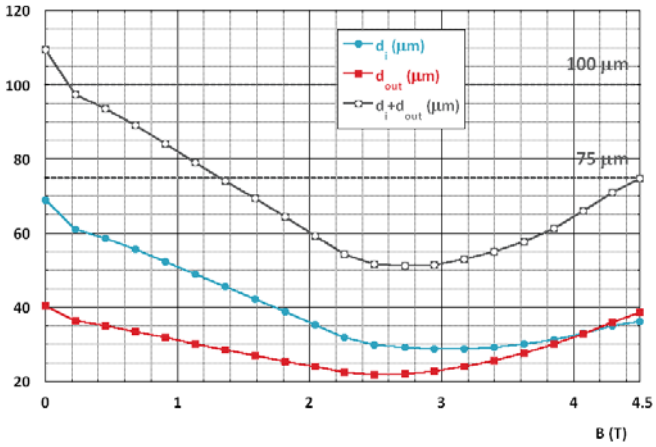

FIG. 47: Distance between the two halves of the iron yoke as function of the magnetic field, from cool-down to full energization.

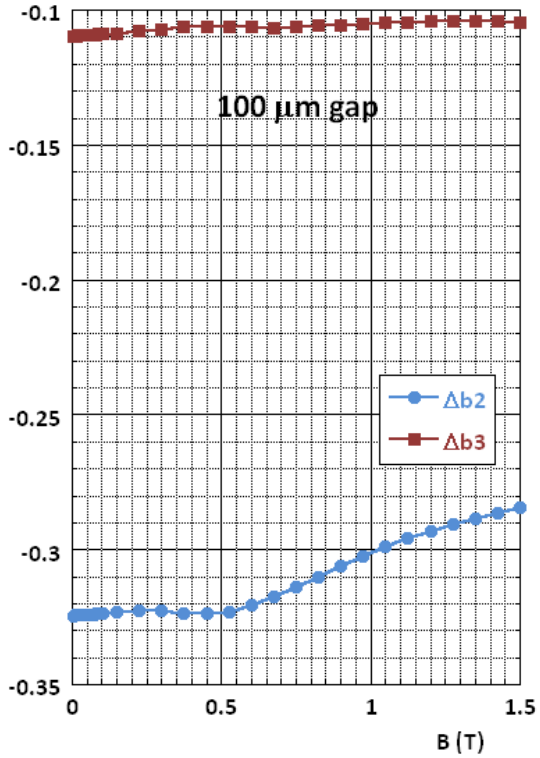

FIG. 48: Quadrupole and sextupole variation in the low field region corresponding to a gap $d_{in}+d_{out}$=100 µm.

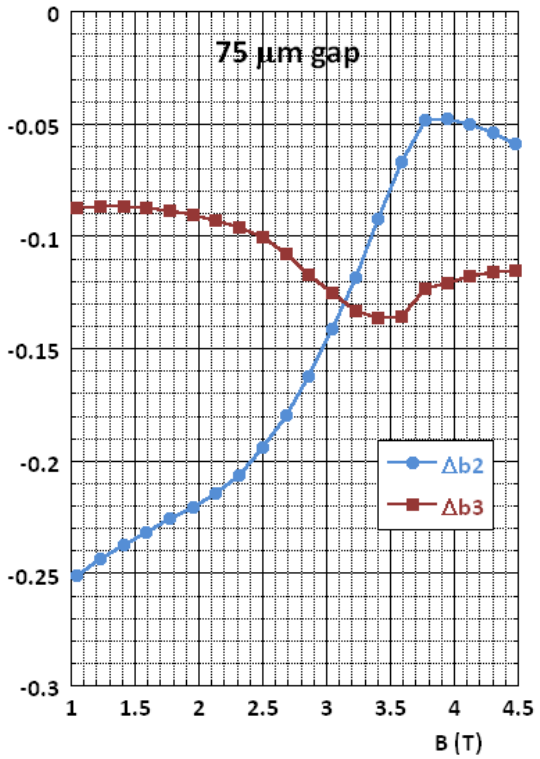

FIG. 49: Quadrupole and sextupole variation in the range between 1 and 4.5 T corresponding to a gap $d_{in}+d_{out}$=75 µm.

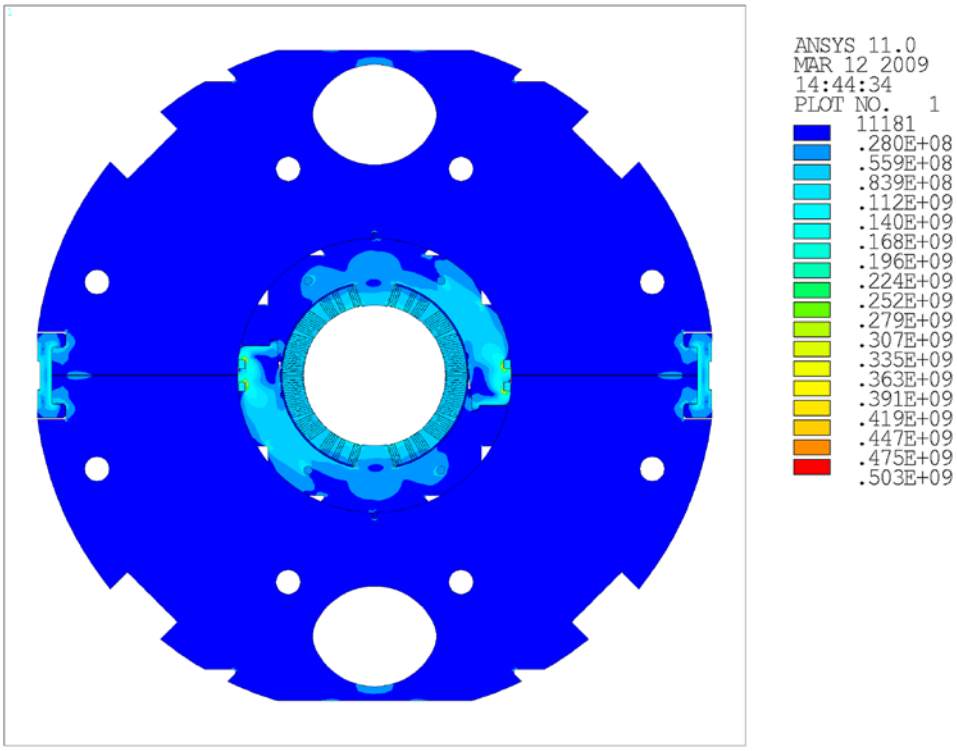

FIG.50: Von Mises stress (Pa) after the fitting of the collared coils into the iron yoke.

TAB.22: Peak Von Mises stresses (MPa) as function of constructive and operating steps.

Step	Collar – key region	Collar – pole region	Keys	Iron yoke	C-clamps
Collaring	667	160	155	-	-
Iron yoke assembly	503	167	124	193	192
Cool-down	368	178	90	50	59
Energization @4.5 T	419	403	93	46	56

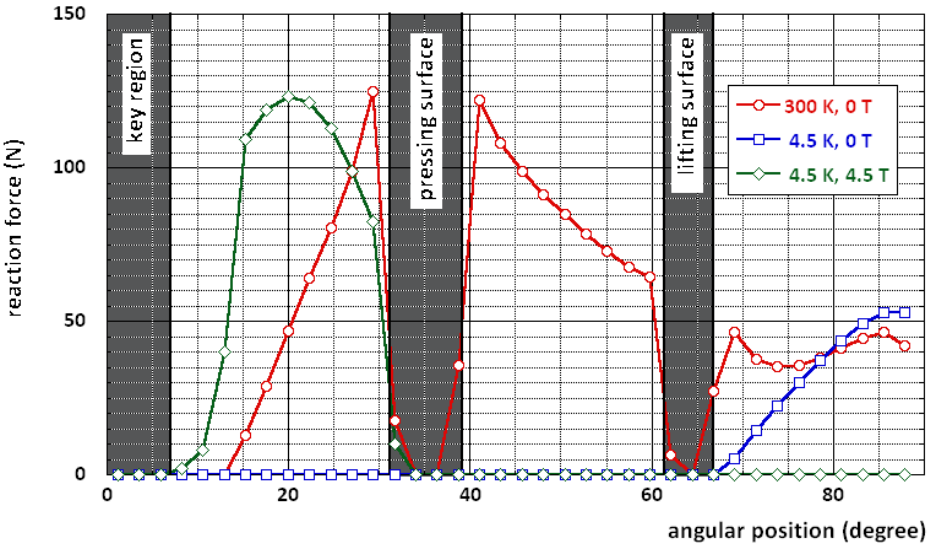

FIG.51: Evolution of the contact force between collars and iron yoke as function of the angular position.

6.1.4 Energization

The main peak Von Mises stresses after energization are listed in Table 22. The yield stress of Nitronic40 ranging from 700 MPa at room temperature up to 1400 MPa at 4.2 K, those values do not appear to be remarkably critical in absolute, but they need to be further analyzed from the fatigue point of view. The simplest and most conservative fatigue criterion is the Sodeberg method, illustrated in Fig.52. Let's consider a material cycling between a minimum (σ_{min}) and a maximum (σ_{max}) Von Mises stress. We can define a graph having the mean stress, $\sigma_{mean}=(\sigma_{min}+\sigma_{max})/2$, on the x-axis and the oscillation amplitude, $\sigma_{alt}=(\sigma_{max}-\sigma_{min})/2$, on the y-axis. A material which is loaded under a purely static load will have $\sigma_{alt}=0$ and $\sigma_{mean}=\sigma_{yield}$. In Fig.52, σ_{yield} has been fixed at 1200 MPa, instead of 1400 MPa, in order to keep a safety factor. This is confirmed by a set of measurements that indicate for Nitronic40 minimum yield strength at 4 K of 1240 MPa.[11)] Conversely, a material which is loaded under a purely oscillating load will have $\sigma_{mean}=0$ and $\sigma_{alt}=\sigma_{fatigue}$. The limit for ten millions cycles under uni-axial load of Nitronic40 can be assumed to be $\sigma_{fatigue}=0.35\cdot\sigma_{yield}=420$ MPa. This value is compatible with 38), where it has been measured at least 450 MPa for 10 millions cycles. Now, connecting with a straight line these two points, the Sodeberg criterion divides the plane into two halves: the region below the line is safe from fatigue, with potentially infinite life, whilst the region above the line corresponds to a likely fatigue failure. Analyzing the data in Table 22, we can deduce that the regions which can possibly suffer from fatigue are the collars around the keys and in the pole corner, even if both these regions have been modeled to reduce as much as possible their stress status (see Fig.103). Their fatigue status between 0 and 4.5 T is represented in Fig.52. Considering the uncertainties on the tolerances and the complexity of the mechanical coupling of the two curved surfaces, collared windings and packed iron laminations, we think that the SIS300

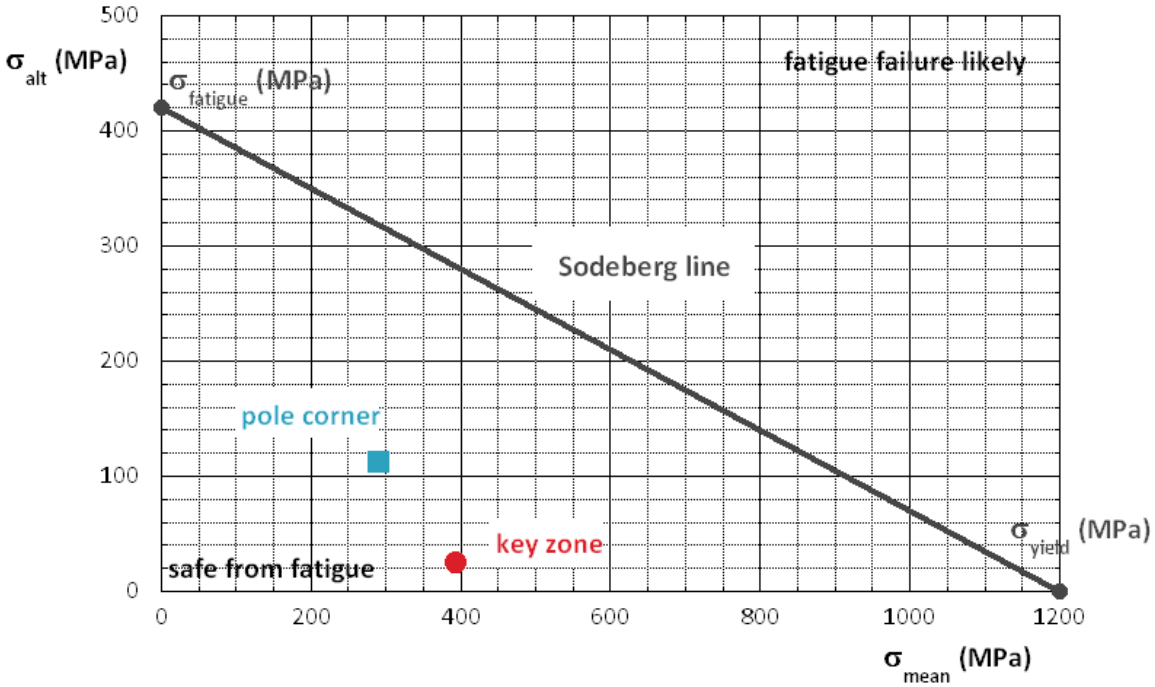

FIG.52: Sodeberg criterion for collar pole corners and key zone.

dipole is working in a adequately safe region below the Sodeberg line.

6.1.5 Stress in the wedges

The stress distribution in the wedges between cool-down and energization is particularly interesting to set up mechanical tests of irradiated G11 samples. It is well known in facts that G11 degrades when subjected to radiation, the level of deterioration depending on the dose and on the stress status of the sample.

In Figs. 53 and 54 the azimuthal (on the left) and Von Mises (on the right) stress in wedges are shown, after cool-down and full energization respectively. Comparing azimuthal and Von Mises maps, it is clear that most of the stress is compressive in the azimuthal direction.

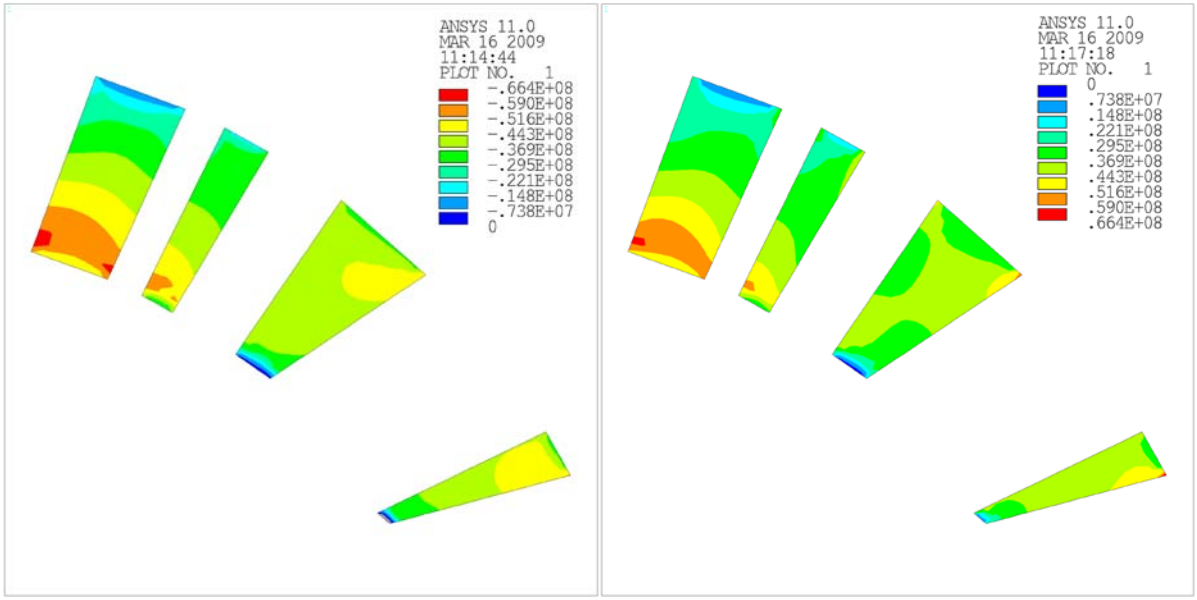

FIG.53: Azimuthal (left) and Von Mises (right) stress in wedges after cool-down. The color scales are inverted to compare the two pictures.

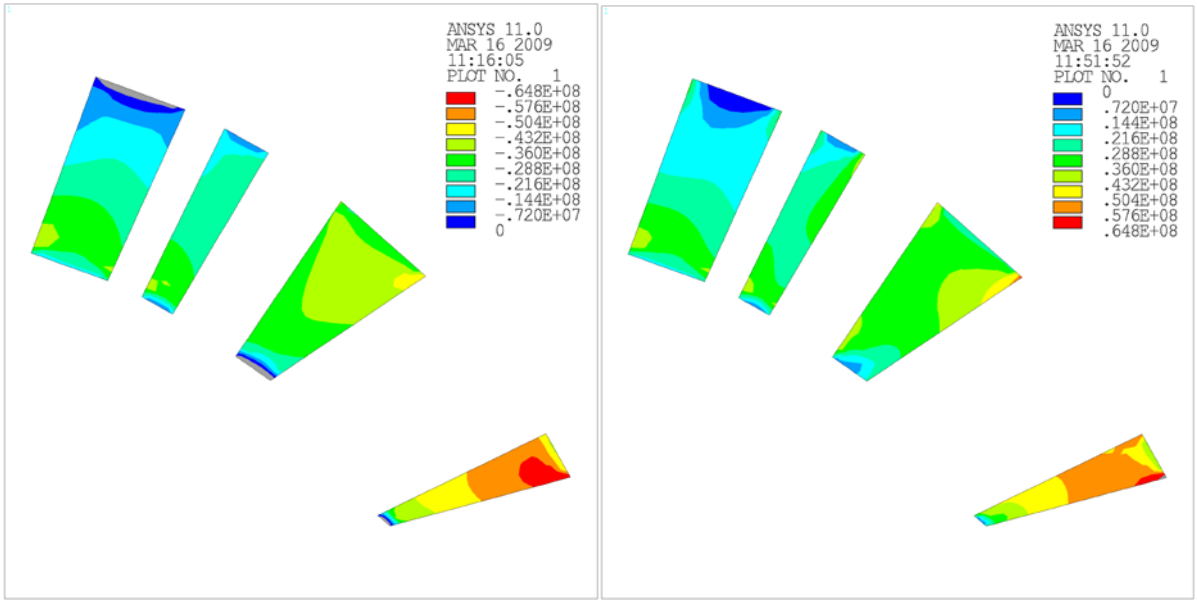

FIG.54: Azimuthal (left) and Von Mises (right) stress in wedges after full energization. The color scales are inverted to compare the two pictures.

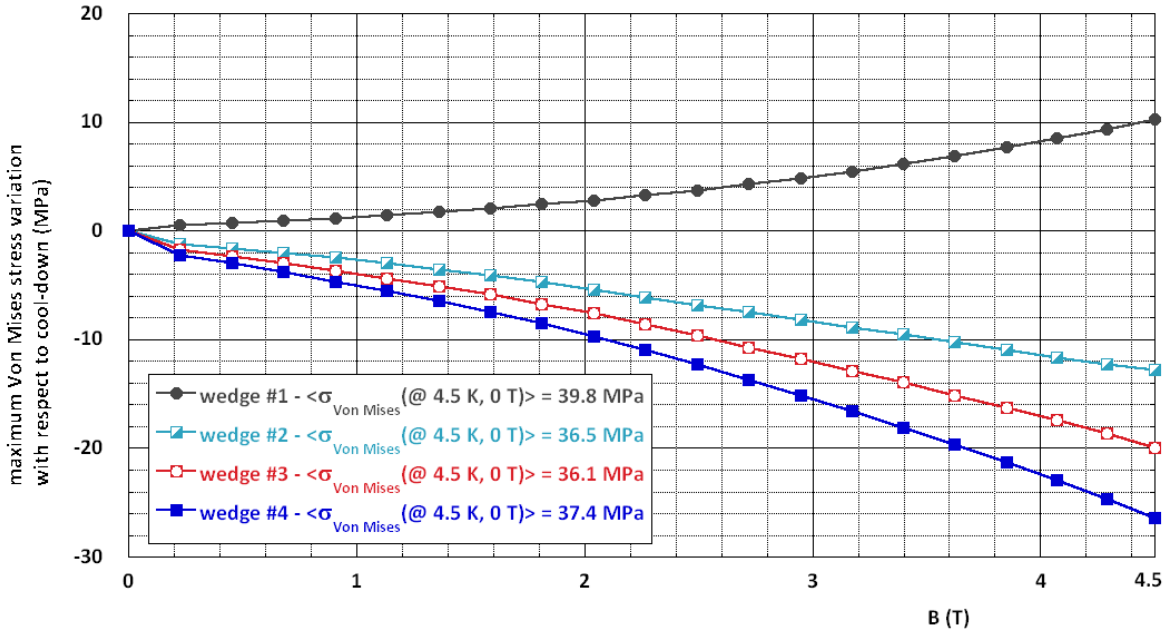

FIG.55: Maximum Von Mises stress variation with respect to cool-down in the 4 wedges. In the legend the average Von Mises stress after cool-down is also given.

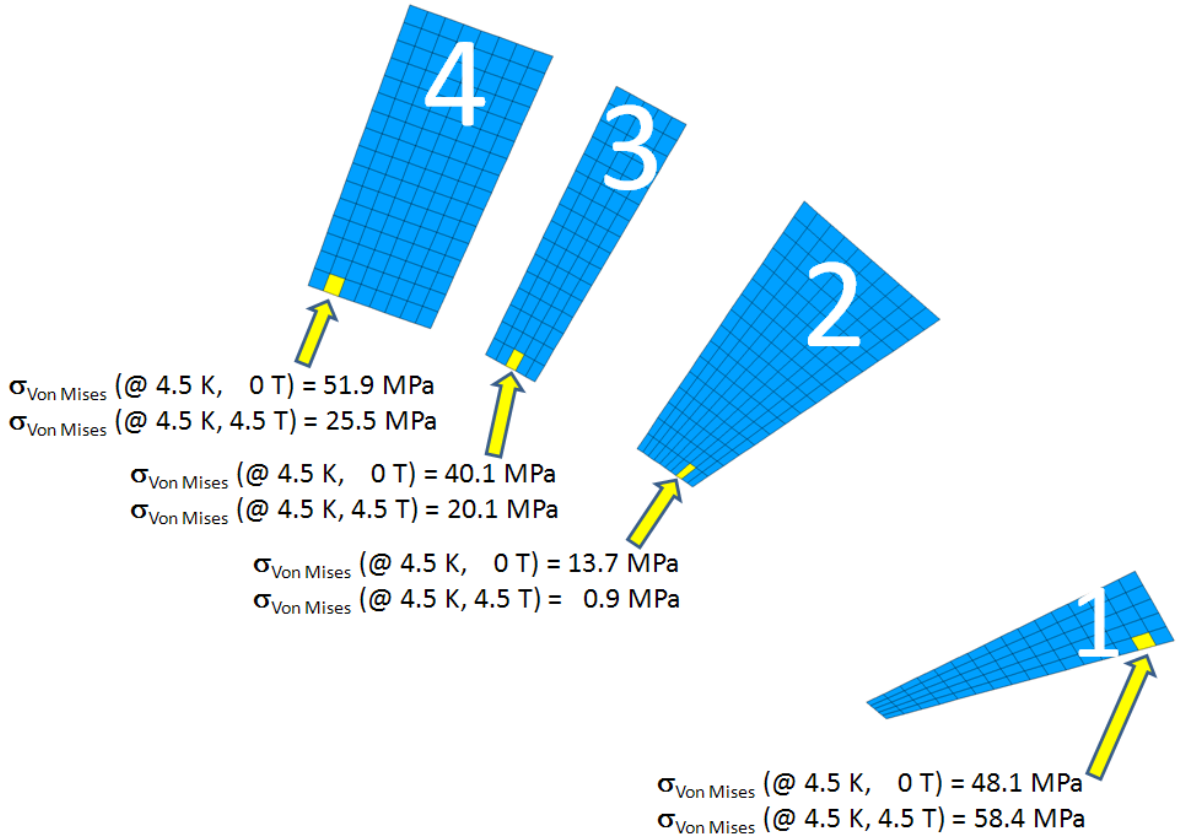

FIG.56: Locations of the maximum Von Mises stress variation at full energization with respect to cool-down and their values in the wedges.

In Fig.55 the maximum Von Mises stress variations with respect to cool-down are shown in the four wedges. The average Von Mises stress after cool-down is also given. All those curves being monotonically increasing or decreasing, it is possible to assert that the worst case consists in full energization. Fig.56 shows the locations of the maximum Von Mises stress variation at full energization with respect to cool-down and their values in the wedges. The most critical wedge is the fourth, in which there is a -26 MPa variation with respect to a peak Von Mises stress of 52 MPa.

6.2 3D analysis

A complete 3D finite element analysis is needed to fully understand the mechanical behavior of such a complex structure. Our first approach consists in modeling a straight dipole: only once all the problems related to the straight model are clear, a curved model also will be analyzed. Preliminary to a 3D mechanical analysis, a 3D electromagnetic analysis has been carried out to calculate the Lorenz forces. Fig.57 shows the resulting magnetic field on conductors. Table 23 shows the good agreement between the Lorentz forces in the straight section calculated using the 2D and the 3D model. In Table 24 the Lorentz forces in the ends

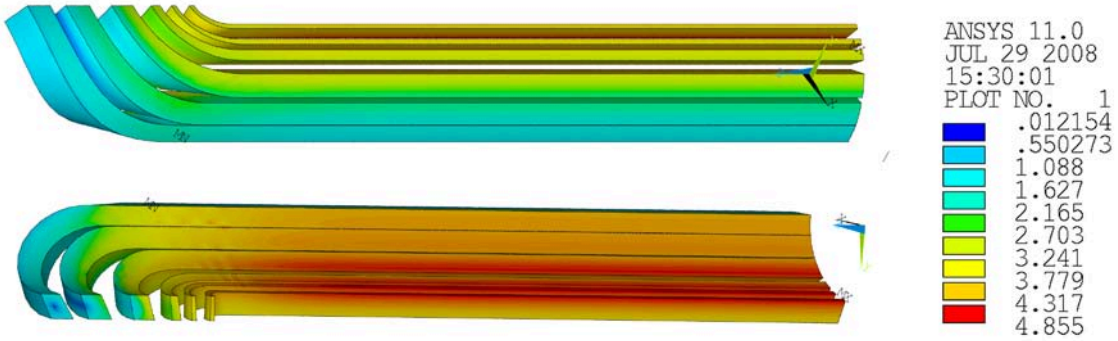

FIG.57: Magnetic field in conductors.

TAB.23: Lorentz forces in the straight section.

	Fx (MN/m)	Fy (MN/m)	Fz(MN/m)
2D model	+0.684	-0.301	0
3D model	+0.678	-0.300	0

TAB.24: Lorentz forces in the ends (1/8 symmetry); blocks are numbered from the midplane to the pole.

	Fx (kN)	Fy (kN)	Fz (kN)
Block #1a	+ 7.2	- 3.6	+ 1.2
Block #1b	+14.0	-11.3	+ 7.2
Block #2	+17.6	-10.1	+ 8.8
Block #3	+ 7.9	- 2.8	+ 3.5
Block #4	+ 3.9	- 1.0	+ 1.6
Block #5	+ 3.1	- 0.5	+ 1.0
Total	+53.7	-29.3	+23.3

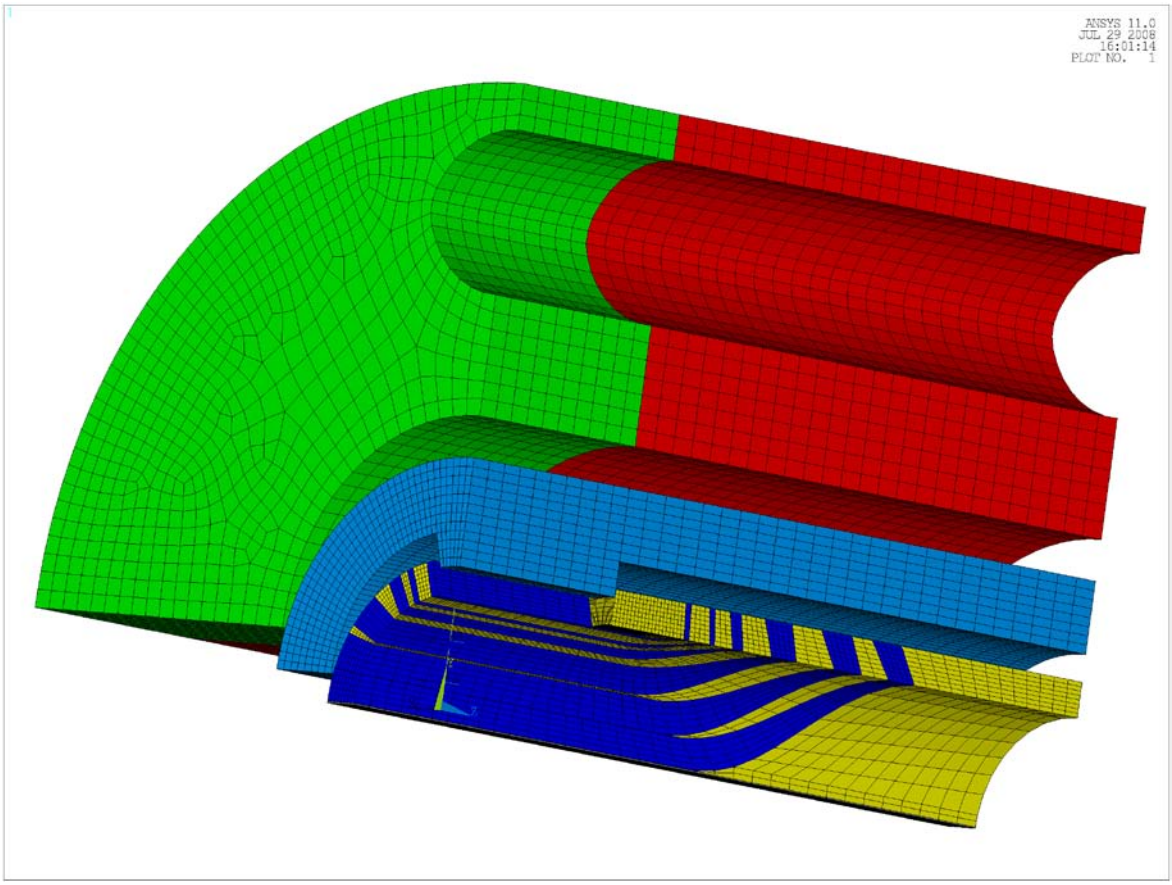

FIG.58: 3D finite element model for mechanical analysis.

on 1/8 model are listed. Note that the first block, the one nearest to the midplane, has been split into two sections. From a mechanical point of view, the most important component is the longitudinal one, as it tends to straighten the windings with nearly 100 kN per end. It will be crucial to evaluate this effect, and, possibly, find a way to strengthen the structure. Finally, Fig.58 shows the 3D finite element model which is ready for the mechanical analyses.

7. STABILITY AND HEAT TRANSFER

The superconducting cable is mainly cooled by the supercritical helium that flows in the room between the beam pipe and the conductors. The main purpose of the cooling is to remove the losses generated inside the conductor during the ramping (up, down) of the magnet.

In this section we will describe the method used and the obtained results to calculate the actual temperature on the conductor due to the heat transfer toward the coolant. This temperature distribution in the conductors allows calculating the temperature margin against the normal transition and to make some consideration on the stability.

At this stage of the thermal analysis, the following simplification and assumption have been adopted:

- The coolant temperature is constant in time and in the whole magnet. The temperature is set to 4.700 K, which corresponds to the warmest temperature of supercritical helium at the exit of the last magnet of a string.
- The thermal analysis has been carried out only in the 2D section of the magnet. In the coil-end region the operating conditions are less severe because both the losses and the magnetic field are lower.
- The cooling of the conductors occurs only through the supercritical helium that flows in room between the beam pipe and the conductors. That means that almost all the heat passes through the narrow side of the conductors, which are in contact with the supercritical helium.
- The losses generated in the collar, in the yoke and in the beam tube have been neglected. In fact, only the collar is in contact with the conductors, and it generates very low power (see Table 17). The other components which generate power (iron yoke, keys, pins and the beam tube) are not directly in contact with the conductors.

The thermal analysis has been performed first assuming a simpler (but excessively severe) static and stationary condition for the losses. Successively a more realistic transient analysis is presented.

7.1 Stationary analysis

Figs. 59 and 60 show the power generated in the conductor during the ramp-up at dB_0/dt=1 T/s, respectively at B_0=1.5 T and B_0=4.5 T. A detailed description of the calculation of these losses has been given in Section 5. The same pictures show the layout of the model for the thermal analysis: each conductor (represented as a single block) is separated from the others by its electrical insulation; the conductor blocks are separated by blocks of G11 (dark green in the picture); between the conductors and the collar, a layer 1.45 mm thick is inserted (light green in the picture). This layer summarizes the heaters, the ground insulation and the stainless steel protection shield of the coil (see Fig.99). This layer is considered like a homogeneous material with thermal properties averaged between its components. The inner

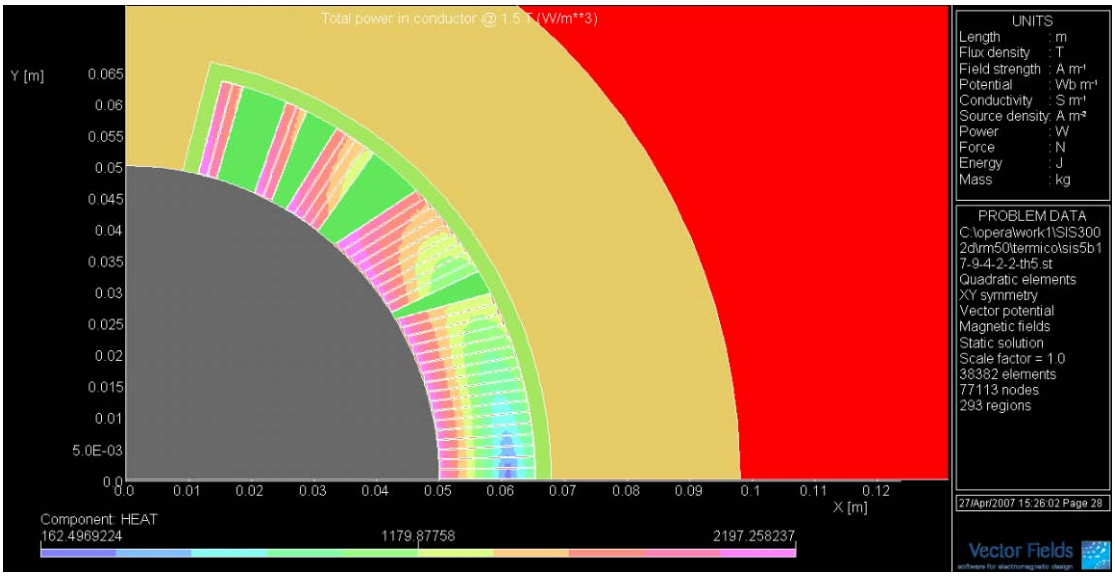

FIG.59: Power density [W/m^3] in the conductors during the ramp, at B_0=1.5 T.

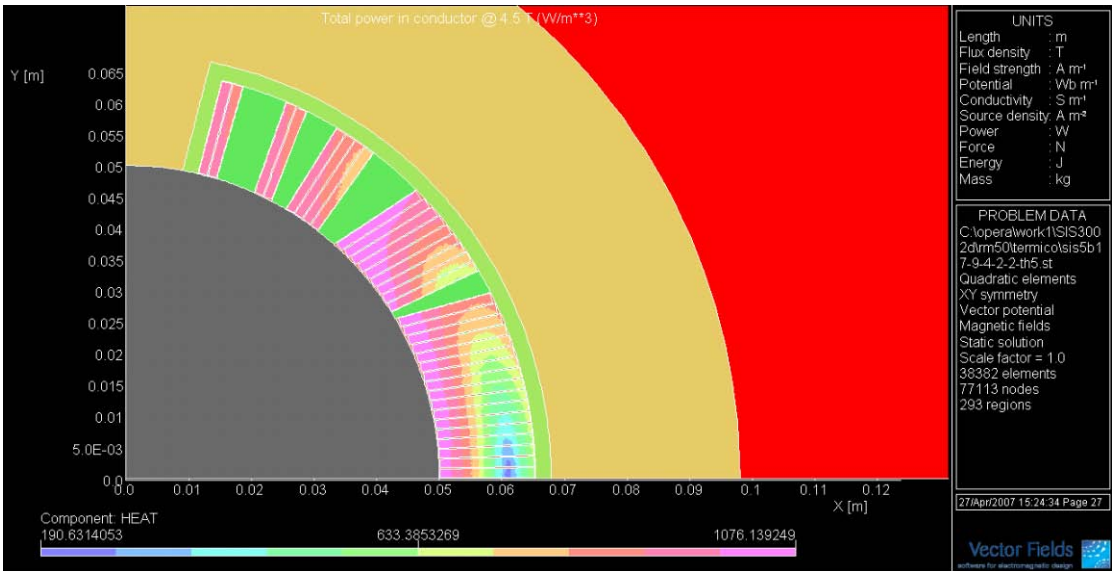

FIG.60: Power density [W/m^3] in the conductors during the ramp, at B_0=4.5 T.

surface of the collar in the pole and the internal narrow side of the conductors are directly cooled by the supercritical helium, consequently they have been set to 4.7 K. The outer surface of the collar is set with adiabatic conditions.

Table 25 reports the thermal properties of the materials, at 4.7 K. Obviously, for this static analysis only the thermal conductivity properties are used. The collar has the property of AISI316.[39)] The spacer has the property of G11[40)] for the thermal conductivity and of G10[39)] for the specific heat and density. The conductor insulation has the property of kapton[41)] for the thermal conductivity and the same property of the spacers for the specific heat and the density. The conductor has the thermal conductivity of copper at T=4.7 K and B=4.9 T,[40)] scaled with the actual copper contents in the strand (46%), the filling factor of conductor

(86%) and the ratio between the conductor width and the strand length in half transposition pitch (0.302); the specific heat and density are approximated to the properties of copper and are from reference 39). The layer between the coil and the collar has properties very similar to the conductor insulation, because the content of kapton prevails.

Figs. 61 and 62 show the temperature distribution in the coil and collar, in the stationary condition with the power generated by the conductors during the ramp-up respectively at

TAB.25: Thermal properties of the materials.

	Thermal conductivity [W/(m·K)]	Specific heat [J/(kg·K)]	Mass density [kg/m^3]
Collar	0.290	2.60	7800
Spacer (G11)	0.066	2.47	1900
Layer coil-collar	0.030	2.47	1900
Conductor	42.19	0.13	8512
Cond. insulation	0.010	2.47	1900

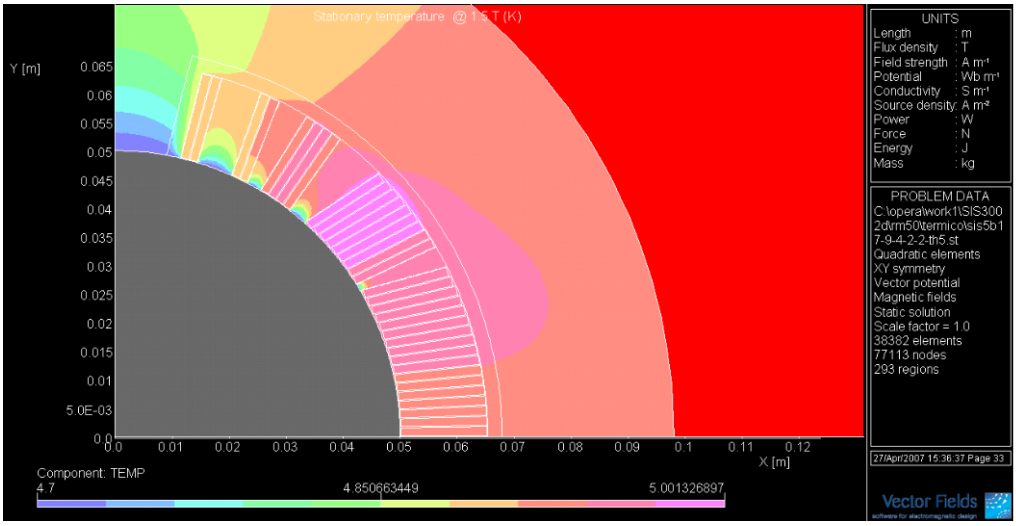

FIG.61: Temperature distribution [K] in the conductors and collar during the ramp, at B_0=1.5 T.

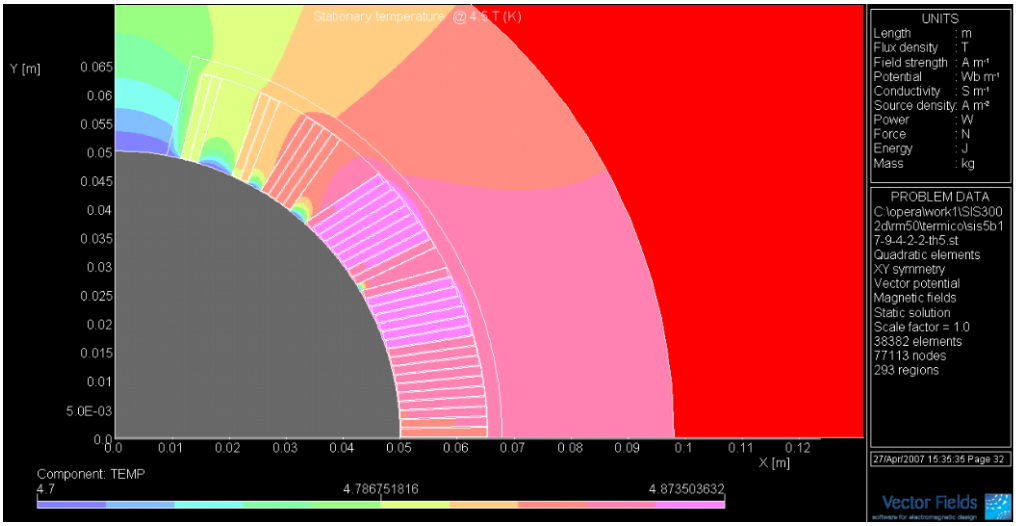

FIG.62: Temperature distribution [K] in the conductors and collar during the ramp, at B_0=4.5 T.

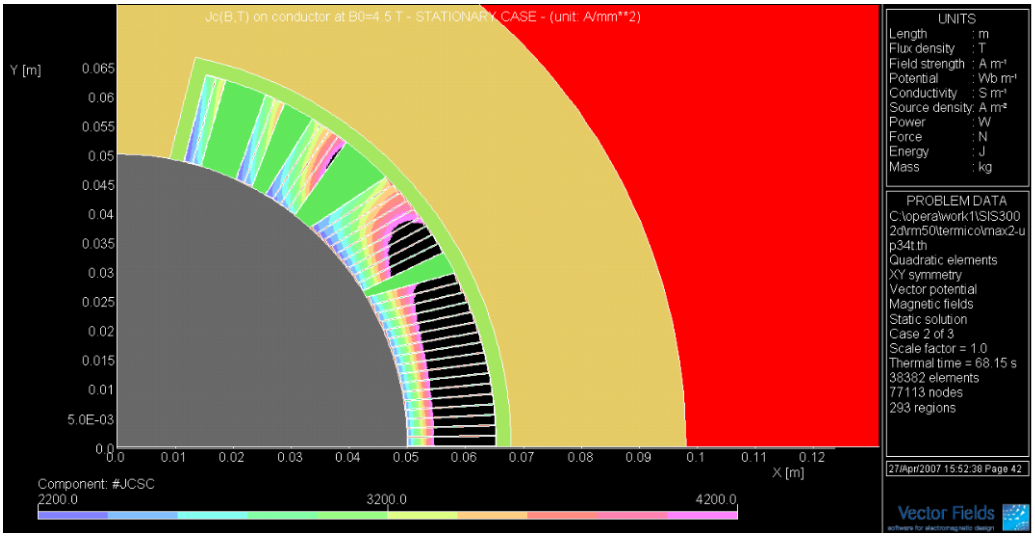

FIG.63: Critical current density in the superconductor [A/mm^2], at B_0=4.5 T.

B_0=1.5 T and B_0=4.5 T. It is possible to observe that inside each conductor the temperature is quite uniform, because the thermal conductivity is relatively large. The maximum temperature is reached in the center of the second block (5.00 K at B_0=1.5 T, and 4.87 K at B_0=4.5 T). The conductors of the last block (the high field conductors) present a relatively lower temperature (4.79 K at B_0=4.5 T) because they benefit of the cooling through the collar.

Despite this lower temperature, the lowest margin in temperature is reached in conductor with high field. Fig.63 shows the critical current density (function of the temperature and magnetic field distribution) in the superconductor at B_0=4.5 T. The lowest value is reached in the peak field zone of the last conductor.

As a consequence, the temperature of the last conductor in Fig.62 allows directly calculating the minimum temperature margin: in that conductor the current sharing temperature is 5.69 K (see Table 12 in Paragraph 2D design with finite permeability for the iron), the actual temperature from the stationary analysis is 4.79 K and consequently the temperature margin is 0.90 K.

This stationary analysis gives some important indication of the conductor temperatures and the conclusion is that the minimum temperature margin occurs at the end of the ramp, when the current and field are at maximum and the losses in the conductor are at the minimum. However a transient analysis is necessary in order to evaluate whether the larger power dissipated at lower field could increase significantly the temperature in the conductors at the end of the ramp respect to this stationary analysis.

7.2 Transient analysis

The transient analysis has been performed with Elektra. The model has already been described in section Stationary analysis, with the thermal property reported in Table 25. Because the stationary analysis has allowed finding that the most critical conductor is the one with highest field (the 34th conductor), in the transient analysis the temperature evolution of that conductor has been monitored. Fig.64 reports the temperature evolution of the 34th conductor during some cycles of the magnet. The initial temperature of the conductors (at

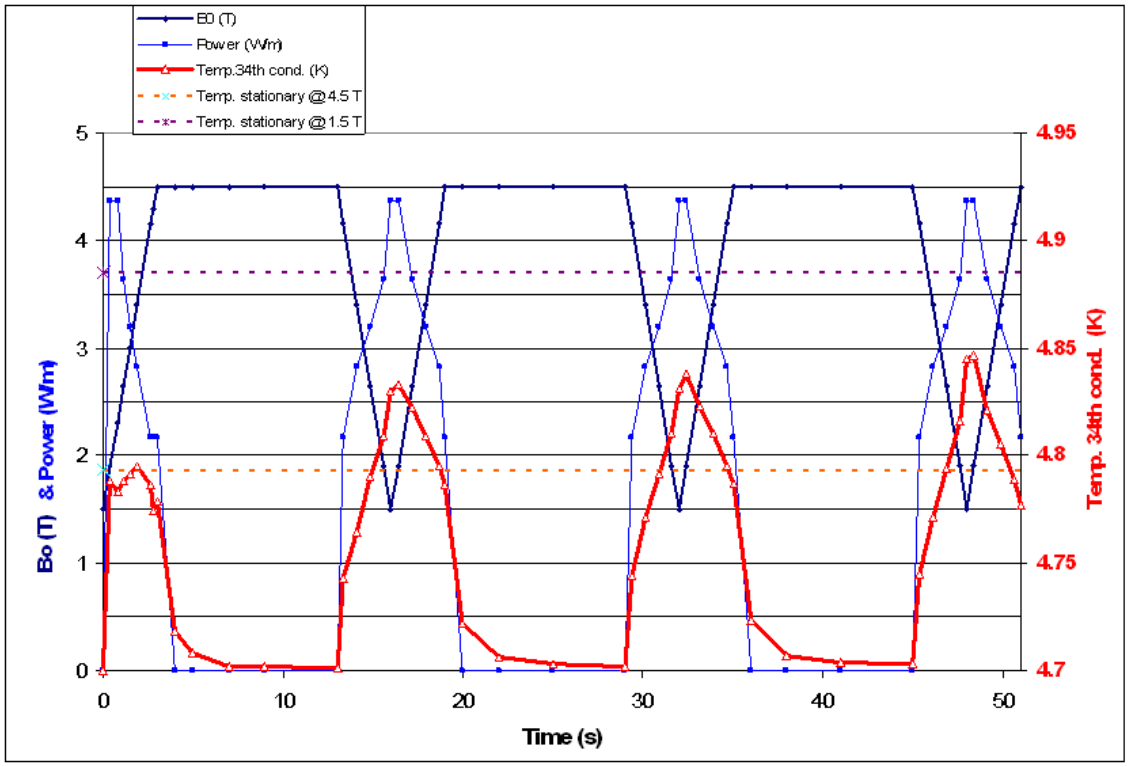

FIG.64: Temperature evolution of the 34th conductor (red line, right scale) during some cycles. In the same graph (left scale): field in the magnet bore (B_0) and power generated by the conductors. The dashed lines represent the temperature reached by the 34th conductor in the stationary analysis with the power at B_0=1.5 T (upper dashed line) and B_0=4.5 T (lower dashed line).

t=0) has been set to 4.700 K. The cycles are constituted by a ramp-up from 1.5 T to 4.5 T at 1 T/s, followed by a plateau at 4.5 T for 10 s and a ramp-down from 4.5 T to 1.5 T at -1 T/s. As shown in Fig.64, in the plateau the temperature returns close to 4.7 K in few seconds, then increases up to 4.85 K during the ramp-down from 4.5 T to 1.5 T, and after that it decreases to about 4.78 K during the ramp-up. The lowest temperature margin occurs at the end of each ramp-up. Even if more than 3 cycles have been executed, the temperature in the 34th conductor has not been still well stabilized to the same values, but the temperature at the ends of the ramp-up is very close 4.78 K.

In order to obtain a more stable evolution of temperature, a larger number of cycles would have to be performed, with a large cpu time consumption. As consequence, for setting an upper limit of the temperature of the 34th conductor at end of the ramp-up, another run has been executed: in this case the initial temperature of conductor has not been set to 4.7 K, but to the upper limit, which corresponds to the temperature in the stationary analysis at the maximum power at B_0=1.5 T. Fig.65 shows the temperature evolution, and it can be seen that at the end of the second ramp-up, the temperature is 4.815 K.

From this transient analysis we can deduce that the temperature on the 34th conductor, at the end of the ramp-up, is 4.80 K with an error of +/- 0.02 K. This error takes into account the

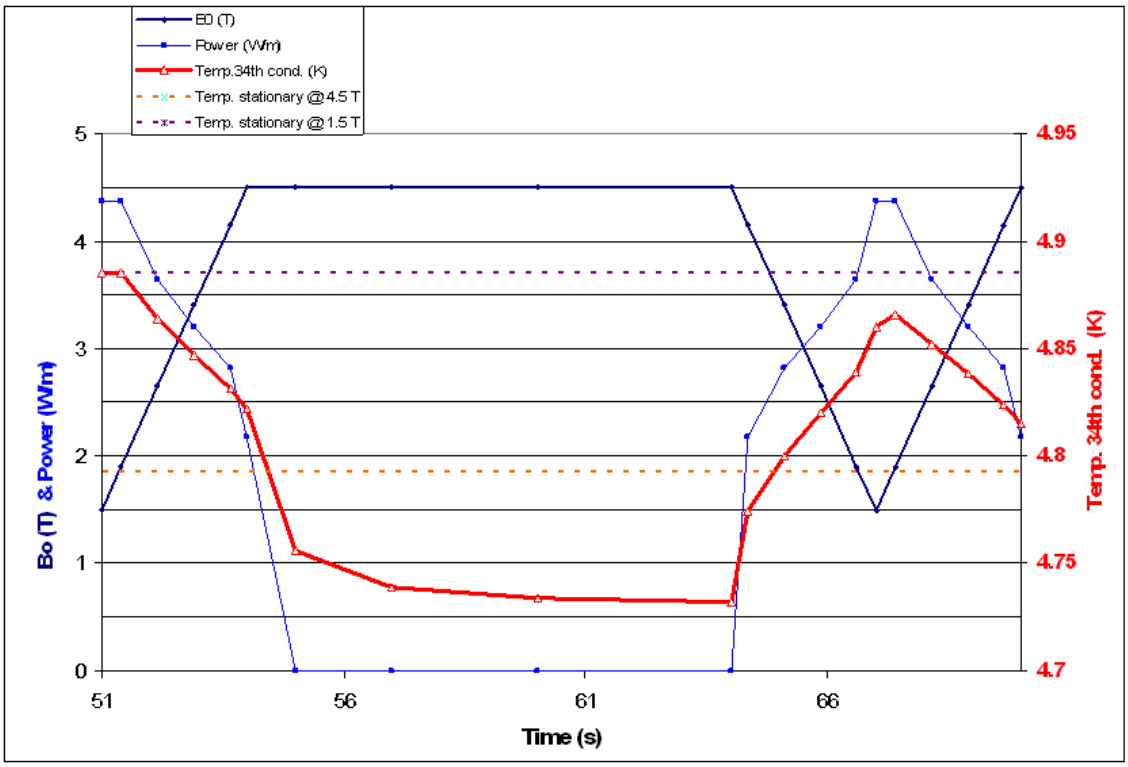

FIG.65: Temperature evolution of the 34th conductor (red line, right scale) during a cycles, with the initial conductor temperatures set to the upper limit (stationary analysis with the power corresponding to B_0=1.5 T). In the same graph (left scale): field in the magnet bore (B_0) and power generated by the conductors. The dashed lines represent the temperature reached by the 34th conductor in the stationary analysis with the power at B_0=1.5 T (upper dashed line) and B_0=4.5 T (lower dashed line).

differences obtained in the different analysis.

7.3 Measurement of thermal conductivity

Additional sources of error could come from:

1. The very large thermal capacity of supercritical helium inside the conductor, which could modify the temperature evolution in the transient analysis.
2. The surface thermal resistance between supercritical helium and kapton insulation. If this resistance is estimated in 600 W/(m^2·K), the additional increase in temperature of the 34th conductor is between 0.03 K and 0.05 K.
3. The surface thermal resistance between the kapton insulation and the conductor.
4. The heat flowing from the collar and yoke and vice versa.

Among these effects, the largest uncertainties come from the first three points. As consequence, in collaboration with CERN, an experiment has been settled, in order to measure the actual thermal exchange between the conductors, insulated with kapton, and the supercritical helium.

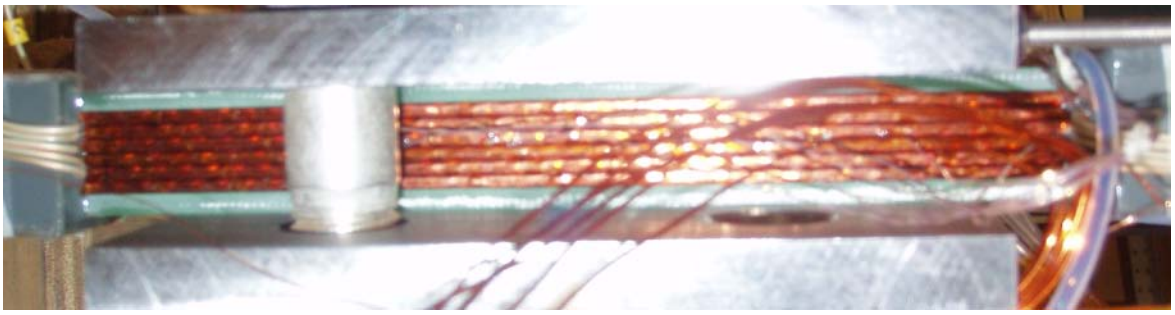

FIG.66: The sample used for thermal heat measurements through the kapton insulation.

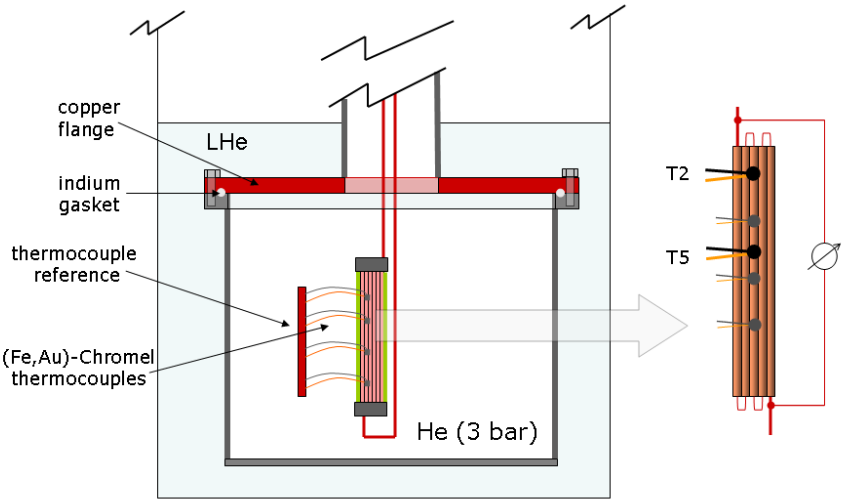

FIG.67: Schematic view of the experimental apparatus.

The sample is a stack[1] of 6 Rutherford cables, insulated with kapton, and instrumented with (Fe,Au)-Chromel thermo-couples in order to measure the temperature of the strands (see Fig.66). The conductor has the same dimensions of the SIS300 conductor, with a LHC-type insulation, which is about 0.04 mm thicker than the SIS300 insulation thickness. The strands are made by a copper-nickel alloy, in order to increase the resistance of the conductors. Heat can be generated inside the conductors with the Joule effect, and the effective generated power is monitored by measuring both the current and the voltage drop in the cables. The conductors are piled along their large sides and are all fired. Consequently it can be assumed that the inner conductor, the one instrumented, can be cooled only through the narrow side of the conductor, which represents the situation in the SIS300 magnet.

The sample is inserted in a chamber which can be pressurized with helium up to 0.3 MPa as shown in Fig.67. The external surfaces of this chamber are in thermal contact with boiling liquid helium at 4.2 K, in order to control and keep constant the temperature of the helium in the chamber in the supercritical phase. In this case the cooling of the sample occurs through a “static” bath of supercritical helium, whereas the magnet is supposed to be cooled by “flowing” supercritical helium. In any case the results from this experiment can give a conservative and safe value for the thermal conductance of the insulation.

[1] The sample was fully instrumented and kindly supplied by David Richter, CERN.

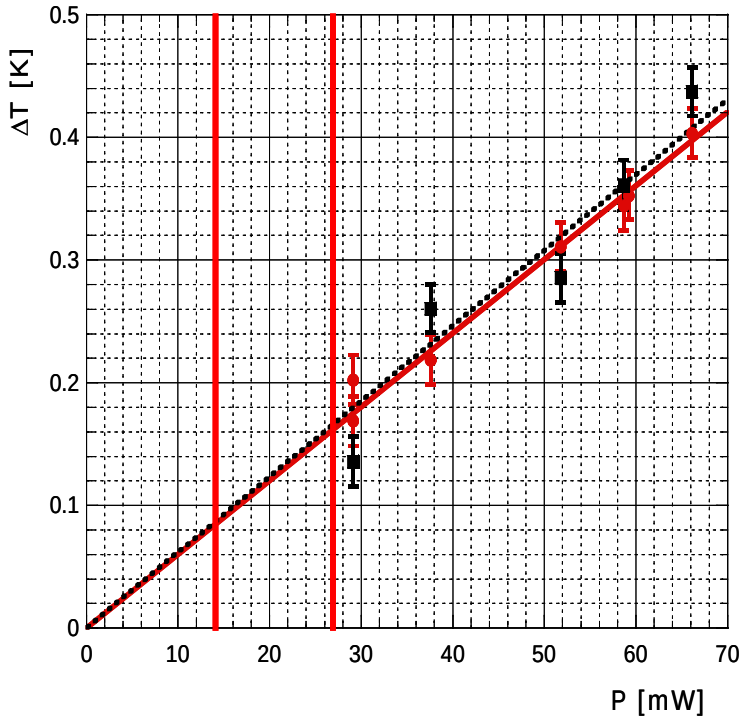

FIG.68: Temperature drop between conductor and supercritical helium @ 4.2 K and 0.3 MPa vs. the heat power generated in the conductor (no mechanical pressure on conductor stack). The two vertical red bold lines indicate the corresponding power range of the 34th conductor of the magnet during ramp-up.

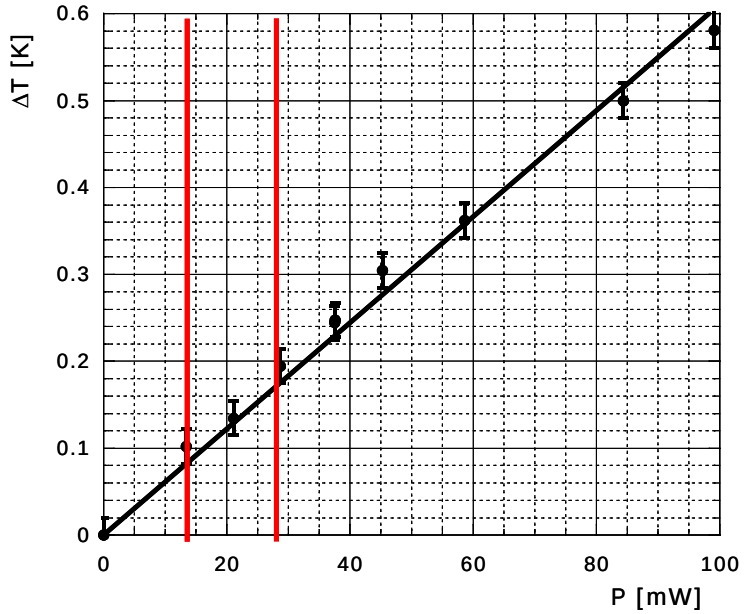

FIG.69: Temperature drop between conductor and supercritical helium @ 4.2 K and 0.3 MPa vs. the heat power generated in the conductor (mechanical pressure on conductors stack ≈50 MPa). The two vertical red bold lines indicate the corresponding power range of the 34th conductor of the magnet during ramp-up.

Two campaigns of measurements have been performed: the first without compression of the sample and the second applying a mechanical pressure of about 50 MPa at the large side of the conductor (beryllium copper washers were used to compensate the thermal contraction). In this way the conductors and the insulation are compacted in the same situation of the real magnet.

The temperature difference between the conductor and the supercritical helium vs. the heating power is reported in Fig.68 (non-pressed stack) and Fig.69 (stack pressed at 50 MPa). The vertical bold red lines in the graphs indicate the corresponding power range of the 34th conductor of the magnet during ramp-up. Comparing the two graphics, it appears as the thermal exchange is not affected by the mechanical pressure.

The drop temperature of the sample is quite linear respect to the power, giving a thermal conductivity for the kapton of about 0.019 W/(m·K). This value is quite larger respect to the one used in the thermal analysis (see Table 25), and for this reason the analysis can be considered safe.

7.4 Conclusions

The thermal analysis has shown that the minimum temperature margin occurs on the 34th conductor of the magnet, at the end of the ramp-up. The calculated margin is 0.90 K, with an error of +/- 0.02 K.

Measurements of the actual thermal conductivity of the insulation confirm that the assumptions in the study are correct.

8. QUENCH AND PROTECTION

The study of quench propagation and the system evolution after the activation of the protection has been carried out with the QLASA code.[42] This code was originally developed at LASA Lab. (INFN Milan) for solenoids and it can be adapted to long straight coil configurations by means of a suitable geometric approximation, described in Section Description of the model for quench analysis. It is written in Fortran 77, with several subroutines that calculate the evolution of the main parameters of a superconducting magnet during a transition (quench velocity, resistance, hot spot temperature, voltages, current, magnetic field in the coils, etc.). The longitudinal and transverse quench velocities are analytically calculated according to standard models.[30] The program is linked to the code MATPRO[39] that provides the electrical and thermal properties of the materials of the magnet.

8.1 Description of the model for quench analysis

The electrical scheme of the magnet circuit is presented in Fig.70. It includes the two windings that form the dipole connected in series, the dump resistor (R_d), the power supply and the main switch. The diode in the branch of the dumping resistor avoids the current to circulate in the dumping resistor during the ramp-up of the magnet. The circuit is grounded at one terminal of the power supply. In the present scenario for the test program, the grounding cannot be set at "half" R_d, because one terminal of the power supply could be already grounded. Table 26 reports some of the main parameters for the protection study.

The opening of the main switch is driven by the Quench Detection System (QDS). In this study, the resistive voltage threshold that triggers the QDS has varied between 0.2 V to 1.0 V. This last relatively high value is due to the consideration that the total inductive voltage of the magnet during ramp-up is about 22 V (44 V for the 7.8 m long dipole). After the threshold voltage has been reached, it is assumed that a time delay occurs before the main

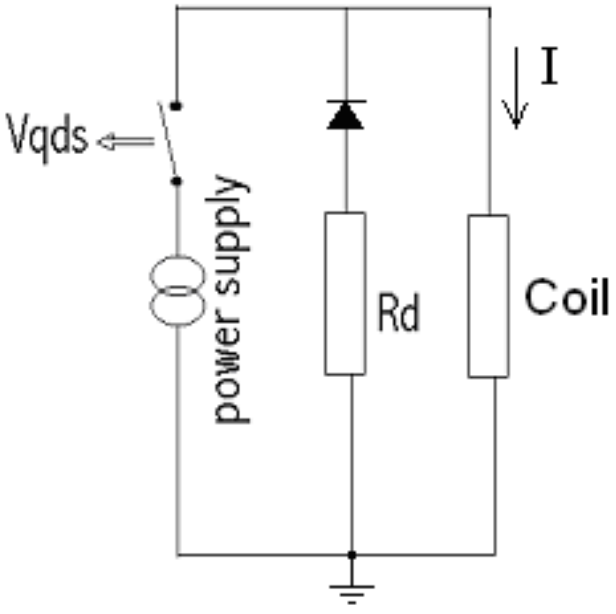

FIG.70: Electrical scheme for magnet protection.

TAB.26: Main parameters for the protection study.

Nominal current	8926 A
Inductance	11.4 mH
Magnetic storage energy	459 kJ
Dumping resistance	44 mΩ
Time constant (L/R_d)	0.26 s
Maximum voltage	400 V

TAB.27: Material volumetric percentage composition of windings.

Copper (RRR=100)	35.8 %
NbTi	28.0 %
Copper-Manganese	14.0 %
Cable insulation (kapton)	13.3 %
Empty	8.9 %

switch is completely opened. This delay time include the “validation time” (the time necessary for the resistive voltage to exceed the threshold voltage in order to trigger the protection from quench, usually 10 ms) and the time necessary for the main switch to completely open (about 20 ms for a mechanical switch). The impact of this delay time on the quench development has been investigated.

In the simulations, each one of the 10 blocks which makes up the dipole (5 blocks per winding), has been schematized to a single solenoid. The average circumferences of the solenoids were chosen to be equal to the average length of the windings, whereas the thickness and the height of the solenoids are equal to the width of the conductor and to the azimuthal length of the blocks. The thermal contacts between two different blocks and between the coils and the mechanical structure have been neglected (except for the first large block of one winding, which is in contact in the mid plane with the same block of the other winding). This hypothesis appears to be conservative, but only moderately so, because the discharge process is quite fast (~1.5 s) and the spacer are made in G11 which is a bad thermal conductor. Table 27 reports the material volumetric percentage composition of windings (unit cell). The presence of the cable insulation (kapton) has been considered in the unit cell area, because the thermal diffusion time in the insulation thickness is few milliseconds, which is a very small time in comparison to the discharge time. The percentage contents of copper, copper-manganese and NbTi in the unit cell has been increased in order to take into account the inclination of the strands in the Rutherford cable for the cable twist-pitch. Because of the cable packing factor, about 9% of the unit cell is empty. The presence of helium which fills this zone has been neglected.

In the simulations, both the presence and the not-presence of the heaters have been considered. The heaters are supposed in contact with the narrow edge of the conductors of the first 2 large blocks of each winding, in order to induce the transition in a large number of conductors (26 conductors per winding).

8.2 Simulation results

The physical quantities investigated in this analysis are the hot spot temperature and the maximum voltage to ground reached in the magnet.

The quench is assumed to originate in the zone with the highest magnetic field, i.e. the 34th conductor. For the point of view of the quench study, this situation represents the worst scenario, because the transition cannot propagate fast to the other conductors because of the spacer barrier. Fig.71 reports the resistive voltage vs. time when a punctual quench is originated in the 34th conductor and it propagates only in the neighbor conductor (the 33th conductor); the other blocks are supposed to stay in the superconducting state. The initial longitudinal propagation velocity of the quench (in the direction of the cable), calculated with QLASA with a correction factor of 0.5, is 13.2 m/s, whereas the radial and axial velocity are respectively 1.2 m/s and 0.70 m/s (with correction factor 1). This means that the turn to turn propagation time of the quench in the axial direction is about 2.1 ms.

Fig.72 reports the MIIT curve, as calculated by QLASA. It is possible to observe that 300 K corresponds to 24.7 MIIT (for the LHC dipole outer layer, 300 K corresponds to 30 MIIT).

The dumping resistance has been set to 44 mΩ, in order to limit the maximum voltage to 400 V during the discharge; the constant time $\tau = L/R_d$ is then 0.26 s. About 85% of the total magnetic storage energy (0.46 MJ) is dissipated in the dumping resistor.

With such an efficient extraction of the magnetic energy, the hot spot temperature can be kept below 300 K even without quench heaters. Fig.73 reports the hot spot temperatures vs. the delay time, considering different threshold voltages for the activation of the QDS; the

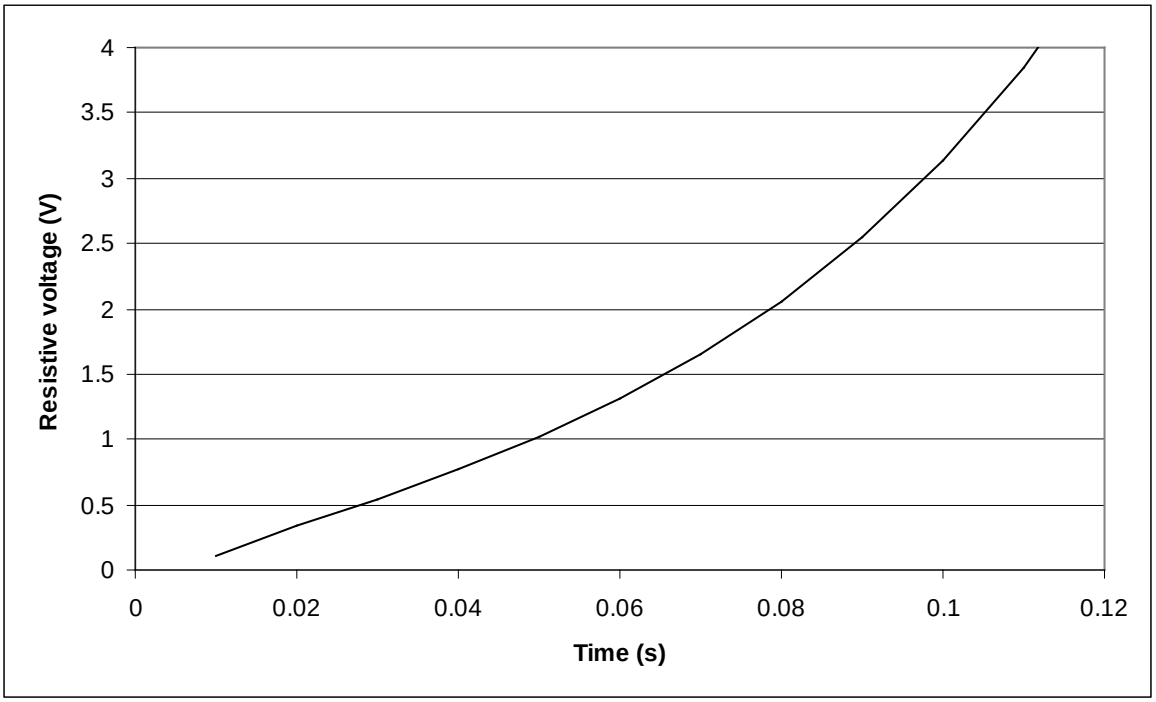

FIG.71: Resistive voltage vs. time in the magnet when a spontaneous quench originates in the 34th conductor.

solid line represents a simulation with the intervention of quench heaters, whereas the dashed line represents simulations without the quench heater interventions. In the simulation, the delay time is the time between the resistive threshold voltage, and the opening of the main switch (the validation time has to be included in this delay time). The active initiation of the quench triggered by the quench heaters occurs at the same delay time of the opening of the main switch of the power supply.

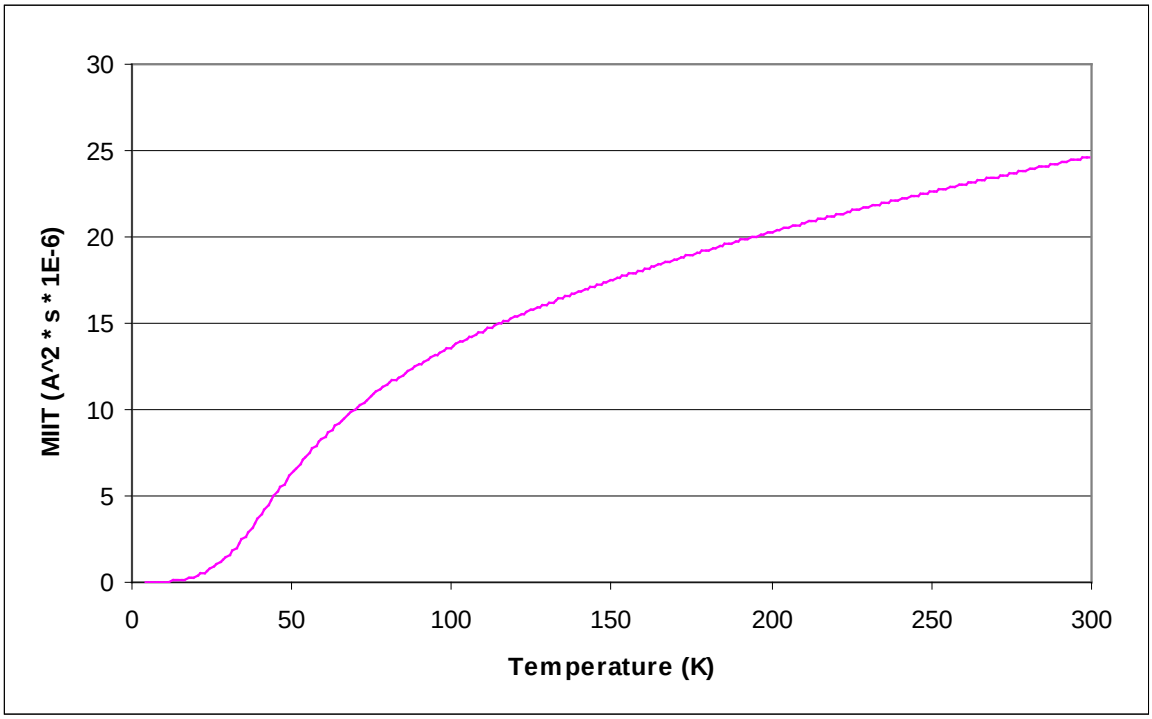

FIG.72: MIIT curve calculated by QLASA. T_0=4.5 K.

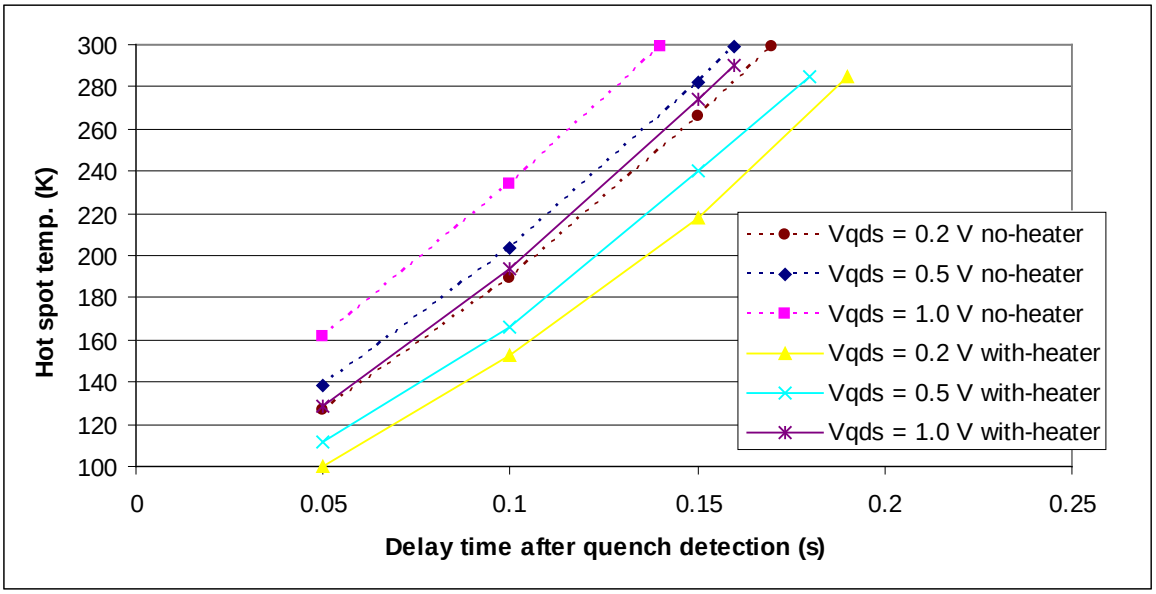

FIG.73: Hot spot temperature vs. the delay time (after the threshold-resistive voltage V_{qds} is reached). Solid lines are with the activation of quench heaters. Dashed lines are without activation of quench heaters.

8.3 Conclusions

The magnet is protected in case of quench also without using quench heaters. The hot spot temperature can be kept well below 300 K with intervention delay time of 50 – 100 ms, which are standard conditions achievable for the electronic and the power supply switch.

A threshold voltage for the QDS of 0.5 V, with a validation time of 20 ms and 30 ms of delay for the opening of the main switch (total delay after the threshold voltage 50 ms), would lead to a hot spot temperature of 140 K. Increasing the threshold voltage for the QDS up to 1 V and the total delay time to 100 ms, the hot spot temperature would be about 235 K.

The propagation of the quench between one block and the others is drastically reduced by the spacers in G11, however the fast discharge of the magnet should induce quench backs in other zones of the winding, contributing to a better uniform distribution of the temperature in the magnet.

The use of quench heater is any case recommended as additional protection and in order to study the protection for the longer magnet (7.8 m long) when installed in the string, where the extraction of the magnetic energy by the dumping resistor is much less efficient.

Quench heater similar to LHC dipole are envisaged. A quench heater (each one with two strips) is mounted on every coil quadrant outer surface (8 strips in total). The quench heaters are positioned in such a way that one strip covers 9 conductors of the first large block (“lower field strip”) and the other strip covers the nine conductors of the second block (“higher field strip”), as shown in Fig.109. The strips are connected in series in pairs in order to obtain 4 independent protection circuits. The most convenient connection between strips in order to assure a faster propagation of the quench is crossing the connection, i.e. the “higher field strip” of 1st quadrant connected with the “lower field strip” of 3rd quadrant, the “lower field strip” of the 1st quadrant connected with the “higher field strip” of the 3rd quadrant, etc. Among these 4 circuits, only 2 are connected to 2 power supplies which are used during the normal operation. In this way the magnet is protected by means of two independent circuits able to fire the quench heaters and to initiate a quench in every quadrant of the magnet. Fig.74 represents the schematic of each electrical circuit of the quench heaters. The resistance of the quench strips has been scaled from the LHC value considering the actual length of the magnet. Table 28 reports the main electrical characteristics of the circuit, with a comparison of the main LHC dipole heater circuit.

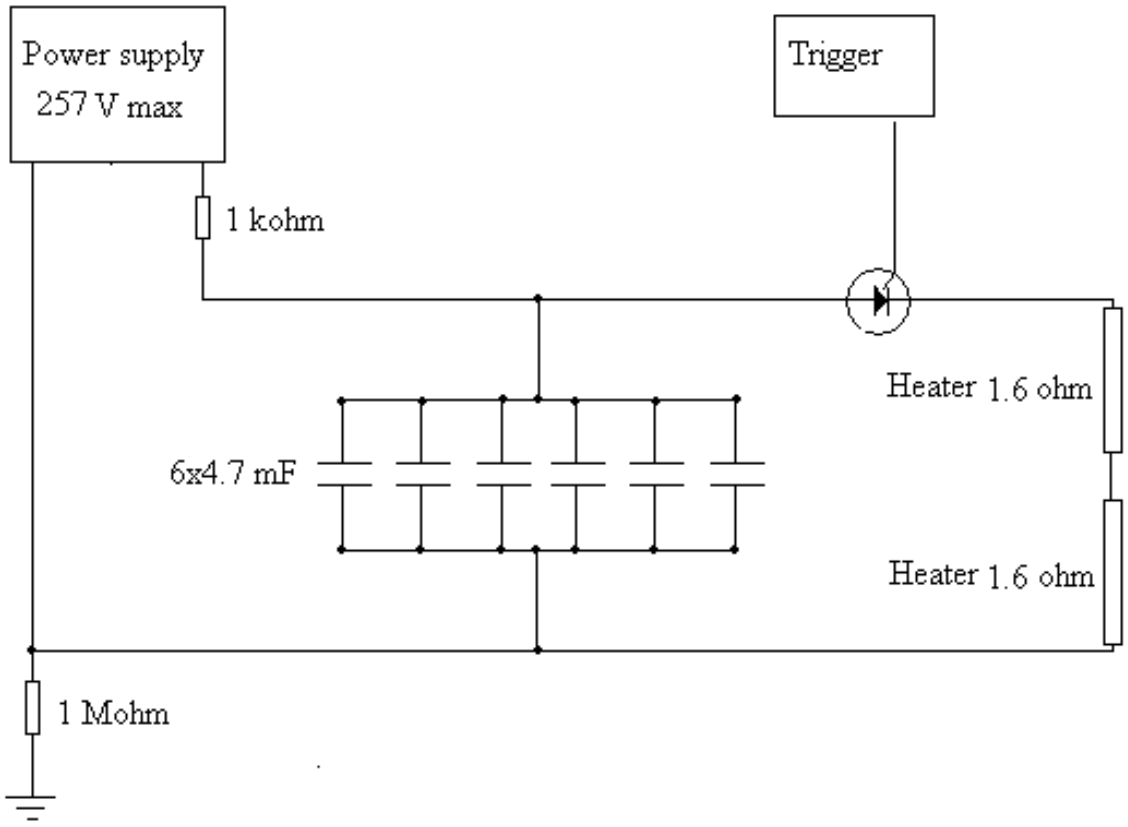

FIG.74: Schematic of the electrical circuit for the quench heater firing.

TAB.28: Main electrical characteristics of the heater circuit and comparison with the LHC dipole.

	DISCORAP	LHC dipole
Heater length	~15 m	~4 m
Resistance/strip	1.6 Ω	6 Ω
Capacitors	6×4.7 mF	6×4.7 mF
Equivalent capacitance	28.2 mF	7.05 mF
Maximum voltage (respect to ground)	+ 257 V	+/- 500 V
Stored energy by capacitor	0.93 kJ	3.5 kJ
Discharge constant τ	90 ms	85 ms
Maximum current I_0	80 A	83 A

9. CRYOSTAT

The cryostat for a superconducting magnet must be designed to perform different roles. First of all, it has to provide good thermal insulation for the low-temperature operation of the magnet, eventually with its associated cryogenic piping and beam vacuum system. Because the cryostat is also the mechanical interface between the superconducting magnet and the environment, it must also rigidly support and precisely position the magnet with respect to the external alignment fiducials.

9.1 General considerations

The design of our cryostat is aimed first at allowing the cold mass test first and eventually investigating specific design solutions useful for the final cryostat to be developed for the series production of magnets. In this framework we first selected the requirements to be fulfilled for our main purpose, which consists in:

a. easy integration procedure of the cold mass, as it is foreseen to perform this action in our laboratory, thus involving limited amount of manpower and tools;

b. possibility to transport the whole assembly to GSI and possibly to another laboratory for testing purposes, thus fixing tools should be foreseen to ensure a stable and stiff environment for the cold mass;

c. the thermal budget for the cryostat is not critical, as the magnet is a highly dissipative one. We set this budget to 2 W maximum at 4.5 K, that is 5% of the magnet expected dissipation. However, within the mechanical considerations coming from the point b), the cryostat design also represents an opportunity of development towards the final cryostat, thus technical solutions according the final cryostat specifications will be considered where possible.

9.2 Geometry and design approach

The sagitta of the cold mass, about 35 mm, allows to consider a simple geometry of the outer cylinder: straight with the ending flanges tilted to accommodate the curved magnet. The same straight approach can be used for the thermal shield. The cryostat outer diameter is chosen within the maximum one set by GSI for the final cryostat, i.e. ϕ_{ext}=910 mm, while the outer diameter of the cold mass to be inserted is 490 mm. The approximate weight of the cold mass is 6000 kg and its length is 3.9 m.

Material for the outer shell and thermal shields are not critical for either structural or electromagnetic point of view, thus we simply followed the choices made in previously dipole projects (LHC, RHIC, SSC): low carbon steel for outer vessel, and high conductivity Al sheet for the thermal shield. The material for the POST is assumed as fiber-glass epoxy (G10) in thermal and structural considerations.

In order to ensure the stable and rigid positioning of the cold mass we choose a solution with three POSTs, one central POST fixed and two side POSTs, sliding to accommodate thermal contractions of the cold mass.

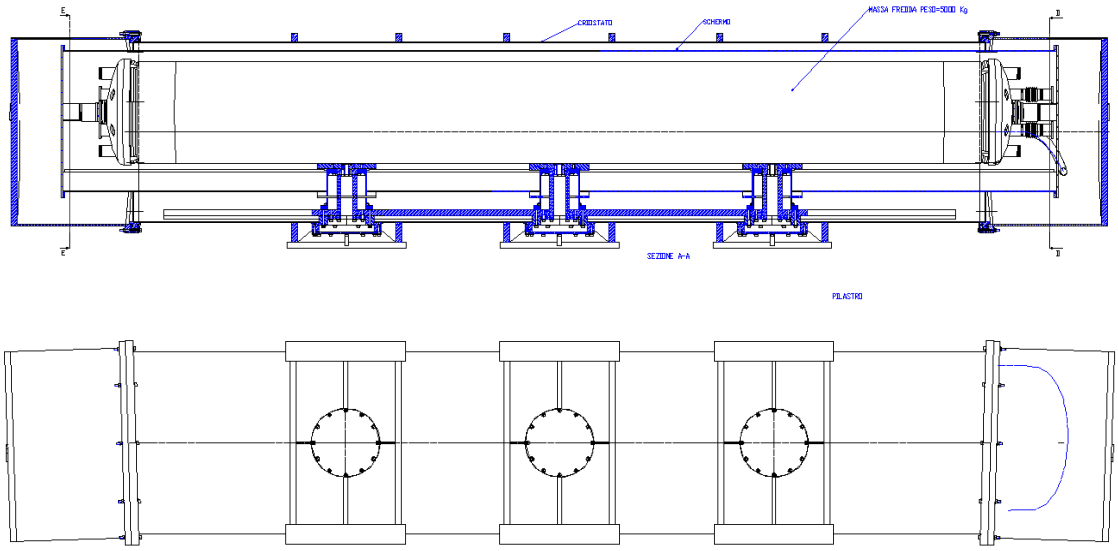

FIG.75: Conceptual view of the cryostat assembly from the side and bottom.

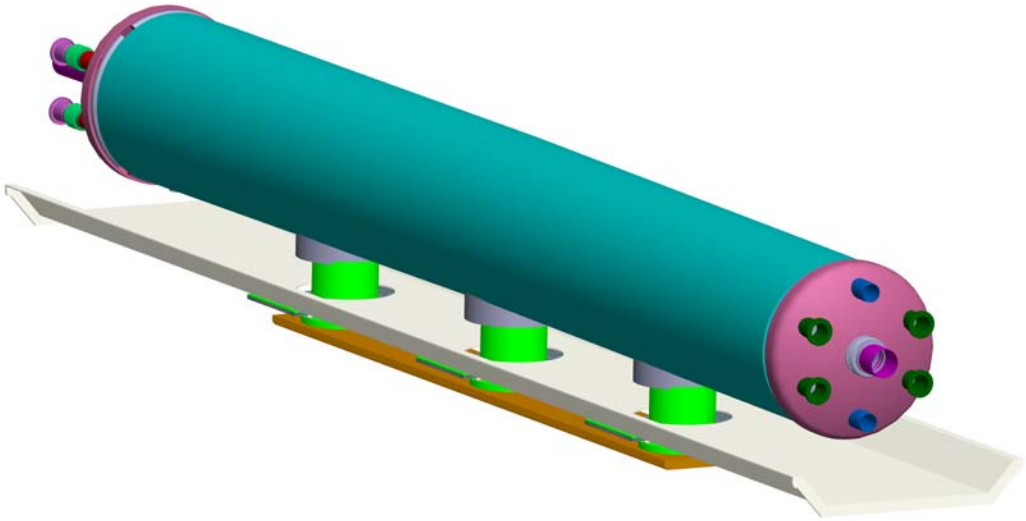

FIG.76: Conceptual view for the partially assembled cold mass over the sliding sheet.

We considered putting the three POSTs either aligned below the bended cold mass, that is not considering the magnet bending, or on the same curvature radius as the magnet. In both cases we assume that the off axis in plane thermal contraction is negligible (less than 0.1 mm).

We also analyzed the position of the three POSTs under the cold mass: either aligned below the bended cold mass, that is not considering the magnet bending, or on the same curvature radius as the magnet. In both cases we assume that the off axis in plane thermal contraction is negligible (less than 0.1 mm).

In Fig.75 it is shown the cryostat assembly (lateral and bottom planar view) at the conceptual stage (POSTs positioning is not the final one).

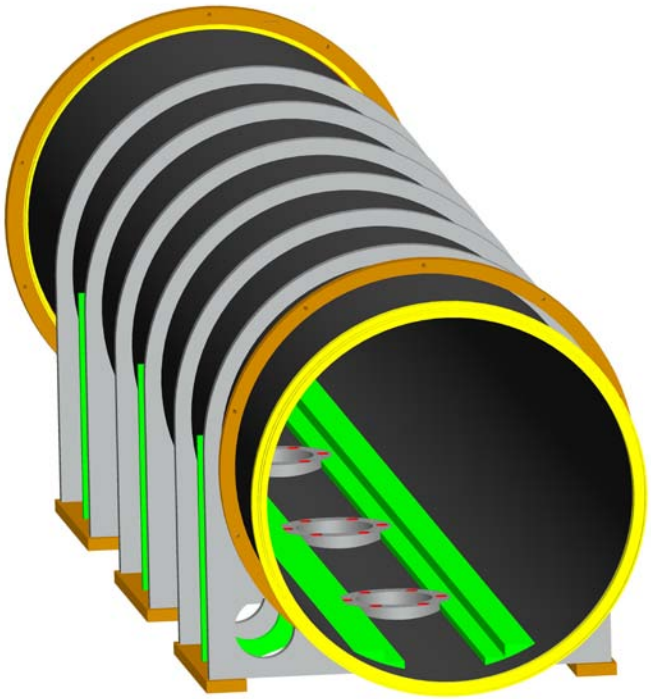

FIG.77: Conceptual design of the outer shell with the stiffening rings, leg supports, and POST fixing places.

One of the design goals is to set reasonable assembling procedure to be performed at INFN-LASA laboratory. We decided to assemble the cold mass over the three POSTs first, then the Al shields around and finally to slide the whole assembly into the outer shell. This will require a 10 meter long workshop space, the availability of a crane and some special tool to slide the cold mass into the outer shell.

The integration process will be as following: we first fix the POSTs on a sliding sheet, then the bottom part of the shield is inserted, then the cold mass is fixed over the POSTs. At this stage we have items as shown in Fig.76. Then we can easily make all diagnostic wiring connections, wrap the Al foil over the cold mass, fix the upper part of temperature shield and wrap the multilayer insulation blanket over the thermal shield. The outer shell is designed to accommodate the sliding sheet in its bottom, as shown in Fig.77. The force to slide the previously assembled parts within the outer shell will be applied straight to the sliding sheet. Once inserted this assembly the central POST is fixed to the cryostat outer shell through the sliding sheet, while the two sliding POSTs will be released. A cross section of the one ending side is shown in Fig.78, where can be noted the asymmetric position of the cradle below the cold mass supported by the POST.

Once assembled, the whole magnet mounted within its cryostat has to be transported by truck, thus special fixing flanges and POSTs reinforcement have to be designed. We will use stainless steel POST fillers, connected to the cold mass and to the outer shell combined with two ending cups matched to the cold mass to withstand axial forces. In this way the

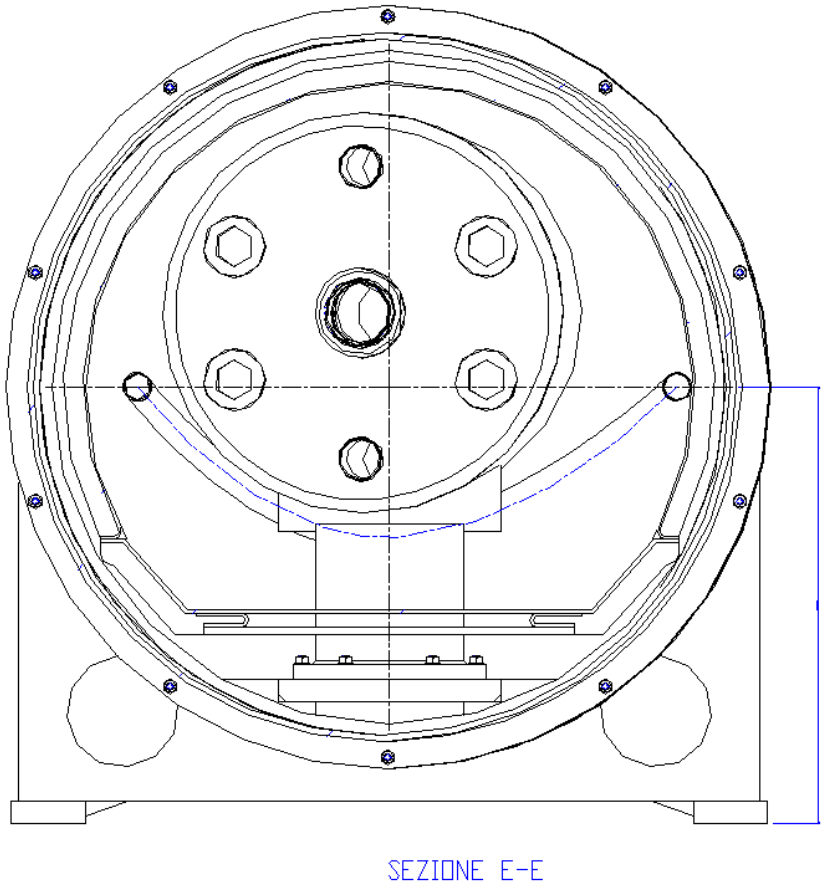

FIG.78: Ending cross section of the cryostat.

operations to be performed in the final test laboratory will be minimized. To preserve the magnet integrity we design the support for transport able to withstand 2g, 1g, 1g accelerations in the vertical, axial and lateral directions, respectively.

9.3 Outer shell first analysis (vacuum pressure)

First of all we analyzed the wall thickness of the outer shell. We shall assume at the beginning to not load this shell with the cold mass weight, that is supposing it will be supported by the cryostat feet through the POSTs. In this condition the outer shell has to be enough stiff to withstand the outer pressure only. The collapsing or critical pressure for cylinder exposed to external pressure is computed in different way. First we have to check whether we are in the long or short cylinder case:[43)]

$$L/D_0 > 1.537 \frac{\sqrt[4]{1-\nu^2})}{\sqrt{t/D_0}} \tag{29}$$

Where our cryostat length is L=3.90 m, with an outer diameter D_0=0.91 m. Being the material Poisson's ratio ν=0.27, we find that, for any reasonable wall thickness value, we always are in

the short cylinder case. In this case, using for the Young modulus E=200 GPa, for a thickness of 5 mm we can found the critical pressure p_c:

$$p_c = \frac{2.42 \cdot E \cdot (t/D_0)^{5/2}}{(1-\nu^2)^{3/4}\left[L/D_0 - 0.45\sqrt{(t/D_0)}\right]} \approx 0.2 \text{ MPa} \tag{30}$$

This value is well above the 0.1 MPa coming from the normal pressure outside the cryostat. We neglected the stiffness rings placed along the cylinder which will make the effective length L<2 m of the free cylinder, thus attaining p_c ≈0.52 MPa. As the safety rules suggest having a p_c 4 times the maximum operating pressure, we conclude that 5 mm wall thickness is sufficient keep the outer shell within the safety rules. Further analyses on the mechanical aspects will follow the complete cryostat design.

Further discussions on the accelerator cryostats led to a scenario where cryostats have to be aligned by means of special feet located just on three points below the cryostat outer shell. This accelerator scenario does not allow to neglect the effect of the cold mass weight on the cryostat structure. In fact the full weight will be supported by the cryostat structure, which of course needs to be stiffer than the previous case. Before setting the right thickness value, larger than 5 mm, we have to find the position where to place the plastic support below the cold mass which will load the outer shell structure.

9.4 Support POST mechanical analysis

Following previous experience in dipole for particle accelerators, we adopted the POST solutions to support the cold mass. This technique provides a stable and stiff positioning, useful for the precise alignment of the beam pipe, together with a low thermal conduction from the warm side to the cold mass. The fact that our magnet is bended led us to the conservative choice of having 3 POSTs instead of two, which from purely weight consideration should be sufficient. First we analyzed the positioning of the POSTs with respect to the cold mass. The cold mass is assumed as a homogeneous mass distribution having a total weight of 6000 kg. Obviously assuming an infinitely rigid cold mass the load would be equally distributed among the POSTs, and the two side POSTs (always there is one

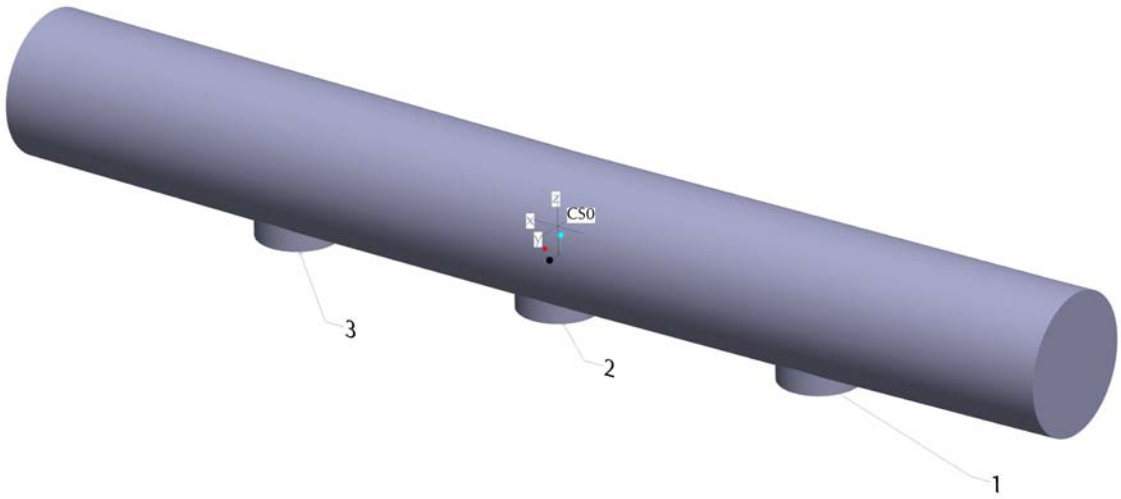

FIG.79: Cold mass placed over equally spaced POSTs.

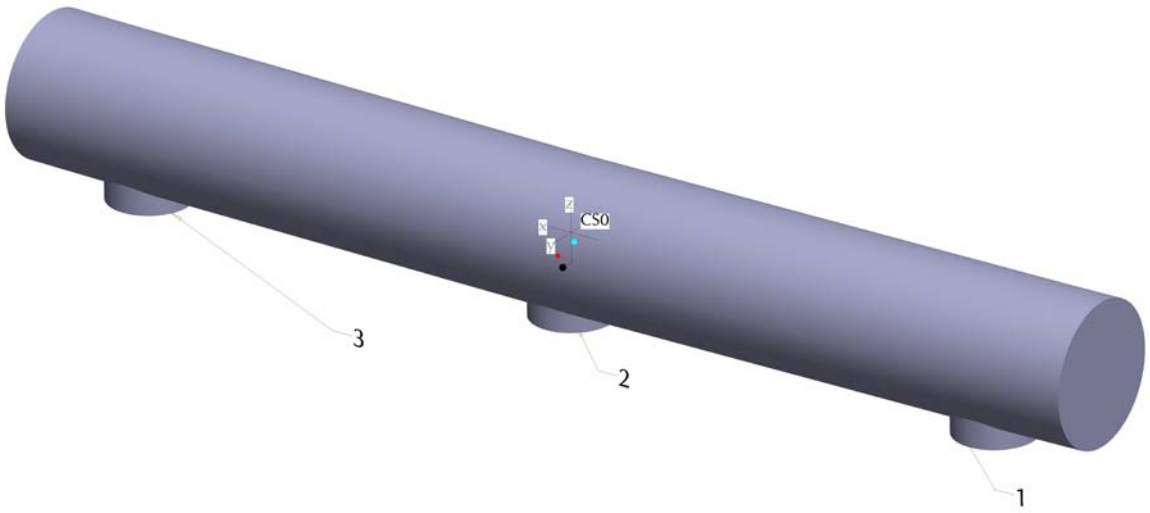

FIG.80: Cold mass over POSTs placed at maximum distance from the centre.

in the centre) can be placed anywhere. Situation will change when considering the elastic modulus of the cold mass. To estimate the Young modulus of our dipole we looked at the flexural rigidity of the LHC dipole, which has a similar mechanical structure. It has been measured for LHC dipole a flexural rigidity of 170 MNm^2.[45),46)] Scaling the geometrical momentum

$$I = \frac{\pi}{4}(r_o^2 - r_i^2) \tag{31}$$

to the dimensions of our dipole, we found a Young modulus of 60.2 GPa. We assume in the following numerical analyses that the cold mass has this Young modulus.

Two situations were considered. The first assumed the two side POSTs were located at 1075 mm away from the centre (Fig.79), that is in equally spaced positions with respect to the centre-ending positions along the cold mass. In this situation the load distribution analysis gives a proportion of the vertical force (z axis) ≈44% on the side POSTs and ≈14% on the central POST.

A second analysis considered the two side POSTs at 1700 mm from the central POST, that is about the maximum allowable distance (Fig.80). In this case we found the vertical force (z axis) distribution ≈42% on central POST and ≈28% on the side POSTs.

Two opposite considerations apply now: being the side POSTs the sliding ones, maybe useful to have less load on these supports, which mean less friction; but friction is also useful for stability during operation as can withstand axial forces more effectively.

As we cannot predict mechanical disturbances during operation, as well as the friction problems during cool-down, we shall assume an equally distributed load on the three POSTs, which is realized placing the two side POSTs at approximately 1266 mm from the central POST. This positioning is also compatible to other mechanical functionality of the cryostat, such as the required sliding sleeves which have to be designed on the outer cylinder. These

sliding sleeves are necessary in order to leave access for connections between two adjacent cryostats. These sleeves thus need at least 500 mm of free space on the side of the outer cylinder, thus they cannot interfere with the stiffening rings which have to be fixed at the POST connection on the outer cylinder.

Further to their positioning, the POSTs must be also designed to withstand the weight of the cold mass. For thermal considerations we foresee POSTs manufactured with a low

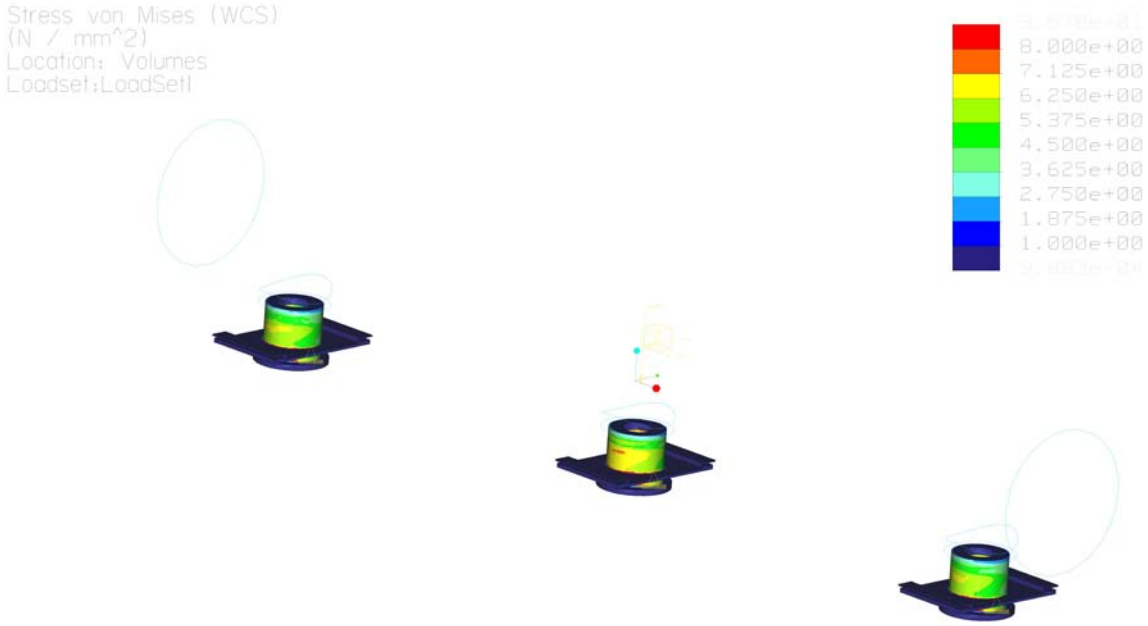

FIG.81: Stress analysis among POSTs placed “in line” at maximum distance from the centre.

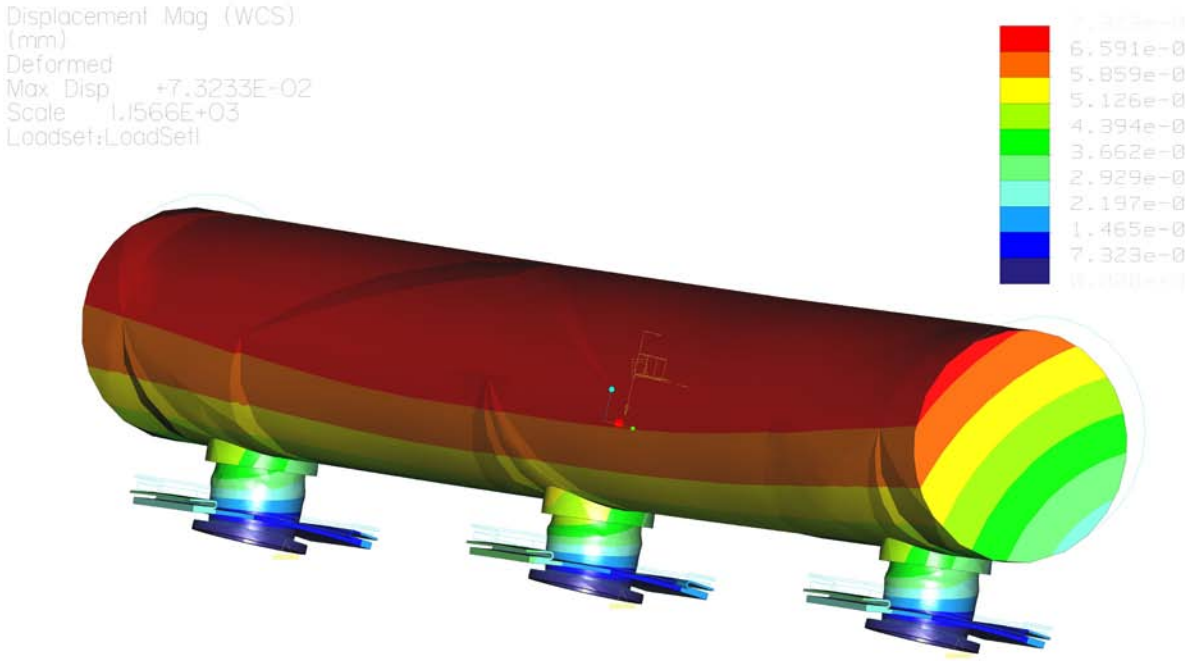

FIG.82: Expected displacement (magnified) of POSTs placed “in line” at maximum distance from the centre.

thermal conductivity material, like the G10. For G10 we consider 40 MPa as a reasonable stress value under compression, thus assuming an outer diameter ϕ_{ext}=200 mm (LHC similar size) for the POST we compute that a wall thickness t=2 mm in just one POST is able to support the whole 6000 kg weight. In fact this thickness will give a transverse section

$$\text{Sez} = \pi(\phi_{ext} t - t^2) \approx 12.5\,\text{cm}^2 . \tag{32}$$

This rough estimation tells us we have a large degree of freedom on the wall thickness with respect the thermal budget, and we can use this margin to increase the mechanical stability which may require improvements (as example against elastic instability of the POSTs). The thermal analysis (see Section Thermal analysis) gives us the opportunity to increase the POST wall thickness up to 5 mm, that is with a transverse section larger than 30 cm^2. In the previous and following analyses we have considered this value as the POSTs wall thickness.

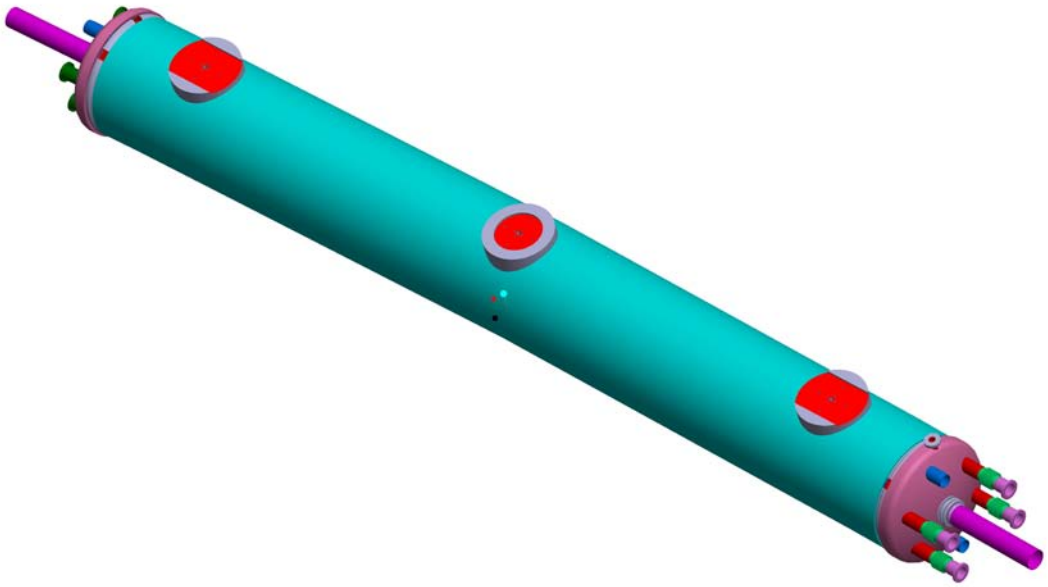

FIG.83: Bottom view of the cold mass and the cradles where POSTs will be connected.

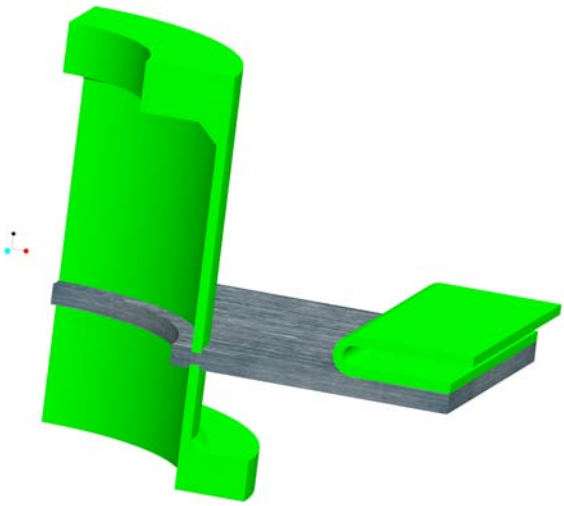

FIG.84: Proposed design for POSTs.

Then we analyzed the two possibilities in positioning the two side POSTs: following the bent magnet axis or “in line” with respect to the central POST, being the latter one always below the centre of the bent cold mass. In the “in line” case the stress analysis reveals the asymmetric stress over the three POSTs due to the out of the vertical axis positioning and to the bending of the cold mass. This means there will be a planar force in effect over the POSTs, which could be dangerous. In addition, this stress difference values are not equal among the POSTs, being larger, about 4÷5 MPa, on the central POST. This situation is shown in Fig.81, where only the three POSTs are shown. This behavior is clearer when analyzing the expected deformation due to the distributed compressive load of the cold mass on the POSTs, as shown in Fig.82. The maximum displacement$\approx 5\ 10^{-2}$ mm occurs on the central POST on the surface where the maximum stress is present (the concave side of the curvature of the magnet).

The presence of planar stress is considered dangerous to the material support, thus we also considered the situation where the POSTs are positioned alongside the curvature of the magnet. Performing the same analysis as before we noted that the effect is still present, as it comes out from the bending of the magnet, but its magnitude is half than before (≈2 MPa).

The above considerations led us to prefer the second solution for the position of the POSTs. Due to the small sagitta we are in any case able to fix the POSTs on a straight sliding sheet which allows for a simple integration process. The outer shell bottom access flanges will be enlarged up to include the sagitta at the POSTs level.

In conclusion the design of the cold mass cradles to be welded to the cold mass should be as shown in Fig.83. The two side connections are manufactured with a slit to allow the sliding of the cold mass during the cooldown, and only the central will be fixed to the POST. The central hole in the cradles are designed to fit the transport (and possibly integration within the cryostat) steel supports.

At the end of these considerations we realized that there is no space within our budget to develop the POSTs suitable for our cold mass. In fact the technology developed for the series mass production of the LHC support POSTs requires special molds which are expensive. To overcome this problem we concluded that the LHC POSTs can be easily adapted to our needs, and even if not optimized for this particular cryostat in terms of dimensions, we can also benefit of the higher mechanical performances without exceeding the thermal budget, avoiding the large cost for new special molds. Of course we have to slightly modify the thermal anchors as we do not need the 4.2 K one, but this will not change the manufacturing process. Another difference is that we shall use the POSTs in upside down position with respect to LHC, but also this will not change neither the manufacture nor their features. This design is shown in Fig.84.

9.5 Full mechanical analysis

Once defined the position and kind of plastic support, the integration process and the position of the three adjustable feet which will support the whole cryostat with the cold mass we started analyses to verify the mechanical properties of the system in order to set

reasonable thickness for the structural parts of the cryostat, i.e. the outer shell and the main sliding plate. In Fig. 85 it is shown the FEM model with loads and constraints.

Essentially loads are the outer pressure and the weights, while the three fixed points are located at the feet (blue rectangles below the cryostats). After some attempts we find an optimal thickness for the outer shell of 10 mm to guarantee acceptable displacement, which are represented in Fig.86. The maximum displacement occurs in the middle of the cryostat, as expected, and it is limited to 0.14 mm. The same analyses gave satisfying results on all the

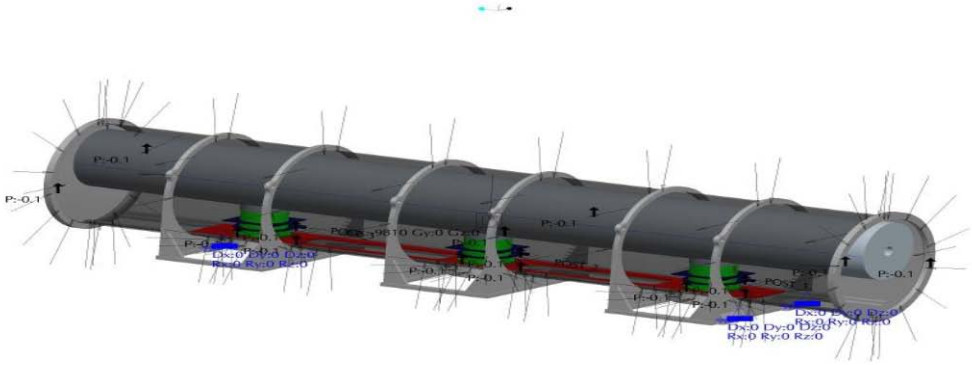

FIG.85: FEM model with loads and ties used to simulate mechanical displacements.

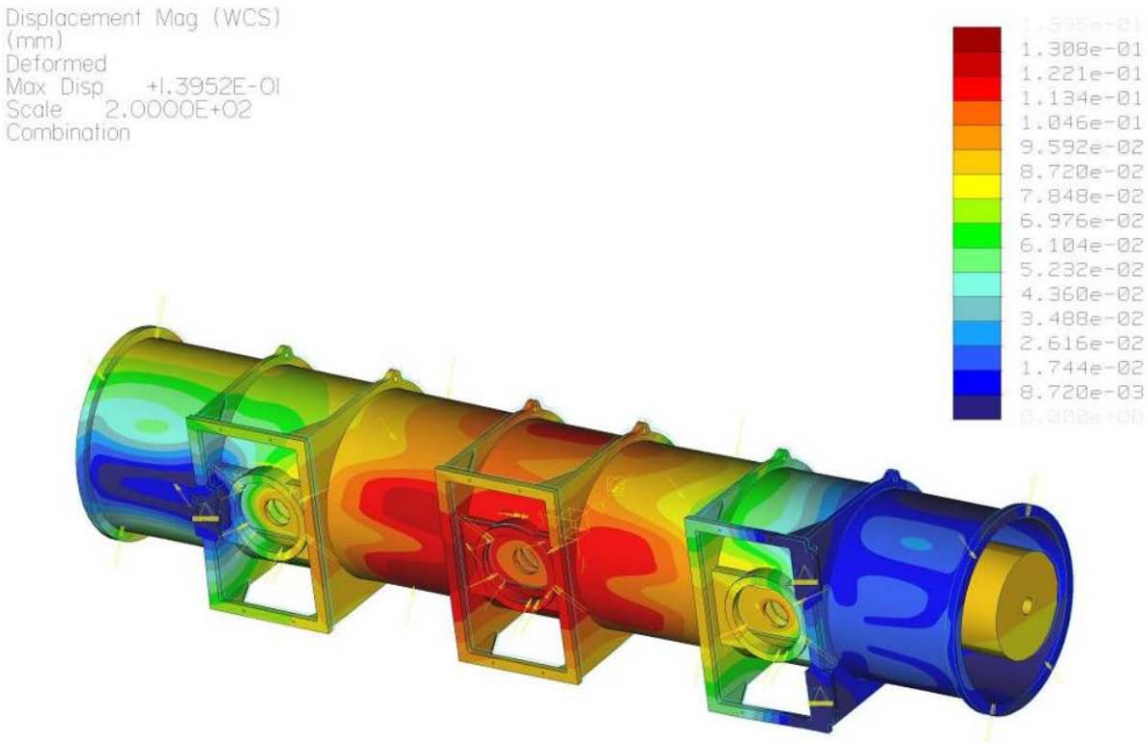

FIG.86: Expected displacements for the structure with loads and constraints.

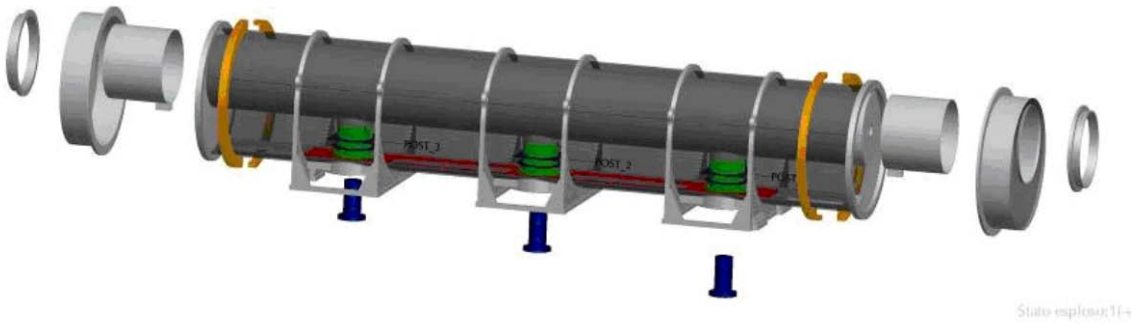

FIG.87: Transport assembly with POST stiffner and side collars.

components of the cryostat, POSTs and sliding plate, confirming that each items works within its possibilities. The maximum compression stress on the side POSTs is 30 MPa, and on the central is 20 MPa, while the shear stress on the POSTs is below 6 MPa. Further we checked the position of fiducial nests, on the side of the stiffener rings looking at the local relative displacements first and after applying the pressure force on the outer shell, and find they are within the required 50 μm.

Finally particular care was devoted to introduce stiffeners and side collars to allow a safe transport of the assembled system. In fact we adopted the solution shown in Fig.87 for the transport of cryostat: the cold mass is supported by the iron pieces and additional side collars tied to the outer shell by means of adapters. In this way we want to withstand axial and side acceleration of 1 g, and vertical acceleration of 2 g which can occur in standard surface truck transport. The forces which arise with these accelerations were also checked with FEM analyses of the model, confirming that the system can safely withstand these loads.

9.6 Thermal analysis

To estimate the input thermal load at 4.5 K we use standard formulation and computed material properties widely available in the literature. As usual we divide the main contributions of the heat loads: conduction and radiation. The gas conduction term[44)] is usually negligible when working at a pressure of 10^{-4} Pa (40 mW), and becomes significant (400 mW on the cold mass) only if the pressure rises 10^{-3} Pa.

The conduction load can be easily computed as the cold mass has only three POSTs which are in contact from room temperature to the 4.5 K stage, and an additional thermal path coming from the stainless steel beam pipe, whose dimensions are well known. In addition we can separate the contribution of room temperature (300 K) to the temperature of the thermal shield (usually 77 K) from the one between 77 K and 4.5 K. The total input power delivered from T2 to T1, with T2>T1, is

$$dQ/dt = \frac{S}{L}\int_{T_1}^{T_2} k(T)dT \qquad (33)$$

where S and L are the transverse cross section of the conducting path, and its length, respectively. $k(T)$ is the thermal conductivity of the material which connects the two temperatures, and usually its integral is available over wide temperature ranges. In this way only the geometries have to be considered to achieve a low thermal load together with reasonable mechanical stiffness.

Table 29 summarizes the main features of connecting elements which give rise to thermal conduction, and the amount of dissipations they introduce. As can be noted, even if we doubled the size of the POST wall thickness (from 2 to 5 mm), the amount of expected thermal load is limited to 0.43 W for each POST. The final estimation for the conductivity part is about 1.9 W at 4.5 K plus 18 W at 77 K.

The radiation load is also split in the two contributions, one over the thermal shield at 77 K and the other on the cold mass at 4.5 K. To keep low these values two precautions have to be implemented: wrap one Al foil over the cold mass outer shell to improve its reflectivity, the use of a multilayer insulation (at least 30 layers). The emissivity E for two nested long cylinders (the cold mass and the thermal shield) can be approximated with:

$$E = \frac{\varepsilon_{cm}\varepsilon_{ts}}{\varepsilon_{ts} + \frac{A_{cm}}{A_{ts}}(1-\varepsilon_{ts})\varepsilon_{cm}} \tag{34}$$

where ε_{cm}, ε_{ts} are the cold mass and thermal shield emissivity, respectively, and A_{cm} and A_{ts} are the cold mass and thermal shield surfaces, respectively. The heat in-leak by radiation from the shield to the cold mass is then:

$$\frac{dQ}{dt} = \sigma E A_{cm}(T_{ts}^4 - T_{cm}^4)\,. \tag{35}$$

The cold mass surface is about 7.0 m^2, while the thermal shield surface is 11.5 m^2, using the ε for Al foil we can lower E=0.01 and obtain a radiated power on the cold mass of 0.17 W. Other minor radiating terms comes from the inner surface of POSTs, but using also for these items the Al foil wrapping the total power can be kept below 0.02 W.

The global estimation for the heat load at 4.5 K is therefore 1.9 W, within the budget.

The largest radiation load is the one coming from the outer shell, 15.28 m^2 of surface at 300 K. The direct load on the Al thermal shield at 77 K should be about 481 W when considering the as found Al and stainless steel emissivity. To reduce this load we introduce a Multi Layer Insulation (MLI) with 30 layers, which reduces the radiation over the Al shield to

TAB.29: Estimated contribution coming from thermal conduction.

	ϕ_{ext} (mm)	Thickness (mm)	$L_{300\div77}$ (mm)	$\int_{77}^{300} k(T)dT$ (W/m)	$L_{77\div4.5}$ (mm)	$\int_{4.5}^{77} k(T)dT$ (W/m)	$W_{4.5\ K}$	$W_{77\ K}$
POST	200	5	60	153	140	20	0.43	8
Beam pipe	89.9	2	150	2711	350	349	0.55	10

about 15.5 W. The contribution over the POSTs where there is not any MLI should be added again to this quantity. This contribution is about 2.8 W for all the POSTs. Finally the global estimation for the heat load at 77 K is therefore 44.8 W.

In order to have a picture of the temperature distribution on the thermal shield we also numerically computed the equilibrium temperature corresponding to the heat loads described

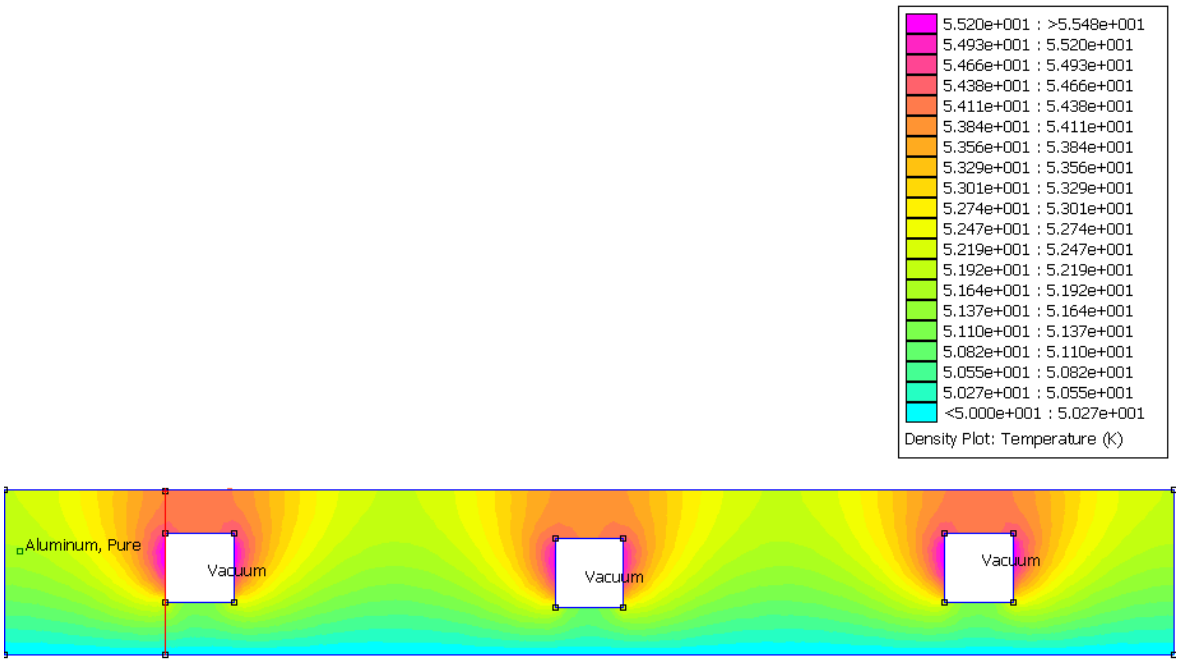

FIG.88: Numerical analysis of equilibrium temperature distribution on the shield bottom tray.

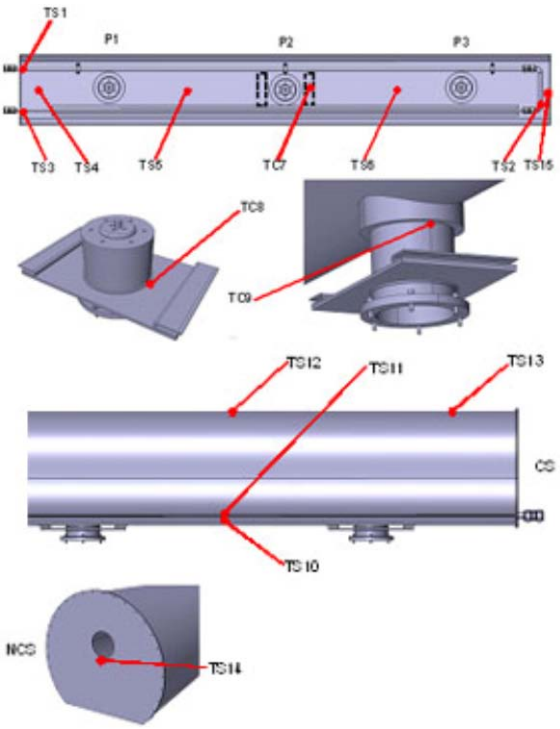

FIG.89: Temperature sensor distribution on strategic places of the shield.

before.

This is useful to check the thermal design of the shield, to be sure that heat is effectively removed by the thermal anchors. In Fig.88 it is reported the stationary temperature distribution on the shield bottom tray, made of pure Al, under the thermal loads of conduction heat coming from POSTs and thermal radiation, cooled by the cold gas flow on one side. The return gas cooling line is considered insulated to avoid thermal shortcut which can prevent the uniform cooldown of the system.

Finally we estimated the heat loads introduced by diagnostic thermometers which will be installed in the cryostat. There will be placed 15 CLTS sensors to read the local temperatures on the shield, as shown in Fig.89. Assuming a 32 AWG wiring of low conductance (phosphor bronze) we compute a total heat load at 50 K less than 4 mW.

10. INDUSTRIAL DEVELOPMENTS

10.1 Winding tests

The design of the model coil was performed in parallel with a crucial industrial R&D activities aimed at demonstrating the construction feasibility of curved collared windings. This activity held place at ASG Superconductors in Genova, under an INFN contract. A special winding machine was developed for winding a cored Rutherford cable on a curved mandrel. Fig.90 shows the winding operation of a curved coil. Several winding tests were performed using first the LHC dipole outer layer cable (Figs. 91 and 92 show the details of the winding during these tests). In a second step, the tests were carried out using the trial winding cored cable obtained by cabling the LHC dipole wire with a stainless steel insert (see Fig.6). An important milestone was then achieved with the successfully completion of two complete poles, proving the developed winding technology. Fig.93 shows the cured model pole. A detail of the coil end (the one with block-to-block connections and exits) is shown.

FIG.90: Winding operation with a dummy conductor. The geometrical curvature is clearly appreciable.

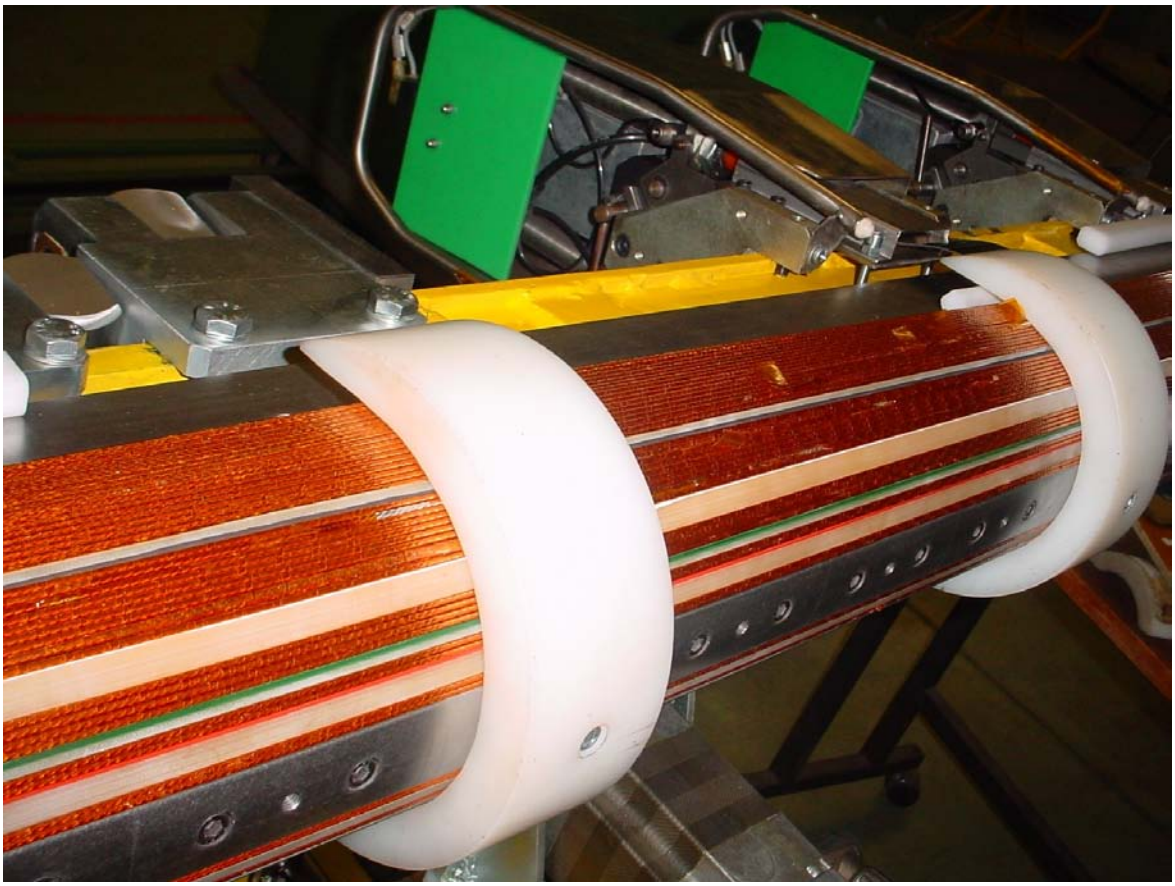

FIG.91: Winding test with LHC conductor: detail of the coil middle zone.

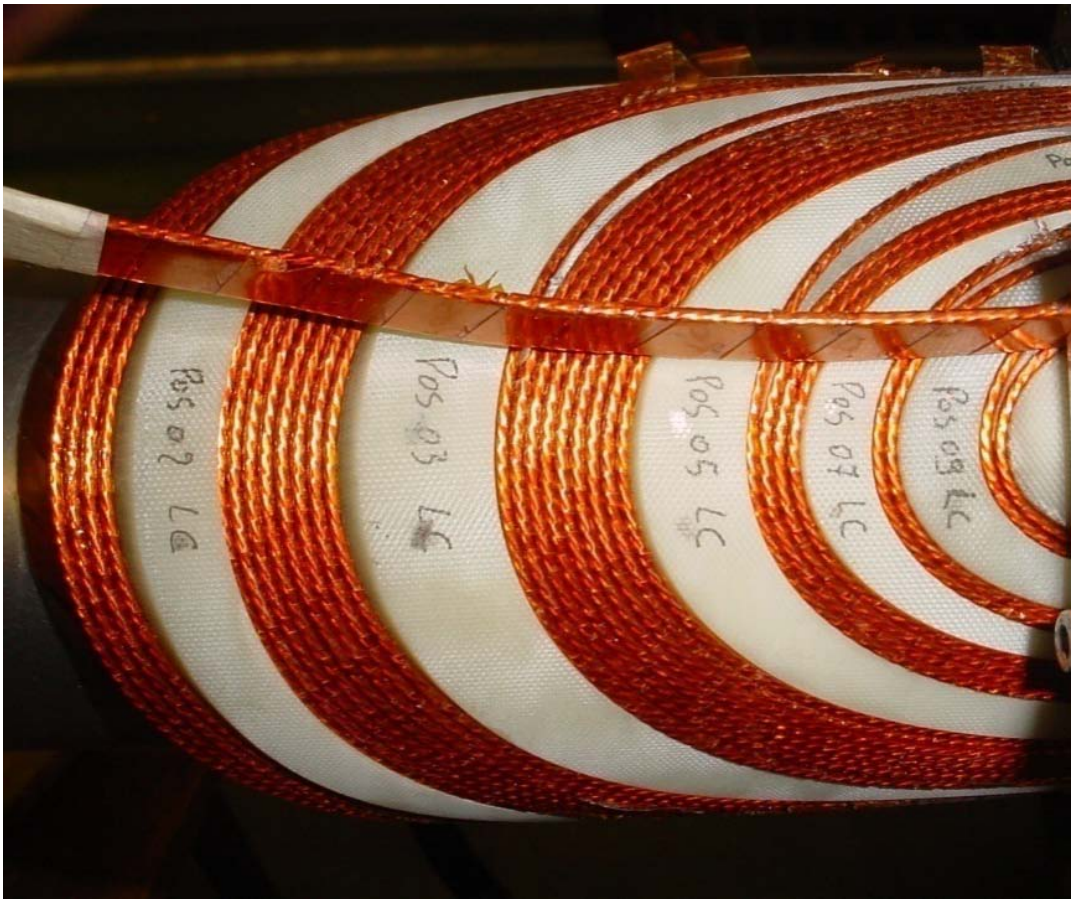

FIG.92: Winding test with LHC conductor: detail of the coil end with G11 spacers.

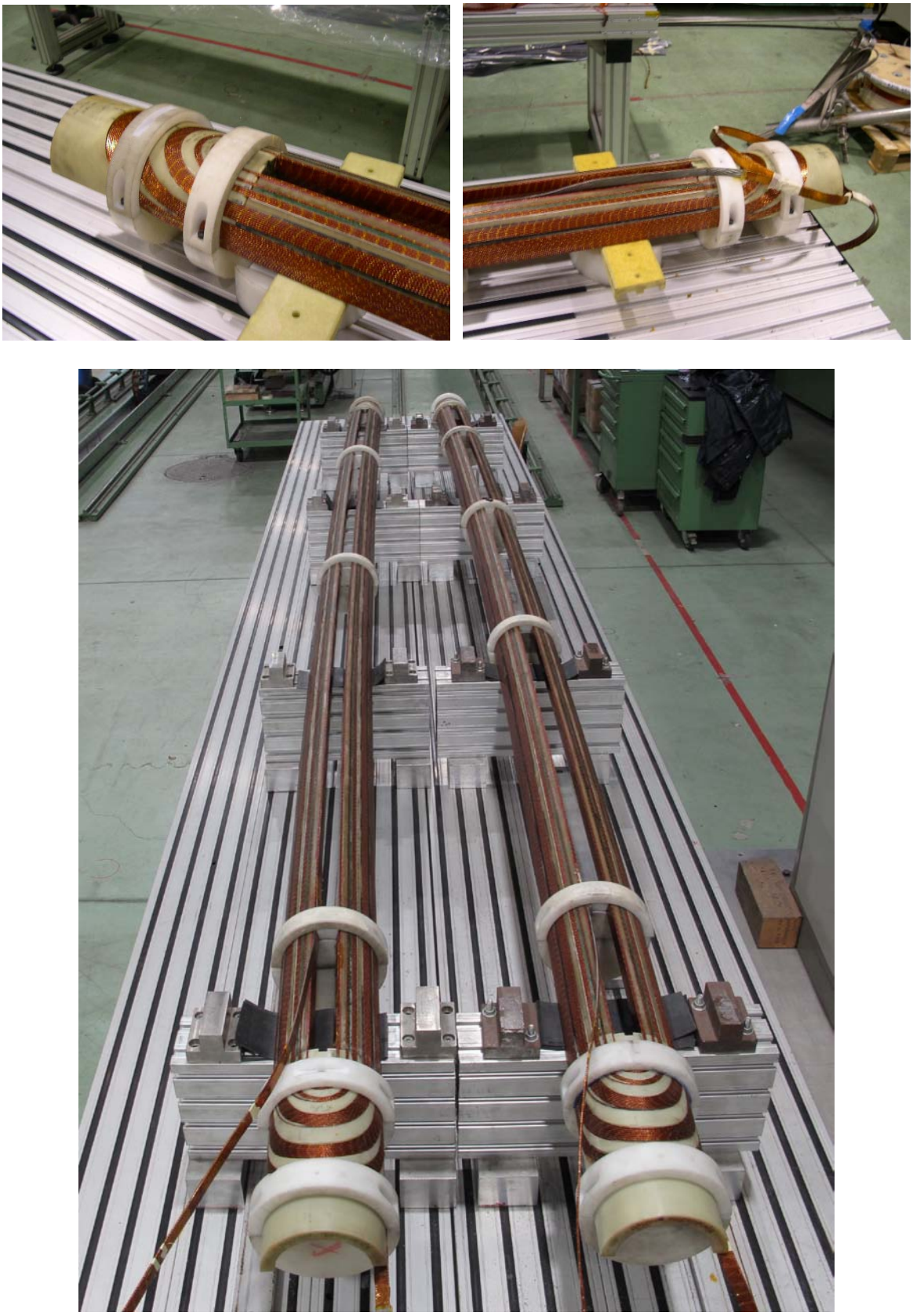

FIG.93: Cured poles (wound with the cored conductor). On the top side the details of the coil ends are shown.

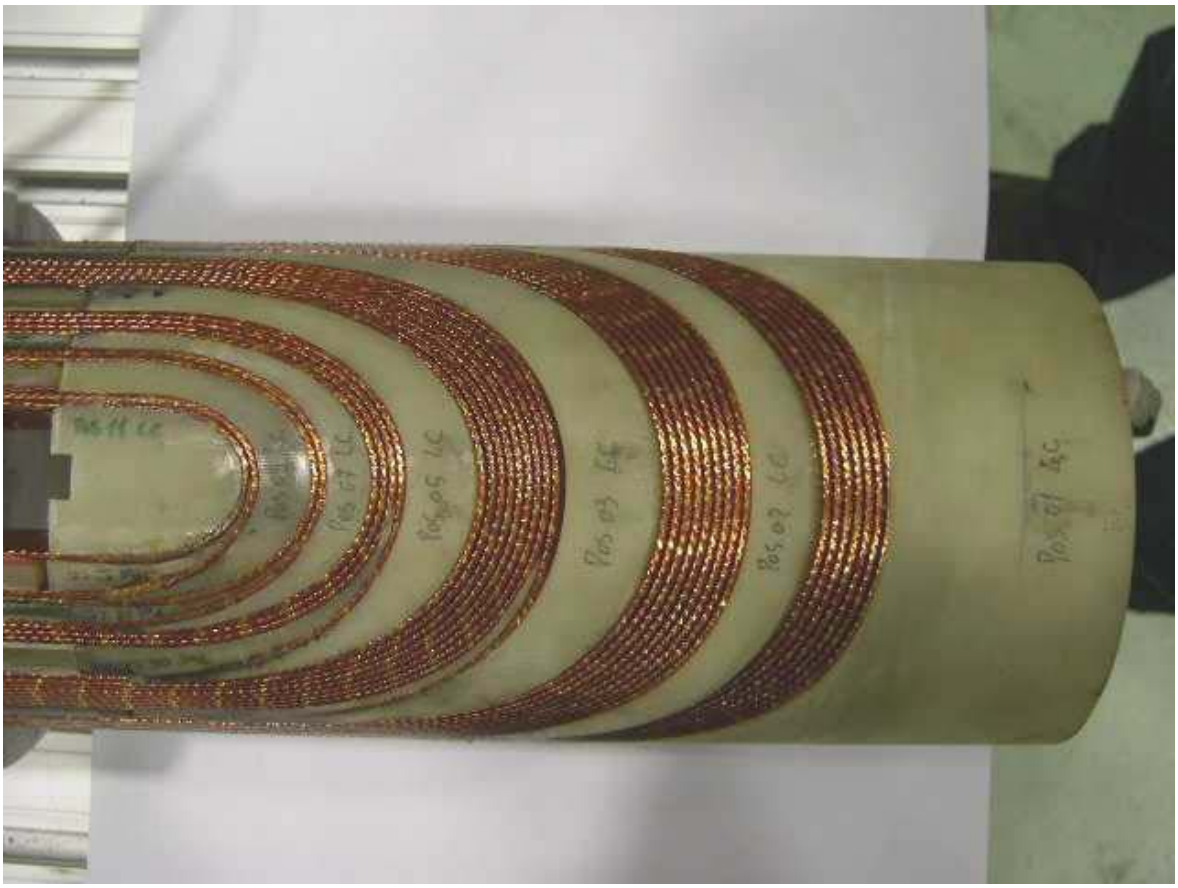

FIG.94: Details of the LC coil ends are shown. The 5 blocks result in 6 sections, being the larger one spitted into two parts.

10.2 Geometrical survey

A geometrical survey of the pole was performed in two conditions: 1) the overall geometrical parameters of the pole were measured without imposing any mechanical constrain (free pole); 2) small portions of the pole were inserted into a special device giving 50-70 MPa vertical pressing, for measuring the pole cross section and the elastic modulus. The results on the constrained pole are discussed in Appendix B. Here the results on the free pole are shown.

- *Overall pole.* Fig.95 shows the drawings of the pole with the relevant dimensions. The pole under analysis is the upper pole. The arc length of the curved part is designed to be 3630 mm. Considering a bending radius of 66.67 m, this arc corresponds to a chord of 3629.55 mm and a geometrical sagitta of 24.7 mm (these data are shown in the drawing). The two end coils (which are geometrically straight) are both 250 mm long. In the drawing of Fig.95 LC means “connection side”, i.e. the end coil with electrical exits and block-to-block connections. LOC means “opposite to connection side”. During the winding, the measured chord was 3629.55 mm for both poles, being determined by the mandrel longitudinal dimension. After curing, the chord shrunk to 3628.25 mm (for the first pole)

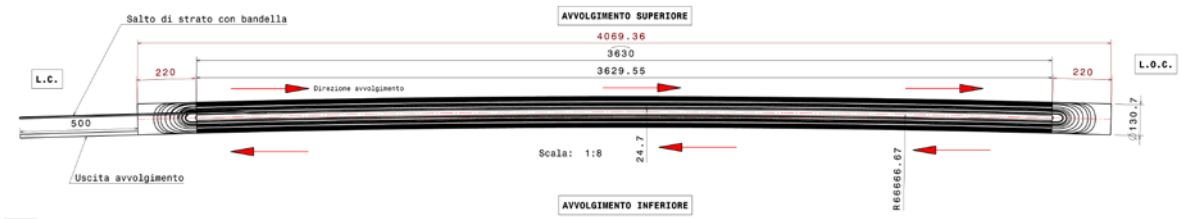

FIG.95: Longitudinal dimensions of the coil according to the design.

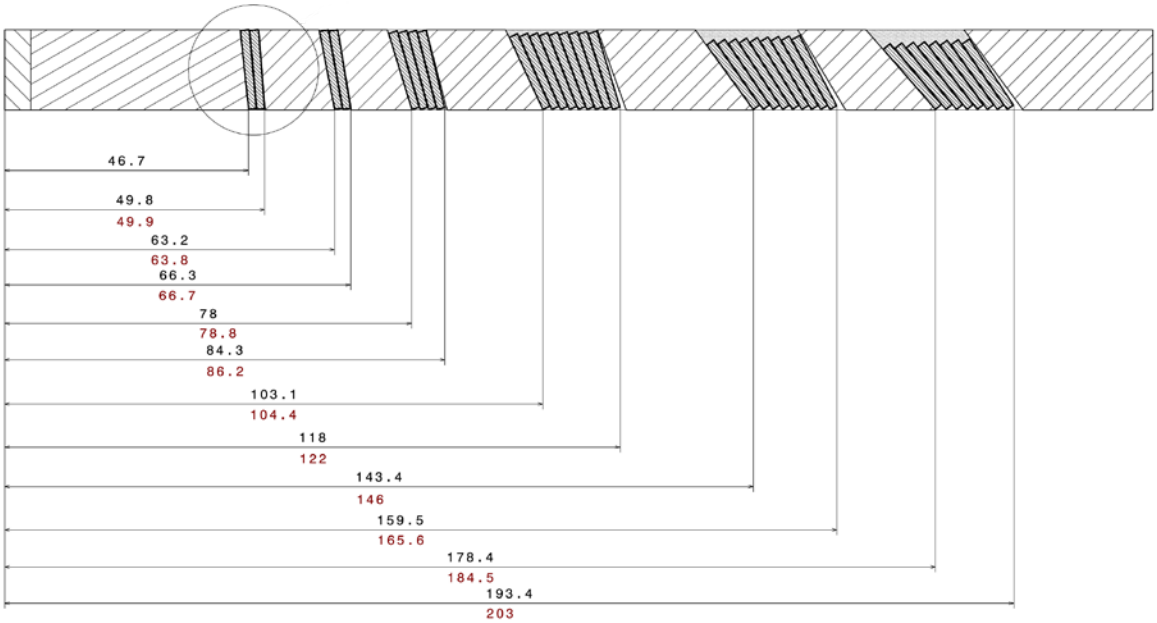

FIG.96: Sketch of the cross section of the LOC coil end (at 90°) as designed (in black) and as built (in red). The dimensions refer to the inner radius.

and 3628.65 mm for the second pole. This effect is attributed to the winding pretension and shall be considered when re-designing the coil during the prototyping phase. The measured curvature radius of the free pole is 73.574 m (83.941 m for the second pole) with negligible variation along the arc. We checked that once placed again on the mandrel, the wanted shape (with radius 66.67 m) is easily re-obtained for both poles. These results are considered very positive: few modifications are required for obtaining the wanted arc length.

- *Coil ends.* The analysis of the coil ends is more complex. As an example, Fig.96 shows the as-built cross section of the coil end at LOC side and at an angle of 90° compared with the expectation (for the first pole). The longitudinal position of the first and last conductor (at thin edge) of each section is reported; the reference is the end of the curved central section of the pole. The mismatching between as-built and designed end coil is mostly due to the conductor deformation in this region. From a trapezoidal shape, the conductor is forced to assume a more rectangular shape causing a not perfect coupling between conductor blocks and end-spacers. Two consequences arise: 1) an unwanted integrated component b_3 in the end is generated, 2) small holes appear between blocks and end spacers. The sextupole

component can be controlled by suitably changing the distance between the blocks in the coil end. The holes can be filled by a resin (stycast) local impregnation. Nevertheless we intend for the future to study deeper this problem and try better adapting the end spacers to the deformed end blocks minimizing the holes in their number and dimensions.

11. COLD MASS MAIN FEATURES

In this section a description of the cold mass is given together some engineering drawings and some information related to the envisaged manufacturing methods.

1 *Turn distribution.* The conductor features are described in Section Conductor. In this section it is only reported the constructive drawing of the insulated conductor, which is the basic brick of the design (see Fig.97). The turn distribution as shown in Fig.98 was the result of a field quality optimization, performed in an early magnetic design phase. Subsequent analyses showed that a slightly different distribution of the conductor would be needed. Since in the meantime we had developed a design for the end coils and since this design had been checked through the construction of a winding model, we decided to freeze the turn distribution as defined through that magnetic optimization. We will check the real field quality of the model with respect the computations and will refine the turn distribution for the next prototypes.

2 *Winding.* The cross section of the winding is shown in Fig.99. Besides the insulated conductor, the components of the winding are: i) the wedge spacers in G11-S type (shown in Fig.100); ii) the quench heaters; iii) a first layer of ground insulation including cooling channels (0.5 mm thick); iv) the ground insulation made of kapton foils up to a total thickness of 0.5 mm; V) finally two kapton foils for a total thickness of 0.125 mm providing further protection to the winding. All these components are shown in Fig.101. The part of ground insulation with cooling channel is intended as a reserve of cooling power. When performing the thermal computations only the thermal exchange with supercritical helium at the winding inner radius has been considered. In fact we can have some additional cooling of the winding also at the outer radius through these channels. The general drawing showing all winding detail is shown in Fig.102. To be noted that the curved central part of the winding is 3630 mm long. The two coil ends are straight and a length of 220 mm as shown.

3 *Collars.* Fig.103 shows the half a collar cross section. All details are visible: i) the nose of the pole, ii) the small protrusion on the pole for centering the collar into the iron yoke, iii) the cuts for connecting a lifting device, iv) the two hole for the pins connecting each collar to the adjacent one, v) the cuts for the longitudinal key. The collars, 3 mm thick, are grouped in number of 10 through the pins to form a pack. The packs are connected each other through 60 mm long keys in a way to follow the geometrical curvature of the winding, with the aid of thin spacers (~0.09 mm) placed between two packs at the convex side. In the coil ends the collar are different, because the pole nose is absent. The beam pipe is supported by the collars through fiberglass components directly attached to the noses (see Fig.104).

4 *Yoke lamination.* The electrical steel lamination made of Silicon steel according to the standard M600-100A is shown in Fig.105. The nominal value of the inner radius of the yoke is 40 μm larger than the outer radius of the collars, for making easy the integration of the collared coil into the yoke. It is appreciable the complexity of this component,

including many features: i) the large quasi-elliptical large hole where the re-cooling tube is passing through. In this tube bi-phasic LHe at 4.4 K is circulated for re-cooling the supercritical helium as described in Section Cryostat; ii) the cuts for lifting the coil integrated into the lamination; iii) the two squared openings placed at the outer radius for allowing the space of the bus-bars; iv) the four holes used for connecting the lamination each other according to a process described soon after, v) the two lateral openings used for the clamping system, widely discussed in Section Mechanical analyses. The top of the lamination is flat for two reasons: a) to have the possibility of using existing pressing system, b) to generate a large surface for applying the vertical force in the assembly phase. The yoke is pre- assembled in 4 curved sectors 1 m long (each one composed of two parts: upper and lower involving each 1000 plates). Differently from the collars no pack is composed but rather the curvature is obtained pressing the concave side more than the convex sides. Inter-plate spacers are suitably inserted at the convex side. Each half-sector is mechanically connected through four pipes passing through the four above mentioned holes. The two extremities of each pipe are fixed to the first and last laminations enclosing the sector. These two laminations are of special kind, being composed of five 1 mm thick laminations glued together in a way to form a sort of side flanges of the sector. In this way we have a solid enclosure of the sectors (all these details are shown in Fig.106. The sectors are joined together using curved rods passing through the pipes and blocked by nuts at the magnet ends, as shown in Fig.107, where one can see other features of the iron yoke. On the both flat top and bottom, a curved rectangular bar is welded to the yoke, with the function to give more stiffness to the whole structure. At the mid-plane two backing strips are attached to the clamps. Later on these strips will be welded to the two halves of the external shell. One can also see a tube passing through the upper hole of yoke. That is the re-cooling tube having no functions in the actual model magnet, which will be tested as a stand-alone unit, but has an important role in the cryogenic system of SIS300, for transferring the heat loss from the supercritical helium to a secondary hydraulic circuit employing bi-phasic LHe.

5 *External shell.* The coil fully integrated into the iron lamination is subsequently enclosed in a 10 mm thick stainless steel curved envelopes, obtained by a single curved large tube, cut into two halves. The two halves are connected through a welding operation including the backing strips fixed to the clamps, resulting into a stiff curved cold mass. Fig.108 shows the whole cold mass cross section.

6 *The end regions.* The magnet end regions are two special locations. The collared coil is straight for a length of 220 mm (this length was reduced with respect to the winding model) and the collars are composed in a circular sector shape (without the noses). The yoke lamination is geometrically identical to the one used for the central curved sections (as described in point 4), except the material, which is stainless steel for minimizing the peak field (as described in Section Eddy currents for perpendicular field). In one of the end regions the electrical ends are placed. In both regions a system

has been designed for allowing the application of an axial pre-stress to the collared coil only. Figs. 109, 110, 111 and 112 show the details of these regions.

7 *The complete cold mass.* Once finished, the cold mass should appear as shown in Fig.113.

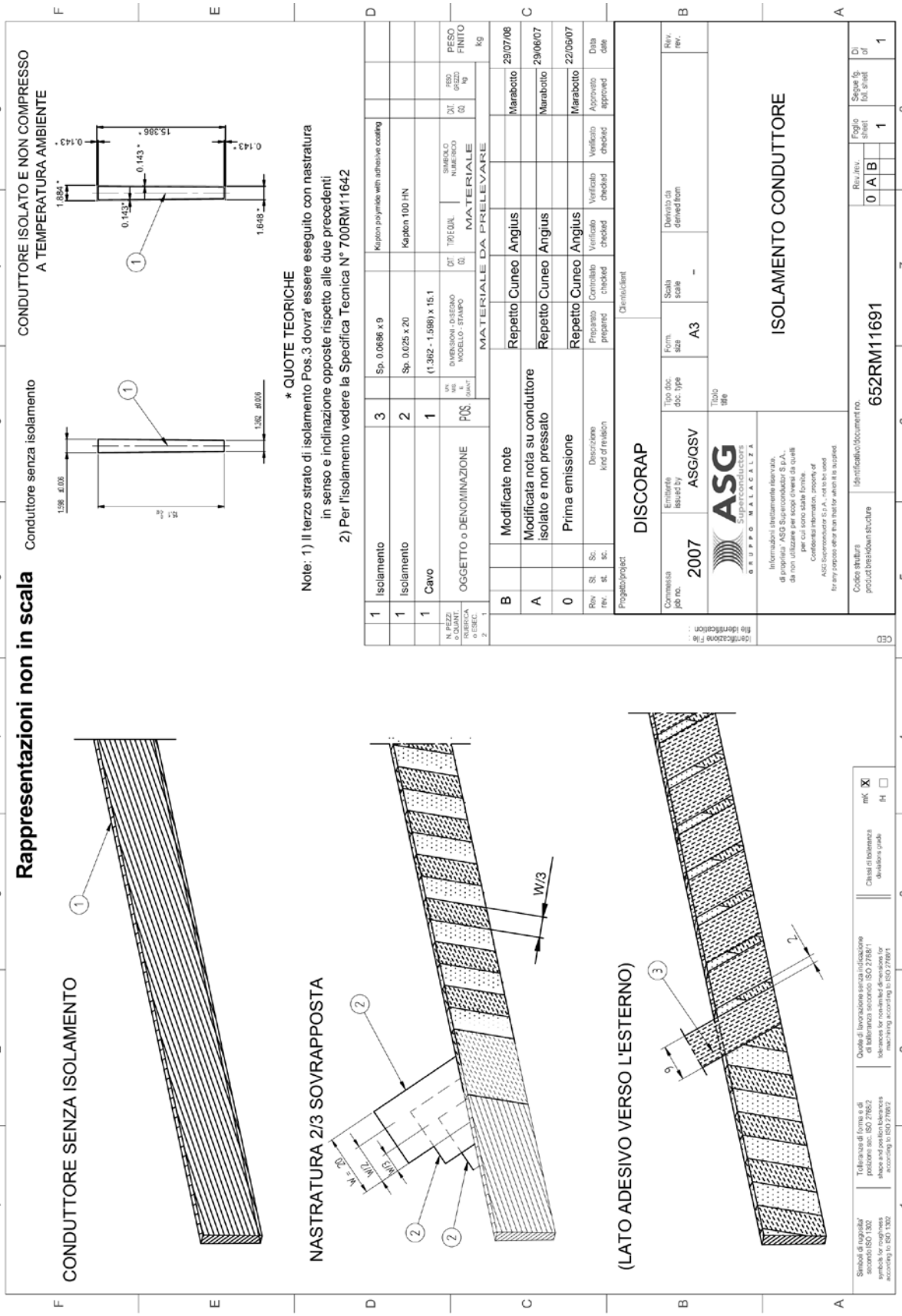

FIG.97: Conductor insulation.

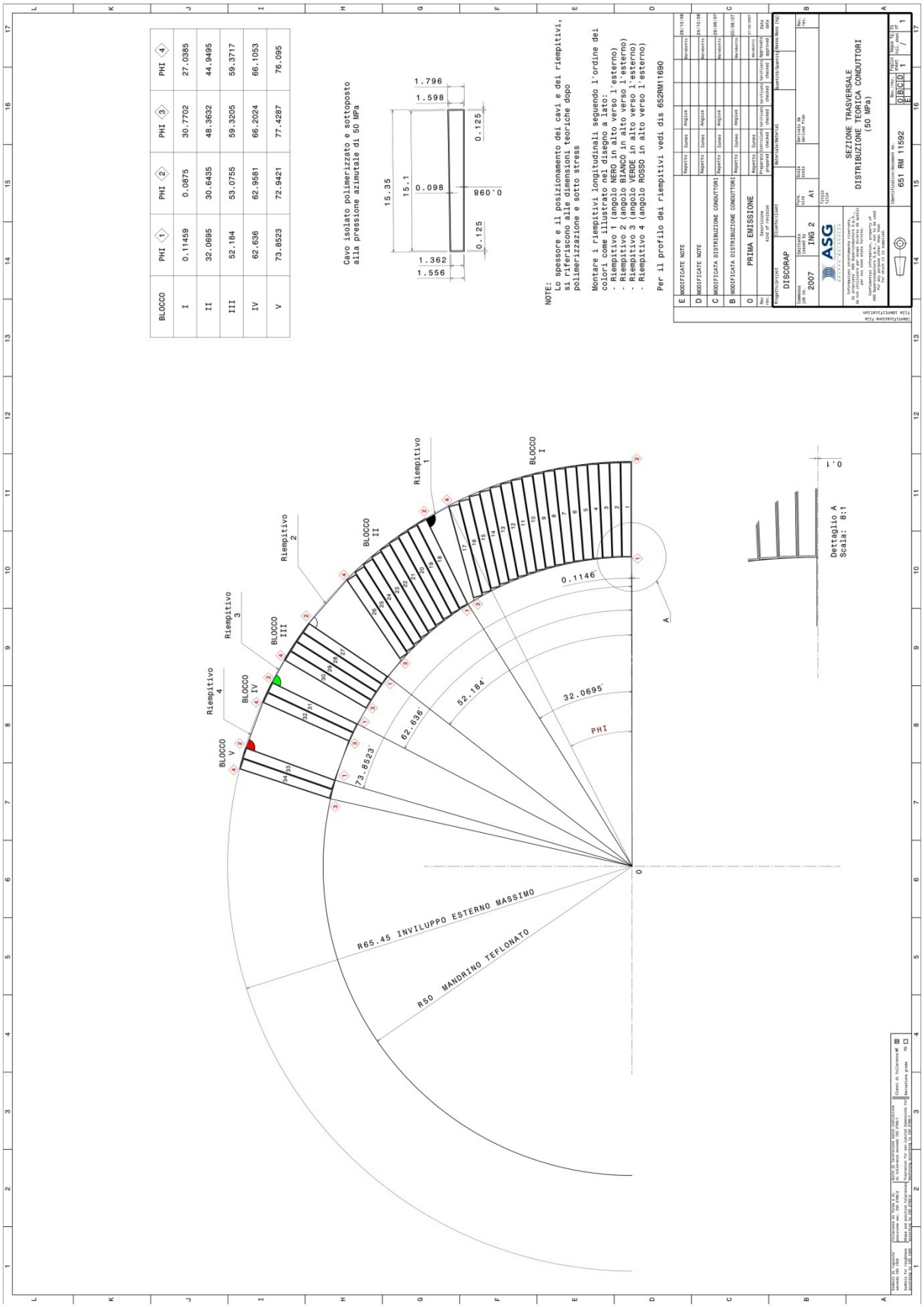

FIG.98: Turn distribution.

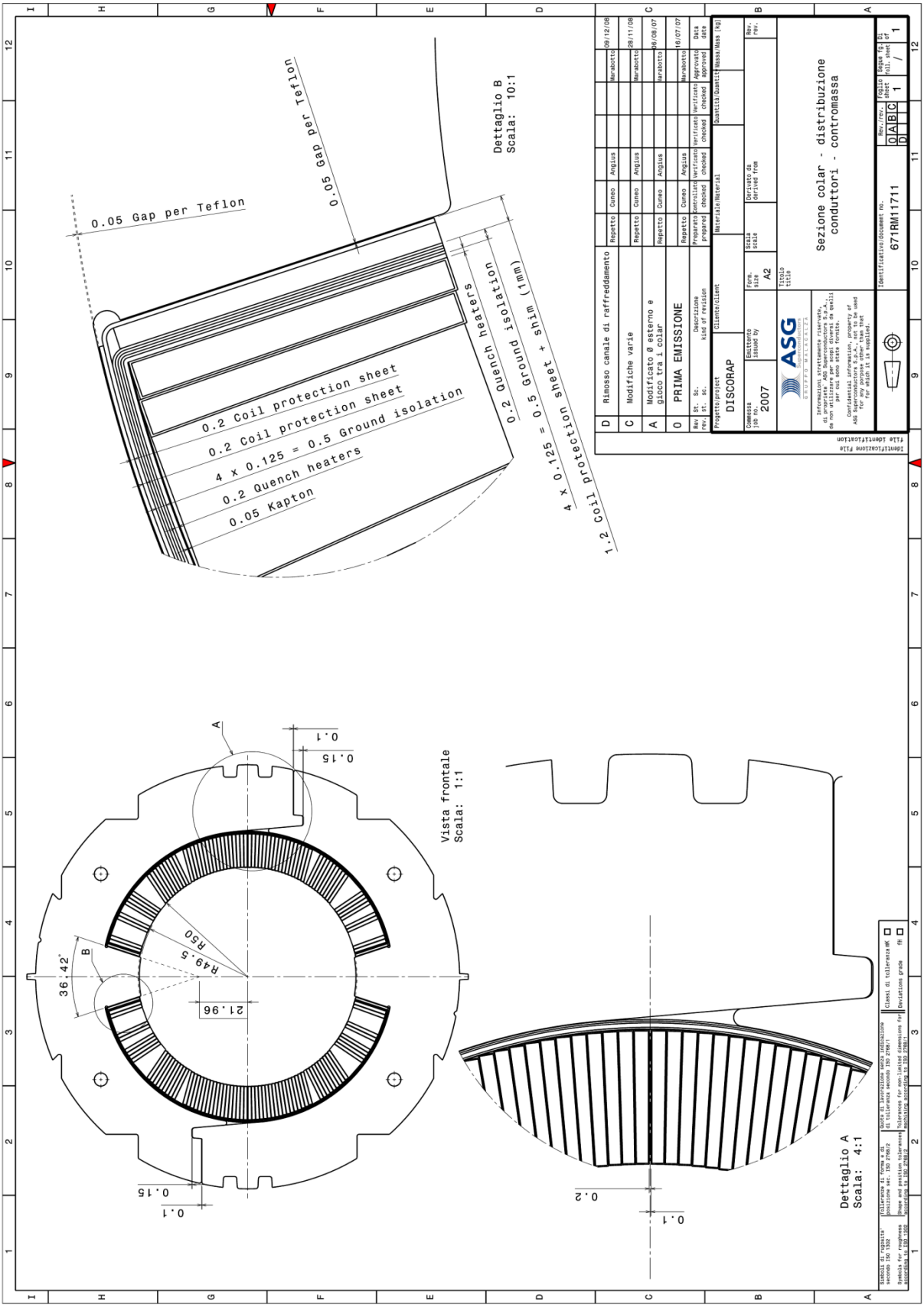

FIG.99: Winding cross section with ground insulation details.

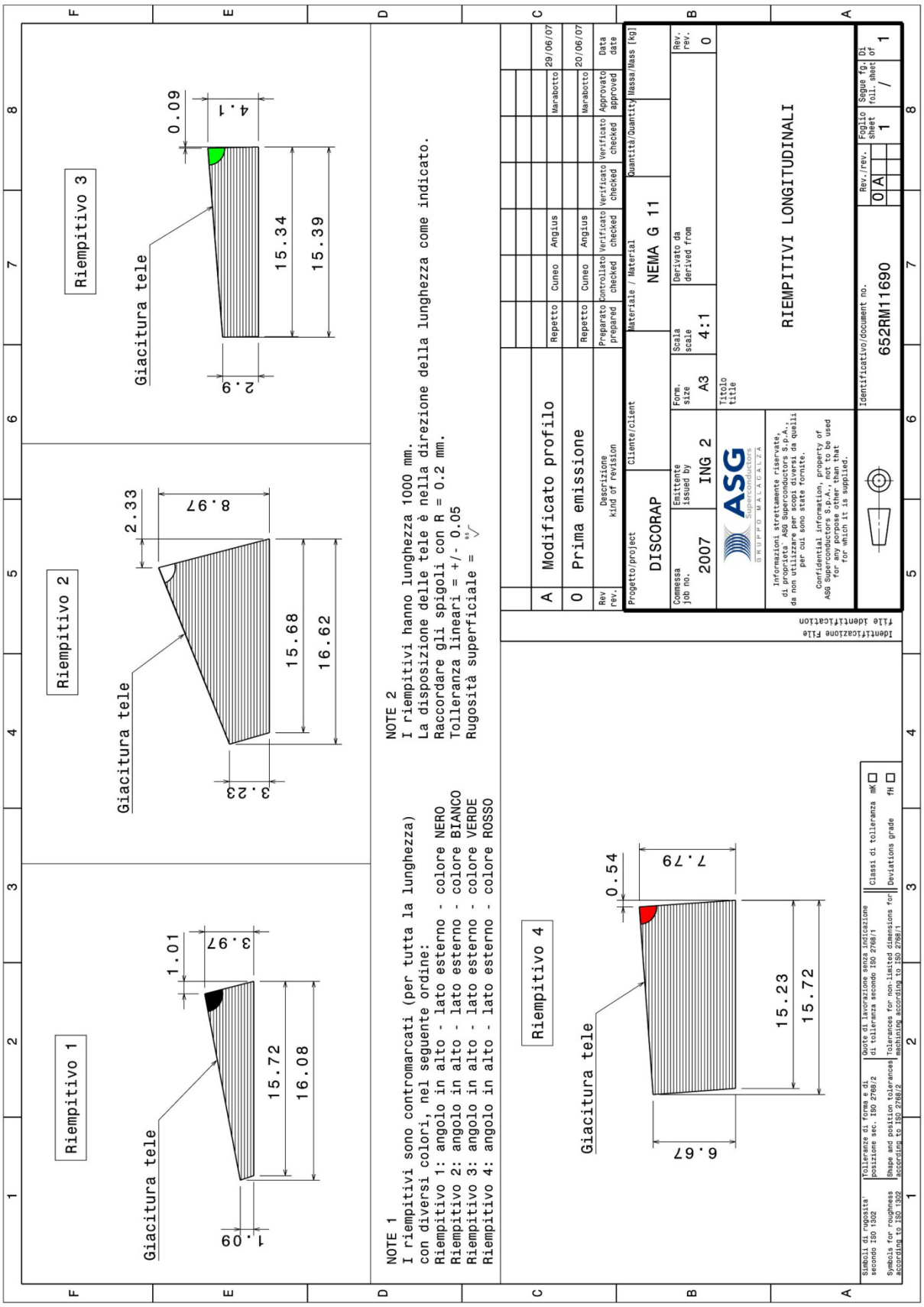

FIG.100: Details of the G11 coil wedges.

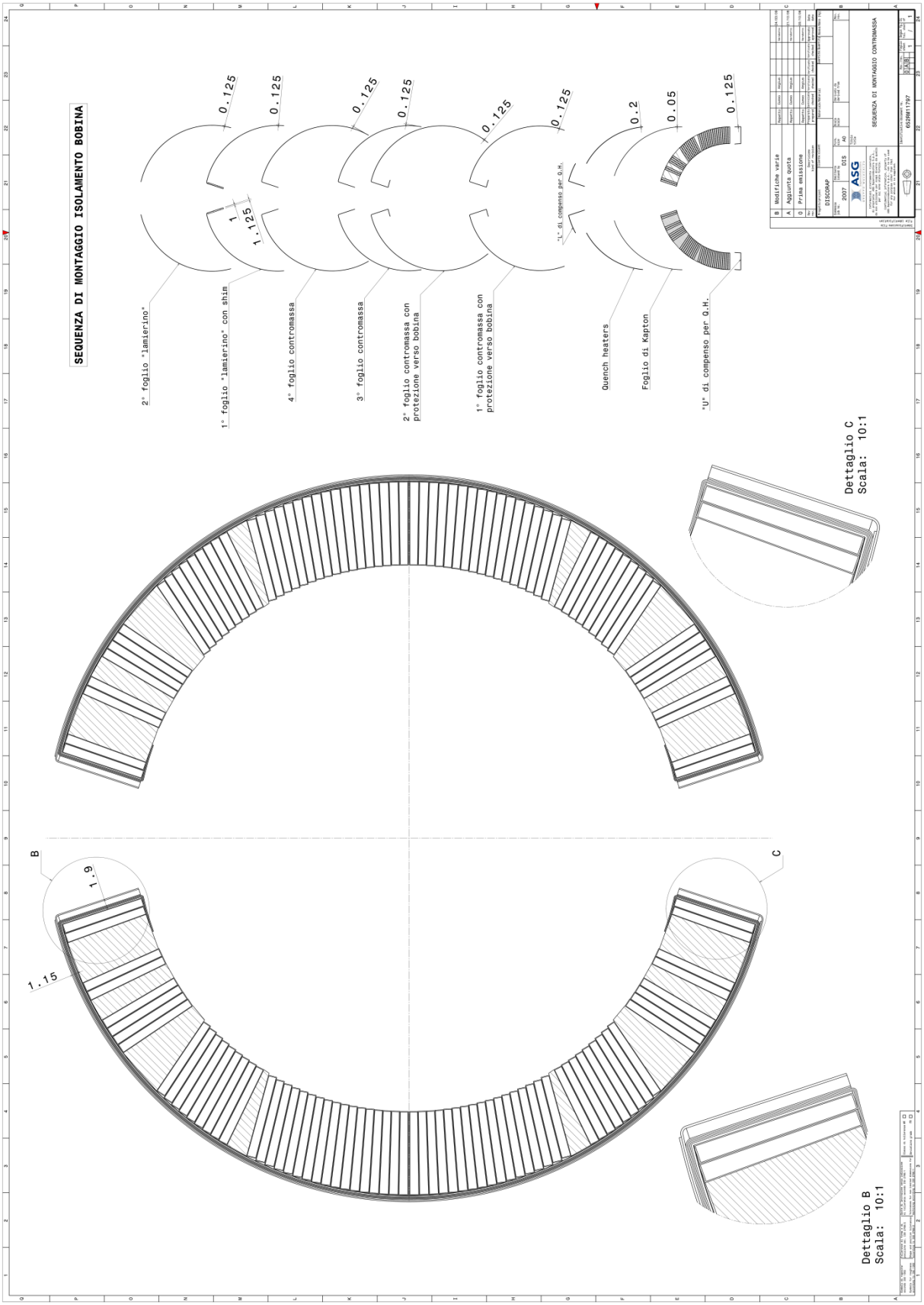

FIG.101: The different layers covering the winding.

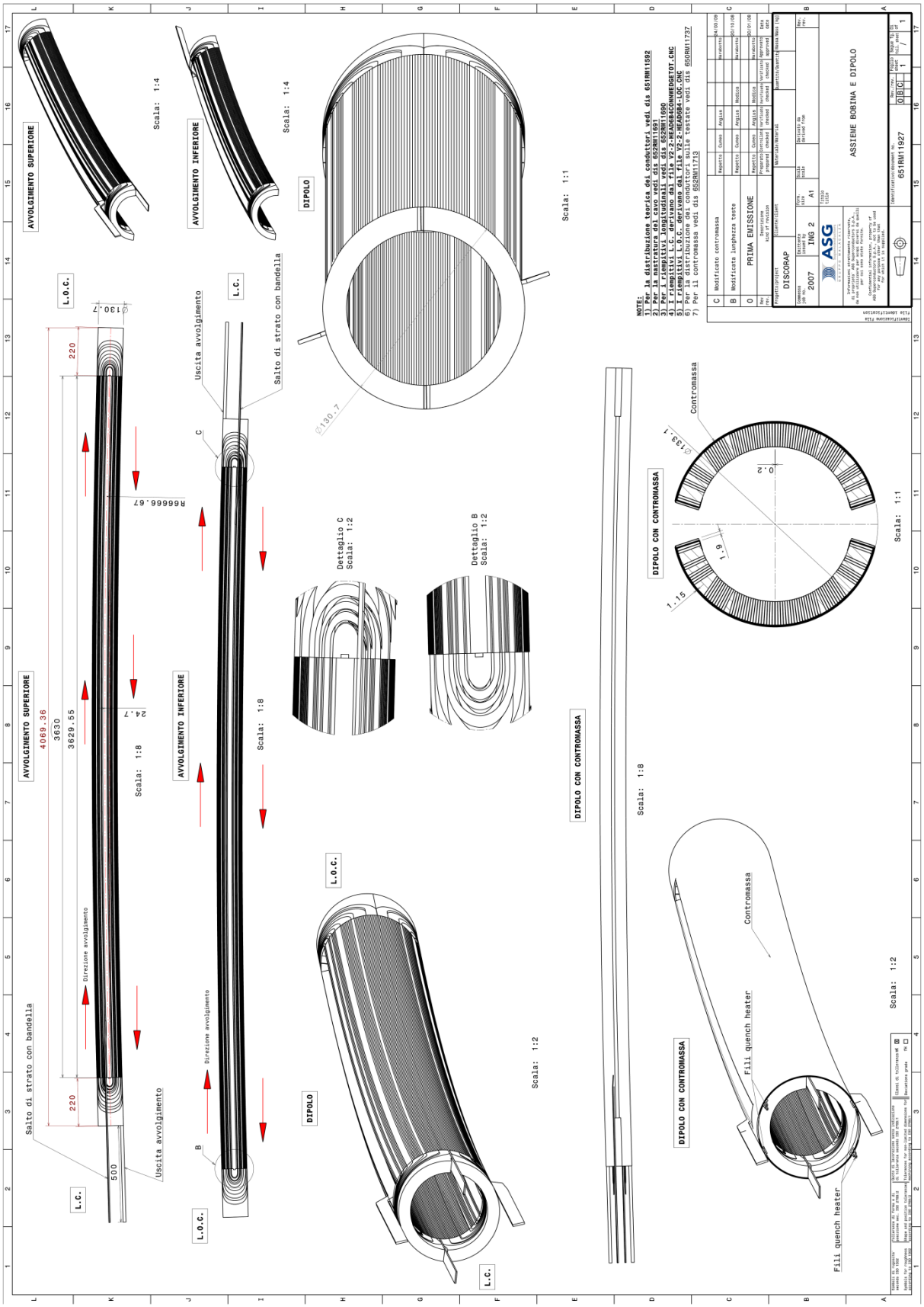

FIG.102: The curved coil.

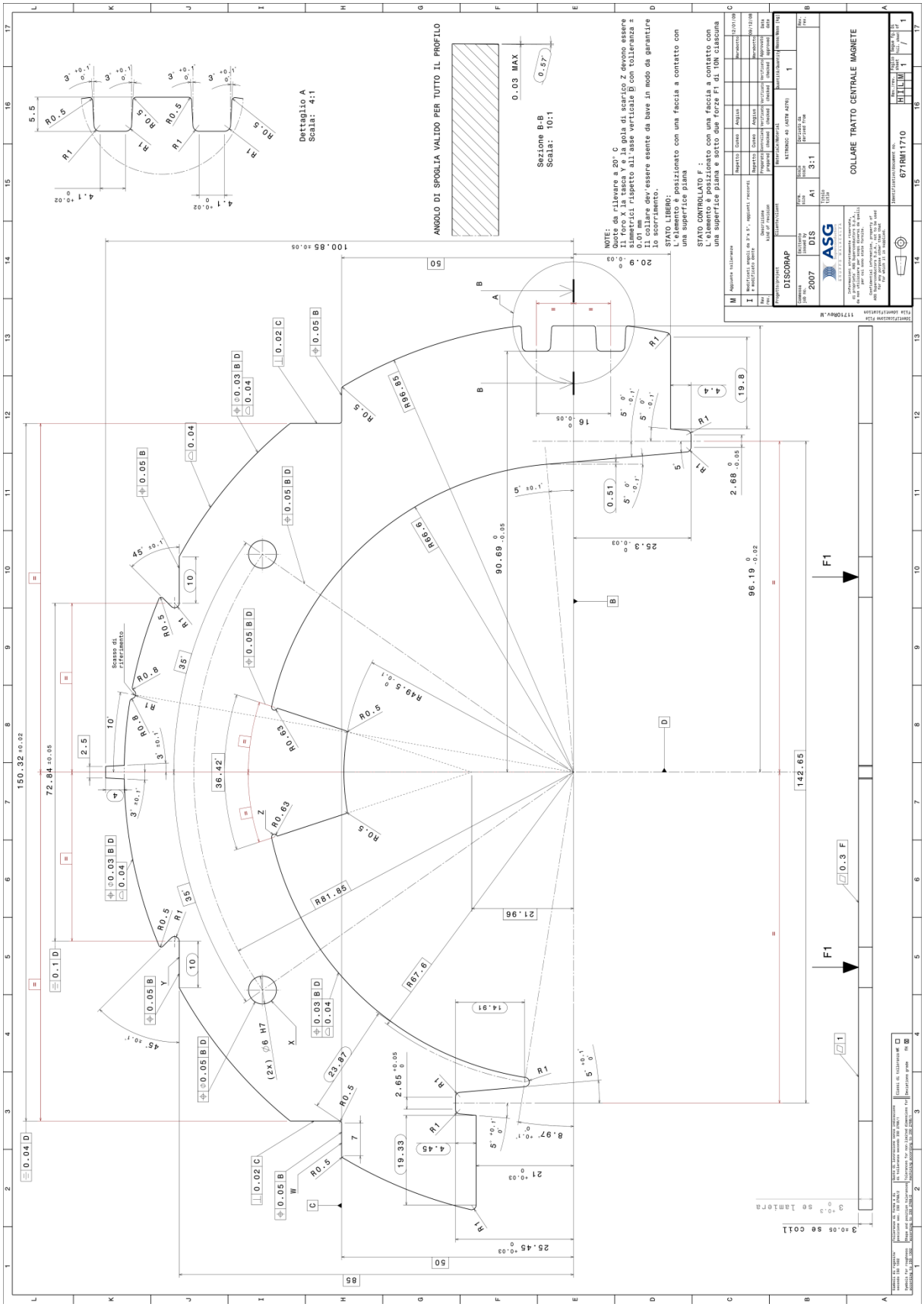

FIG.103: Collar lamination dimensions.

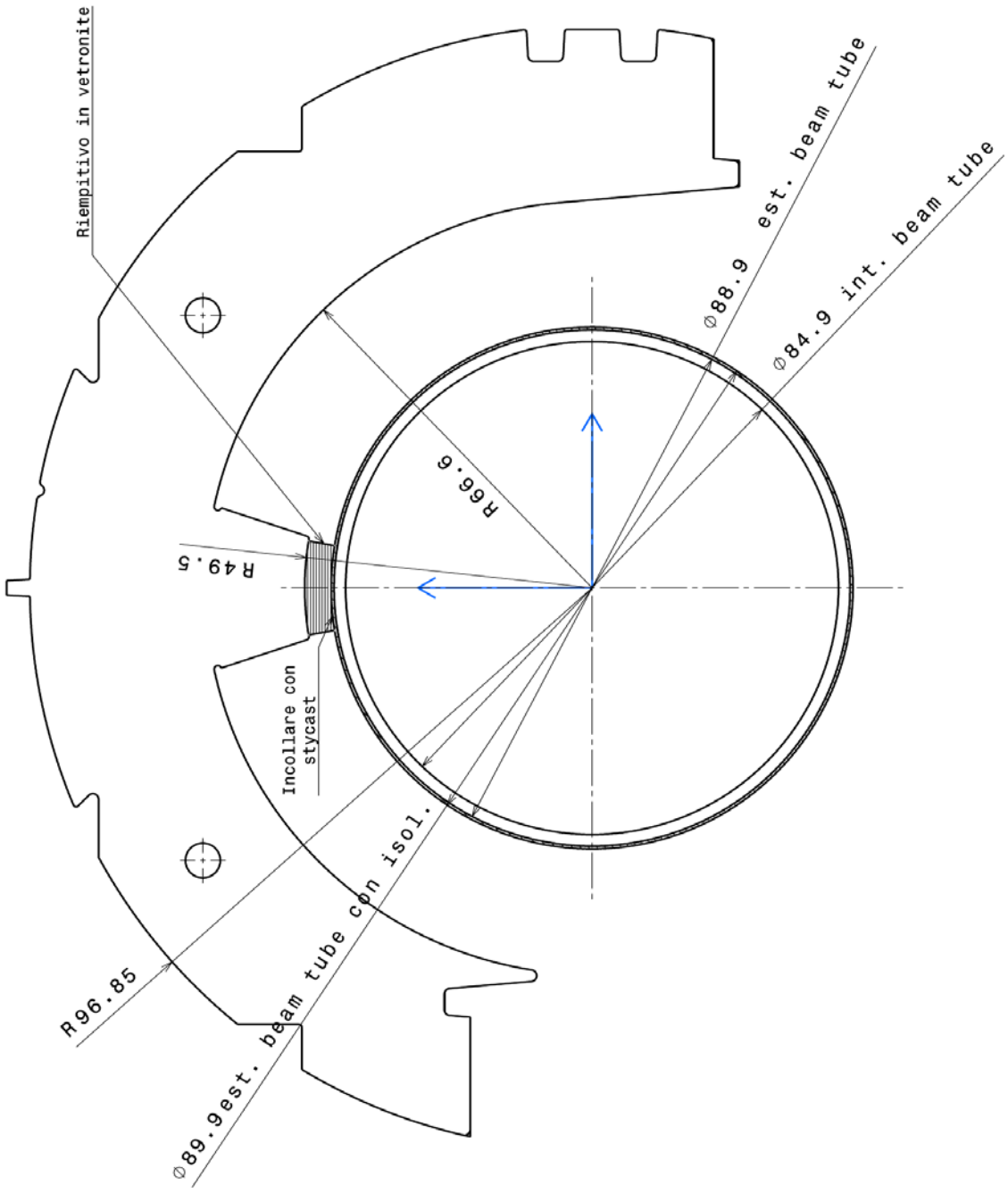

FIG.104: How the beam pipe is supported by the collars.

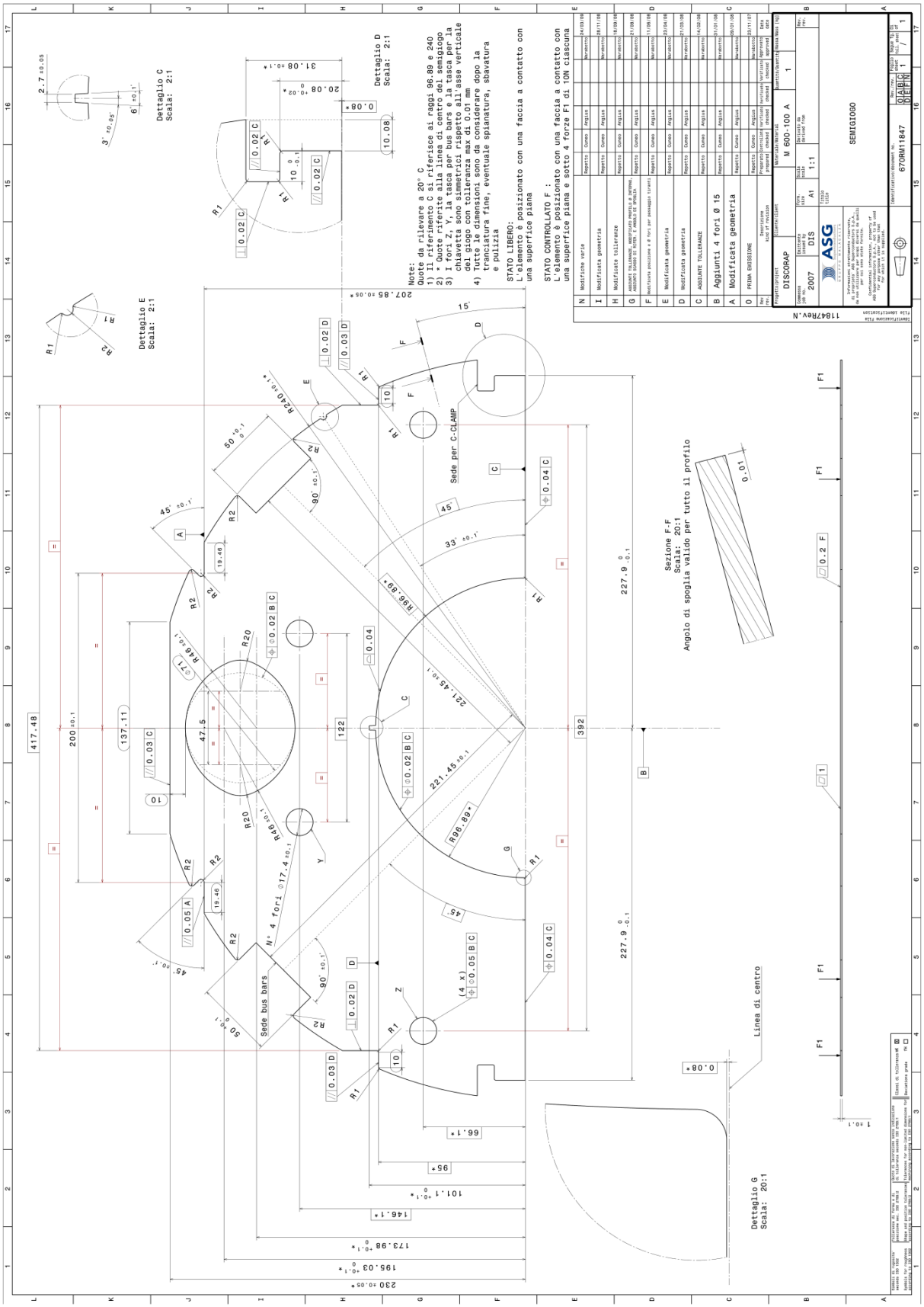

FIG.105: Iron yoke lamination dimensions.

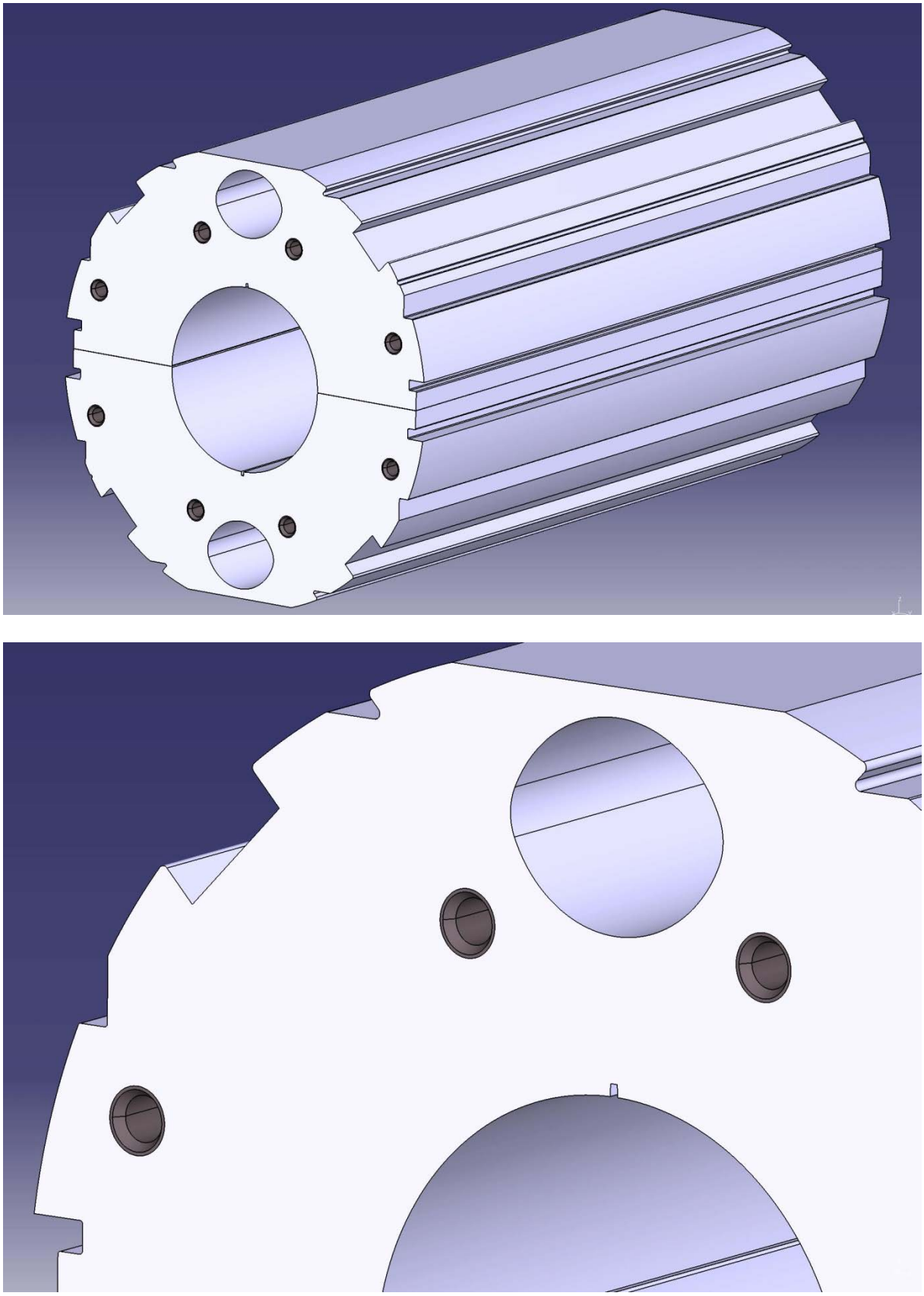

FIG.106: One meter long yoke sector (top); a detail of the lamination connection through stainless steel pipes (bottom).

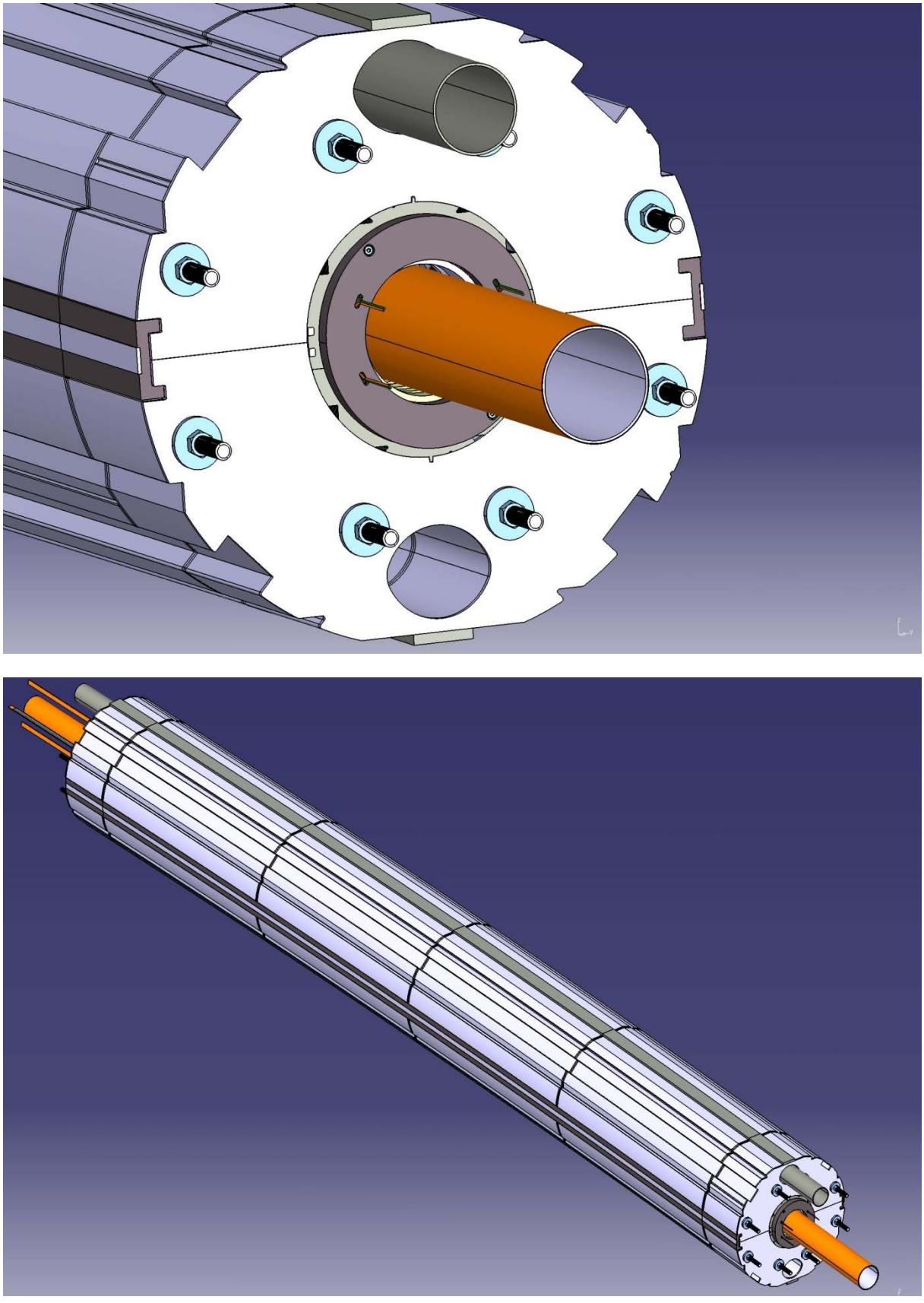

FIG.107: A 3D view of the collared coil enclosed in the yoke (an enlargement is shown in the top figure).

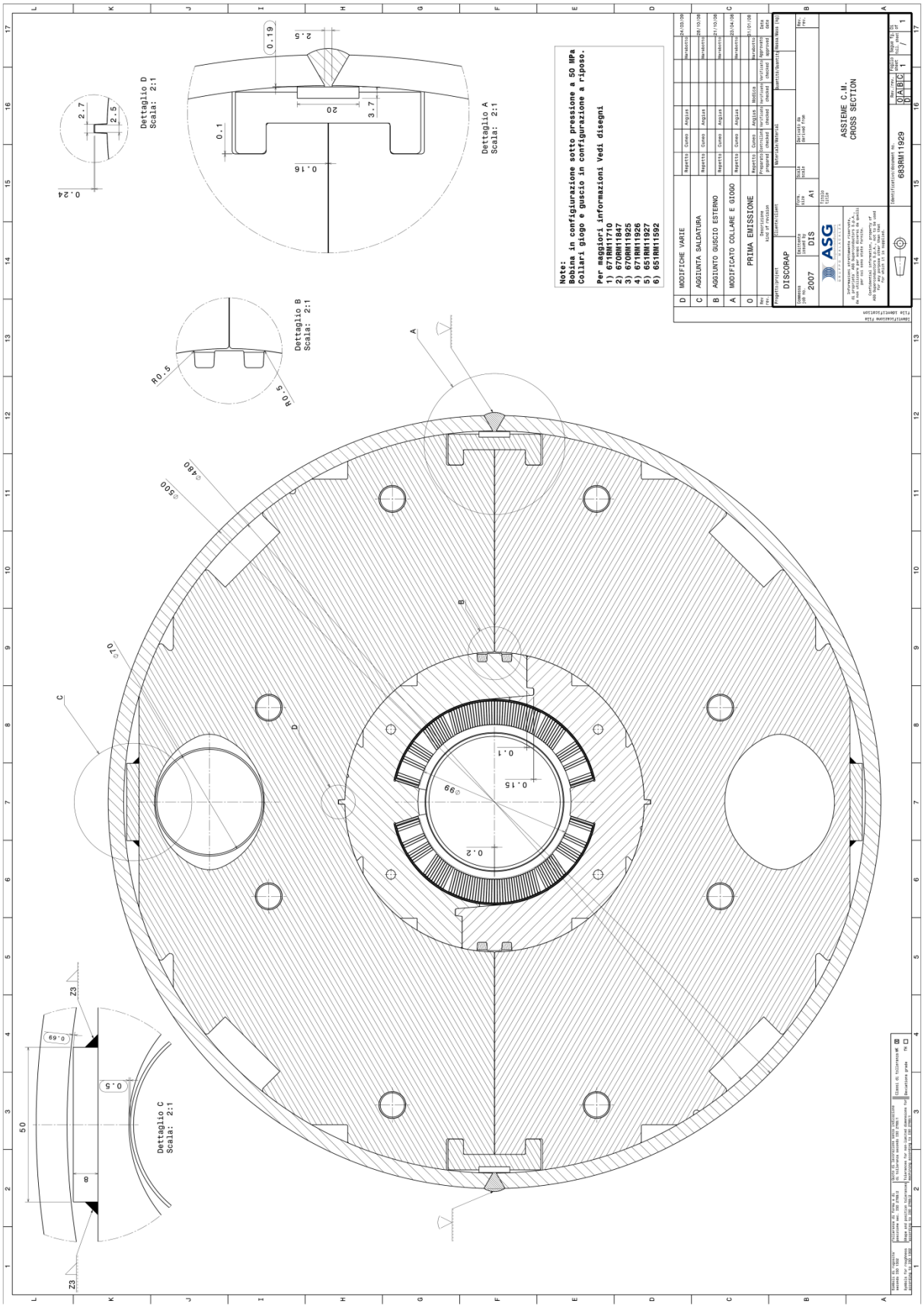

FIG.108: Cross section of the cold mass.

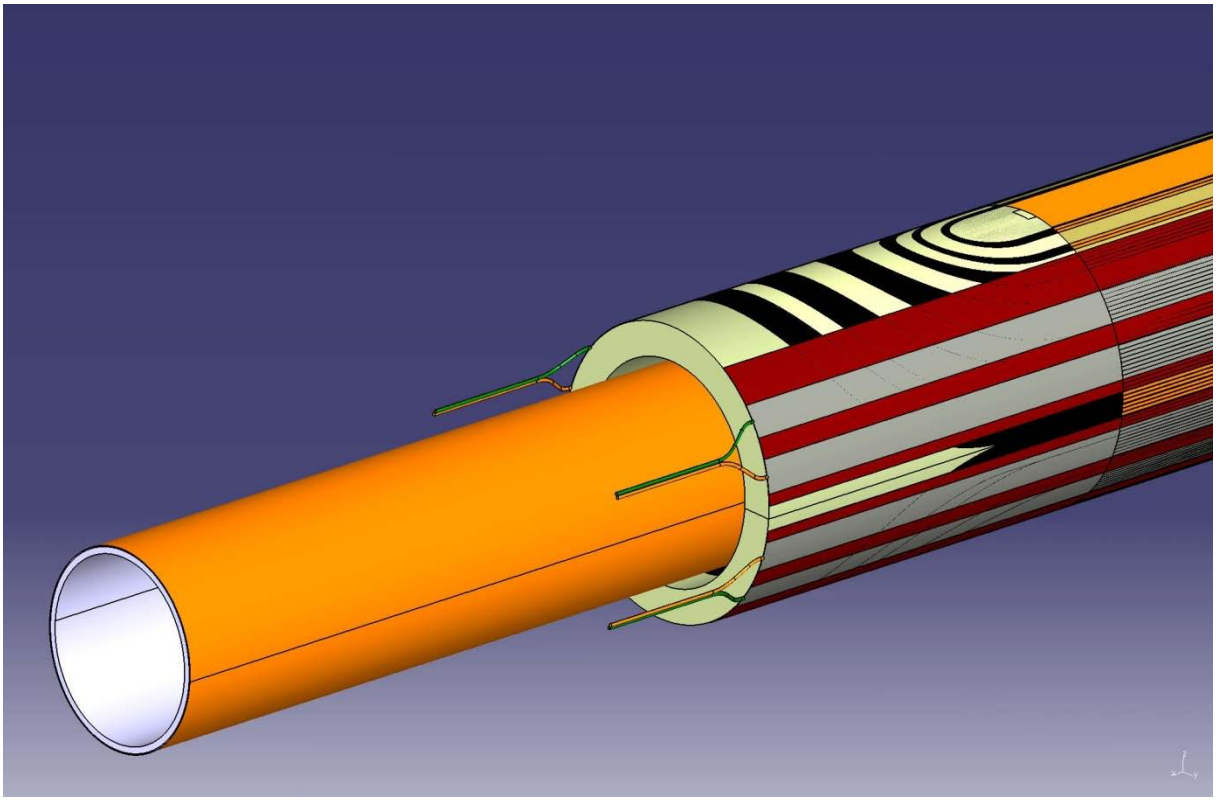

FIG.109: Coil end (the quench heaters are shown as well).

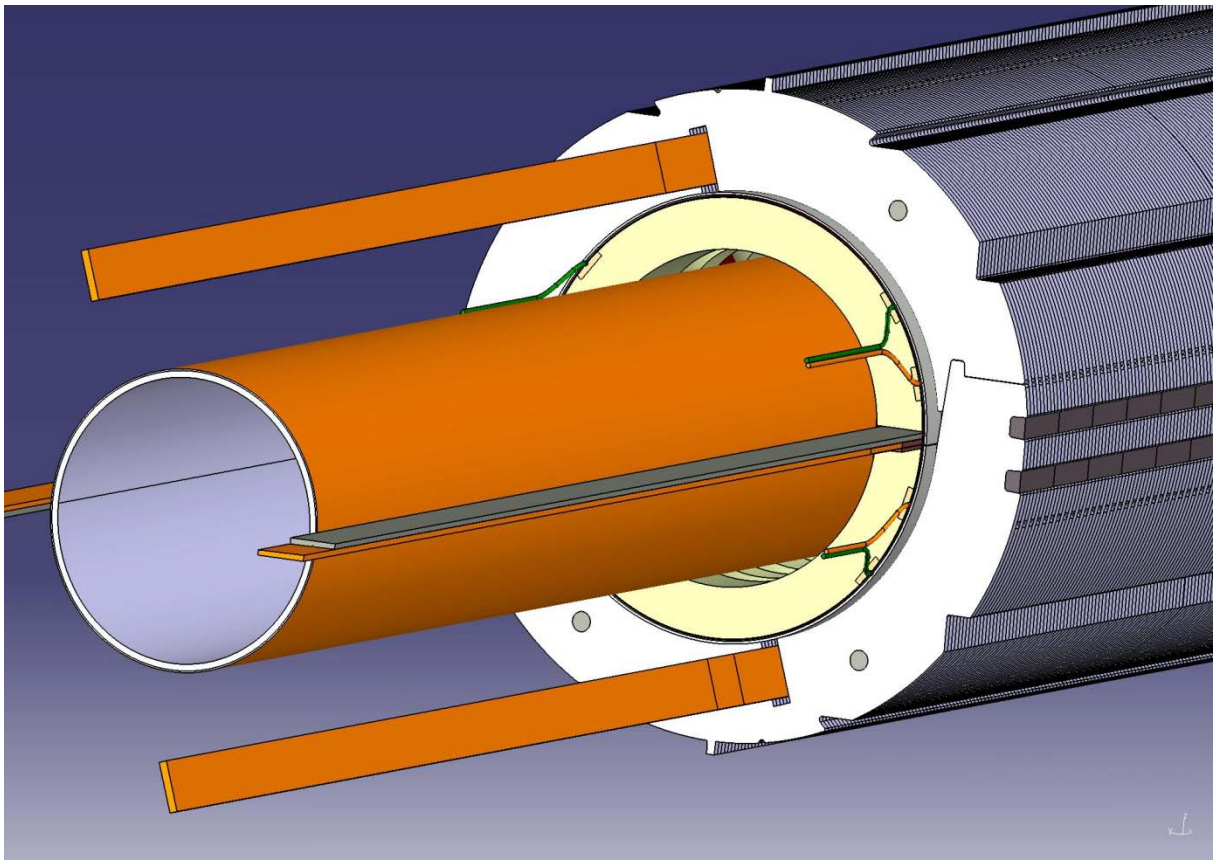

FIG.110: Collared coil end.

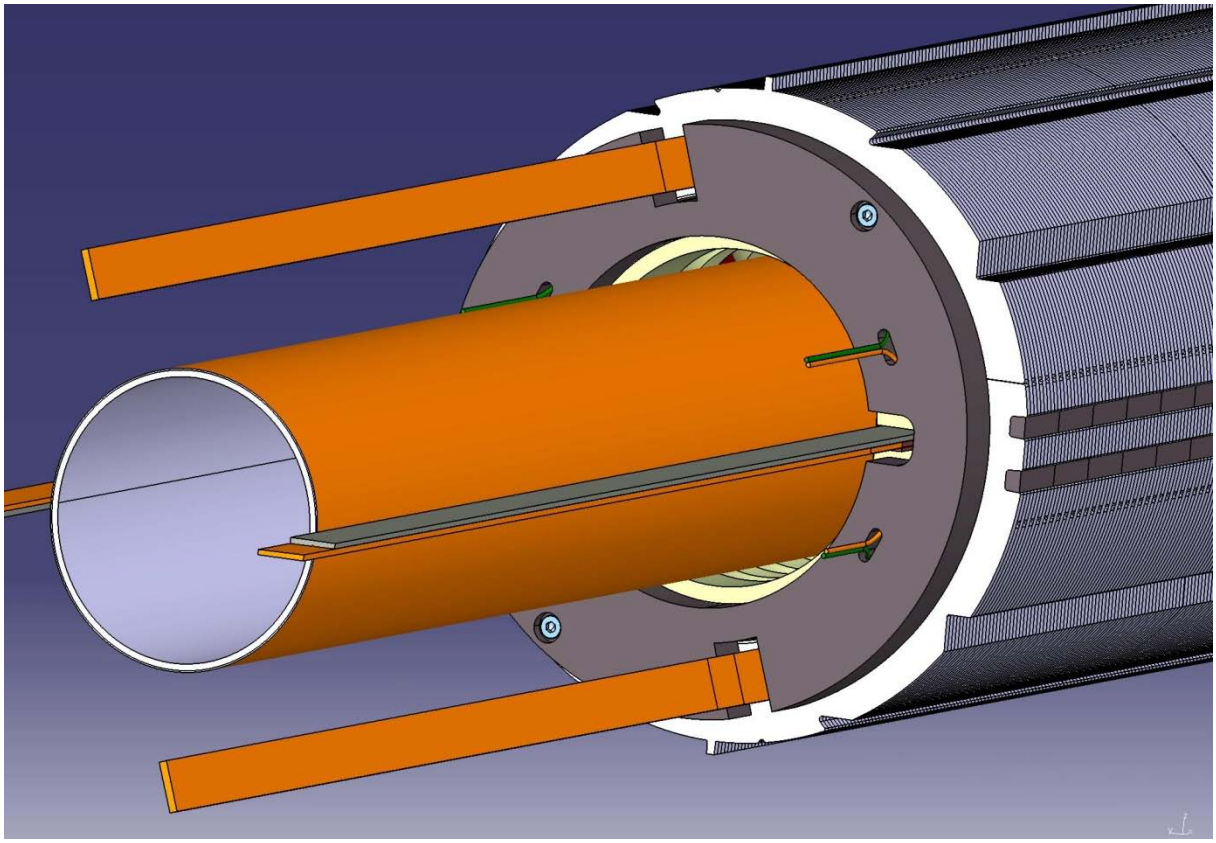

FIG.111: Finished coil end.

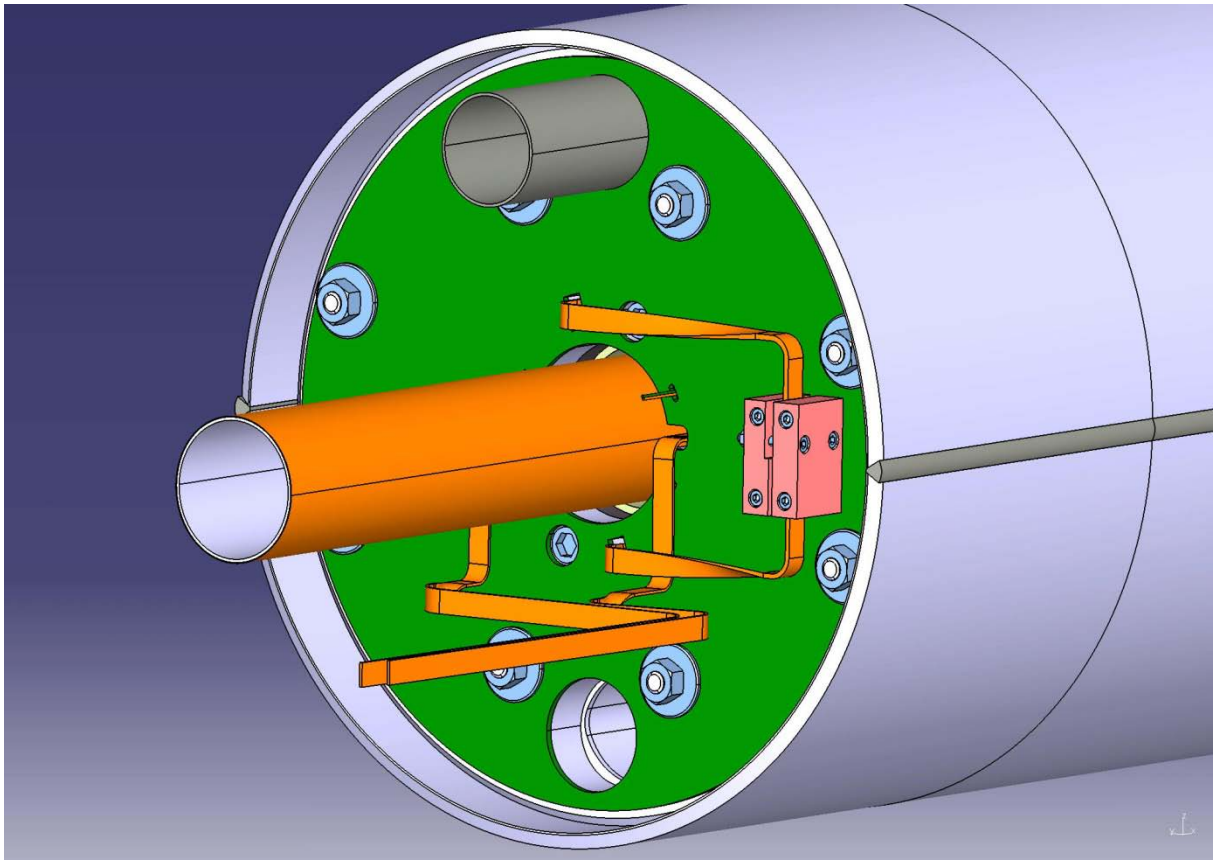

FIG.112: Conceptual scheme of the electrical exits.

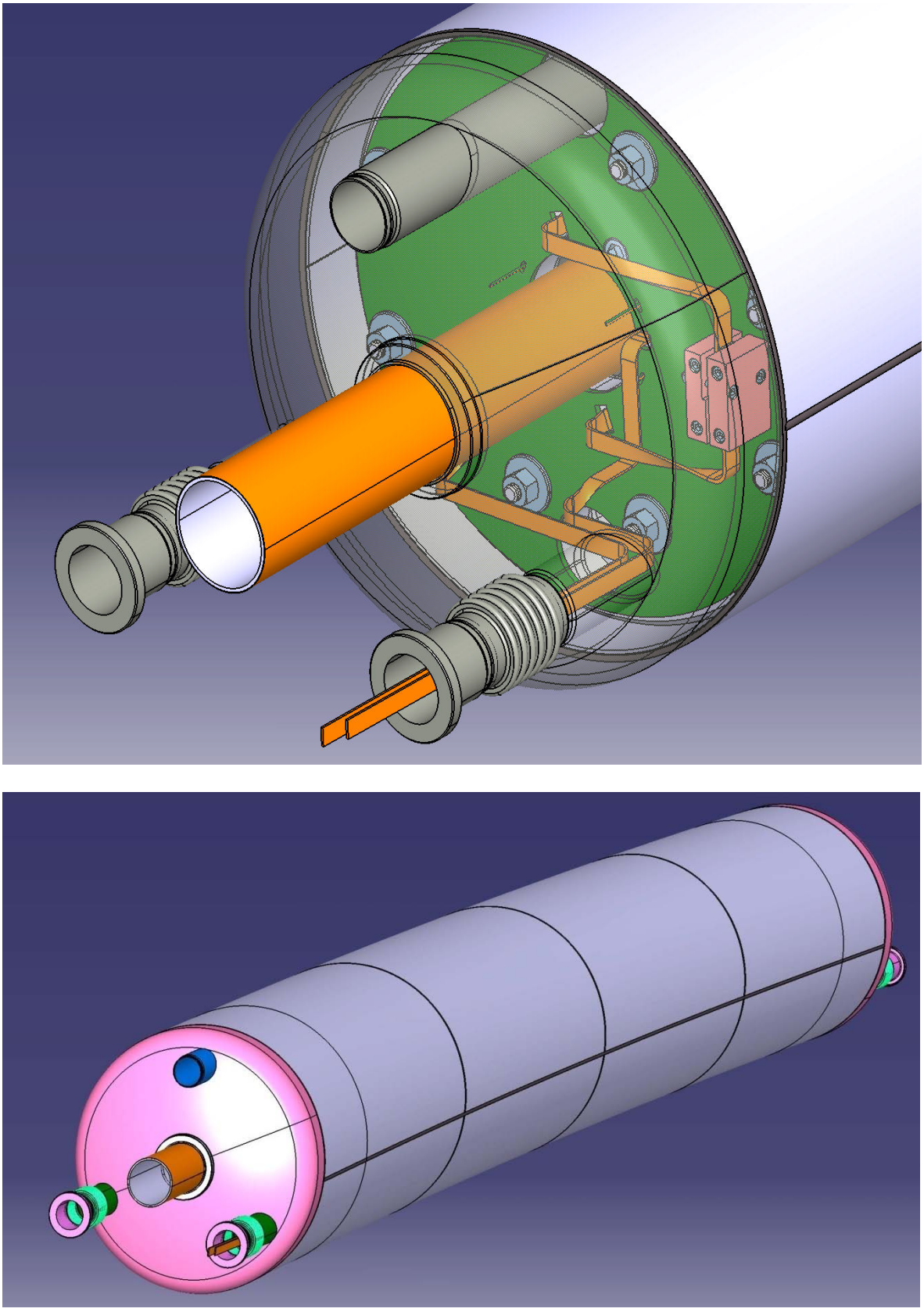

FIG.113: The finished cold mass (a detail of the extremity is shown in transparency in the top figure).

12. ORGANIZATION, PLANNING AND FUTURE PERSPECTIVES

12.1 The INFN groups

Since 2005 the INFN groups working in applied superconductivity expressed a strong interest in developing the fast cycled superconducting dipole for SIS300.

These groups, located in Frascati, Genova and Milano-LASA, were coming from large commitments in the design and construction of superconducting magnets. In particular:

1 Milano LASA was involved in the following projects: S/C cyclotron, LHC dipole developments, wire characterizations. Recently this laboratory was in charge of the construction of the coils of ATLAS barrel (coil+thermal shield).

2 Genova was involved in BaBAR coil design and construction for SLAC, cable characterization, magnetic measurements. Recently this laboratory was in charge of design and construction of CMS cold mass.

3 In Laboratori di Frascati there is an expertise on magnetic characterization of S/C wires and cryogenics.

These groups sat the DISCORAP collaboration, which defined the target of the R&D activity, proposed a scheme and applied for fund to the INFN committee for strategic developments in New Accelerator Technologies. In 2006, preliminary investigations were performed. The DISCORAP activity started in 2007 after a formal agreement between INFN and GSI-FAIR formalized through the signature of a Memorandum of Understanding on December 2006. On the basis of this agreement part of the program was also funded by GSI-FAIR (about 20% of the costs excluding personnel costs).

12.2 Planning

The scheme of DISCORAP R&D program is shown in Fig. 114, whilst a more detailed GANTT chart is shown in Fig.115. It develops in a time period of 5 years. After the preliminary activities performed in 2006, the program is being carrying out through two parallel developments: the conductor development and the model construction. In 2009 the two lines will converge since the developed conductor will be used for the model construction.

In the summer 2008 the design activities (Conceptual and engineering designs) were almost concluded as well as the winding test in the industry. Just the result of these activities is reported in this Technical Design Report, who is the basis for the manufacture of the model. Here we remark that for Conceptual Design we mean complete development of the concept of the cold mass including all basic choices supported by computations. For Engineering Design we mean the set of engineering drawings and engineering reports covering the whole cold mass design issues: geometrical and electrical layout, winding procedures, collaring and implementation of the iron yoke, interfaces with the cryostat. The cold mass is foreseen to be ready in the half of 2009. It will be not immediately integrated into the horizontal cryostat, but a functional test in bi-phase LHe (in a vertical cryostat) will be performed: cycles to the nominal at the proper ramp rate will be done, for checking if major problems are.

After this preliminary test, the cold mass will be integrated into the horizontal cryostat and delivered to GSI for final tests in the horizontal cryostat with supercritical helium.

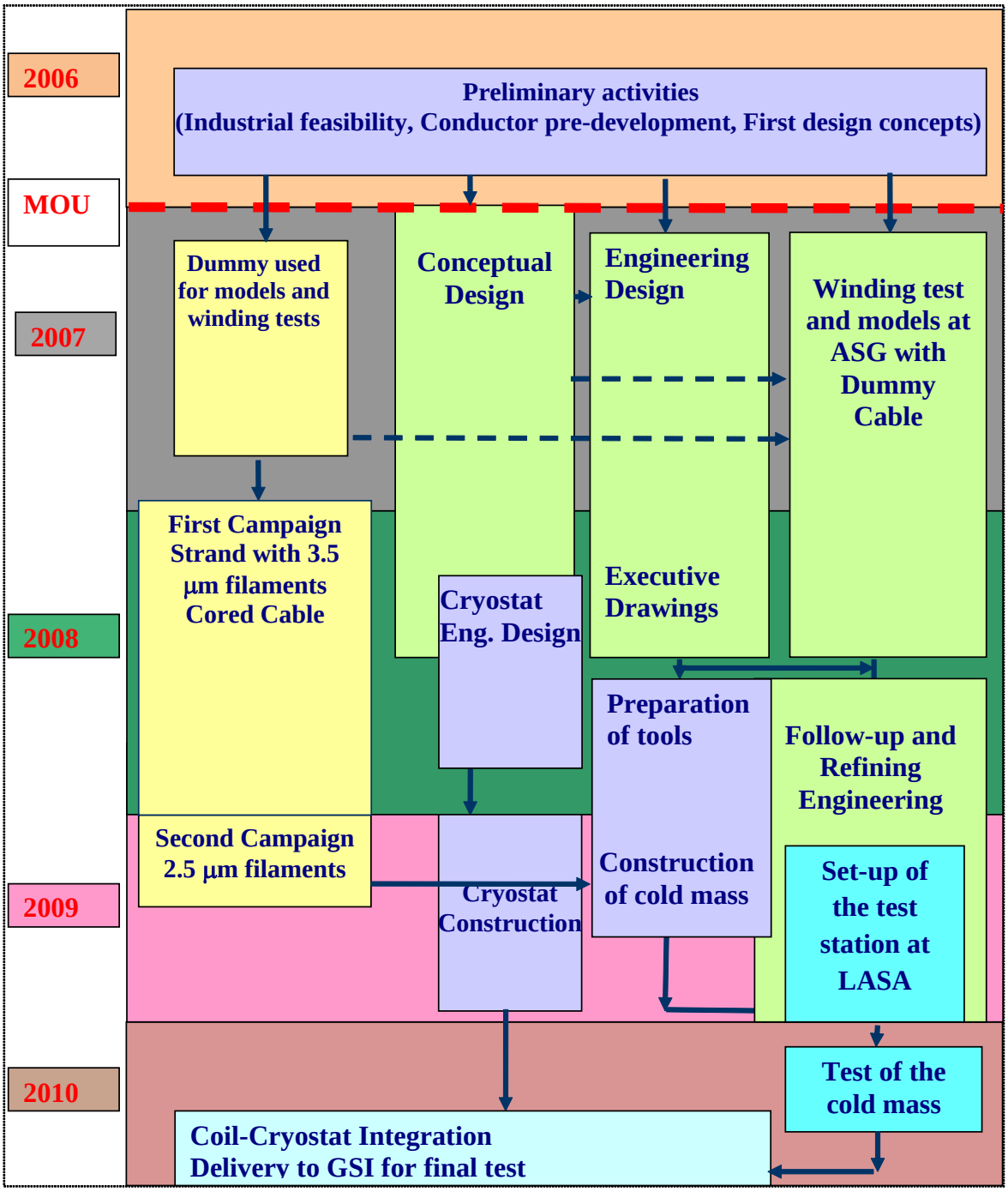

FIG.114: The scheme of DISCORAP R&D activities. The different activities are grouped with different colors. In yellow the conductor developments; in green the design and industrial R&D activities, in violet the construction activities and in light blue the test activities.

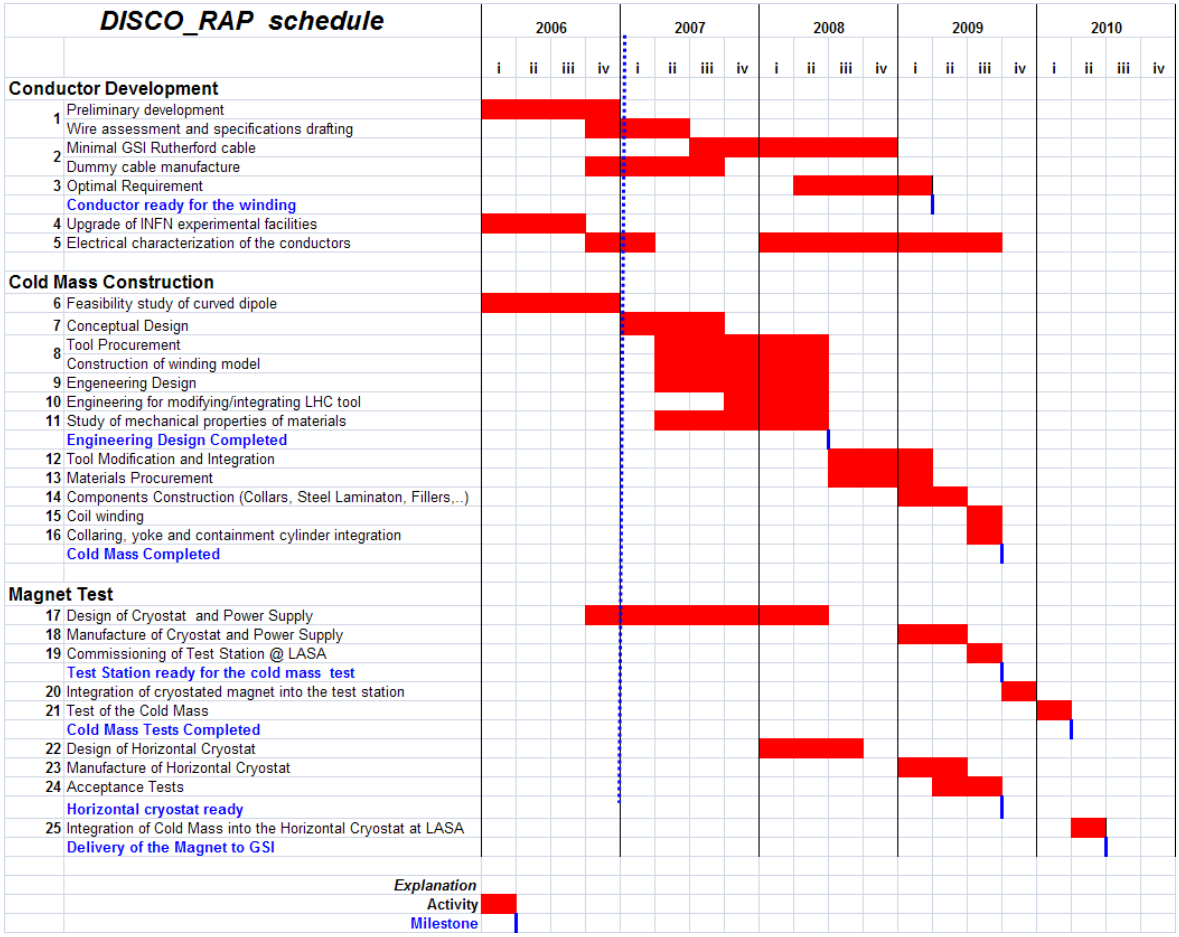

FIG.115: The GANTT chart of the DISCORAP R&D.

12.3 Future activities

In Fig.114 it can be seen that in 2009 design activities still will be going on. These activities will be related to some critical areas of the project, for which a temporary choice was done with the aim to define the model to be built, but which require further reflection. We refer in particular to the 3D analysis (e.g. the axial pre- stress was determined on the basis of a preliminary analysis) that require very long time, fatigue analysis and studies of heat transfer (which could lead to identify a different type of insulation for future developments). At the same time it is common experience that the objects under development undergo changes during construction for various reasons (unavailability of materials, constructive solutions differ from those assumed, ..), requiring further design efforts. The rationale of past, present and future activities can be represented through the scheme showed in Fig.116.

The design and test phase leading to the TDR, will be followed by construction and test activities supported by design activities. At the end of this process the information is complete and a final document will be issued. This document will be the Technical Design Report for the SIS300 dipoles and should be the starting point for the construction of prototypes.

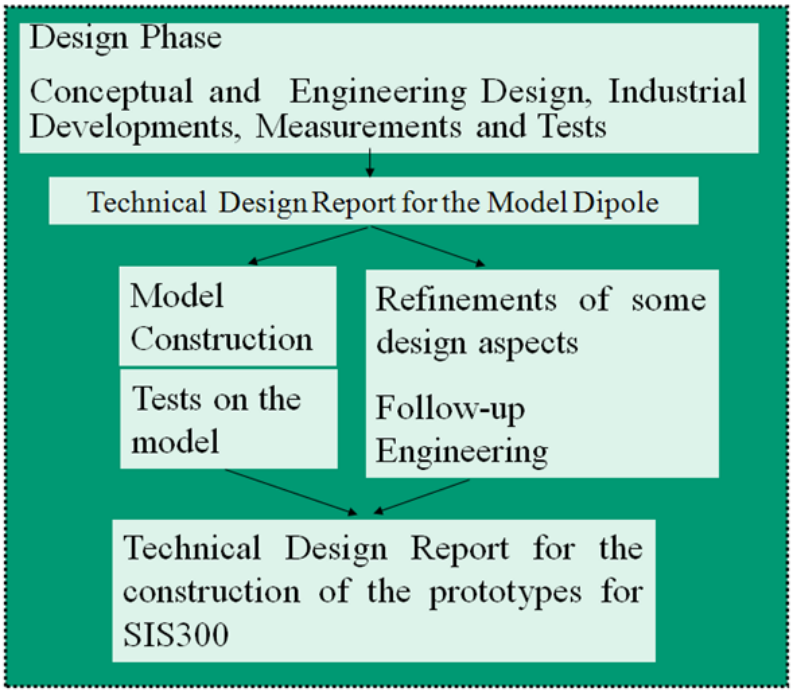

FIG.116: Synopsis of R&D DISCORAP.

Of course what will happen after the issuing of the final TDR is out of the purpose of the R&D. We could aspect that a certain number of magnets should be constructed and tested before a real pre-series and the mass productions.

13. APPENDIX A: BASIC CONSIDERATION FOR SELECTING LAMINATED STEEL

In this section we provide the arguments leading to the choice of the electrical steel of the yoke. After a brief introduction to the steel standards, the basic formulae used in the paper for the losses calculation, are summarized. Then, these formulae are used to separate the contribution to losses due to the magnetic hysteresis from the contribution due to dynamic effects (eddy currents and anomalous effects) for the laminated sheaths commercially available.

13.1 Commercial steel plates

Table 30 shows the standards for typical silicon steels used in magnetic applications. Looking at the standard EN 10106, we can see two numbers and two letters. As an example M300-50A means that it is a magnetic steel (letter M), dissipating 3.00 W/kg at 50 Hz and B oscillating between -1.5 T and + 1.5 T, the thickness is 0.5 mm of not oriented grains (letter A). For application in DISCORAP dipole we need a low loss steel when operating in low frequency conditions. In fact, in our case the field is cycled at 1T/s; in the standards discussed before the average field rate is 300 T/s. We will show that at the field rate of our interest only the hysteretic losses give a significant contribution, while the frequency depending losses are negligible. This means that we need to extract the information about the hysteretic losses for comparing different laminations and make a choice. This can be better understood looking at Fig.117 showing a typical commercial data sheath (in this case from Cogent) for the laminated electrical steel classified according the standard EN10106. The technical information provided by the vendors is quite limited. In particular we have no information how the losses are shared by hysteretic and dynamic effects. A lamination classified as M250-50A at 50 Hz has a loss of 40% with respect the one of M600-100A. But, when considering only the hysteretic contribution the situation can drastically change. It is not a case that just these two examples came into consideration; the M250-50A is the low loss lamination chosen by IHEP when developing the 6T straight option for SIS300 dipoles, the M600-100 is the lamination we considered because its large thickness. In our case the geometrical curvature imposes a simplification of the structures: we believe that the assembling in a curved shape of 1 mm thick lamination is considerably simpler than assembling a 0.5 mm thick lamination.

TAB.30: Typical standards for laminated electrical steel.

IEC 404-8-4 (1998)	EN10106 (2007)	AISI	ASTM A677 (2005)	JIS 2552 (2000)	GOST 2142.2 (1983)
250-35-A5	M250-35A	M15	36F145	35A250	2413
270-35-A5	M270-35A	M19	36F158	35A270	2412
300-35-A5	M300-35A	M22	36F168	35A300	2411
350-50-A5	M330-50-A	M36	47F205	50A350	2411

SURA® Grade	Thickness	Max specific total loss		Minimum magnetic polarization			Conventional density
		$\hat{J}$=1,5 T	1,0T*	Ĥ=2500	5000	10000 A/m	
	mm	W/kg	W/kg	T	T	T	kg/dm³
M210-27A	0,27	2,10	0,85	1,49	1,60	1,70	7,60
M235-35A	0,35	2,35	0,95	1,49	1,60	1,70	7,60
M250-35A	0,35	2,50	1,00	1,49	1,60	1,70	7,60
M270-35A	0,35	2,70	1,10	1,49	1,60	1,70	7,65
M300-35A	0,35	3,00	1,20	1,49	1,60	1,70	7,65
M330-35A	0,35	3,30	1,30	1,49	1,60	1,70	7,65
M700-35A	0,35	7,00	3,00	1,60	1,69	1,77	7,80
M250-50A	0,50	2,50	1,05	1,49	1,60	1,70	7,60
M270-50A	0,50	2,70	1,10	1,49	1,60	1,70	7,60
M290-50A	0,50	2,90	1,15	1,49	1,60	1,70	7,60
M310-50A	0,50	3,10	1,25	1,49	1,60	1,70	7,65
M330-50A	0,50	3,30	1,35	1,49	1,60	1,70	7,65
M350-50A	0,50	3,50	1,50	1,50	1,60	1,70	7,65
M400-50A	0,50	4,00	1,70	1,53	1,63	1,73	7,70
M470-50A	0,50	4,70	2,00	1,54	1,64	1,74	7,70
M530-50A	0,50	5,30	2,30	1,56	1,65	1,75	7,70
M530-50HP	0,50	5,30	2,30	1,63	1,71	1,81	7,80
M600-50A	0,50	6,00	2,60	1,57	1,66	1,76	7,75
M700-50A	0,50	7,00	3,00	1,60	1,69	1,77	7,80
M800-50A	0,50	8,00	3,60	1,60	1,70	1,78	7,80
M940-50A	0,50	9,40	4,20	1,62	1,72	1,81	7,85
M310-65A	0,65	3,10	1,25	1,49	1,60	1,70	7,60
M330-65A	0,65	3,30	1,35	1,49	1,60	1,70	7,60
M350-65A	0,65	3,50	1,50	1,49	1,60	1,70	7,60
M400-65A	0,65	4,00	1,70	1,52	1,62	1,72	7,65
M470-65A	0,65	4,70	2,00	1,53	1,63	1,73	7,65
M530-65A	0,65	5,30	2,30	1,54	1,64	1,74	7,70
M600-65A	0,65	6,00	2,60	1,56	1,66	1,76	7,75
M600-65HP	0,65	6,00	2,60	1,63	1,72	1,82	7,80
M700-65A	0,65	7,00	3,00	1,57	1,67	1,76	7,75
M800-65A	0,65	8,00	3,60	1,60	1,70	1,78	7,80
M1000-65A	0,65	10,00	4,40	1,61	1,71	1,80	7,80
M600-100A	1,00	6,00	2,60	1,53	1,63	1,72	7,60
M700-100A	1,00	7,00	3,00	1,54	1,64	1,73	7,65
M800-100A	1,00	8,00	3,60	1,56	1,66	1,75	7,70
M1000-100A	1,00	10,00	4,40	1,58	1,68	1,76	7,80

FIG.117: Electrical steel commercially available (by Cogent in this case) classified according EN10106.

13.2 Basic formulae for the losses

Let us consider an electrical steel plates placed in an oscillating magnetic field $B = B_{\max}\cos(\omega t)$. There are three different types of losses:

Hysteretic losses. These losses can be written as the close integral of the magnetic field H with respect the magnetic induction B:

$$E_H\left[J/m^3\right]=\oint HdB \tag{36}$$

Considering a cycle leading the magnetic field beyond the saturation, we can approximate the maximum loss as:

$$E_{H\cdot MAX}\left[J/m^3\right]=4kH_c B_{sat} \tag{37}$$

where H_c is the coercitive field, B_{sat} the saturation field and k is a constant depending on the lamination. For field lower than the saturation one, we can use the Steinmertz's equation

$$E_H\left[J/m^3\right]=\eta B_{\max}^{\alpha} \tag{38}$$

where the constant η and α depend on the material properties. We have used α=1.6, while η has been found equating the two relations for the losses: $\eta = 4H_c B_{sat}^{1-1.6}$. The hysteretic losses are then calculated using:

$$E_H\left[J/m^3 \text{ cycle}\right]=4kH_c B_{sat}^{-0.4} B_{\max}^{1.6} \tag{39}$$

As seen before, for commercial plates the losses are given in W/kg at f=50 Hz and for B_{max}=1.5 T. The formula to be used is then:

$$W_H\left[W/kg\right]=4kH_c B_{sat}^{-0.4} B_{\max}^{1.6} * f/\delta = 4kH_c B_{sat}^{-0.4} B_{\max}^{1.6} * 50/7800 \tag{40}$$

where we have multiplied the energy density by the frequency f and divided by the specific weight δ.

Eddy currents losses. These losses for plates of thickness d, placed in an oscillating field parallel to the plate, are given by

$$E_E\left[J/m^3 cycle\right]=\frac{d^2}{12\rho}\int_0^T\left(\frac{dB}{dt}\right)^2 dt=\frac{d^2}{12\rho}\omega B_{\max}^2\pi \tag{41}$$

The average power is then:

$$W_E\left[W/m^3\right]=\frac{d^2}{24\rho}\omega^2 B_{\max}^2=\frac{d^2}{24\rho}(2\pi f)^2 B_{\max}^2 \tag{42}$$

or in W/kg

$$W_E\left[W/kg\right]=\frac{d^2}{24\rho\delta}(2\pi f)^2 B_{\max}^2 \tag{43}$$

Anomalous losses. These losses are given by:

$$E_A\left[J/m^3 cycle\right]=\sqrt{\frac{GV_0S}{\rho}}\int_0^T\left|\frac{dB}{dt}\right|^{1.5} dt = 8.73\sqrt{\frac{GV_0S}{\rho}} f^{0.5} B_{\max}^{1.5} \tag{44}$$

and consequently the average power

$$W_A\left[W/m^3\right]=8.73\sqrt{\frac{GV_0S}{\rho}} f^{1.5} B_{\max}^{1.5} \quad \text{or} \quad W_A\left[W/kg\right]=\frac{8.73}{\delta}\sqrt{\frac{GV_0S}{\rho}} f^{1.5} B_{\max}^{1.5} \tag{45}$$

In these expressions S is the plate cross section normal to the magnetic field, while G and V_0 are two parameters related respectively to the friction between the magnetic objects (a structure of domain walls) and to the field dependence of the number of active magnetic objects. These losses are difficult to evaluate. In the next sections we can see how this information is obtained from the knowledge of the total losses.

13.3 Analysis of losses in commercial steel plates

We can use the above relations (40), (43) and (45) and separate the different contributions to losses for commercial steel plate. We applied this method to steel laminations for which we had enough information[33),35),47)] as reported in Table 31. We remark here two points: a) the data on material have some fluctuations; b) the information related to the magnetic hysteresis is rarely available. These steel laminations were taken into consideration because they are classical low losses laminations. Our method consisted in calculating the ac losses, in the conditions defined by the standards, coming from magnetic hysteresis (setting k=1) and eddy currents. The anomalous contribution is calculated by subtracting these contributions to the total losses.

Applying our formulae, we found the results shown in Table 32, where the values of the parameters used for the computations are also reported. Many considerations can be drawn from Tables 31 and 32:

1) In DISCORAP magnet the equivalent frequency is 0.056 Hz (a hypothetic field cycle 0 to - 4.5 T to+ 4.5 T and finally to 0 would be performed in 18 s). According to the formulae (40), (43) and (45), the losses will scale as f, f^2 and $f^{1.5}$. Starting from the values shown in Table 32 the eddy current and anomalous losses at 0.056 Hz are negligible with respect to the hysteretic losses.
2) The hysteretic losses are proportional to the coercitive field. If we want a low loss magnet we have to choice a lamination with low H_c, without reducing too much the saturation field.
3) The calculated magnetic hysteretic losses are 65% to 70% of the ones (the average values) declared by providers. When computing the losses with equation (40), one should apply a suitable correcting factor (1.4 to 1.5) to the calculated hysteretic losses.

TAB.31: Material data as a result from commercial information.

Type	H_c(A/m)	ρ (μΩ·m)	B_{sat} (T)	Si content (%)	Hysteretic losses (W/kg)
M250-50A	29-32	0.59-0.61	1.95	3.2	1.45-1.60
M350-50A	42-50	0.38-0.43	2.04	2.4	1.95-2.28
M350-65A	34-40	0.42-0.52	1.98	3.0	1.57-1.84
M600-100A	30-40	0.44-0.50	2.00	3.1	1.48-1.97

TAB.32: Loss computation for the lamination of Table 31 at 50 Hz and ±1.5 T with average data. (This table has only a comparative meaning.)

Steel	H_c (A/m)	ρ (μ·Ωm)	B_{sat} (T)	Hysteretic (with k=1) (W/kg)	Eddy Currents (W/kg)	Anomalous (W/kg)
M250-50A	30	0.60	1.95	1.01	0.52	0.97
M350-50A	47	0.40	2.04	1.54	0.76	1.20
M350-65A	37	0.47	1.98	1.23	1.09	1.18
M600-100A	35	0.47	2.00	1.15	2.69	2.16

4) From the magnetic hysteretic loss point of view the best lamination (among the ones in Table 31) would be the M250-50A. Nevertheless, as already remarked, M600-100A has the advantages of a double thickness (so reducing the needed laminations for the magnet of a factor 2) and a higher saturation field. These two advantages compensate the larger loss (12% higher according to data in Table 32).
5) Finally the question could arise, whether other laminations among the ones shown in Fig.117 are more suitable for application in DISCORAP dipole. For 1 mm thickness M600-100A is the best option for the losses (all the other have higher losses). For 0.65 mm thickness, Table 32 shows that M350-65A is equivalent to M600-100A for the hysteretic losses. Better option could be M310-65A and M330-65A. The data for the coercitive field for these two lamination grades are respectively 30 A/m and 40 A/m, so we do not expect a magnetic hysteretic loss significantly lower for M310-65A (since these losses scale linearly with H_c) with respects M600-100A (M330-65 is equivalent to M600-100A). Regarding 0.5 mm lamination, we already remarked our preferences for thicker laminations.

The above considerations shall be viewed as the result of a comparative analysis. In fact for M600-100A we have used information coming from detailed experimental studies performed at IHEP34, as reported in section Hysteretic losses of iron yoke.

14. APPENDIX B: MECHANICAL TESTS

The conductor described in Section Conductor is very similar the one used to wind the outer layer of the LHC dipoles, but with some differences. Among them, the main one from a mechanical point of view is the presence of a 25 μm thick high resistance metallic core in the middle of the Rutherford cable. Mechanical properties of such a conductor cannot be found in literature but have to be measured. For this reason, we have performed a measurement campaign on short straight samples, both stacked and arc piled. Mechanical properties of the first dipole winding tests have also been measured.

All samples have undergone the same polymerization cycle: it is the same curve ASG Superconductors used for the LHC dipoles,[48)] shown in Fig.118, the only difference being the polymerization pressure which, in our case, is 75 MPa.

14.1 Short straight samples

All short samples have been prepared using a dummy conductor made by introducing a 25 μm thick stainless steel foil in the middle of the LHC dipole outer layer conductor. As a consequence, there are two main differences with the final designed conductor:

1. the filaments composing the strands of LHC conductor are thicker, 6 μm instead of nearly 3 μm: this has great influence on the electrical behavior of the conductor, resulting in a reduction of its performances, but no effect on its mechanical properties;
2. the LHC conductor has not the copper-manganese matrix we foreseen for our conductor: this could have some influence on the mechanical properties, in the sense that the real conductor could be somewhat stiffer.

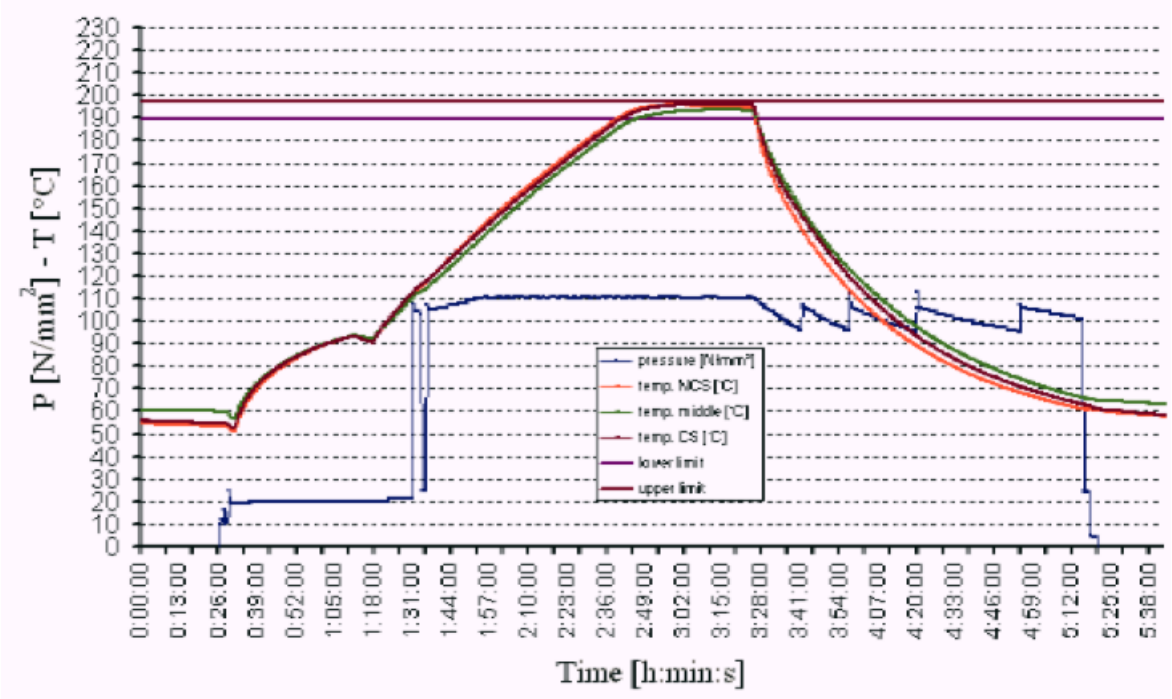

FIG.118: Typical curing cycle for the LHC inner layer.[48)]

We clearly foresee to measure the mechanical properties of the final conductor as soon as it becomes available. In the meanwhile, we operatively work with the mechanical properties coming from the dummy conductor measurements: on one side, we cannot infer how the Cu-Mn matrix would affect the mechanical behavior of the conductor, on the other side, we are convinced that the matrix effect would not be so large to invalidate all the conclusions based on the measured mechanical properties of the dummy conductor.

14.1.1 Stacked samples

The first and simplest approach directed to the understanding of the mechanical behavior of our conductor consists in performing stacking tests. The tool used to assemble and cure the samples is shown in Fig.119. It can host 12 conductors stacked in alternate position in order to cancel the effect of the keystoning, it can be heated through the two heater plugs shown in Fig.119 and the pressure can be applied on the top surface of the tool through an external press. Fig.120 shows the stacked conductors ready to be cured and a cured sample.

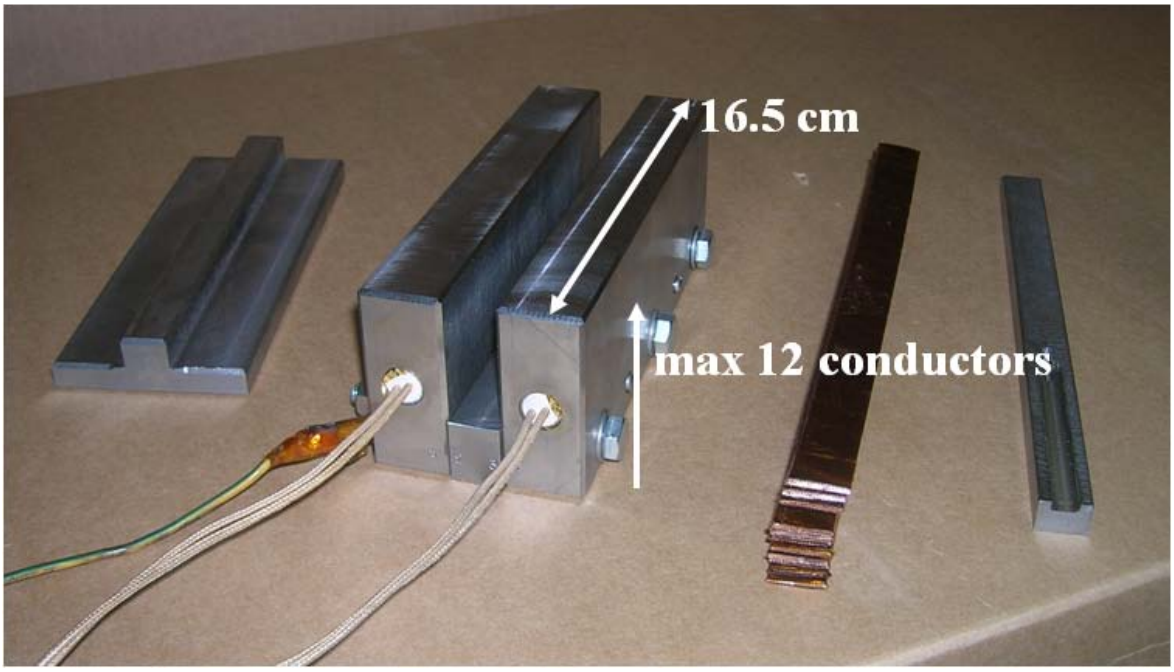

FIG.119: Tool for curing the stacking samples.

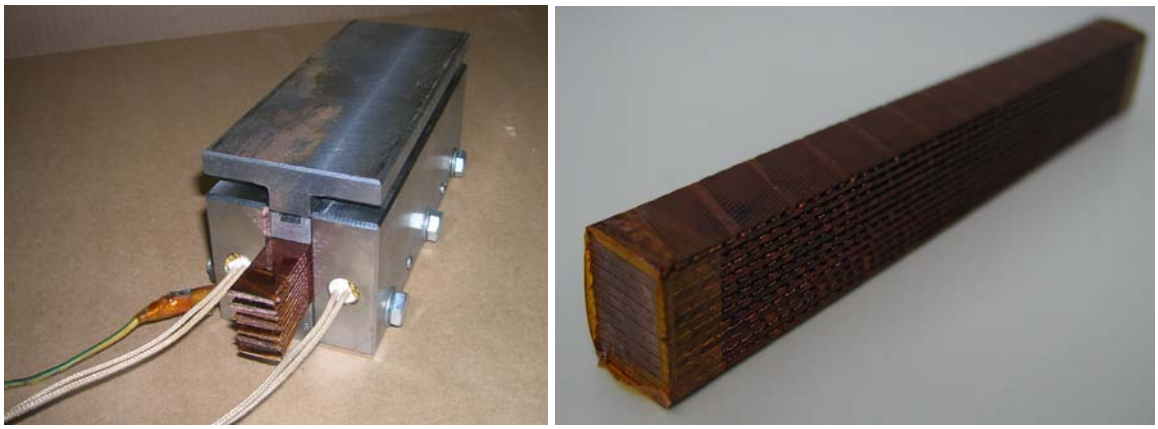

FIG.120: Stacked conductor ready to be cured, on the left, and a cured sample, on the right.

Several measurements have been performed on this kind of samples in different locations: Fig.121 shows a typical stress-strain measurement carried out at ASG Superconductors premises, whilst the measurement in Fig.122 has been carried out at LASA Laboratories in Milan. In both cases the measurement consists in applying an increasing pressure to a sample while measuring its displacement. Once the maximum value of about 80 MPa is reached, the pressure is gradually released. A certain number of these cycles are

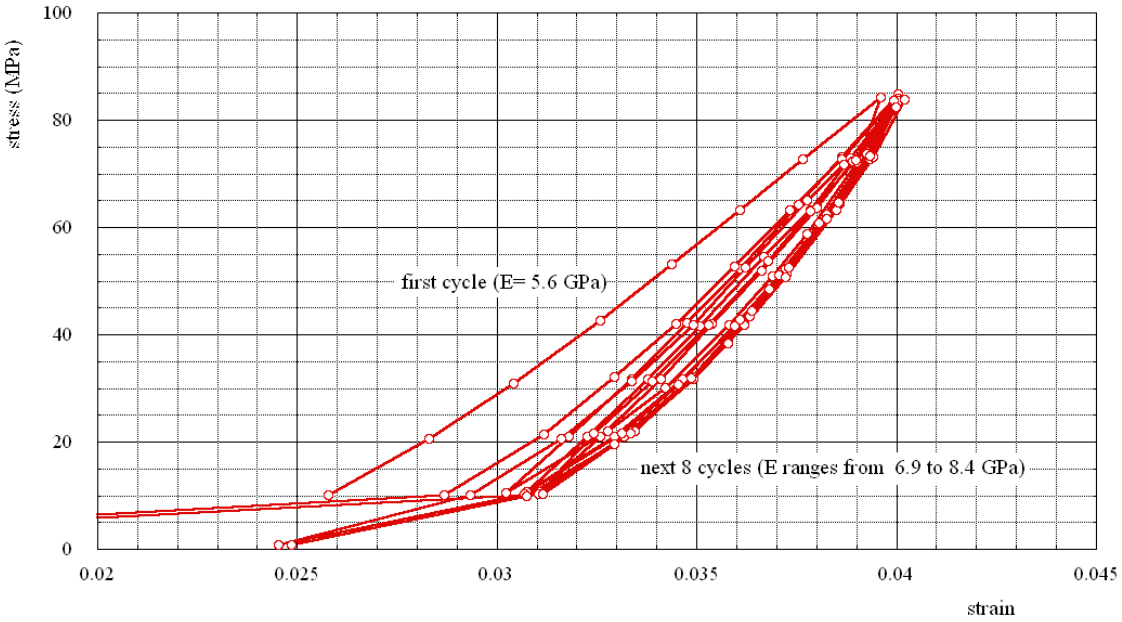

FIG.121: Stress strain measurement performed at ASG-Superconductors on a stacking sample.

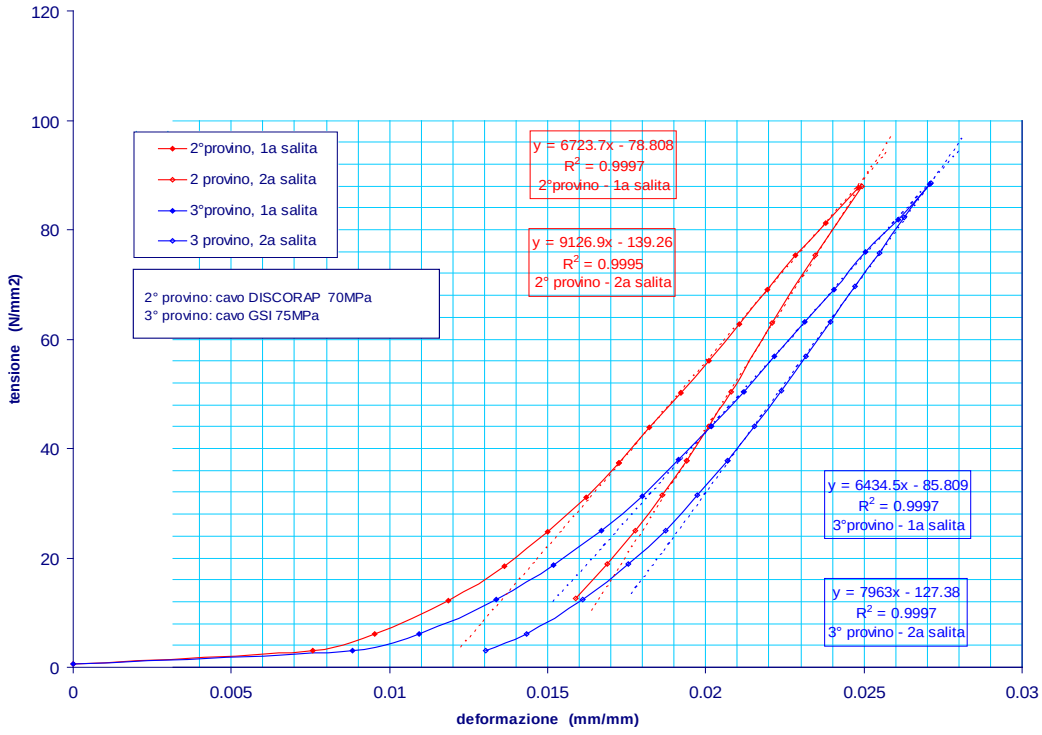

FIG.122: Stress strain measurement performed at LASA Laboratories on a stacking sample.

then completed to investigate the asymptotic behavior of the samples. The Young modulus can be defined as the slope of these curves while applying the pressure. What we found is a Young modulus of about 6-7 GPa for the first cycle, and a range of variation between 7 and 9 GPa for the next cycles. The Young modulus of conductors in the mechanical FE analysis has been chosen to be 8 GPa (see Table 19 in Section Mechanical analyses).

14.1.2 Arc piled samples

The arc piled samples are straight samples, 20 cm long, with the conductors stacked as they would be in the real dipole, by using the real G11 wedges manufactured for the SIS300 dipole. A special structural FE model has been developed to compare the measurements with our modelization of the winding. Fig.124 shows a comparison between the measured displacement-applied force curve and the one obtained through FE analysis with 8 GPa as Young modulus of the winding, where the displacement is the distance of the stainless steel pressing tool to the ideal winding midplane. It clearly emerges that there are two different types of questions: the two curves have different slopes and they are shifted one with respect to the other. The difference in slope can only be accounted for by changing the Young modulus assigned to the winding (the Young modulus of the other materials, wedges, kapton, etc., cannot answer for such a large variation). Changing the Young modulus of the winding up to 11.5 GPa, we obtain the agreement shown in Fig.125. The conductor being a composite material, it not surprising that in different geometrical configurations it can have slightly

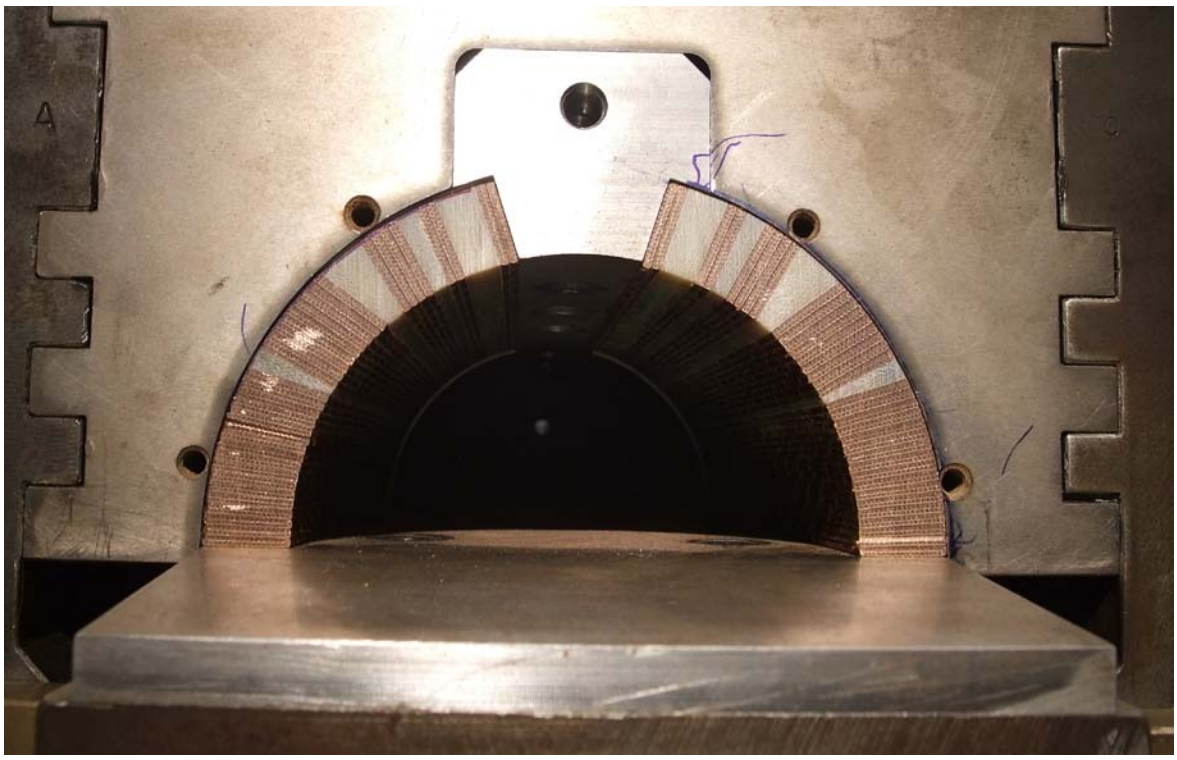

FIG.123: Arc piled sample for stress-strain measurements.

different equivalent properties. It remains unexplained the distance between the two curves, 185 μm, meaning that the real sample is bigger than the FE model. This difference could be due to the tolerances on the coil wedges (see Fig.100), which is 50 μm, leading to 200 μm totally for 4 wedges. Also, the stainless steel core 25 μm thick in the middle of the Rutherford cable could contribute to this difference; actually, in the FE modelization we are using as reference dimensions @ 50 MPa (see Table 6) the ones of the LHC conductor, which has no stainless steel core. The maximum accountable difference in this case is 25 μm × 34 turns = 850 μm. Finally, the tolerance on conductors (6 μm×34 turns = 204 μm) and insulation (7 μm×3 layers×2 sides×34 turns=1428 μm) can play a role in explaining this difference.

Given all the previous considerations, a difference of 185 μm in the dimensions of the

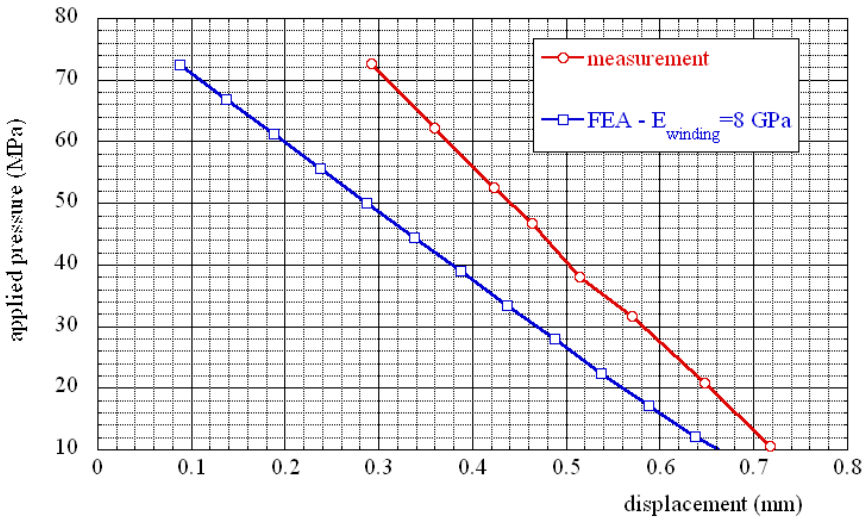

FIG.124: Comparison between the measured displacement-applied force curve and the one obtained through FE analysis with 8 GPa as Young modulus of the winding (the displacement is the distance of the pressing tool to the ideal winding midplane).

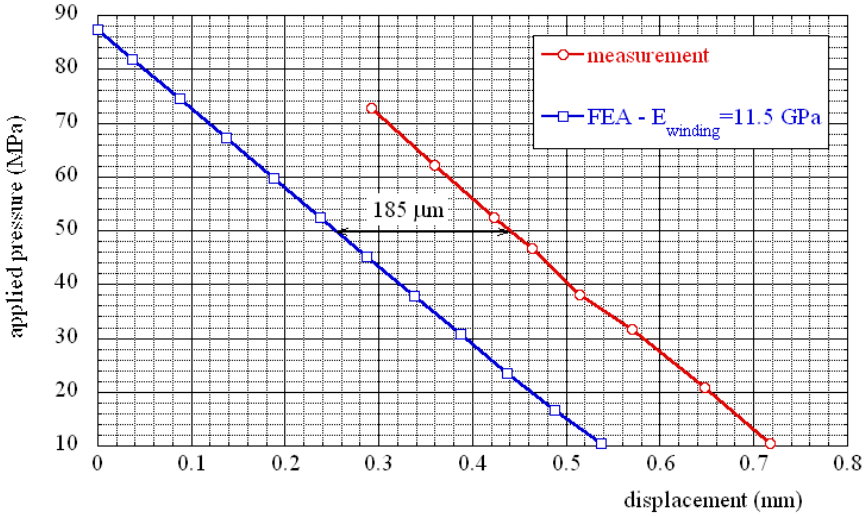

FIG.125: Comparison between the measured displacement-applied force curve and the one obtained through FE analysis with 11.5 GPa as Young modulus of the winding (the displacement is the distance of the pressing tool to the ideal winding midplane).

measured arc piled sample and the FE model can be considered acceptable.

14.2 Complete dipole

A set of measurements, in different locations longitudinally, have been performed on the first complete winding. The measurements have been carried out by using the same tool shown in Fig.123. The winding can slide on special rails, making it possible to enter the pressing tool, as shown in Fig.126.

Fig.127 shows a comparison among the measurements on the complete dipole in 4 different locations, the measurement on the arc piled sample and the FE analysis results with 9 GPa as Young modulus of the winding, which at best represents the slope of the real dipole.

The real dipole is still bigger than the ideal design, the difference being comprises between 230 and 290 μm, that is well inside the tolerances described in the previous paragraph. The equivalent Young modulus of the winding, 9 GPa, is compatible with both the stacked and the arc-piled samples and confirms the value, 8 GPa, which has been used in FE mechanical analysis described in Section Mechanical analyses.

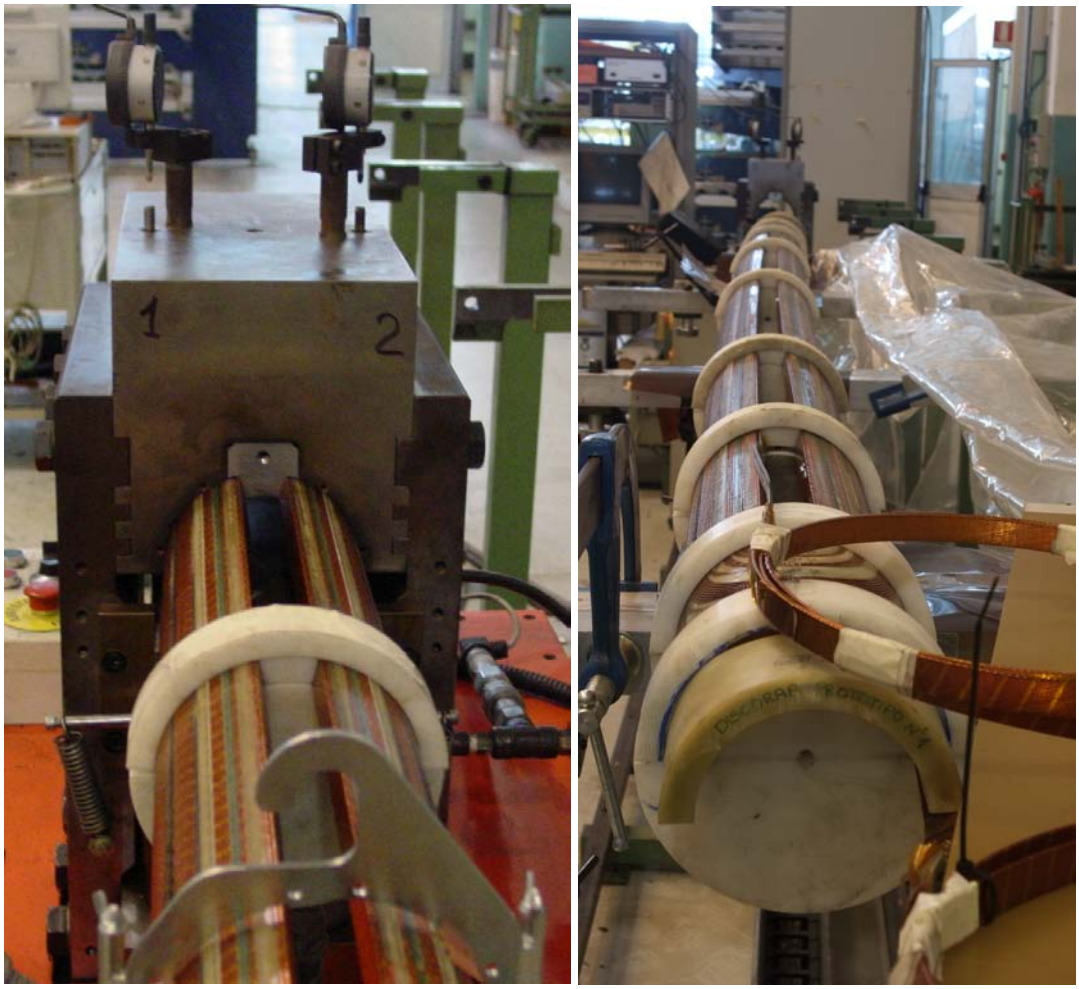

FIG.126: Stress-strain measurement on the first dipole.

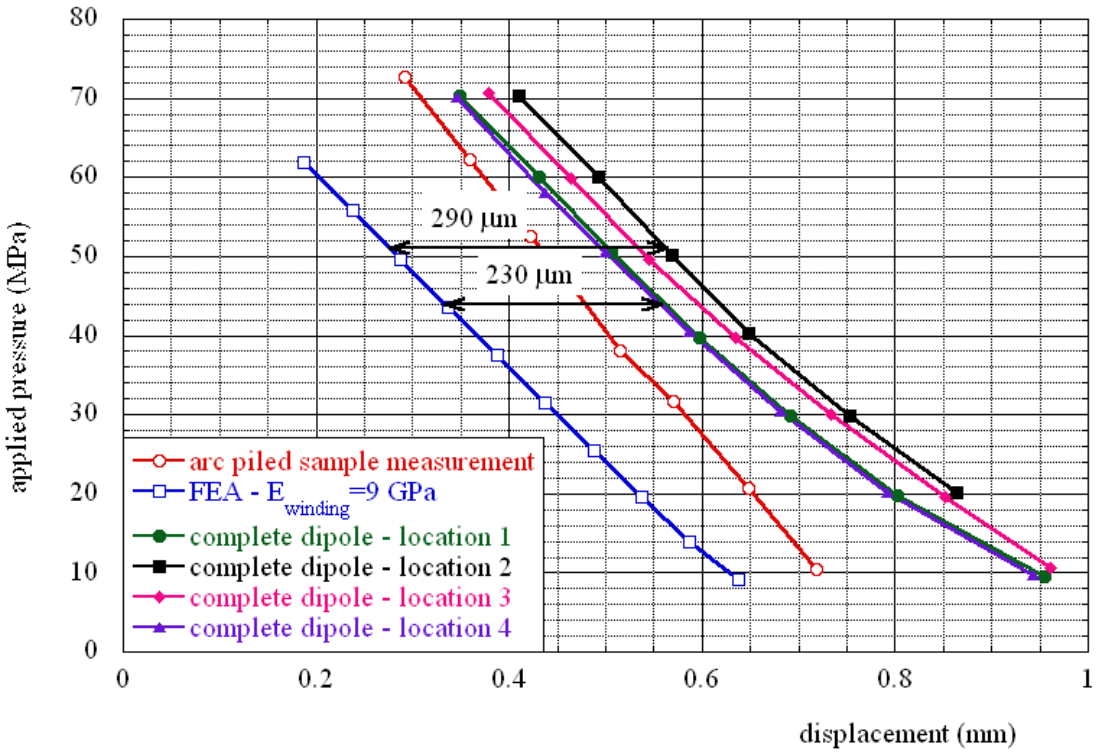

FIG.127: Comparison of the displacement-applied force curves obtained through the measurements on the complete dipole in 4 different locations, the measurement on the arc piled sample and the FE analysis results with 9 GPa as Young modulus of the winding.

15. REFERENCES

(1) W.F.Henning, “The GSI project: An international facility for ions and antiprotons”, Nucl. Phys. A, Nuclear ad hadronic physics, **734**, 654–660 (2004).

(2) G.Moritz, “Superconducting magnets, for the International accelerator facility for beams of ions and antiprotons at GSI”, IEEE Trans. Appl. Supercond. **13** (2), 1329–1334, (2003).

(3) P.Fabbricatore, S.Farinon, U.Gambardella and G.Volpini, “Rapid cycling superconducting magnets” Nucl. Phys. B **154**, 157-162 (2006).

(4) P.Fabbricatore, F.Alessandria, G.Bellomo, S.Farinon, U.Gambardella, J.Kaugerts, R.Marabotto, R.Musenich, G.Moritz, M.Sorbi, and G.Volpini, “Development of a curved fast ramped dipole for FAIR SIS300”, IEEE Trans. Appl. Supercond. **18** (2), 232-235 (2008).

(5) M.Sorbi, F.Alessandria, G.Bellomo, P.Fabbricatore, S.Farinon, U.Gambardella, and G.Volpini, “Field quality and losses for the 4.5 T superconducting pulsed dipole of SIS300”, IEEE Trans. Appl. Supercond. **18** (2), 138 141 (2008).

(6) G.Volpini, F.Alessandria, G.Bellomo, P.Fabbricatore, S.Farinon, U.Gambardella, and M.Sorbi, “Low-loss NbTi Rutherford cable for application to the development of SIS-300 dipoles”, IEEE Trans. Appl. Supercond. **18** (2), 997 1000 (2008).

(7) S.Farinon, P.Fabbricatore, R.Musenich, F.Alessandria, G.Bellomo, M.Sorbi, G.Volpini, U.Gambardella, R.Marabotto “A model dipole for FAIR SIS300: design of the mechanical structure”, IEEE Trans. Appl. Supercond. **19** (3), (2009). In publication.

(8) M.Sorbi, F.Alessandria, G.Bellomo, P.Fabbricatore, S.Farinon, U.Gambardella, R.Musenich and G.Volpini “Electromagnetic design of the coil-ends for the FAIR SIS300 model dipole”, IEEE Trans. Appl. Supercond. **19** (3), (2009). In publication.

(9) J.E.Kaugerts, G.Moritz, C.Muehle, A.Ageev, I.O.Bogdanov, S.Kozub, P.Shcherbakov, V.Sytnik, L.Tkachenko, V.Zubko, D.Tommasini, M.N.Wilson, W.Hassenzahl, “Design of a 6 T, 1T/s fast-ramping synchrotron magnet for GSI’s planned SIS 300 accelerator”, IEEE Trans. Appl. Supercond. **15** (2), 1225–1227, (2005).

(10) C.Lanza and D.Perini, “Characteristics of the Austenitic Steels Used in the LHC Main Dipoles”, IEEE Trans. Appl. Supercond. **12** (1),1252–1255 (2002).

(11) “Handbook on materials for superconducting machinery”, Metals and ceramics information center Battelle, Columbus Ohio (1977).

(12) M.N.Wilson, M.Anerella, G.Ganetis, A.K.Ghosh, P.Joshi, A.Marone, C.Muehle, J.Muratore, J.Schmalzle, R.Soika, R.Thomas, P.Wanderer, J.Kaugerts, G.Moritz, W.V.Hassenzahl, “Measured and calculated losses in model dipole for GSI's heavy ion synchrotron”, IEEE Trans. Appl. Supercond. **14** (2), 306–309 (2004).

(13) C.Peters, K.Mirk, A.Wandesforde, and C.Taylor, “Use of tapered key collars in dipole models for the SSC”, IEEE Trans. Magn. **24** (2), (1988).

(14) H.Kanithi, W.Wiegert, P.Valaris, M.D.Sumption, and E.W.Collings, “Current density and magnetization of fine filamentary NbTi superconductors”, Supercollider 5, Edited by P. Hale, Plenum Press, New York (1994).

(15) G.Volpini, F.Alessandria, G.Bellomo, M.Sorbi, P.Fabbricatore, S.Farinon, R.Musenich, U.Gambardella, J.Kaugerts, G.Moritz, M.N.Wilson, “Low-Loss Wire Design for the DISCORAP Dipole”; WAMSDO Workshop, CERN, (2008).

(16) M.N.Wilson, GSI Fast-Pulsed Synchrotron Project Report 29 v. 2, (2007).

(17) J.Kaugerts, G.Moritz, M.N.Wilson, A.Ghosh, A.den Ouden, I.Bogdanov, S.Kozub, P.Shcherbakov, L.Shirshov, L.Tkachenko, D.Richter, A.Verweij, G.Willering, P.Fabbricatore, G.Volpini, "Cable Design for FAIR SIS 300", IEEE Trans. Appl. Supercond. **17** (2), 1477-1480 (2007).
(18) H.C.Kanithi, P.Valaris and B.A.Zeitlin, "Superconductors with 2.5 micron NbTi filaments" Supercollider 3, (1991).
(19) M.N.Wilson *et al.*, "Measured and calculated losses in model dipole for GSI's heavy ion synchrotron" IEEE Trans. Appl. Supercond. **14** (2), 306-309 (2002).
(20) J.Kaugerts *et al.*, "Design of a 6 T, 1T/s fast-ramping synchrotron magnet for GSI's planned SIS 300 accelerator" IEEE Trans. Appl. Supercond. **15** (2), 1225-1228 (2005).
(21) M.N.Wilson *et al.*, "Design studies on superconducting Cos θ magnets for a fast pulsed synchrotron", IEEE Trans. Appl. Supercond. **12** (1), 313-316 (2002).
(22) R.Soika, M.D.Anerella, A.K.Ghosh, P.Wanderer, M.N.Wilson, W.V.Hassenzahl, J.Kaugerts and G.Moritz, "Inter-strand resistance measurements in cored Nb-Ti Rutherford cables", IEEE Trans. Appl. Supercond. **13** (2), 1704-1709 (2003).
(23) G.P.Willering, A.P.Verweij, J.Kaugerts and H.H.J.ten Kate, "Stability of NbTi Rutherford Cables Exhibiting Different Contact Resistances" IEEE Trans. Appl. Supercond. **18** (2), 1263-1266 (2008).
(24) "NTA_DISCORAP Superconducting low loss Rutherford cable technical specification", INFN-LASA-DiscoRap note n. 16 v. 8 (2007).
(25) P.Fessia *et al.*, "Curing of LHC main dipole coils insulated with all Polyimide PIXEO® adhesive tape", IEEE Trans. Appl. Supercond. **16** (2), 1782-1785 (2006).
(26) A.Devred, "Pratical low-temperature superconductors for electromagnets," report CERN-2004-006, 43-44.
(27) L.Rossi and M.Todesco, "Electromagnetic design of superconducting dipoles based on sector coils," Phys. Rev. ST Accel. Beams **10**, 112401 (2007).
(28) A.P.Verweij and R.Wolf, "Field errors due to interstrand coupling currents in the LHC dipole and quadrupoles", CERN internal note AT/MA 94-97 (1995).
(29) G.Volpini, "Analisi della magnetizzazione del Cu-0.5%wt Mn e applicazione ai fili superconduttori," INFN internal note, 9 March 2009.
(30) M.N.Wilson, "Superconducting Magnets", Clarendon Press Oxford, (1983).
(31) S. Russenschuck "Electromagnetic Design and Mathematical Optimization Methods in Magnet Technology," eBook, January 2006, http://russ.home.cern.ch/russ, ISBN: 92-9083-242-8.
(32) M.N. Wilson, "Pulsed Superconducting Magnets", CERN Academic Training Course (2006).
(33) F.Alves, R.Lebourgeois and T.Waeckerle. "Soft magnetic materials for electrical engineering: State of the art and recent advances", Euro. Trans. Electr. Power **15**, 467–479 (2005).
(34) G.Bertotti "General properties of power losses in soft ferromagnetic materials", IEEE Trans. Magn. **24** (1), 621–630 (1988).
(35) I.Bogdanov, S.Kozub et al. "Study of electrical steel magnetic properties for fast cycling magnets of SIS100 and SIS300 rings", Proceedings of EPAC 2004, 1741–1743 (2004).
(36) M.Latour, "Note on losses in sheet iron at radio frequencies", Proceedings of the IRE **7** (1), 61–71 (1919).

(37) Free finite element package for 2D planar/axisymmetric problems in low frequency magnetic available at http://femm.foster-miller.net/wiki/HomePage.
(38) A.F:Clark, R.P.Reed and E.C.Van Reuth, “Materials research in support of superconducting machinery – IV”, Fourth semi-annual Technical Report, National Bureau of Standards (1975).
(39) L. Rossi, M. Sorbi, “MATPRO: a computer library of material property at cryogenic temperature”, INFN Technical Note (2006), http://www.lnf.infn.it/sis/preprint/pdf/getfile.php?filename=INFN-TC-06-2.pdf.
(40) Cryocomp Libraries 1995: from Cryodata Inc. (Horizon Technologies, www.htess.com).
(41) YUTOPIAN, Useful thermal and mechanical properties, http://www.yutopian.com/Yuan/prop/index.html.
(42) L.Rossi, M.Sorbi, “QLASA: a computer code for quench simulation in adiabatic multicoil superconducting windings”, INFN/TC-04/13 (2004). http://www.lnf.infn.it/sis/preprint/pdf/getfile.php?filename=INFN-TC-04-13.pdf
(43) R. Barron, “Cryogenic Systems”, MacGROW-HILL (1967).
(44) G.K.Withe, “Experimental techniques in low temperature physics”, Clarendon Press, Oxford, (1979).
(45) M.La China, J.Garcia Perez, G.Gubello, C.Hauviller, W.Scandale, E.Todesco, “Geometrical position of the Large Hadron Collider main dipole inside the cryostat”, LHC project report 576, presented at 8th EPAC, 3-7June 2002, La Villette, Paris, F.
(46) F.Seyvet, J.B.Jeanneret, A.Poncet, D.Tommasini, J.Beauquis, E.D.Fernandez Cano, E.Wildner, “Improvement of the geometrical stability of the LHC cryodipoles when blocking the central support POST”, proc. of 2005 PAC.
(47) L.Helmersen, Danfysik, private communication.
(48) F.Savary, M.Bajko, M.Cornelis, P.Fessia, J.Miles, M.Modena, G.de Rijk, L.Rossi, and J.Vlogaert, “Status report on the series production of the main superconducting dipole magnets for LHC”, IEEE Trans. Appl. Supercond. **16** (2), 425–428 (2006).